Physics of Atomic Nuclei, Vol. 67, No. 12, 2004, pp. 2107–2121. Translated from Yadernaya Fizika, Vol. 67, No. 12, 2004, pp. 2131–2144.
Original Russian Text Copyright © 2004 by Varlamov, Ishkhanov, Rudenko, Stepanov.

NUCLEI
Experiment

Energy Resolution of Experiments with Quasimonoenergetic Annihilation Photons and Structure of a Giant Dipole Resonance

V. V. Varlamov*, B. S. Ishkhanov[1)], D. S. Rudenko[1)], and M. E. Stepanov[1)]

Institute of Nuclear Physics, Moscow State University, Vorob'evy gory, Moscow, 119992 Russia

Received March 27, 2003; in final form, October 22, 2003

Abstract—Reasons behind the known systematic discrepancies between the results of photonuclear experiments performed with different photon beams are investigated in detail. Information about the cross sections obtained for the reactions ^{63}Cu$(\gamma, n)^{62}$Cu and ^{197}Au(γ, xn) at all stages of experiments with quasimonoenergetic photons from relativistic positrons annihilating in flight is studied, and a comparison with the data of experiments with beams of bremsstrahlung gamma radiation is performed. Data obtained in experiments of both types for the reaction ^{16}O(γ, xn) are used in the present analysis. It is shown that the difference procedure typically used experiments with quasimonoenergetic annihilation photons hinders the estimation of the actual energy resolution substantially, thus leading to a considerable distortion of information about the structure of cross sections for photonuclear reactions. © *2004 MAIK "Nauka/Interperiodica".*

INTRODUCTION

It is well known that investigation of photon-induced reactions and of the properties of giant dipole resonances in nuclei has played an extremely important role in evolving currently prevalent ideas of the structure and dynamics of nuclei and in clarifying the mechanisms of nuclear reactions. The discrepancy between the experimentally observed properties of giant dipole resonances and their theoretical counterparts from shell-model calculations, which was firmly established in the mid-1950s, led to discovering collective nuclear states and the mechanism of their formation in the shell model. The ensuing development of nuclear physics was associated to a considerable extent with the investigation of collective nuclear states, their role in various reactions, their interaction with single-particle degrees of freedom, their decay modes, and other similar phenomena involving these degrees of freedom. It should be noted in this connection that, while the position of giant dipole resonances on the energy scale and their shape are well described within the simplest collective nuclear model both in spherical and in deformed nuclei, attempts at describing, on the basis of this model, the features of the decay of highly excited nuclear states ran into some difficulties. To overcome these difficulties, it was required to develop first the single-particle and then the multiparticle shell model. The latter, which predicts the appearance of strong coherent $E1$ excitations in the region of energies substantially higher than the energies of single-particle electric-dipole vibrations, was able to describe correctly the position of a giant dipole resonance on the energy scale but not its shape. As a matter of fact, the theoretical spectrum of $E1$ excitations is much poorer than its experimental counterpart, the special features of the latter including the following:

(i) The gross structure (structural features of width about 1 MeV) and the width (size of the region over which the strongest $E1$ nuclear excitations are spread) of photoabsorption cross sections are determined by single-particle–single-hole $(1p1h)$ states.

(ii) The intermediate structure (structural features of width about 0.1 MeV) of giant dipole resonances is formed owing to the coupling of doorway states to more complicated states of a collective character.

(iii) The fine structure (structural features of width about 0.01 MeV) of giant dipole resonances arises owing to the coupling of doorway states to noncollective multiparticle–multihole states.

Effects caused, for example, by the difference in the configuration structure of nuclear shells and by isospin selection rules also complicate significantly the shape of giant dipole resonances.

The overwhelming majority of data presented in the literature [1–5] for photonuclear-reaction cross sections were obtained by using bremsstrahlung gamma rays or quasimonoenergetic photons produced upon the in-flight annihilation of relativistic

[1)]Moscow State University, Vorob'evy gory, Moscow, 119899, Russia.
*e-mail: varlamov@depni.sinp.msu.ru

positrons. As soon as the first data obtained by the two methods in question appeared, it became clear—presently, this is well known—that they disagree systematically to a considerable extent (in shape, magnitude, and position on the energy scale), and this complicates significantly the application of such data in practice. The main distinction here is that, in the overwhelming majority of cases, the reaction cross sections are much smoother in data from experiments with quasimonoenergetic annihilation photons [1, 5] than in data from experiments with bremsstrahlung gamma rays. As a rule, cross sections obtained by using bremsstrahlung photons involve distinct structural features (changing sizably from one nucleus to another), resonances having various widths. For almost all nuclei (with the exception of light ones), cross sections obtained with quasimonoenergetic annihilation photons have the form of a smooth resonance (two smooth resonances in the case of deformed nuclei), despite the fact that the energy resolutions quoted by the authors of the corresponding experimental studies (about 250 to 400 keV) are quite sufficient for isolating, in reaction cross sections, resonances of not only the gross but also the intermediate structure.

In view of these discrepancies, the problem of assessing the reliability of the observation of resonances in the structure of a giant dipole resonance (especially in medium-mass and heavy nuclei) and the problem of finding out why such resonances are present within one method and why they are absent within the other method are of great interest. Although the experiments being discussed were performed rather long ago (about 10 to 15 years ago), the problem of studying the reasons behind the above discrepancies and the more important problem of developing methods for removing these discrepancies are quite pressing even now for a number of reasons, including that associated with the extensive use of the respective results, which are included in numerous databases, in fundamental and applied investigations. A great number of studies [6–14] were devoted to various aspects of these problems. For a large number of nuclei, these efforts resulted in constructing systematics of various parameters that characterize the discrepancies being discussed and in revealing basic regularities in the relation between these discrepancies and conditions of specific experiments and of the interpretation of their results. It was found that the main distinction in the conditions of experiments aimed at extracting reaction cross sections consisted in the difference of effective photon spectra. It was shown that a rather complex shape of such spectra in experiments with quasimonoenergetic annihilation photons complicates (renders unjustified), in many cases, the interpretation of the results as the sought cross sections proper. Special methods were developed for recasting the results of different experiments into a unified representation that admits their interpretation in terms of reaction cross sections obtained with a specific energy resolution.

The present study is devoted to a detailed investigation of the energy resolution actually achieved at all stages of typical experiments with quasimonoenergetic annihilation photons and to analyzing the reasons behind the discrepancies between their results and traditional estimates based on the width of the annihilation line in the spectrum of photons inducing the reaction being considered. Our investigations were performed on the basis of processing not only well-known ultimate results of experiments with quasimonoenergetic annihilation photons but also their intermediate results that are close to the results of typical experiments with bremsstrahlung photons in what is concerned with the conditions of the derivation of data and which are published very rarely. In particular, we use data of Sund *et al.* [15] and Fultz *et al.* [16], whose facilities for determining, according to the scheme of a typical experiment with quasimonoenergetic annihilation photons, the cross sections for the reactions ^{63}Cu(γ, n)^{62}Cu and ^{197}Au(γ, xn), respectively, are virtually identical from the point of view of the problems being discussed.

1. BASIC FEATURES OF THE METHODS FOR OBTAINING INFORMATION ABOUT THE CROSS SECTIONS FOR PHOTONUCLEAR REACTIONS IN DIFFERENT EXPERIMENTS

1.1. Experiments with Beams of Bremsstrahlung Gamma Rays

Historically, the first experiments that provided data on a large width of a giant dipole resonance and its complicated shape were based on measurements in beams of bremsstrahlung photons. Since the photon spectrum is continuous in such experiments and is described by expressions obtained by various authors, including Schiff, Seltzer and Berger, and Bethe and Heitler, one cannot measure directly the reaction cross section σ itself. Instead, the result is obtained in the form of its convolution with the photon spectrum (integral of their product)—that is, the reaction yield Y,

$$Y(E_{jm}) = \frac{N(E_{jm})}{\varepsilon D(E_{jm})} = \alpha \int_{E_{\rm thr}}^{E_{jm}} W(E_{jm}, E)\sigma(E)dE, \quad (1)$$

where $\sigma(E)$ is the cross section at a photon energy E for the reaction having an energy threshold $E_{\rm thr}$,

$W(E_{jm}, E)$ is the bremsstrahlung-photon spectrum having an endpoint energy E_{jm}, $N(E_{jm})$ is the number of reaction events, $D(E_{jm})$ is the gamma-radiation dose, ε is the detector efficiency, and α is a normalization factor.

Information about the reaction cross section σ is extracted from data on the reaction yield Y by using one of numerous mathematical methods specially developed for this purpose (these include the photon-difference method, the inverse-matrix method, the Penfold–Leiss method, the method of Cook structure, Tikhonov's regularization method, and the least reduction method). Within these methods, procedures used to treat values of Y are constructed in such a way that the effective spectrum $F(E_{jm}, E)$ of photons causing the reaction in question (instrumental function characterizing the method or its resolution function) would be rather well localized (see Fig. 1). In the majority of relevant experiments, the width of the quasimonoenergetic line in the instrumental function near photon energies at which one evaluates the cross section σ is 100 to 200 keV. Thus, the use of one of the above methods for determining the reaction cross section $\sigma(E)$ from the experimental reaction yield $Y(E_{jm})$ actually provides information about the estimated cross section

$$\sigma^{\text{est}}(E) = \int F(E_{jm}, E)\sigma(E)dE, \qquad (2)$$

its deviation from the sought cross section $\sigma(E)$ being controlled by the deviation of $F(E_{jm}, E)$ from a delta function.

Of particular importance for the ensuing discussion are the following two circumstances:

(i) Complicated shapes of the instrumental functions in the methods for extracting information about the reaction cross section from the experimental reaction yield introduce distortions in the cross section to be determined and errors in the estimate of the energy resolution that is actually achieved.

(ii) Since the basic lines of the instrumental functions in experiments with bremsstrahlung photons are rather well localized on the energy scale, the results obtained in such experiments can be interpreted, despite some obvious flaws, as precisely the sought reaction cross section.

1.2. Experiments with Quasimonoenergetic Photons Obtained upon the In-Flight Annihilation of Relativistic Positrons

Since the beginning of photonuclear investigations, the need for solving an ill-posed inverse problem [integral Eq. (1)] has given impetus to searches for alternative methods that would make it possible to create conditions under which a quasimonoenergetic character of the effective spectrum of photons causing the reaction under study is achieved directly in an experiment. The method of obtaining quasimonoenergetic photons upon the in-flight annihilation of accelerated positrons became one of such alternatives. The method is based on the fact that, in the case of relativistic-positron annihilation in a converter target, photons of energy localized within quite a narrow interval are emitted into the forward hemisphere. Such photons are inevitably accompanied by positron-bremsstrahlung photons having a spectrum similar (there are reasons to believe that it is identical) to the spectrum of electron-bremsstrahlung photons. In view of this, a difference scheme of an experiment was proposed for determining the cross section for the reaction induced by such photons. This scheme includes three steps of measurements (see Fig. 2):

(i) measurement of the yield $Y_{e^+}(E_j)$ (1) in the reaction induced by a beam formed by positron-bremsstrahlung photons and quasimonoenergetic positron-annihilation photons;

(ii) measurement of the yield $Y_{e^-}(E_j)$ (1) in the reaction induced by electron-bremsstrahlung photons;

(iii) evaluation (after the corresponding normalization) of the difference of the measured yields,

$$Y_{e^+}(E_j) - Y_{e^-}(E_j) = Y(E_j) \approx \sigma(E). \qquad (3)$$

Assuming that the positron- and electron-bremsstrahlung spectra are identical and considering that the calculated width of the annihilation line is relatively small, one interprets this difference as the cross section $\sigma(E)$.

By definition, the reaction-yield difference (3) corresponds to an experiment where the instrumental function $F(E_{jm}, E)$ (2) is the difference of the two corresponding experimental photon spectra; under the assumption that the positron- and the electron-bremsstrahlung spectra are identical, this is the line associated with annihilating positrons. It is obvious, however, that, in contrast to what we have in experiments with bremsstrahlung photons, where the instrumental function for the method used is calculated irrespective of the conditions of a specific experiment (moreover, precisely those conditions for which the bremsstrahlung spectrum was calculated are created in an experiment, as a rule), the instrumental function in experiments with quasimonoenergetic annihilation photons is actually determined anew each time. It should also be noted that, while the shape of the calculated annihilation line [1, 5, 17] depends only on the geometric and energy conditions of in-flight positron annihilation, the shape of the instrumental function for the whole experiment depends on the accuracy in determining the experimental reaction yields (3) and on the accuracy to which these yields

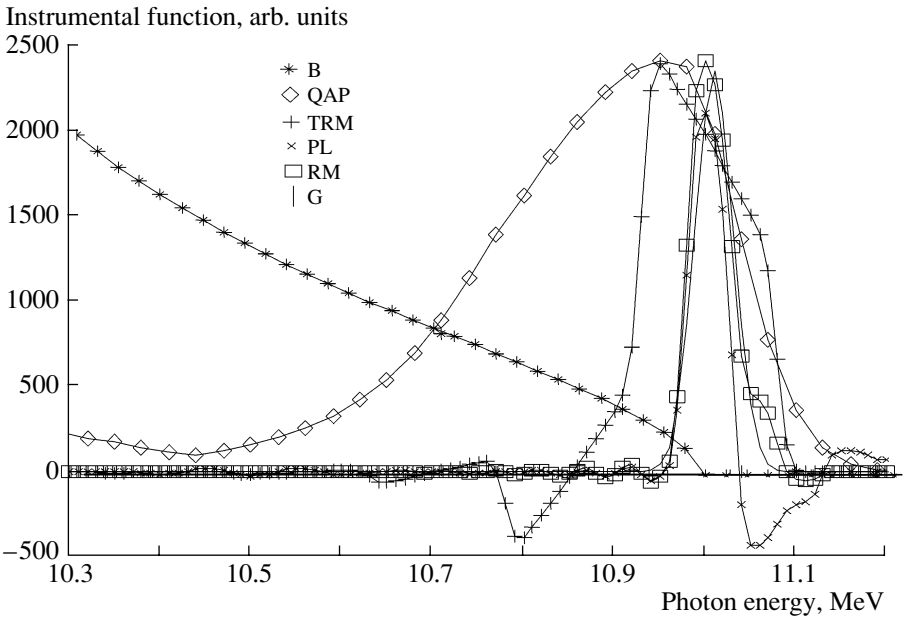

Fig. 1. Comparison of instrumental functions (effective photon spectra) corresponding to various methods for deriving information about cross sections for photonuclear reactions: (B) spectrum of bremsstrahlung photons (example for $E_\gamma^{\max} =$ 11 MeV), (QAP) spectrum of quasimonoenergetic annihilation photons (the width of the annihilation line is 350 keV), (PL) instrumental function in the Penfold–Leiss method (the step of processing is 100 keV); (TRM) instrumental function in Tikhonov's regularization method (the step of processing is 50 keV), (RM) instrumental function in the reduction method (the resolution is 50 keV), and (G) Gaussian function of width 50 keV.

are normalized with respect to one another. However, the latter accuracy is quite poor, since annihilation photons originate from a multistep process (which involves the production of bremsstrahlung photons by electrons in a special target, $e^- + A \to A + e^- + \gamma$; the production of bremsstrahlung gamma radiation from electron–positron pairs by photons, $\gamma + A \to A + e^- + e^+$; and the annihilation of product positrons, $e^+ + e^- \to 2\gamma$); as a result, the intensity of the "beam" of quasimonoenergetic photons is rather low.

The above circumstances result in that the instrumental function $F(E_{jm}, E)$ (see Figs. 1, 2) in experiments with quasimonoenergetic annihilation photons differs in shape substantially from a simple symmetric annihilation line [1, 5, 17]. The main distinctions are the following:

(i) Since the annihilation target is insufficiently thin, the line is highly asymmetric (the decrease toward the region of low energies is strongly extended).

(ii) By and large, the instrumental function is actually not localized on the energy scale (in addition to the annihilation line, the spectrum involves alien contributions extended in energy—a pedestal and a bremsstrahlung tail).

Not only do the above alien contributions complicate substantially the estimation of the actually achieved energy resolution, but, in view of the presence of extra photons in the spectrum near the annihilation line, they also lead to considerable distinctions in amplitude between the reaction cross sections from experiments with bremsstrahlung photons and from experiments with quasimonoenergetic annihilation photons and, because of the shift of the centroid of the spectrum away from the annihilation-line maximum, to distinctions between their positions on the energy scale. It appears to be rather difficult to estimate the resolution actually achieved for such a "cross section," and the problem of assessing the degree to which it agrees with the respective estimate based on the calculated width of the annihilation line in the photon spectrum remains in fact unclear.

Concurrently, the following circumstance is worthy of note: in the majority of the experiments performed thus far, the annihilation-line width was significant, about 250 to 400 keV (sometimes, it was as large as 500 keV, more rarely falling between 150 and 300 keV), because of the use of rather thick annihilation targets, which were dictated by the low intensity of the multistep annihilation-photon-production process. All of the aforesaid affects significantly the spectrum of quasimonoenergetic annihilation photons.

2. SYSTEMATIC DISAGREEMENT BETWEEN THE PHOTONUCLEAR-REACTION CROSS SECTIONS OBTAINED IN EXPERIMENTS WITH BREMSSTRAHLUNG PHOTONS AND IN EXPERIMENTS WITH QUASIMONOENERGETIC ANNIHILATION PHOTONS

As a matter of fact, the disagreement between the instrumental functions in the different methods implies the difference of the conditions under which one obtains results in experiments with bremsstrahlung photons and in experiments with quasimonoenergetic annihilation photons, this being interpreted in either case as reaction cross sections. Naturally, this is reflected in that the results of experiments with bremsstrahlung photons and experiments with quasimonoenergetic annihilation photons, where the overwhelming majority of data on the cross sections for photonuclear reactions have been obtained thus far, differ systematically [1, 5].

As a typical example of the manifestation of the aforementioned distinctions, a comparison of data on the cross section for the reaction $^{16}\mathrm{O}(\gamma, xn)$ that were obtained in an experiment with bremsstrahlung photons [18] and in the experiments with quasimonoenergetic annihilation photons in Saclay [19] and in Livermore [20] is illustrated in Fig. 3. Strong resonances are clearly seen in the reaction cross sections, for which a rather high energy resolution was claimed in those experimental studies (200 keV [18], 180–280 keV [19], and 200–300 keV [20]). This figure shows that, although almost all of the special features (maxima and minima) are present in all three of the cross sections under comparison, they differ in shape, fully in accord with the foregoing. Although, in the case being considered, the estimates of the energy resolution that are presented in [19, 20] for experiments with quasimonoenergetic annihilation photons are close to the resolution of the above experiment with bremsstrahlung photons, the cross sections produced by the former method look like smoothed versions of the cross section from the experiment with bremsstrahlung photons in [18]: in them, the resonances have much smaller amplitudes and larger widths. This must also be reflected in the relationship between the integrated cross sections. By way of example, we indicate that, in the common energy region, which extends up to 25 MeV, the integrated cross sections from [18, 19] are quite close to each other (36.91 and 34.6 MeV mb, respectively). At the same time, the integrated cross section in [20], 27.92 MeV mb, differs from the above values significantly. According to the results obtained from an analysis [7, 8] of a vast set of data on the absolute values of the cross section for the total photoneutron

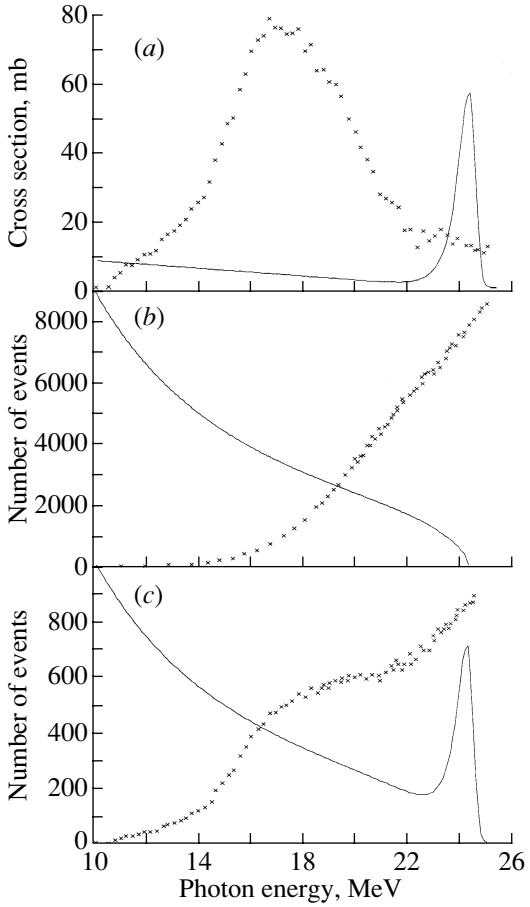

Fig. 2. Experimental data from [15] on the yields from the reaction $^{63}\mathrm{Cu}(\gamma, n)^{62}\mathrm{Cu}$ (crosses) and simulated effective photon spectra (curves): (*a*) results of an experiment with quasimonoenergetic annihilation photons [yield difference $Y_{e^+}(E_j) - Y_{e^-}(E_j) = Y(E_j) \approx \sigma(E)$ (2)] and corresponding difference of the spectra of photons produced by positrons and electrons, (*b*) yield $Y_{e^-}(E_j)$ (2) in an experiment with electron-bremsstrahlung photons and corresponding photon spectrum, and (*c*) yield $Y_{e^+}(E_j)$ (2) in an experiment with a photon beam formed by positron-bremsstrahlung photons and quasimonoenergetic positron-annihilation photons and corresponding total spectrum of photons.

reaction, (γ, xn), an additional normalization of the data obtained in Livermore from an experiment with quasimonoenergetic annihilation photons is required for bringing them in correspondence with a global systematics. The normalization factor of 1.12, which was determined on the basis of the global systematics, leads to the value of 31.27 MeV mb for the integrated cross section from [20], this result being in much better agreement with the data quoted in [18, 19].

A detailed comparison [21] of the amplitude ratios ($A_\mathrm{B}/A_\mathrm{QAP}$) and of the width ratio ($\Gamma_\mathrm{B}/\Gamma_\mathrm{QAP}$) for all resonances that were identified in the reaction cross sections for a different oxygen isotope,

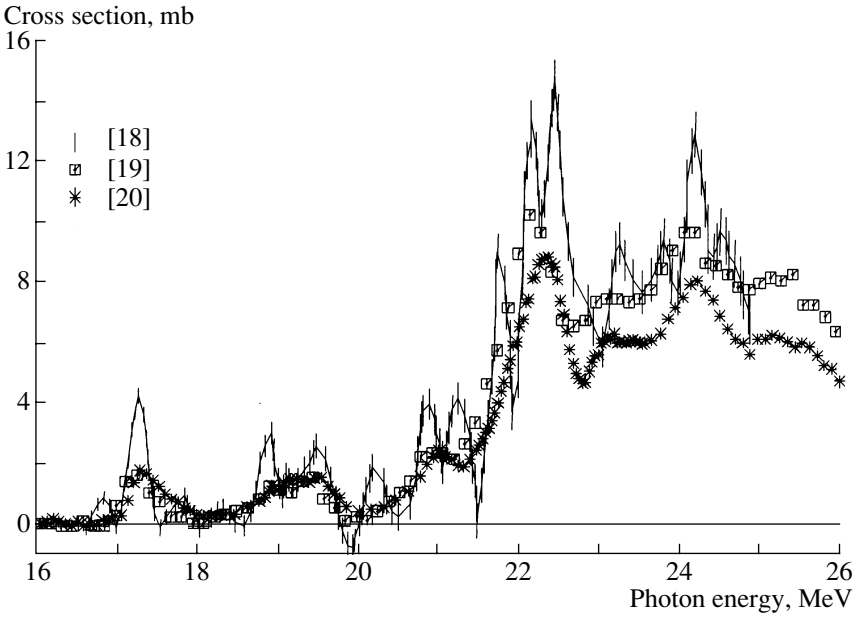

Fig. 3. Cross sections for the reaction $^{16}O(\gamma, xn)$ according to data from an experiment with bremsstrahlung photons (the energy resolution there was 200 keV) [18] and from two experiments performed with quasimonoenergetic annihilation photons in Saclay [19] and in Livermore [20] (the resolution claimed in those studies was 180–280 and 200–300 keV, respectively).

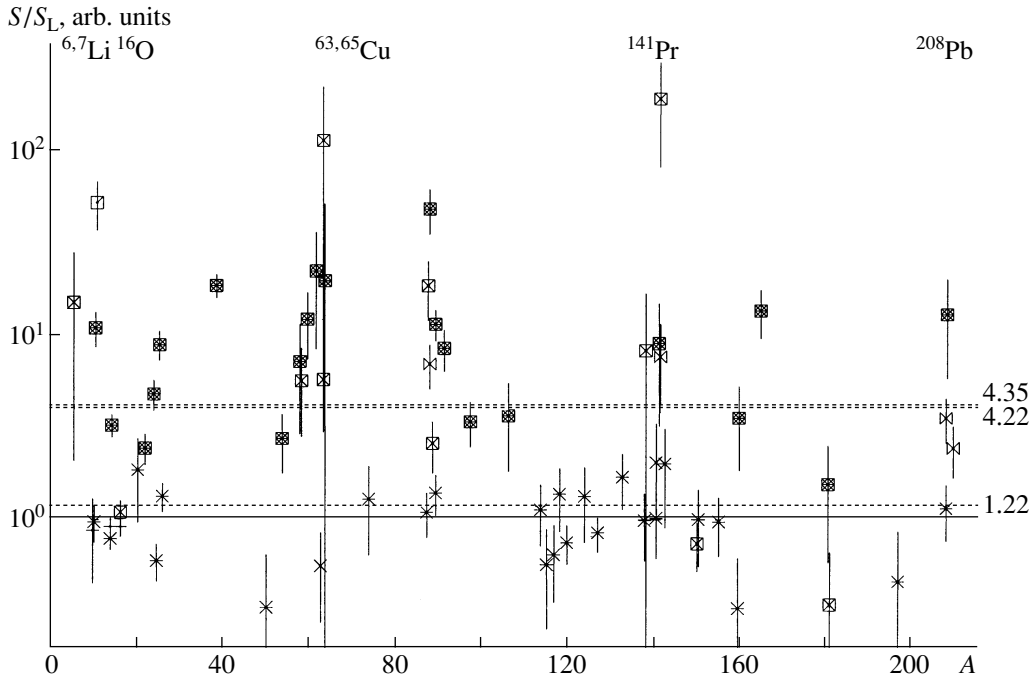

Fig. 4. Systematics of data on the parameter S/S_L of the photonuclear-reaction cross sections for various nuclei: data from experiments with bremsstrahlung photons [(⊠) Moscow, (⊠) Melbourne, and (⊡) other experiments], data from experiments with quasimonoenergetic annihilation photons [(×) Saclay, (+) Gießen, and (×) other experiments], and tagged-photon data [(⋈) Illinoice].

$^{18}O(\gamma, xn)$, that were obtained in experiments with bremsstrahlung photons (Melbourne, [21]) and with quasimonoenergetic annihilation photons (Livermore, [22]) provides more precise quantitative information about the scale of the discrepancies being discussed. Although procedures for determining the

widths and amplitudes of resonances in cross sections having a complicated structure involve a considerable degree of arbitrariness, almost all of the resonances in the cross section from the experiments with quasimonoenergetic annihilation photons have a smaller amplitude and a larger width than their counterparts from the experiments with bremsstrahlung photons ($\langle A_B/A_{QAP}\rangle = 1.17$ and $\langle \Gamma_{QAP}/\Gamma_B\rangle = 1.35$, respectively).

The general character of the dependence of the manifestation of structural features in cross sections on the method used to determine these cross sections can be illustrated by the systematics of the specially introduced structure parameter S describing, on the whole, deviations of each cross section from that which was strongly smoothed (with a step of $\Delta = 1$ MeV),

$$S = \frac{1}{N}\sum_{i=1}^{N}\frac{(\sigma_i - \langle\sigma_i\rangle)^2}{\langle\langle\sigma\rangle\rangle^2}, \quad (4)$$

$$\langle\sigma_i\rangle = \frac{1}{\Delta}\int\limits_{E_i-\Delta/2}^{E_i+\Delta/2}\sigma(E)dE, \quad (5)$$

$$\langle\langle\sigma\rangle\rangle = \frac{1}{D}\int\limits_{D}\sigma(E)dE, \quad (6)$$

where D is the common energy region of the cross sections under comparison.

Figure 4 shows the ratios S/S_L (the values of S were calculated on the basis of data from various laboratories, while the values of S_L were determined by using the data from the Livermore experiment with quasimonoenergetic annihilation photons; for some nuclei, there are no Livermore data, in which case the ratios S/S_S and S/S_H were calculated on the basis of data from the experiments performed with quasimonoenergetic annihilation photons in Saclay and Gießen). It can be seen that, among all data subjected to analysis, two data sets stand out distinctly in what is concerned with the manifestation of structural features: they are formed by cross sections measured in experiments with quasimonoenergetic annihilation photons (the mean value is $\langle S/S_L\rangle = 1.22$) and by cross sections determined in experiments with bremsstrahlung photons ($\langle S/S_L\rangle = 4.35$). It should be emphasized that, for all cross sections from experiments with quasimonoenergetic annihilation photons, the values of the parameter S/S_L (S/S_S and S/S_H) are concentrated quite closely around unity. This means that, in all three laboratories employing quasimonoenergetic annihilation photons (Livermore, Saclay, Gießen), the estimation of the experimental energy resolution on the basis of the annihilation-line width (in the majority of cases, 250–400 keV; sometimes, 500 keV; more rarely, 150–300 keV) does not lead to revealing the actual structure of a giant dipole resonance: all cross sections from the experiments with quasimonoenergetic annihilation photons are significantly oversmoothed (with a resolution of about 1 MeV).

This is also confirmed by the fact that, for the parameter being discussed, data obtained in Illinoice [23] by using a beam of tagged photons yield a value ($\langle S/S_L\rangle = 4.22$) that exceeds considerably its counterpart in the experiments with quasimonoenergetic annihilation photons and which is close to that in the experiments with bremsstrahlung photons. Since, in the experiments with tagged photons, the instrumental function is in fact a regular Gaussian line, the above indicates that data from experiments with bremsstrahlung photons reflect the actual structure of the cross sections much better than data from experiments with quasimonoenergetic annihilation photons.

3. CORRECTION OF THE RESULTS OF EXPERIMENTS WITH QUASIMONOENERGETIC ANNIHILATION PHOTONS FOR THE SHAPE OF THE EFFECTIVE PHOTON SPECTRUM AND ESTIMATION OF THE ENERGY RESOLUTION ACTUALLY ACHIEVED IN SUCH EXPERIMENTS

As was indicated above, it was shown previously [6–14] that, instead of the reaction cross section, a specific experiment where the instrumental function differs significantly from that which is close to an ideal one (for example, a Gaussian line of small width) yields the convolution (2) of the cross section with the effective photon spectrum $F(E_{jm}, E)$. Obviously, the possibility of interpreting this convolution as a cross section depends on the shape of the effective photon spectrum.

For instance, the convolution of the cross section from an experiment employing bremsstrahlung photons with the instrumental function for one of the most popular methods for reconstructing the cross section on the basis of the experimental yield (see Fig. 1) can be interpreted, owing to a strong localization of this instrumental function, as the cross section itself, although this cross section is somewhat distorted, since the shapes of the instrumental functions used deviate from regular shapes—say, Gaussian ones. As a matter of fact, the reaction yield (1) itself in an experiment with bremsstrahlung photons can also be interpreted as the reaction cross section as measured with an instrumental function whose width is very large (tends to infinity).

At the same time, the situation around the results of experiments with quasimonoenergetic annihilation photons is much more intricate: in view of the definition in (3) and in view of the existence of extended alien contributions (see Figs. 1, 2) to the instrumental function, these results are again only the reaction yields rather than the cross sections proper localized in energy. In order to obtain data on the reaction cross section, it is necessary to correct the results for the shape of this instrumental function. The authors of [6–14] employed the reduction method for introducing such a correction [24, 25]. Not only does this method make it possible to transform quite straightforwardly the reaction cross section from its form for a specific shape of the effective photon spectrum $F(E_{jm}, E)$ to a form that this cross section would have for a different shape of the effective photon spectrum (for example, in the form of a regular Gaussian curve), but it also permits calculating errors in the estimated cross section.

3.1. Reduction Method

Briefly, the fundamentals of the reduction method [24, 25] are as follows. The integral Eq. (1) for various photonuclear experiments is represented in a matrix form ([A, Σ] model), the relation between the reaction yield and the reaction cross section being taken in the form

$$y = A\sigma + \nu, \tag{7}$$

where y is the experimental reaction yield, A is the instrumental function such that it transforms the input signal σ into the output signal y, σ is the reaction cross section, ν is a noise, and ν_i stands for random errors in Y_i such that $\Delta Y_i^2 = M(\nu_i)^2 = M((\nu_i - M\nu_i)^2)$ is the mathematical expectation value. The error vector is characterized by the correlation matrix

$$\Sigma = \begin{pmatrix} \Delta Y_1^2 & & \dots & 0 \\ & \Delta Y_2^2 & \dots & \\ & & \dots & \\ 0 & & \dots & \Delta Y_n^2 \end{pmatrix}. \tag{8}$$

Within the model where the error is minimized, the reduction method [24, 25] makes it possible to find the operator R [hereafter, the symbol $(\ )^-$ denotes the pseudoinversion operator],

$$R = U(\Sigma^{-1/2}A)^-\Sigma^{-1/2} = U(A^*\Sigma^{-1}A)^-A^*\Sigma^{-1}, \tag{9}$$

such that, for a minimum level of errors,

$$M||Ry - U\sigma|| = \min, \tag{10}$$

and under the condition that a solution exists for any σ,

$$RA = U, \tag{11}$$

it enables one to obtain the vector

$$Ry = R(A\sigma + \nu) = U\sigma + (RA - U)\sigma + R\nu = \sigma^{\text{est}}, \tag{12}$$

which is interpreted as the result obtained by measuring the cross section σ with a device of preset quality U and distorted by the noise $\nu^{\text{est}} = R\nu$:

$$\sigma^{\text{est}} = Ry = U\sigma + R\nu. \tag{13}$$

The error in the estimated cross section,

$$\nu^{\text{est.}} = R\nu = G^{1/2} \tag{14}$$

is determined by the covariation matrix Σ (8):

$$G = R\Sigma R^* = U(A^*\Sigma^{-1}A)^-U^*. \tag{15}$$

A comparison of relations (13) and (2) reveals that, for a device of preset quality U, one can take, for example, a device whose instrumental function (resolution function) is a Gaussian function of width $U = \int F(E_{jm}, E)dE$.

Relations (9) and (15) specify a solution to the reduction problem formulated as follows: it is necessary to find an optimum monoenergetic representation of the reaction cross section on the basis of information contained in the reaction yield—that is, the reaction cross section for a monoenergetic effective photon spectrum with a specific energy resolution. Obviously, the reduction method is not a method for solving the ill-posed inverse problem specified by the integral Eq. (1). This is a method that makes it possible to recast the reaction cross section "measured" with the aid of a "device" having an instrumental function A into a form that this cross section would have if it were "measured" by another "device" having a different (better) instrumental function U [as applied to experiments with bremsstrahlung photons, the yield Y is the cross section "measured by a device" whose instrumental function is W (1)].

3.2. New Data on the Cross Sections for the Reactions $^{63}Cu(\gamma, n)^{62}Cu$ and $^{197}Au(\gamma, xn)$ According to an Analysis of the Results of Experiments with Quasimonoenergetic Annihilation Photons by the Reduction Method

As was shown above, the result of an actual experiment with quasimonoenergetic annihilation photons is the difference (3) of two independent measurements, each being close to a measurement in a typical experiment with bremsstrahlung photons.

In this connection, a solution to the problem of assessing the degree to which the actual resolution in an experiment with quasimonoenergetic annihilation photons differs from the traditional estimate based on the annihilation-line width can be obtained from a detailed comparison of the results of such measurements with one another and with the results of a typical experiment with bremsstrahlung photons. Upon scanning all possible sources in the literature [1–4] and available databases [26], we found only two such studies [15, 16]. With the aid of virtually identical facilities (only the methods used to detect reaction products were different), the cross sections for the reactions ^{63}Cu(γ, n)^{62}Cu and ^{197}Au(γ, xn) were determined in San Diego and Livermore, respectively, according to the scheme of a typical experiment with quasimonoenergetic annihilation photons.

All published intermediate and ultimate [in the sense of Eq. (3)] experimental results used to derive information about the cross sections for the reactions ^{63}Cu(γ, n)^{62}Cu [15] (they are presented in Fig. 2, along with the instrumental functions corresponding to the measurements) and ^{197}Au(γ, xn) [16] were individually processed [27–29] by the reduction method [see Eqs. (9)–(15)] [24, 25]. These data include

(i) the reaction yield $Y_{e^-}(E_j)$ measured in a beam of electron-bremsstrahlung photons (result of a typical experiment with bremsstrahlung photons);

(ii) the reaction yield $Y_{e^+}(E_j)$ measured in a beam formed by photons of bremsstrahlung gamma radiation and photons from positron annihilation (result close to the result of a typical experiment with bremsstrahlung photons);

(iii) the difference $Y(E_j) = Y_{e^+}(E_j) - Y_{e^-}(E_j)$ (3) of the yields, which, in a traditional experiment with quasimonoenergetic annihilation photons, is interpreted as the sought reaction cross section.

For both nuclei, all three reaction cross sections evaluated with the aid of the reduction method on the basis of the intermediate and ultimate [in the sense of Eq. (3)] results of the experiments under identical conditions (the same form of the instrumental function with a precisely determined resolution) were compared with one another (and with the results obtained in typical experiments with bremsstrahlung photons [30, 31] and also rescaled to the corresponding resolution). For a detailed comparison, we used a number of generalized parameters [27–29]. These include

(a) the integrated cross section σ^{int};

(b) the energy centroid $E_{\text{c.}}$;

(c) the sum of errors, Σ;

(d) the structure parameter S [see Eqs. (4)–(6)];

(e) the informativeness I [this is a parameter that, in a sense, describes an increase in the amount of information in the cross section as the errors ν in it decrease and as the energy resolution is improved (that is, the quantity ΔE is reduced)]:

$$I = \frac{1}{N\Delta E}\sum_{i=1}^{N}\frac{1}{\nu_i}. \qquad (16)$$

On the basis of the data in Table 1, the generalized features of the reaction cross sections from the experiments with quasimonoenergetic annihilation photons [15, 16] prior to and after processing them by the reduction method can be compared in detail with the features of the corresponding experimental cross sections from the experiments with bremsstrahlung photons [30, 31]. This makes it possible to draw some specific conclusions [27–29] concerning the actual experimental resolution in the relevant experiments.

Among the conclusions that can be drawn from the results presented in Table 1, the most important are the following:[2)]

(i) Upon treatment by the reduction method, strongly different results of different experiments appear to be close to one another in all of the parameters being considered [variations in some of the parameters are the following: from 35 to 39 in Σ for Cu (rows 2–4) and from 212 to 247 in Σ for Au (rows 7–9), from 371 to 435 in I for Cu (rows 2–4) and from 96 to 103 in I for Au (rows 7–9), and from 264 to 308 in S for Cu (rows 2–4) and from 175 to 301 in S for Au (rows 7–9)].

(ii) Upon treatment by the reduction method, the results (3) of the experiments with quasimonoenergetic annihilation photons are virtually indistinguishable, in all of the parameters, from all other results of similar treatments for Cu [15], $\Sigma = 36$, $I = 426$, and $S = 272$ (row 4), while, for Au [16], $\Sigma = 212$, $I = 98$, and $S = 175$ (row 9), the levels of errors being commensurate.

(iii) The main conclusion is that, in all of the parameters, the published results (3) of the experiments with quasimonoenergetic annihilation photons differ dramatically from the results of treatment by the reduction method for Cu [15], $\Sigma = 32$, $I = 77$, and $S = 67$ (row 5), while, for Au [16], $\Sigma = 244$, $I = 49$, and $S = 74$ (row 10), the levels of errors being commensurate.

(iv) In all of the parameters subjected to analysis, data for the Cu nucleus that were deduced with the aid of the reduction method are commensurate with the results obtained in the experiment of Sund *et al.*

[2)]The quantities Σ, I, and S are given in, respectively, mb, (MeV mb)$^{-1}$, and arbitrary units.

Table 1. Generalized features of the cross sections obtained for the reactions ^{63}Cu(γ, n)^{62}Cu and ^{197}Au(γ, xn) in [15] and [16], respectively, by using various effective photon spectra

No.	Results subjected to analysis	$E_{c.}$, MeV	σ^{int}, MeV mb	Σ, mb	I, 1/(MeV mb)	S, arb. units	ΔE, MeV
	^{63}Cu(γ, n)^{62}Cu						
1	Result of the experiment reported in [30] and performed in a beam of bremsstrahlung gamma radiation (Fig. 5*a*)	17.8	658	34	422	319	0.21
2	Result obtained by processing the yield $Y_{e^-}(E_j)$ (Fig. 5*b*)	18.0	497	39	371	308	0.21
3	Result obtained by processing the yield $Y_{e^+}(E_j)$ (Fig. 5*c*)	17.9	497	35	435	264	0.21
4	Result of processing the yield $Y(E_j) = Y_{e^+}(E_j) - Y_{e^-}(E_j)$ (Fig. 5*d*)	17.8	497	36	426	272	0.21
5	Result from [15] in the form of the yield $Y(E_j) = Y_{e^+}(E_j) - Y_{e^-}(E_j)$ (Fig. 5*e*)	17.8	497	32	77	67	0.2–0.4*
	^{197}Au(γ, xn)						
6	Result of the experiment reported in [31] and performed in a beam of bremsstrahlung gamma radiation	15.4	3660	288	45	193	0.5
7	Result of processing the yield $Y_{e^-}(E_j)$	15.2	2970	235	96	301	0.24
8	Result of processing the yield $Y_{e^+}(E_j)$	15.6	2970	247	103	229	0.24
9	Result of processing the yield $Y(E_j) = Y_{e^+}(E_j) - Y_{e^-}(E_j)$	15.4	2970	212	98	175	0.24
10	Result from [16] in the form of the yield $Y(E_j) = Y_{e^+}(E_j) - Y_{e^-}(E_j)$	15.3	2970	244	49	74	0.4**

* Energy resolution claimed by the authors of [15].

** Energy resolution claimed by the authors of [16].

[15] with bremsstrahlung photons and rescaled to a rather high energy resolution of $\Delta E = 210$ keV; in the case of the Au nucleus, the resulting data appear to be much better than the results of the experiment of Fultz *et al.* [16] with bremsstrahlung photons, this being quite natural since the energy resolution there was as poor as $\Delta E = 500$ keV.

Thus, we see that, for commensurate levels of errors, the original results (3) of experiments with quasimonoenergetic annihilation photons are characterized by substantially (severalfold) lower values of the structure parameter S and of the informativeness I in relation to the results of treatment by the reduction method for the same energy resolution as that which was claimed for the original data. From here, it obviously follows that the resolution actually achieved in [15, 16] was poorer by approximately the same factor [5.5 (= 426/77) for Cu and 2 (= 98/49) for Au].

With the aim of more precisely determining the actual values of the energy resolution in experiments with quasimonoenergetic annihilation photons, all four cross sections under comparison for both nuclei (for each nucleus, one cross section from the experiments with bremsstrahlung photons [30, 31] and three results obtained by processing, with the aid of the reduction method, the cross sections from the experiments with quasimonoenergetic annihilation photons [15, 16]) were smoothed by using Gaussian functions of variable width (ΔE) until each of these appeared to be in the best agreement ($\chi^2 = \min$) with the fifth cross section under discussion, the result (2) of the corresponding experiment with quasimonoenergetic annihilation photons [15, 16]. For the Cu nucleus, the best agreement with the cross section from [15] was achieved with a smoothing Gaussian function of width $\Delta E = 1.2$–1.3 MeV at $\chi^2_{min} = 0.03$–0.05. For the Au nucleus [16], the corresponding values are $\Delta E = 1.6$ MeV and $\chi^2_{min} = 0.11$–0.18. From these data, we can draw the conclusion that it is the width ΔE of the smoothing Gaussian

function that controls the energy resolution actually achievable in an experiment with quasimonoenergetic annihilation photons. It is three to four times greater than the estimate obtained by the authors of [15, 16] on the basis of the calculated width of the annihilation line in the spectrum of photons produced by a positron beam and agrees with the systematics from [6] (see Fig. 4). A low (1.2–1.6 MeV) actual energy resolution of experiments with quasimonoenergetic annihilation photons is the reason why structural features similar to those observed in experiments with bremsstrahlung photons cannot be revealed in the reaction cross sections obtained in [15, 16], despite the proximity of values claimed for the energy resolution (about 200 keV). It is obvious that such structural features can manifest themselves only in cross sections determined with an energy resolution close to 200 keV, and this is what one observes in cross sections obtained upon treatment by the reduction method.

In Fig. 5, one can clearly see which structural features manifest themselves [27–29] in the cross section obtained for the reaction ^{63}Cu(γ, n)^{62}Cu from the result (3) of the experiment of Sund *et al.* [15] with quasimonoenergetic annihilation photons by using the reduction method for the instrumental function in the form of a Gaussian line of width 0.21 MeV. All three cross sections obtained with the aid of the reduction method have quite distinct structural features, whose properties are quite consistent (see Table 2), their positions on the energy scale also being in agreement with the positions of the resonances in the cross section obtained in [30] and smoothed to achieve the same resolution (absolute normalization was not performed). The structural features of the corresponding cross sections for the reaction ^{197}Au(γ, xn) that were obtained with the aid of the reduction method are also in fairly good agreement [27, 28].

From all of the aforesaid, it is obvious why the structural features being discussed are not manifested in the results reported in [15, 16]: these results cannot be interpreted as cross sections for the energy resolution claimed there (0.2–0.4 MeV). The results presented in [15, 16] should be interpreted either as yields (that is, as the convolutions of cross sections with effective photon spectra of a complicated form and, hence, as results corresponding to a much poorer resolution) or as cross sections obtained with a resolution as low as about 1.2 to 1.6 MeV. It should be emphasized once again that, upon the relevant treatment of these results (that is, upon the application of the procedure recasting them into a form that they would have for the claimed resolution), they also exhibit [for the example of the reaction ^{63}Cu(γ, n)^{62}Cu, see Fig. 5 and Table 2] the corresponding structural features distinctly.

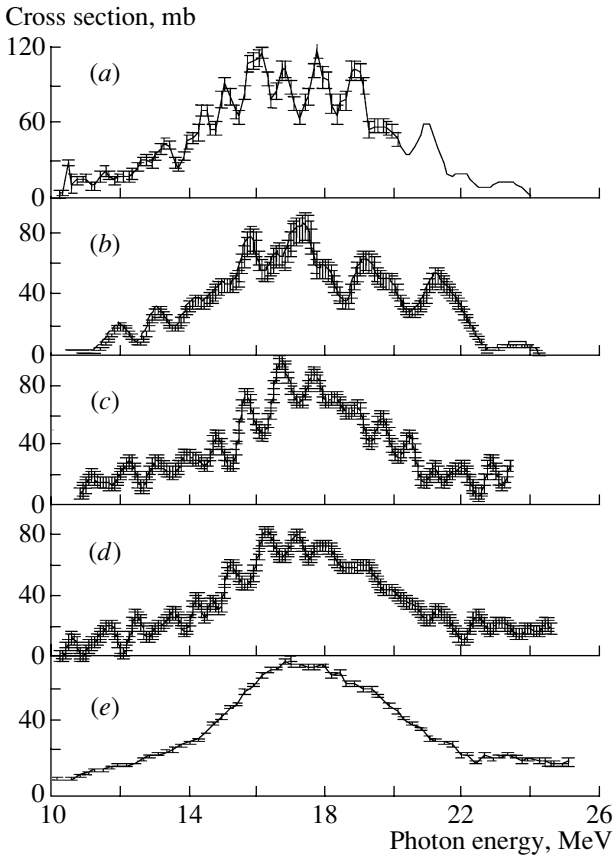

Fig. 5. Comparison of the cross sections for the reaction ^{63}Cu(γ, n)^{62}Cu that were obtained by various methods: (*a*) result of the experiment with bremsstrahlung photons that was reported in [30] (the energy resolution there was 210 keV); (*b*) result derived by processing, according to the reduction method at a resolution of 210 keV, an intermediate result of Sund *et al.* [15] that is the reaction yield $Y_{e^-}(E_j)$ within the procedure employing quasimonoenergetic annihilation photons; (*c*) result derived by processing, according to the reduction method at a resolution of 210 keV, an intermediate result of Sund *et al.* [15] that is the reaction yield $Y_{e^+}(E_j)$ within the procedure employing quasimonoenergetic annihilation photons; (*d*) result derived by processing, according to the reduction method at a resolution of 210 keV, an ultimate result [see Eq. (2)] of Sund *et al.* [15] that is the yield difference $Y_{e^+}(E_j) - Y_{e^-}(E_j) = Y(E_j)$; and (*e*) an ultimate result [see Eq. (2)] of Sund *et al.* [15] that is the yield difference $Y_{e^+}(E_j) - Y_{e^-}(E_j) = Y(E_j) \approx \sigma(E)$, the resolution claimed for this result being between 200 and 400 keV.

Obviously, the revealed considerable (severalfold) disagreement between the actual resolution of experiments with quasimonoenergetic annihilation photons and the estimate on the basis of the calculated width of the annihilation line in the effective photon spectrum leads to a considerable distortion (as a matter

Table 2. Positions of the structural features of the cross sections for the reaction ^{63}Cu(γ, n)^{62}Cu on the energy scale and amplitudes of these features according to the results of various experiments upon treatment by the reduction method for the energy resolution of $\Delta E = 0.21$ MeV

Resonance energy E_γ, MeV	Reaction cross sections obtained by the reduction method, mb			
	Cross section from the experiment of Ishkhanov *et al.* [30]*	Yield $Y_{e^-}(E_j)$ in the experiment of Sund *et al.* [15]	Yield $Y_{e^+}(E_j)$ in the experiment of Sund *et al.* [15]	Yield difference $Y(E_j) = Y_{e^+}(E_j) - Y_{e^-}(E_j)$ in the experiment of Sund *et al.* [15]
15.8–16.1	112	61	57	53
16.7–16.9	95	55	70	70
17.7–18.0	104	68	64	68
19.3–19.5	94	51	50	52
21.7–22.0	50	45	20	28

* The absolute value of the reaction cross section was not normalized.

Table 3. Structure parameter S (in arbitrary units) for the ^{16}O(γ, xn) cross sections obtained with the aid of the reduction method for various values of the energy resolution ΔE

ΔE, keV	Experiment with bremsstrahlung photons [18]	Experiment with quasimonoenergetic annihilation photons [19]	Experiment with quasimonoenergetic annihilation photons [20]
Original (claimed) resolution:			
150	270		
200–300		95	
180–280			80
Achieved resolution:			
250		180	154
200		212	192
150		246	239

of fact, to a loss) of information about the structure of cross sections for photonuclear reactions, information that should have been contained in experiments of claimed resolution. Thus, we see that the reason behind the well-known systematic discrepancies between the results of experiments employing different photon beams proves to be quite simple: data from experiments with quasimonoenergetic annihilation photons are oversmoothed in relation to data from experiments with bremsstrahlung photons.

3.3. Manifestation of the Structural Features of the Photonuclear-Reaction Cross Sections versus the Energy Resolution for the Example of Data on $^{16}O(\gamma, xn)$ Reactions

The results of our investigations directly relate the problem of manifestations of structural features in experimental reaction cross sections to an actually achievable energy resolution. In order to trace this relationship quantitatively, we processed, by means of the reduction method, two ^{16}O(γ, xn) cross sections obtained in [19, 20] from experiments with quasimonoenergetic annihilation photons, these cross sections being given in Fig. 3 as an illustration of typi-

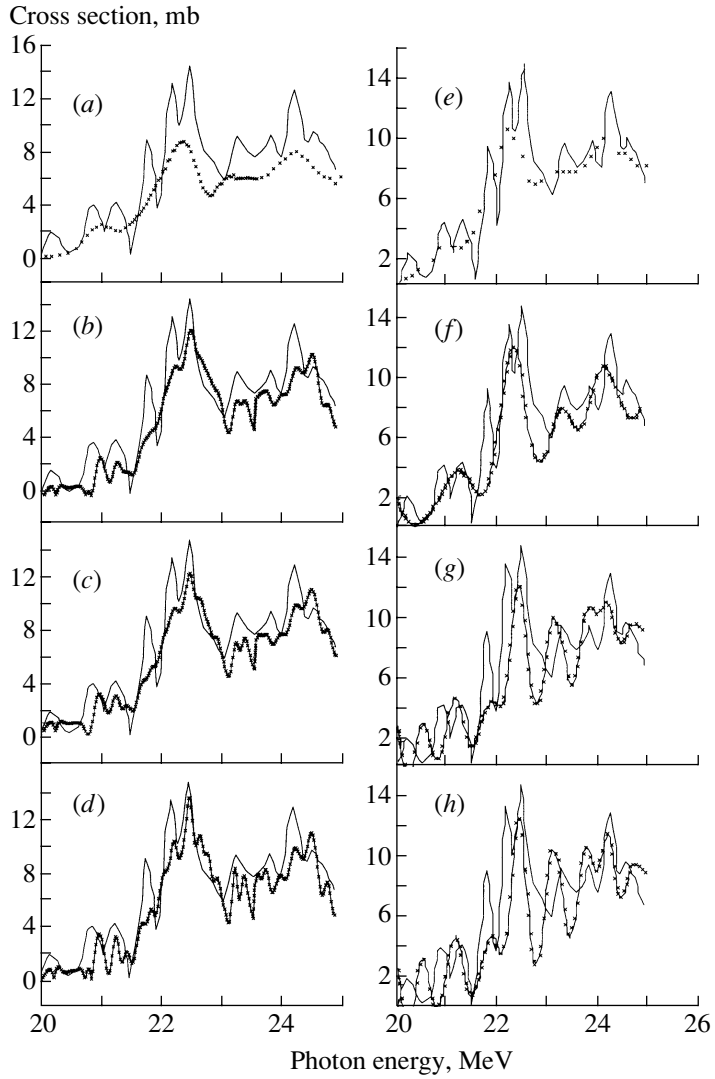

Fig. 6. (+) ^{16}O(γ, xn) cross sections derived by the reduction method from the results (2) obtained by the authors of (left panels) [19] and (right panels) [20] from experiments with quasimonoenergetic annihilation photons, along with (solid curves) the results of the experiment with bremsstrahlung photons that was reported in [18] (the energy resolution there was 200 keV): (a, e) results for the energy resolution claimed in the experiments with quasimonoenergetic annihilation photons ($\Delta E = 200$–300 keV in [19] and $\Delta E = 180$–280 keV in [20]), (b, f) results for the achieved energy resolution of $\Delta E = 250$ keV, (c, g) results for the achieved energy resolution of $\Delta E = 200$ keV, and (d, h) results for the achieved energy resolution of $\Delta E = 150$ keV.

cal discrepancies between the results of different experiments. Both cross sections for a relatively light nucleus from the experiments with quasimonoenergetic annihilation photons involve distinct and readily identifiable structural features that make it possible to trace their shape quite reliably versus the width of the corresponding instrumental function. In Fig. 6 (and in Fig. 3 as well), the reaction cross sections obtained for various values of the energy resolution are compared with the result of the experiment of Ishkhanov *et al.* [18], who employed bremsstrahlung photons. Both from the shape of the emerging resonances and from the values of the structure parameter S [see Eq. (4)–(6)] that are quoted in Table 3, one can get the idea of the form (Figs. 6*c*, 6*g*) that the results of the two experiments in [19, 20] with quasimonoenergetic annihilation photons would have had if the energy resolution actually achieved in them had been close to that which was claimed there. Thus, we see that a unified interpretation (an optimum single-energy representation at close values of the energy resolution) of the different experiments removes almost completely the problem of their systematic discrepancies and the related problem of the reliability of the structural features revealed in the reaction cross

sections, and these structural features were precisely the subject of the present study.

CONCLUSIONS

The main results of our present investigations have cast some doubt on the statement that the energy resolution of experiments with quasimonoenergetic annihilation photons is determined by the calculated width (Figs. 1, 2) of the annihilation line in the effective photon spectrum. These results lead to the following conclusions:

(i) In the majority of the experiments with quasimonoenergetic annihilation photons, the actually achieved energy resolution is substantially (severalfold) poorer than that which was claimed for this quantity and which was estimated on the basis of the calculated annihilation-line width; it is in fact between 1.2 and 1.6 MeV.

(ii) The reason behind the well-known systematic discrepancies between the results of experiments employing different photon beams is quite simple: reaction cross sections from experiments with quasimonoenergetic annihilation photons are overly smoothed in relation to the results of experiments with bremsstrahlung photons—quasimonoenergetic photons are insufficiently "monoenergetic" for performing detailed investigations into cross sections for photonuclear reactions.

(iii) That the actually achieved energy resolution is rather low leads to a significant distortion (loss) of information about the structure of cross sections for photonuclear reactions in relation to what is expected to be manifested in experiments characterized by the claimed resolution.

(iv) Information about reaction cross sections that is lost in the ultimate result (3) $[Y_{e^+}(E_j) - Y_{e^-}(E_j)]$ of a typical difference experiment with quasimonoenergetic annihilation photons can be recovered upon treatment (for example, by means of the reduction method) by introducing additional information about the shape of the actual photon spectrum.

(v) Upon such a treatment, reaction-cross-section data that are close in shape, magnitude, and energy resolution at the claimed (about 300 keV) or even higher energy resolution can be obtained not only from the ultimate result [difference $\sigma(E) \approx Y(E_j) = Y_{e^+}(E_j) - Y_{e^-}(E_j)$ (3)] but also from both intermediate results [$Y_{e^+}(E_j)$ and $Y_{e^-}(E_j)$] of measurements.

It should be emphasized that one of the aforementioned intermediate results (3) $[Y_{e^-}(E_j)]$ of an experiment with quasimonoenergetic annihilation photons is nothing but the reaction yield in a conventional experiment with bremsstrahlung photons. A slight distinction consists in that the former type of experiments employs, for a photon source, a target (it also plays the role of a converter for positron annihilation) from a light rather than from a heavy element. This distinction reduces substantially the intensity of the photon beam used and, hence, the statistical accuracy in measuring the reaction yield $Y_{e^-}(E_j)$. Here, it is reasonable to mention once again that the intensity of the beam of photons from positrons is very low (annihilation is a multistep process); as a result, the statistical accuracy in determining the yield $Y_{e^+}(E_j)$ also proves to be quite low. The consequences of interpreting, as the sought reaction cross section, the difference $Y_{e^+}(E_j) - Y_{e^-}(E_j)$ of the experimental yields measured under such conditions have been demonstrated in the present study above.

All of the aforesaid, together with the results of previous investigations reported in [6–14, 27–29] and devoted to studying the effect of the instrumental function (effective photon spectrum) in an experiment with quasimonoenergetic annihilation photons on the parameters of the resulting cross section, leads to a reappraisal of advantages and disadvantages of the two basic methods for experimentally studying photonuclear reactions. Our results make it possible to conclude that, in performing detailed investigations into cross sections for photonuclear reactions, the complicated and expensive procedure of measurements in beams of quasimonoenergetic annihilation photons does not have any advantages in the energy resolution over the procedure of measurements in beams of bremsstrahlung gamma radiation; on the contrary, it is far inferior to it in this respect. Moreover, the former is also inferior to the latter in statistical accuracy as well, because of a much lower intensity of the beam of quasimonoenergetic annihilation photons inducing the reactions being studied.

In addition, we note that, apart from the absence of advantages of applying, in practice, the procedure employing quasimonoenergetic annihilation photons, it is much more complicated and expensive than the well-developed procedure of measurements in beams of bremsstrahlung photons.

ACKNOWLEDGMENTS

We are grateful to I.M. Kapitonov and Yu.P. Pyt'ev for stimulating discussions. This work was funded in part by a presidential grant (no. 1619.2003.2) for support of leading scientific schools of the Russian Federation. The support of the Russian Foundation for Basic Research within projects nos. 03-07-90431 and 04-02-16275 is also gratefully acknowledged.

REFERENCES

1. S. S. Dietrich and B. L. Berman, At. Data Nucl. Data Tables **38**, 199 (1988).
2. A. V. Varlamov, V. V. Varlamov, D. S. Rudenko, and M. E. Stepanov, INDC(NDS)-394, IAEA NDS (Vienna, Austria, 1999).
3. E. G. Fuller and H. Gerstenberg, *Photonuclear Data—Abstracts Sheets 1955–1982*, NBSIR 83-2742 (USA Natl. Bureau of Standards, 1986).
4. V. V. Varlamov, V. V. Sapunenko, and M. E. Stepanov, *Photonuclear Data 1976–1995. Index* (MGU, Moscow, 1996) [in Russian].
5. B. L. Berman and S. C. Fultz, Rev. Mod. Phys. **47**, 713 (1975).
6. V. V. Varlamov, N. G. Efimkin, N. A. Lenskaja, and A. P. Chernjaev, Preprint No. 89-66/143, MSU INP (Moscow State Univ., Inst. of Nucl. Phys., Moscow, 1989).
7. V. V. Varlamov and B. S. Ishkhanov, in *Proceedings of the International Conference on the Properties of Excited Nuclear States and Mechanisms of Nuclear Reactions. LI Meeting on Nuclear Spectroscopy and Nuclear Structure, Sarov, Russia, 2001,* p. 180.
8. V. V. Varlamov and B. S. Ishkhanov, INDC(CCP)-433, IAEA NDS (Vienna, Austria, 2002).
9. V. V. Varlamov, B. S. Ishkhanov, N. G. Efimkin, and A. P. Chernyaev, Izv. Akad. Nauk, Ser. Fiz. **55**, 1021 (1991).
10. N. G. Efimkin, B. S. Ishkhanov, Ju. P. Pyt'ev, and V. V. Varlamov, Preprint No. 91-35/239, MSU INP (Moscow State Univ., Inst. of Nucl. Phys., Moscow, 1991).
11. V. V. Varlamov, N. G. Efimkin, B. S. Ishkhanov, and V. V. Sapunenko, Vopr. At. Nauki Tekh., Ser. Yad. Konst., No. 1, 52 (1993).
12. N. G. Efimkin and V. V. Varlamov, in *Proceedings of the International Symposium on Nuclear Data Evaluation Methodology, BNL, USA, 1992*, ISBN 981-02-1285-2 (World Sci., 1993), p. 585.
13. V. V. Varlamov, B. S. Ishkhanov, and M. E. Stepanov, Izv. Ross. Akad. Nauk, Ser. Fiz. **62**, 1035 (1998).
14. V. V. Varlamov, D. S. Rudenko, and M. E. Stepanov, Izv. Ross. Akad. Nauk, Ser. Fiz. **65**, 1589 (2001).
15. R. E. Sund, M. P. Baker, L. A. Kull, and R. B. Walton, Phys. Rev. **176**, 1366 (1968).
16. S. C. Fultz, R. L. Bramblett, J. T. Caldwell, and N. A. Kerr, Phys. Rev. **127**, 1273 (1962).
17. L. Z. Dzhilavyan, N. P. Kucher, and V. S. Yurchenko, Preprint No. P-0252, IYaI AN SSSR (Inst. Nucl. Res., USSR Acad. Sci., Moscow, 1980).
18. B. S. Ishkhanov, I. M. Kapitonov, E. M. Lazutin, *et al.,* Yad. Fiz. **12**, 892 (1970) [Sov. J. Nucl. Phys. **12**, 484 (1971)].
19. A. Veyssiere, H. Beil, R. Bergere, *et al.*, Nucl. Phys. A **227**, 513 (1974).
20. R. L. Bramblett, J. T. Caldwell, R. R. Harvey, and S. C. Fultz, Phys. Rev. **133**, B869 (1964); J. T. Caldwell, R. L. Bramblett, B. L. Berman, and R. R. Harvey, Phys. Rev. Lett. **15**, 976 (1965).
21. R. E. Pywell, M. N. Thompson, and B. L. Berman, Nucl. Instrum. Methods **178**, 149 (1980).
22. J. G. Woodworth, K. G. McNeill, J. W. Jury, *et al.*, Phys. Rev. C **19**, 1667 (1979).
23. L. M. Young, Ph. D. Thesis (University of Illinois, USA, 1972).
24. Yu. P. Pyt'ev, *Methods for an Analysis and an Interpretation of Experiments* (MGU, Mosow, 1990).
25. Yu. P. Pyt'ev, *Mathematical Methods for an Interpretation of Experiments* (Vyssh. Shkola, Moscow, 1989).
26. I. N. Boboshin, V. V. Varlamov, E. M. Ivanov, *et al.*, INDC(NDS)-427, IAEA NDS (Vienna, Austria, 2001), p. 49; http://depni.sinp.msu.ru/cdfe.
27. V. V. Varlamov, B. S. Ishkhanov, D. S. Rudenko, and M. E. Stepanov, Preprint No. 2002-19/703, NIIYaF MGU (Sci. Res. Inst. of Nucl. Phys., Moscow State Univ., Moscow, 2002).
28. V. V. Varlamov, B. S. Ishkhanov, M. E. Stepanov, and D. S. Rudenko, in *Proceedings of the 52nd International Meeting on Nuclear Spectroscopy and Nuclear Structure, Moscow, 2002*, ISBN 5-211-06078-4 (MGU, Moscow, 2002), p. 207.
29. V. V. Varlamov, B. S. Ishkhanov, M. E. Stepanov, and D. S. Rudenko, Izv. Akad. Nauk, Ser. Fiz. (in press).
30. B. S. Ishkhanov, I. M. Kapitonov, E. M. Lazutin, *et al.,* Vestn. Mos. Gos. Univ., Ser. 3: Fiz. Astron., No. 6, 606 (1970).
31. E. G. Fuller and M. S. Weiss, Phys. Rev. **112**, 560 (1958).

Translated by A. Isaakyan

Physics of Atomic Nuclei, Vol. 67, No. 12, 2004, pp. 2122–2133. Translated from Yadernaya Fizika, Vol. 67, No. 12, 2004, pp. 2145–2156.
Original Russian Text Copyright © 2004 by Varlamov, Ishkhanov, Peskov, Stepanov, Pshenichnov.

NUCLEI
Experiment

Electromagnetic Dissociation of Ultrarelativistic Heavy Ions and Cross Sections for Photonuclear Reactions in the Region of a Giant Resonance

V. V. Varlamov*, B. S. Ishkhanov[1)], N. N. Peskov, M. E. Stepanov[1)], and I. A. Pshenichnov[2)]

Institute of Nuclear Physics, Moscow State University, Vorob'evy gory, Moscow, 119992 Russia

Received August 27, 2003

Abstract—In calculating cross sections for the electromagnetic dissociation of heavy ions by the Weizsäcker–Williams method, use is made of approximations and extrapolations of experimental data on photonuclear reactions. On the basis of the predicted cross sections for the mutual dissociation of nuclei in beams of ultrarelativistic colliders, it is proposed to measure, among other things, the yields of neutrons from such a dissociation in order to monitor the luminosity of accelerators. Considerable discrepancies between the results of different photonuclear experiments impose limitations on the accuracy of the method. The reasons behind these discrepancies are determined on the basis of a systematic analysis of available data on the cross sections for photoneutron reactions, and a method for removing them is proposed. By considering the example where new data on the dissociation of ^{208}Pb nuclei at an energy of 30 GeV per nucleon are compared with the results of calculations, it is shown that the use of evaluated cross sections for partial photoneutron reactions of the (γ, n) and $(\gamma, 2n)$ types makes it possible to improve the accuracy in calculating cross sections for electromagnetic dissociation. © *2004 MAIK "Nauka/Interperiodica"*.

INTRODUCTION

Investigation of the properties of photonuclear reactions plays an important role both in fundamental and in applied nuclear-physics studies. In the past years, cross sections for photoneutron reactions have been required in the realms of the most advanced inquiries into nuclear interaction that were aimed at searches for quark–gluon plasma, which is a new state of hadron matter. Such investigations are already being or will be conducted in colliding beams of ultrarelativistic nuclei at the two largest facilities in the world, the Relativistic Heavy Ion Collider (RHIC) [1] at the Brookhaven National Laboratory (BNL) in the United States of America and the Large Hadron Collider (LHC) [2] at CERN. The investigations at BNL are being predominantly performed for collisions of gold nuclei, and it is planned at CERN to study collisions of lead nuclei. Special features of the kinematics of colliding beams create serious difficulties for monitoring the luminosity of such accelerators. In order to solve the problem of monitoring, it was proposed in [3] to record correlated pairs of neutrons from processes of the mutual electromagnetic dissociation of each of the colliding nuclei. Such a dissociation occurs under the effect of the Lorentz-contracted Coulomb fields of the nuclei even in the absence of overlap at the instant of closest approach of the nuclei. The excitation of giant dipole resonances in each of the colliding nuclei and their subsequent decays through the one-neutron channel form the main mechanism of mutual electromagnetic dissociation.

The above method for collider-luminosity monitoring is based above all on a reliable calculation of the cross sections for channels of mutual electromagnetic dissociation. Such a calculation, used together with data on the number of neutrons recorded per unit time, will make it possible to determine the luminosity of a collider. Detailed calculations of cross sections for the main processes of mutual electromagnetic dissociation in AuAu and PbPb collisions at the RHIC and LHC energies were performed in [4, 5] with the aid of the RELDIS computer code developed by the authors of those studies; also, uncertainties in final results due to uncertainties in input data were estimated there. In the calculations of mutual electromagnetic dissociation in colliders by the Weizsäcker–Williams method, use is made of cross sections for (γ, n) photoneutron reactions over a broad range of equivalent-photon energies, from the neutron-emission threshold (7 to 8 MeV) to a few hundred gigaelectronvolts [4, 5]. As was shown in [4, 5], the one-neutron mode of giant-dipole-resonance decay is the most significant channel of mutual electromagnetic dissociation—it saturates about two-

[1)]Faculty of Physics, Moscow State University, Vorob'evy gory, Moscow, 119899 Russia.
[2)]Institute for Nuclear Research, Russian Academy of Sciences, pr. Shestidesyatiletiya Oktyabrya 7a, Moscow, 117312 Russia.
*e-mail: Varlamov@depni.npi.msu.su

thirds of the cross section for the emission of one neutron. Photonuclear reactions induced by more energetic photons may also lead to the emission of a single neutron along with other particles. Therefore, electromagnetic dissociation in colliders cannot be calculated on the basis of experimental data on (γ, n) reactions alone—such data are available only at photon energies ranging up to 25 or 30 MeV. The problem becomes even more acute if one considers other partial channels of mutual dissociation—in particular, those that involve the emission of two or three neutrons. In this case, one has also to invoke models of photonuclear reactions that are capable of predicting the cross sections for the $(\gamma, 2n)$ and $(\gamma, 3n)$ channels over a broad energy range.

Thus, mutual electromagnetic dissociation can be calculated reliably only upon a detailed verification of the predictions of photonuclear-reaction models for partial-photoneutron-reaction cross sections via a comparison with relevant experimental data. The most reliable data of this type [6] were obtained in direct experiments at facilities that employ quasimonoenergetic photons originating from the in-flight annihilation of relativistic positrons. For ^{197}Au and ^{208}Pb nuclei, such data were obtained in Saclay (France) [7] and Livermore (USA) [8].

Significant (up to a few tens of percent) systematic discrepancies between the results of the experiments performed for these nuclei at the above two laboratories present a serious problem here. These discrepancies were widely discussed in the literature [9–13]. The results of repeated measurements were quoted in [9], and a special procedure for the mutual rescaling of the data obtained in Saclay [7] and in Livemore [8] was proposed there for each of the target nuclei. However, the possible reasons behind the above discrepancies were not discussed in [9]. In [10–13], the discrepancies in question were subjected to a systematic analysis that resulted in disclosing their reasons; also, methods were proposed there that make it possible to remove the discrepancies between the data from the two laboratories and to obtain precise, reliable, and consistent values of cross sections for partial photoneutron reactions.

It should be noted that there was a great methodological distinction between the analysis in [9] and the analyses in [10–13]. In contrast to what was done in [9], no new measurements were reported in [10–13], and the method used in those studies to rescale the cross sections obtained in Saclay [7] and in Livermore [8] was based on the assumption that the procedure employed in Saclay to determine the multiplicity of photoneutrons was incorrect. For an additional argument in favor of the validity of this assumption, it is desirable to invoke other experimental data—in particular, new data on the cross sections for the electromagnetic dissociation of ^{208}Pb [14].

In view of the aforesaid, the main objectives of the present study are (i) to reveal and remove systematic discrepancies between the results of the photonuclear experiments in [7] and [8] on ^{197}Au and ^{208}Pb nuclei; (ii) to derive estimated data on the cross sections for the (γ, n), $(\gamma, 2n)$, and $(\gamma, 3n)$ reactions on ^{197}Au and ^{208}Pb nuclei (such data will make it possible to test the predictions of photonuclear-reaction models prior to using these models in calculating the electromagnetic dissociation of relativistic nuclei); and (iii) to perform an independent verification of evaluated photoneutron data by comparing the results of the calculations of the electromagnetic dissociation of ^{208}Pb that are based on them with new experimental data obtained at an energy of 30 GeV per nucleon [14].

1. SYSTEMATIC DISAGREEMENT BETWEEN DATA FROM PHOTONUCLEAR EXPERIMENTS WITH QUASIMONOENERGETIC ANNIHILATION PHOTONS

In the region of giant-dipole-resonance energies, the total-photoabsorption cross section $\sigma(\gamma, \mathrm{abs})$; the total-photoneutron-reaction cross sections $\sigma(\gamma, xn)$ and $\sigma(\gamma, sn)$; and the partial-reaction cross sections $\sigma(\gamma, n)$, $\sigma(\gamma, 2n)$, $\sigma(\gamma, 3n)$, and $\sigma(\gamma, p)$, which will be discussed in the following, are related by the equations

$$\sigma(\gamma, \mathrm{abs}) = \sigma(\gamma, sn) + \sigma(\gamma, p) = \sigma(\gamma, n) + \sigma(\gamma, np) + \sigma(\gamma, 2n) + \sigma(\gamma, 3n) + \sigma(\gamma, p), \quad (1)$$

where

$$\sigma(\gamma, sn) = \sigma(\gamma, n) + \sigma(\gamma, np) + \sigma(\gamma, 2n) + \sigma(\gamma, 3n). \quad (2)$$

For the total-photoneutron-reaction cross section, which is determined directly in experiments, we then have

$$\sigma(\gamma, xn) = \sigma(\gamma, n) + \sigma(\gamma, np) + 2\sigma(\gamma, 2n) + 3\sigma(\gamma, 3n). \quad (3)$$

The energy thresholds for the reactions in question are given in Table 1. In the process of measurements, there arises the problem of determining the multiplicity of neutrons: it is necessary to pinpoint the reaction—(γ, n), $(\gamma, 2n)$, or $(\gamma, 3n)$—from which a neutron recorded in an experiment originates.

The aforementioned discrepancies (see Introduction) between the results of the experiments reported in [7] and [8] were considered in [10, 11] for 12 nuclei. Table 2 gives the ratios of the integrated cross

Table 1. Energy thresholds (in MeV) for the photonuclear reactions on ^{197}Au and ^{208}Pb nuclei

Nucleus	(γ, n)	(γ, p)	(γ, np)	$(\gamma, 2n)$	$(\gamma, 3n)$
^{197}Au	8.1	5.8	13.7	14.8	23.1
^{208}Pb	7.4	8.0	15.9	14.1	22.2

sections [6] obtained in Saclay and in Livermore for (γ, n), $(\gamma, 2n)$, and (γ, xn) reactions. One can see the following:

(i) The cross sections directly determined in the experiments for the total photoneutron reaction (γ, xn) were larger in magnitude in the Saclay measurements than in the Livermore measurements by about 6 to 16%; this conclusion is in agreement with the global systematics presented in [12] and obtained on the basis of a vast body of data on (γ, xn) reactions from various laboratories.

(ii) By and large, the cross sections found in Saclay for (γ, n) reactions are larger than their counterparts obtained in Livermore, their ratio being considerably in excess of the discrepancies for (γ, xn) reactions (the excess of the Saclay data over the Livermore data is 18% for ^{197}Au and 54% for ^{208}Pb [9–11]).

(iii) For the $(\gamma, 2n)$ cross sections, the excess of the Livermore data over the Saclay data for ^{197}Au and ^{208}Pb is 62 and 162%, respectively!

In [13], these data were refined and extended (see Table 2).

The global systematics presented in [13] for the ratios of the cross sections determined for the partial reactions (γ, n) and $(\gamma, 2n)$ on 19 nuclei in the two laboratories is given in Fig. 1. It illustrates clearly the above discrepancies, which are directed oppositely. While the cross sections obtained in Saclay for (γ, n) reactions are larger than their counterparts in Livermore (boxes in the region above unity), the relationship for the $(\gamma, 2n)$ cross sections is inverse (triangles in the region below unity). Three "particular" cases (triangles in the region above unity) and two "ideal" cases (triangles and boxes that are close to each other and to unity), which do not fit in the above general trend, were considered in [13] individually.

It can be seen that, without performing a detailed analysis of the reasons behind the discrepancies and without developing efficient methods for removing them, the use of the experimental data being discussed is quite dubious. In [10, 11, 13], such an analysis was performed, and a method for removing the discrepancies in question was developed there.

2. SPECIAL FEATURES OF EXPERIMENTS WITH QUASIMONOENERGETIC ANNIHILATION PHOTONS

2.1. Difference Scheme for Measuring Photonuclear-Reaction Cross Sections

The method that employs quasimonoenergetic photons from the in-flight annihilation of relativistic positrons was proposed as an alternative to the method for studying photonuclear reactions that combines the use of the continuous spectrum of bremsstrahlung gamma rays with special mathematical procedures for extracting information about the reaction cross section $\sigma(k)$ from the reaction yield $Y(E_j)$ defined as

$$Y(E_j) = \alpha \int_{E_{\text{thr}}}^{E_j} W(E_j, k)\sigma(k)dk, \qquad (4)$$

where E_{thr} is the energy threshold for the reaction in question; $W(E_j, k)$ is the spectrum of bremsstrahlung gamma rays, its endpoint energy being denoted by E_j; and α is a normalization factor.

In order to find the cross section from the integral Eq. (4), it is required to solve an ill-posed inverse problem. To avoid this, an experimental method where photons of energy distributed over a relatively narrow region are emitted into the forward hemisphere upon the annihilation of relativistic positrons in a converter target was developed for obtaining quasimonoenergetic photons. Such photons are accompanied by positron-bremsstrahlung photons, whose spectrum is similar to the spectrum of bremsstrahlung from electrons. In order to determine the reaction cross section, a difference experimental scheme was employed that includes the following three stages:

(i) measurement of the reaction yield $Y_{e^+}(E_j)$ (4) in a beam of photons whose spectrum is formed by bremsstrahlung photons and quasimonoenergetic annihilation photons produced by positrons;

(ii) measurement of the reaction yield $Y_{e^-}(E_j)$ (4) in a beam of electron-bremsstrahlung photons;

(iii) derivation (upon appropriate normalization) of the difference

$$Y_{e^+}(E_j) - Y_{e^-}(E_j) = Y(E_j) \approx \sigma(k), \qquad (5)$$

of the measured yields, which is precisely the quantity that is interpreted as the required cross section $\sigma(k)$.

This method imposes stringent requirements on the absolute normalization of the quantities measured experimentally. The authors of [9] themselves thought that the possible errors in determining the photon flux and the neutron-detector efficiency could be the main reason for the discrepancy between their results (Livermore) and the Saclay data.

Table 2. Comparison [11, 13] of the ratios of the integrated cross sections [6] obtained in Saclay and Livermore for (γ, n), $(\gamma, 2n)$, and (γ, xn) reactions [$R^{\text{int}}(n) = \sigma_{\text{S}}^{\text{int}}(\gamma, n)/\sigma_{\text{L}}^{\text{int}}(\gamma, n)$, $R^{\text{int}}(2n) = \sigma_{\text{S}}^{\text{int}}(\gamma, 2n)/\sigma_{\text{L}}^{\text{int}}(\gamma, 2n)$, and $R^{\text{int}}(xn) = \sigma_{\text{S}}^{\text{int}}(\gamma, xn)/\sigma_{\text{L}}^{\text{int}}(\gamma, xn)$]

Nucleus	$R^{\text{int}}(n)$ [6, 11]	$R^{\text{int}}(2n)$ [6, 11]	$R^{\text{int}}(xn)$ [6, 11]	$R^{\text{int}}(n) \approx R^{\text{int}}(xn)$* [13]	$R^{\text{int}}(2n)$ [13]
^{51}V				1.07	0.79
^{75}As				1.21	1.22
^{89}Y	1.33 (1279/960)	0.75 (74/99)	1.26	1.25	0.87
^{90}Zr				1.26	0.73
^{115}In	1.09 (1470/1354)	0.55 (278/508)	0.94	0.97	0.76
^{116}Sn				1.10	0.92
^{117}Sn	0.97 (1334/1380)	0.46 (220/476)	1.01	1.02	0.93
^{118}Sn	1.06 (1377/1302)	0.59 (258/531)	1.06	1.07	0.86
^{120}Sn	0.98 (1371/1389)	0.75 (399/673)	0.99	1.00	0.86
^{124}Sn	0.82 (1056/1285)	0.75 (502/670)	0.93	0.93	0.94
^{127}I				1.34	1.07
^{133}Cs	1.24 (1828/1475)	0.65 (328/503)	1.11	1.10	0.88
^{159}Tb	1.37 (1936/1413)	0.68 (605/887)	1.06	1.07	0.71
^{165}Ho	1.20 (2090/1735)	1.03 (766/744)	1.14	1.20	1.05
^{181}Ta	1.68 (2180/1300)	0.90 (790/881)	1.22	1.25	0.89
^{197}Au	1.18 (2588/2190)	0.62 (479/777)	1.00	1.00	0.69
^{208}Pb	1.54 (2731/1776)	0.38 (328/860)	1.30	1.21	0.77
^{232}Th				0.84	0.69
^{238}U				0.76	0.79

* Below the threshold for the $(\gamma, 2n)$ reactions, the ratios virtually coincide (distinctions appear only in the third decimal place).

The aforementioned systematics from [12] indicates that there is a glaring discrepancy between the Livermore data and data from the majority of laboratories. Although there are distinctions between data obtained in different laboratories, the cross-section ratio being investigated shows a clear trend toward a concentration of its values around the mean value of $\langle R_{\text{syst}}^{\text{int}} \rangle = 1.12$. At this point, it is especially important to emphasize that the Saclay data agree in absolute value with data obtained in other laboratories either with quasimonoenergetic photons or with bremsstrahlung photons. As has already been mentioned, such discrepancies between the absolute values of the cross sections in question depend on the efficiency of the neutron detectors used and may be due to various reasons such as distinctions between the energy calibrations of the experimental facilities and errors in absolute normalizations.

2.2. Accuracy in Determining Cross Sections for Reactions Featuring Various Multiplicities and Neutron-Detector Efficiency

The need for separating the contributions from (γ, n), $(\gamma, 2n)$, and $(\gamma, 3n)$ reactions with allowance for the fact that the efficiency of the detection of two particles is equal to the squared efficiency of the detection of one particle required creating special neutron detectors of 4π coverage that are suitable for measuring the multiplicity of neutrons. For this, highly efficient (40–60%) detectors of the slowing-down type, where neutrons formed throughout a short pulse of photons from an accelerator were moderated and recorded within the time interval between accelerator pulses, were developed. For detectors of moderated neutrons, the experimentalists in Livermore employed BF_3 counters shaped as long tubes and arranged in paraffin. A large-volume liquid scintillator

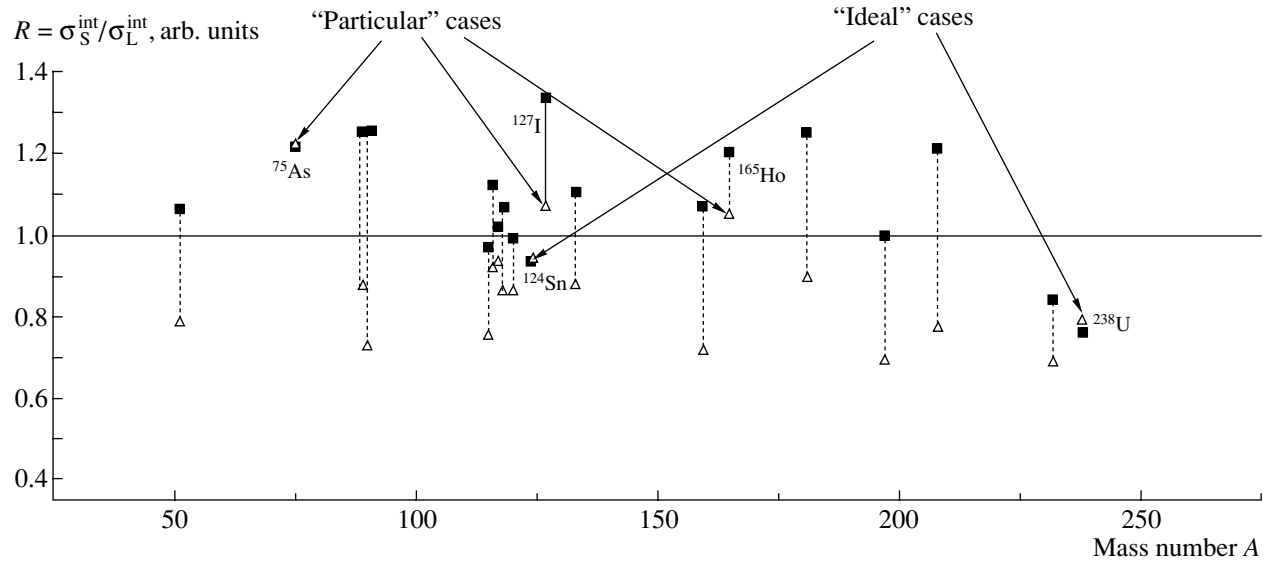

Fig. 1. Systematics of the ratios $R(n) = \sigma_S^{int}(\gamma, n)/\sigma_L^{int}(\gamma, n)$ (boxes lying predominantly in the region above unity) and $R(2n) = \sigma_S^{int}(\gamma, 2n)/\sigma_L^{int}(\gamma, 2n)$ (triangles lying predominantly in the region below unity) from [13] that were obtained for matched ranges of integration according to data of experiments performed in Saclay and Livermore. "Particular" (triangles in the region above unity) and "ideal" (triangles and boxes are close to each other and lie in the vicinity of unity) cases were considered in [13] individually.

enriched in gadolinium was used for this purpose in Saclay.

Hereafter, it should be borne in mind that, since the method of direct photoneutron detection was used in the experiments performed in Saclay and Livermore and since the thresholds for (γ, np) reactions are rather low (see Table 1), it would be more correct to denote one-neutron reactions by $(\gamma, n) + (\gamma, np)$ rather than by (γ, n).

Determination of the photoneutron multiplicity by the method of ring ratios, which was applied in Livermore. In order to separate the contributions from (γ, n), $(\gamma, 2n)$, and $(\gamma, 3n)$ reactions, the highly efficient neutron detector used in Livermore was constructed is such a way that there was the possibility of recording moderated neutrons by means of BF_3 counters that were arranged as concentric rings at various distances from the target. The ratio of the number of counts in the internal and the external ring of BF_3 counters is a monotonically increasing function of the mean photoneutron energy. Owing to the use of ring ratios, the mean neutron energies and, accordingly, the ratios for events of reactions featuring one and two neutrons are determined independently. If use is additionally made of the efficiency of detection of neutrons having various energies, this enables one to determine the cross sections for partial reactions of various multiplicity.

Method used in Saclay to calibrate the energy dependence of the neutron-detection efficiency. The method developed in Saclay is based on a precision calibration of large-volume liquid gadolinium scintillator by means of a ^{252}Cf source. In this way, one determines a region where the detection efficiency is virtually independent of the neutron energy. Although the neutron-energy dependence of the detection efficiency does not in fact reduce to a constant in any segment [6], it was assumed that the detection efficiency deviates from a constant only for neutrons of energy $E_n \sim 5$ MeV. It was also assumed that the energy of photoneutrons in the giant-dipole-resonance region does not exceed a value of $E_n \sim 3$ MeV. The latter assumption is not quite correct since it is well known that the spectra of photoneutrons from (γ, n) and $(\gamma, 2n)$ reactions extend up to an energy of about 10 MeV. It is precisely this circumstance that generated errors in determining the absolute values of the cross sections for photoneutron reactions. Special attention will be given to them below in discussing systematics of data obtained by different methods. Moreover, information published on the procedure used there indicates that, while the detection efficiency determined with the aid of a ^{252}Cf source was close to unity, the time conditions for the detecting system in the actual experiments were such that the efficiency only amounted to a value of about 0.6. A heavy detector background was an obvious and quite important drawback of the procedure used in Saclay to determine the multiplicity of photoneutrons. This heavy background and a signal-to-background ratio that was much poorer than in Livermore complicated

the separation and subtraction of the background and the introduction of corrections for random coincidences in the actuation of the counters. All of this leads to an obvious overestimation of the fraction of events of one-neutron reactions (γ, n) in relation to events of reactions involving the emission of two (three or more) neutrons.

We can conclude that, although the efficiency of the detector in Livermore was somewhat below the efficiency of the detector in Saclay, the application of the ring-ratio method in Livermore compensated for this drawback to a considerable extent. Moreover, the efficiency of the detector in Saclay in specific experiments was well below that which is achievable in principle (see above). All of the aforesaid indicates that, while the procedure used in Livermore to determine the multiplicity of photoneutrons seems well justified, the procedure employed in Saclay is open to criticism. The question of which procedure is erroneous is of particular interest under such conditions.

In [11], data obtained in Saclay and Livermore for one of the 12 nuclei subjected to investigation (^{181}Ta) were analyzed along with the results obtained in [15–17] by studying the (e, xn), (e, n), and $(e, 2n)$ reactions on this nucleus. Since the cross sections for the electro- and photodisintegration of nuclei are related to each other [16, 17] via the spectrum of virtual photons, it is possible to estimate the $(e, 2n)$ cross sections on the basis of data on the respective $(\gamma, 2n)$ cross sections. The experimental cross section for the reaction ^{181}Ta$(e, 2n)$ was found in [15] on the basis of the obvious relation

$$\sigma(e, 2n) = (\sigma(e, xn) - \sigma(e, n))/2, \qquad (6)$$

which is valid below the threshold for the emission of three neutrons and which involves the experimentally determined cross sections $\sigma(e, xn)$ and $\sigma(e, n)$. The cross section $\sigma(e, n)$ was measured by two methods, that in which one determines the multiplicity of neutrons, $\sigma_1(e, n)$, and that of induced activity (decay ^{180}Ta $\rightarrow ^{180}$Hf, 93.3 keV, Ge–Li detector), $\sigma_2(e, n)$. A value of $\langle \sigma_1(e, n)/\sigma_2(e, n) \rangle = 1.057 \pm 0.023$ was obtained for the weighted mean ratio of the measured cross sections. The proximity of this value to unity means that the procedure used to determine the multiplicity of photoneutrons is quite reliable. Concurrently, it was shown that the cross section $\sigma(e, 2n)$ as determined by formula (6) agrees with data rescaled from the Livermore data on $(\gamma, 2n)$ reactions, but that it disagrees with the corresponding Saclay data. The data obtained in Saclay are underestimated for the $(\gamma, 2n)$ cross sections, but they are on the contrary overestimated for the (γ, n) cross sections.

3. METHOD FOR CORRECTING DATA OBTAINED IN SACLAY AND LIVERMORE ON THE CROSS SECTIONS FOR (γ, n), $(\gamma, 2n)$, AND $(\gamma, 3n)$ PHOTONEUTRON REACTIONS

In order to remove the discrepancies being discussed and to bring the two data sets into correspondence with each other, a method was proposed in [10, 11, 13] for correcting data on the cross sections for $(\gamma, 2n)$ reactions.

3.1. Evaluating Cross Sections for $(\gamma, 2n)$ Reactions

In [10, 11], the discrepancies between the data obtained in Saclay and in Livermore were interpreted as a consequence of the incorrectness of the procedure used in Saclay to determine the multiplicity of photoneutrons—there, some neutrons from a $(\gamma, 2n)$ reaction were erroneously associated with the corresponding (γ, n) reaction. Therefore, that part of the (γ, n) reaction which was erroneously associated with the one-neutron reaction should have been included in the cross section for the two-neutron reaction. This rescaling was performed in the following way. First, the energy scale of the cross sections under comparison was corrected on the basis of data on the directly measured cross sections for the total photoneutron reaction (γ, xn). For this, the cross sections obtained in Livermore were shifted in energy by a quantity ΔE toward the Saclay data (see Figs. 2, 3). Second, the factor

$$R = R(xn) = \sigma_{\rm S}^{\rm int}(\gamma, xn)/\sigma_{\rm L}^{\rm int}(\gamma, xn), \qquad (7)$$

which normalizes the cross sections for the total photoneutron reaction in the energy region up to the threshold for the respective $(\gamma, 2n)$ reaction, was determined. In this region, the data obtained in the two laboratories for the (γ, xn) cross sections must be identical under the condition that corrections for the neutron-detection efficiency were introduced correctly; in addition, the relation $\sigma(\gamma, xn) = \sigma(\gamma, n) + 2\sigma(\gamma, 2n)$ must hold in this case. The use of the factor R makes it possible to derive the relations that implement the above return of part of the (γ, n) cross section obtained in Saclay to a new (corrected) cross section for the relevant $(\gamma, 2n)$ reaction:

$$R = \sigma_{\rm S}^{xn}/\sigma_{\rm L}^{xn} = (\sigma_{\rm S}^{n} + 2\sigma_{\rm S}^{2n})/(\sigma_{\rm L}^{n} + 2\sigma_{\rm L}^{2n}), \qquad (8)$$

$$\sigma_{\rm S}^{xn} = (\sigma_{\rm S}^{n} + 2\sigma_{\rm S}^{2n}) = R\sigma_{\rm L}^{xn} = R(\sigma_{\rm L}^{n} + 2\sigma_{\rm L}^{2n}), \qquad (9)$$

$$R\sigma_{\rm L}^{2n} = \sigma_{\rm S}^{2n*} = \sigma_{\rm S}^{2n} + (\sigma_{\rm S}^{n} - R\sigma_{\rm L}^{n})/2. \qquad (10)$$

The right-hand side of the basic relation (10) in the method for correcting the data obtained in Saclay for the $(\gamma, 2n)$ cross sections has the meaning indicated above: to the value $\sigma_{\rm S}^{2n}$ obtained in Saclay for the

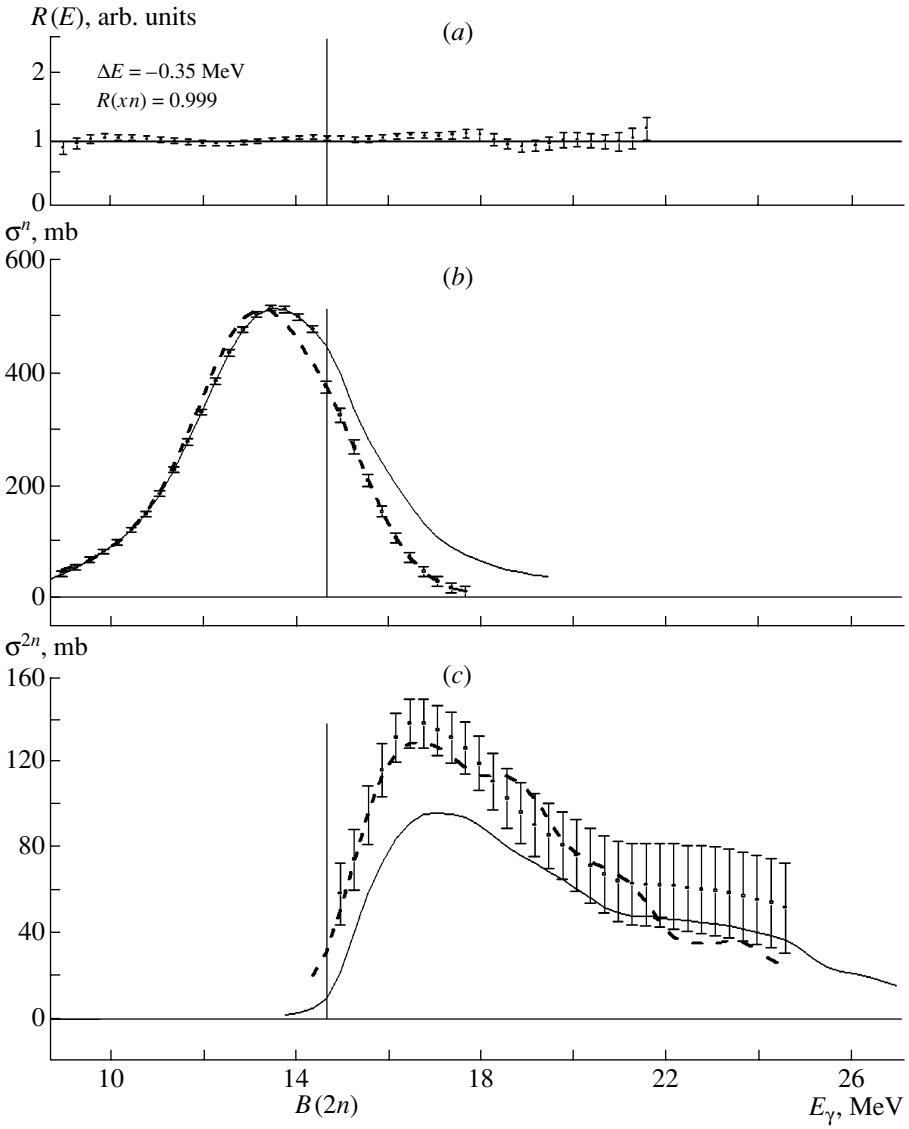

Fig. 2. Results obtained by simultaneously correcting the Saclay and Livermore data on the cross sections for the total photoneutron reaction and partial photoneutron reactions on a ^{197}Au nucleus: (*a*) ratios $R(E)$ of the (γ, xn) cross sections, (*b*) data on the (γ, n) cross sections [(solid curve) original Saclay data, σ_S^n; (points) evaluated Saclay data, σ_S^{n*} (13); and (dashed curve) evaluated Livermore data, $R\sigma_L^n$], and (*c*) data on the $(\gamma, 2n)$ cross sections [(solid curve) original Saclay data, σ_S^{2n}; (points) evaluated Saclay data, σ_S^{2n*} ((8)–(10)); and (dashed curve) evaluated Livermore data, $R\sigma_L^{2n}$].

$(\gamma, 2n)$ cross section, one adds that part of the (γ, n) cross section which was calculated with allowance for the factor $R(7)$—that is, $(\sigma_S^n - R\sigma_L^n)/2$. If the discrepancy between the Livermore and Saclay data is due exclusively to the error that the experimentalists in Saclay made in determining the multiplicity of photoneutrons, then, according to the left-hand side of relation (10), the rescaled Saclay cross section σ_S^{2n*} must be in accord with the Livermore cross section σ_L^{2n} multiplied by the factor $R(7)$. For ^{197}Au and ^{208}Pb nuclei, the corrected Saclay data [$\sigma_S^*(\gamma, 2n)$] are given in Figs. 2*c* and 3*c*, along with the original cross sections from the Saclay experiments.

The cross sections for the reactions being discussed were determined in a relatively narrow energy region in Livermore and in a broader region in Saclay. Within the method described above, the $(\gamma, 2n)$ cross sections can be evaluated only in the common (that is, rather narrow) energy region. In order to evaluate the $(\gamma, 2n)$ cross section over the widest accessible region, we employed the following procedure:

(i) In the common narrow energy regions, the ratio $K(E)$ of the $(\gamma, 2n)$ cross sections evaluated on the basis of relations (8)–(10) and their experimental

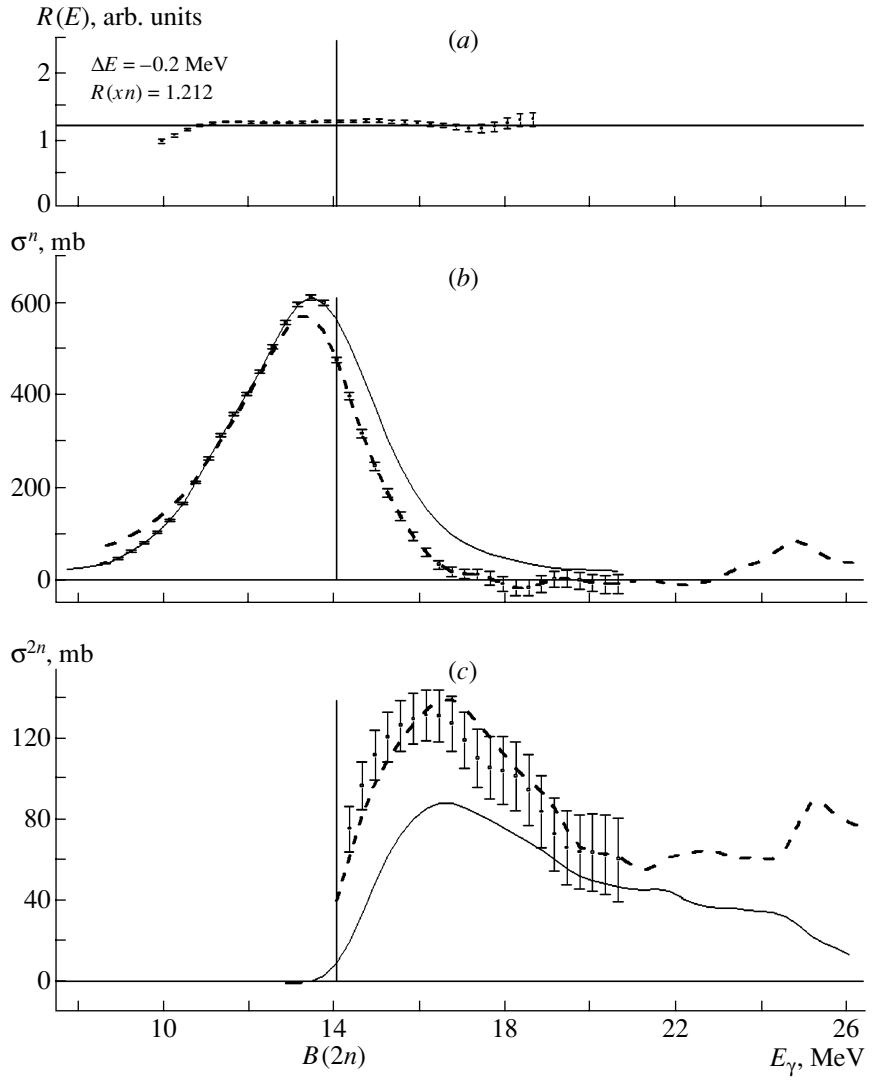

Fig. 3. As in Fig. 2, but for the ^{208}Pb nucleus.

counterparts obtained in Saclay were calculated for both nuclei:

$$K(E) = \sigma^*_{\mathrm{S}}(\gamma, 2n)/\sigma_{\mathrm{S}}(\gamma, 2n). \qquad (11)$$

(ii) The function $K(E)$ was extrapolated to the broad energy region where the $(\gamma, 2n)$ cross section was determined in Saclay; the coefficients K decreased linearly, from 1.35 (at 22 MeV) to 1.33 (at 27 MeV) and 1.30 (at 37 MeV) for the ^{197}Au nucleus and, respectively, from 1.21 to 0.98 and 0.52 for the ^{208}Pb nucleus.

(iii) Upon the use of the function $K(E)$, the evaluated cross sections for the $(\gamma, 2n)$ reactions assumed the following form over all energy regions investigated in Saclay (see Figs. 4*c*, 4*d*):

$$\sigma^*_{\mathrm{S\,(broad)}}(\gamma, 2n) = K(E)\sigma^*_{\mathrm{S\,(narrow)}}(\gamma, 2n). \qquad (12)$$

To conclude this subsection, we would like to comment on the behavior of the cross sections obtained in Livermore for $(\gamma, 2n)$ reactions (Fig. 4*d*, closed circles) in the energy range from the threshold for the respective $(\gamma, 3n)$ reaction to an energy of about 26 MeV. The cross section measured in Livermore exhibits a distinct maximum at an energy of about 25 MeV, but there is no such maximum in the corresponding cross section measured in Saclay. The origin of this maximum is unclear, since the (γ, sn) and (γ, n) cross sections obtained in Livermore also have similar maxima at energies of about 25 MeV, while the (γ, xn) cross sections show a weak monotonic growth at energies above a value of about 23 MeV.

3.2. Evaluating (γ, n) Cross Sections

As a matter of fact, the simultaneous-correction method applied in [10, 11, 13] consists in giving

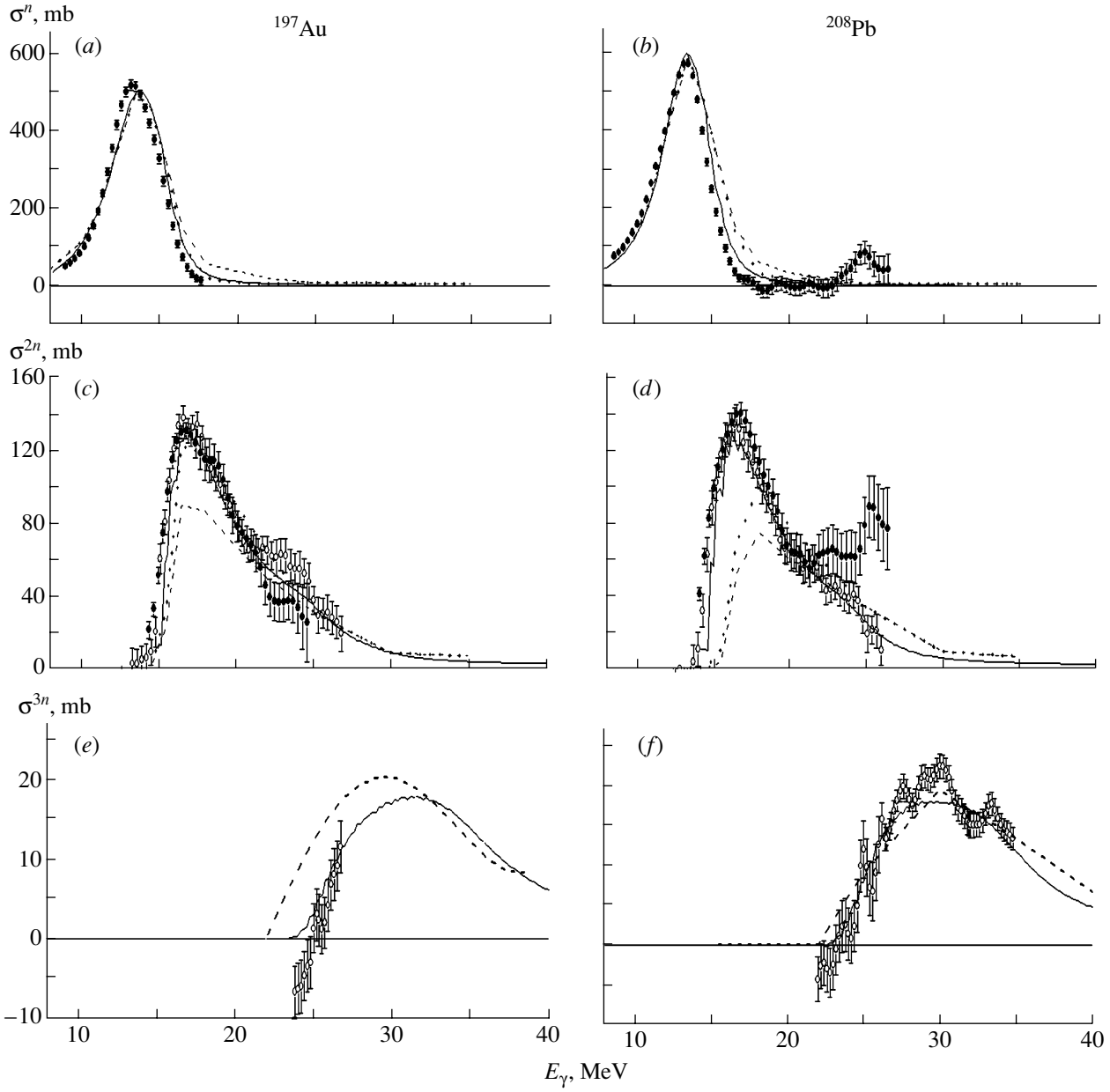

Fig. 4. Comparison of evaluated cross sections {(open circles) Saclay [7] and (closed circles) Livermore [8]} for various photoneutron reactions with the results of theoretical calculations based on (solid curves) the GNASH code [18, 19] or the RELDIS code [4] implemented (dashed curves) with or (curves) without allowance for prompt neutron emission.

back, to the $(\gamma, 2n)$ cross section, its part that was erroneously associated with the corresponding (γ, n) reaction. It follows that, from the (γ, n) cross section, one must remove that part of it which was erroneously included in this cross section and which must be added to the $(\gamma, 2n)$ cross section in accordance with relation (10). The (γ, n) cross section corrected according to [13] must then assume the form

$$R\sigma_{\rm L}^n = \sigma_{\rm L}^{n*} = \sigma_{\rm S}^{n*} = \sigma_{\rm S}^n - (\sigma_{\rm S}^n - R\sigma_{\rm L}^n), \qquad (13)$$

where the difference $\sigma_{\rm S}^n - R\sigma_{\rm L}^n$ is calculated in the energy region above the threshold for the corresponding $(\gamma, 2n)$ reaction.

For ^{197}Au and ^{208}Pb nuclei, the corrected Saclay data $[\sigma_{\rm S}^*(\gamma, n)]$ are given in Figs. 2*b* and 3*b*, respectively, along with the original cross sections. It should be noted that, in either case, the corrected cross sections $\sigma_{\rm S}^*(\gamma, n)$ develop discontinuities in the region of the thresholds for the $(\gamma, 2n)$ reactions. This is because the Livermore data were subjected to a shift in energy by ΔE with respect to the Saclay data

in order to reach constant ratios of the cross sections for the total photoneutron reactions at energies below the thresholds for the relevant $(\gamma, 2n)$ reactions. Under such conditions, the corrected Livermore cross sections $\sigma_{\mathrm{L}}^{n*} = R\sigma_{\mathrm{L}}^{n}$ (see Figs. 4*a*, 4*b*) appear to be the best estimates of the (γ, n) cross sections.

3.3. Evaluating $(\gamma, 3n)$ Cross Sections

The above scheme cannot be used to evaluate the cross section for a reaction involving the emission of three neutrons, since, for either nucleus, the respective reaction has a rather high energy threshold (see Table 1); it does not have an overlap in energy with the (γ, n) reaction at all, the overlap with the $(\gamma, 2n)$ reaction being only partial.

In the energy region where the (γ, n) cross section is close to zero, the cross section for the total photoneutron reaction (γ, xn) has the form

$$\sigma(\gamma, xn) = 2\sigma(\gamma, 2n) + 3\sigma(\gamma, 3n), \qquad (14)$$

so that one can determine the $(\gamma, 3n)$ cross sections by using the relation

$$\sigma(\gamma, 3n) = 1/3[\sigma(\gamma, xn) - 2\sigma(\gamma, 2n)]. \qquad (15)$$

In accordance with what was said above on estimating the $(\gamma, 2n)$ cross sections, the $\sigma^*(\gamma, 3n)$ cross sections were also evaluated with the aid of relation (15) and the functions $K(E)$ (11):

$$\sigma_{\mathrm{S}}^*(\gamma, 3n) = 1/3[\sigma_{\mathrm{S}}(\gamma, xn) - 2\sigma_{\mathrm{S}}^*(\gamma, 2n)] \qquad (16)$$
$$= 1/3[\sigma_{\mathrm{S}}(\gamma, xn) - 2K(E)\sigma_{\mathrm{S}}(\gamma, 2n)].$$

The results obtained via this estimation are displayed in Figs. 4*e* and 4*f*.

It should be emphasized that the cross section for the reaction ^{208}Pb$(\gamma, 3n)^{205}$Pb (see Fig. 4*f*) overlaps the cross section for the reaction ^{208}Pb$(\gamma, 2n)^{206}$Pb (see Figs. 3*c* and 4*d*) only within the narrow energy range 22.0–26.4 MeV; at higher energies, the former is one-third of the cross section of the total photoneutron reaction ^{208}Pb(γ, xn). In the common energy region, the evaluated cross section $\sigma_{\mathrm{S}}^*(\gamma, 3n)$ is consistent (see Fig. 4*f*) with the experimental cross section determined for the reaction ^{208}Pb$(\gamma, 3n)^{205}$Pb in Saclay. This indicates that, in contrast to the cross section for the reaction ^{208}Pb$(\gamma, 2n)^{206}$Pb, the cross section for the reaction ^{208}Pb$(\gamma, 3n)^{205}$Pb was determined in Saclay correctly [in all probability, this is because the cross section in question is merely a tail of the experimental cross section for the reaction ^{208}Pb(γ, xn) and requires no additional rescaling].

Table 3. Measured and calculated cross sections (in b) for the electromagnetic dissociation of lead nuclei on a lead target at an energy of 30 GeV per nucleon (quoted in this table are the cross sections for the dissociation channels involving the emission of one or two neutrons and the sum of these cross sections)

Channel	Experiment [14]	RELDIS code [4]		GNASH code [18, 19]
		$P_n^{\mathrm{dir}} = 0.25$	$P_n^{\mathrm{dir}} = 0.00$	
$1nX$	16.7 ± 1.5	18.8	18.0	17.6
$2nX$	5.2 ± 0.5	2.5	3.1	3.4
Sum	21.9 ± 1.6	21.3	21.1	21.0

4. CALCULATION OF ELECTROMAGNETIC-DISSOCIATION CROSS SECTIONS WITH THE AID OF EVALUATED PHOTONEUTRON DATA

The results obtained by measuring neutron emission in the electromagnetic dissociation of ^{208}Pb at an energy of 30 GeV per nucleon were reported in [14]. The measurements were performed in a beam from the SPS accelerator at CERN. As was shown in [14], the specially chosen geometry of the facility used made it possible to record neutrons originating from electromagnetic-dissociation events and to suppress the contribution of neutrons originating from the hadronic interactions of colliding nuclei.

These new experimental data provide the possibility of independently testing the quality of evaluated data concerning photoabsorption in ^{208}Pb. In the present study, we employed the Weizsäcker–Williams method to obtain the cross sections for the processes where the electromagnetic dissociation of ^{208}Pb on a lead target is accompanied by the emission of one or two neutrons (see Table 3). In this calculation, the maximum energy of equivalent photons exceeds 400 MeV; therefore, processes in which the dissociation of ^{208}Pb is accompanied by neutron emission also receive a contribution from events of quasideuteron absorption on *pn* pairs within this nucleus. There are no data on the (γ, n) and $(\gamma, 2n)$ cross sections above 28 to 30 MeV; therefore, it is necessary to invoke one model of photonuclear reactions or another in the calculations. Of course, the predictions of such a model must be preliminarily verified at energies below 30 MeV by using the evaluated data from the present study.

The theoretical results obtained on the basis of the RELDIS code [4], which implements the cascade–evaporation–fission model of photonuclear reactions, and the GNASH code [18, 19], which implements the preequilibrium exciton model, are presented in Figs. 4*b*, 4*d*, and 4*f*. The theoretical curves displayed

in these figures were borrowed from [4]. It should be noted that the evaluated cross sections for the partial reactions (γ, n), $(\gamma, 2n)$, and $(\gamma, 3n)$ are close to the results of the theoretical calculations based on the GNASH computer code; they are also close to the theoretical results obtained with the RELDIS code, but only in the case where it is implemented without taking into account prompt neutrons [that is, where the total fraction of direct (nonstatistical) giant-dipole-resonance decays through the neutron channel is set to $P_n^{\mathrm{dir}} = 0$].

Each of the aforementioned methods for simulating photonuclear reactions was then employed in calculating the electromagnetic-dissociation cross sections. The results of such calculations are presented in Table 3 for the channels $^{208}\mathrm{Pb}(\gamma, n)^{207}\mathrm{Pb}$ and $^{208}\mathrm{Pb}(\gamma, 2n)^{206}\mathrm{Pb}$. Strictly speaking, the cross sections measured experimentally corresponded to processes where the emission of a specific number of neutrons was accompanied by the emission of other particles X that were not detected, $^{208}\mathrm{Pb}(\gamma, 1nX)$ and $^{208}\mathrm{Pb}(\gamma, 2nX)$; however, theoretical predictions state that such cross sections are not expected to differ in absolute value by more than 0.2 b from the $^{208}\mathrm{Pb}(\gamma, n)^{207}\mathrm{Pb}$ and $^{208}\mathrm{Pb}(\gamma, 2n)^{206}\mathrm{Pb}$ cross sections, which are quoted in Table 3.

As can be seen from Table 3, the $1nX$ channel of lead dissociation is best of all described by the calculation employing the results obtained with the aid of the GNASH code. We recall that results closest to the evaluated cross sections from our present study are obtained by using precisely this code to calculate photoneutron cross sections. The $2nX$ channel is described by the theory much worse; however, the version that employs the GNASH code is preferable in this case as well. The calculations of electromagnetic dissociation [4] are based on the assumption that the probabilities of multiphoton excitations are controlled by a Poisson distribution, as is the case in the example of a harmonic oscillator. Theoretical values of the cross sections for the emission of two neutrons below their experimental counterparts were also found in a number of studies [20, 21]. One cannot rule out the possibility that the failure of the theory in describing the $2nX$ channel may also stem here from the deviation of the actual pattern of nuclear excitations from that in the case of a harmonic oscillator [22, 23].

It should be emphasized that the sum of the cross sections for the electromagnetic-dissociation channels involving the emission of one and two neutrons is successfully described by all versions of the calculations. This is in accord with the results presented in [4], where it was shown that the sum of these cross sections depends more weakly on the parameters of the calculations than each of the partial cross sections for dissociation. It was proposed to use the sum of the cross sections for the channels involving the emission of one and two neutrons in the method for collider-luminosity monitoring by means of measuring the yields of neutrons from mutual electromagnetic dissociation [4].

5. CONCLUSIONS

On the basis of the data presented in Figs. 3 and 4 for $^{197}\mathrm{Au}$ and $^{208}\mathrm{Pb}$ nuclei, we can draw the following conclusions:

(i) A correction of the Saclay and Livermore data on the cross sections for one- and two-neutron reactions with allowance for the error in the procedure for determining the photoneutron multiplicity in Saclay renders consistent the data from the two laboratories on the cross sections for $(\gamma, 2n)$ reactions.

(ii) The corrected cross sections from the experiments in Saclay [rescaling according to formulas (8)–(10)] and from the experiments in Livermore [multiplication by the factor $R = R(xn)$ (7)] can be used on equal terms as evaluated cross sections for $(\gamma, 2n)$ reactions.

(iii) As evaluated cross sections for (γ, n) reactions, one can employ only the corrected cross sections from the experiments performed in Livermore [multiplication by the factor $R = R(xn)$ (7)]; the use of the data from Saclay is impossible (a shift in energy leads to a discontinuity).

(iv) The evaluated cross sections for the partial reactions (γ, n) and $(\gamma, 2n)$ are close to the results of theoretical calculations based on the GNASH computer code [18, 19], as well as to the results obtained with the RELDIS code [4] but only in its version that takes no account of prompt neutrons [that is in the version where the total fraction of direct (nonstatistical) decays of giant dipole resonances through the neutron channel is $P_n^{\mathrm{dir}} = 0$].

(v) In the case of $^{197}\mathrm{Au}$ nuclei, the evaluated cross sections for the partial reaction $(\gamma, 3n)$ agree better with the results of the calculations that employ the GNASH computer code, while, in the case of $^{208}\mathrm{Pb}$ nuclei, there is agreement with both theoretical versions, which are rather close.

(v) Those cross sections for the electromagnetic dissociation of $^{208}\mathrm{Pb}$ at an energy of 30 GeV per nucleon that were obtained on the basis of theoretical photoneutron cross sections consistent with the evaluated cross sections for (γ, n) and $(\gamma, 2n)$ reactions ensure the best agreement with experimental data.

ACKNOWLEDGMENTS

We are grateful to A. Ventura and S. Masetti for placing at our disposal the results obtained with the GNASH code.

This work was funded in part with a presidential grant (no. 1619.2003.2) for support of leading scientific schools of the Russian Federation. The support of the Russian Foundation for Basic Research within projects nos. 02-02-16013, 03-07-90431, and 04-02-16275 is also gratefully acknowledged.

REFERENCES

1. G. Baym, Nucl. Phys. A **698**, XXIII (2002).
2. B. Alessandro, P. Aurenche, R. Baier, *et al.*, CERN-ALICE-INTERNAL-NOTE-2002-025.
3. A. J. Baltz, C. Chasman, and S. N. White, Nucl. Instrum. Methods Phys. Res. A **417**, 1 (1998).
4. I. A. Pshenichnov, J. P. Bondorf, I. N. Mishustin, *et al.*, Phys. Rev. C **64**, 024903 (2001).
5. I. A. Pshenichnov, J. P. Bondorf, A. B. Kurepin, *et al.*, CERN-ALICE-INTERNAL-NOTE-2002-07.
6. S. S. Dietrich and B. L. Berman, At. Data Nucl. Data Tables **38**, 199 (1988).
7. A. Veyssiere, H. Beil, R. Bergere, *et al.*, Nucl. Phys. A **159**, 561 (1979).
8. R. R. Harvey, J. T. Caldwell, R. L. Bramblett, and S. C. Fultz, Phys. Rev. **136**, B126 (1964).
9. B. L. Berman, R. E. Pywell, S. S. Dietrich, *et al.*, Phys. Rev. C **36**, 1286 (1987).
10. E. Wolynec, A. R. V. Martinez, P. Gouffon, *et al.*, Phys. Rev. C **29**, 1137 (1984).
11. E. Wolynec and M. N. Martins, Rev. Bras. Fis. **17**, 56 (1987).
12. V. V. Varlamov and B. S. Ishkhanov, INDC(CCP)-433, IAEA NDS (Vienna, Austria, 2002).
13. V. V. Varlamov, N. N. Peskov, D. S. Rudenko, and M. E. Stepanov, Vopr. At. Nauki Tekh., Ser. Yad. Konstanty, No. 1/2, 48 (2003).
14. M. B. Golubeva, F. F. Guber, T. L. Karavicheva, *et al.*, Phys. Rev. C (in press).
15. W. W. Gargaro and D. S. Onley, Phys. Rev. C **4**, 1032 (1971).
16. C. W. Soto Vargas, D. S. Onley, and L. E. Wright, Nucl. Phys. A **288**, 45 (1977).
17. W. R. Dodge, E. Hayward, and E. Wolinec, Phys. Rev. C **28**, 150 (1983).
18. P. G. Young, E. D. Arthur, and M. B. Chadwick, *Nuclear Reaction Data and Nuclear Reactors,* Ed. by A. Gandini and G. Reffo (World Sci., Singapore, 1988), Vol. I, p. 227.
19. M. B. Chadwick and P. G. Young, Acta Phys. Slovaca **45**, 633 (1995).
20. T. Aumann, J. V. Kratz, E. Stiel, *et al.*, Phys. Rev. C **47**, 1728 (1993).
21. T. Aumann, C. A. Bertulani, and K. Summerer, Phys. Rev. C **51**, 416 (1995).
22. C. Volpe, F. Catara, Ph. Chomaz, *et al.*, Nucl. Phys. A **589**, 521 (1995).
23. P. F. Bortignon and C. H. Dasso, Phys. Rev. C **56**, 574 (1997).

Translated by A. Isaakyan

Physics of Atomic Nuclei, Vol. 67, No. 12, 2004, pp. 2134–2138. Translated from Yadernaya Fizika, Vol. 67, No. 12, 2004, pp. 2157–2161.
Original Russian Text Copyright © 2004 by Kadmensky.

NUCLEI
Theory

Channel-Coupling Contribution to the Widths of Decay Nuclear States and to Their Wave Functions

S. G. Kadmensky*

Voronezh State University, Universitetskaya pl. 1, Voronezh, 394693 Russia

Received November 27, 2003; in final form, March 17, 2004

Abstract—By using the formalism of the quantum theory of fission, the amplitudes of partial decay widths and the asymptotic behavior of the wave function for a decaying nucleus are found with allowance for open-decay-channel coupling not only for fission, but also for the binary decays of nuclei through protonic, alpha-particle, cluster, and other channels. © *2004 MAIK "Nauka/Interperiodica".*

1. INTRODUCTION

In performing a quantum-mechanical investigation into protonic [1–3], alpha-particle [4], and cluster [5] radioactivity and into the binary [6–8] and ternary [8–10] fission of nuclei, there arises the problem of taking into account the coupling of various decay channels. Since the off-diagonal components of the potentials representing the interaction of nuclear-decay products are not small in general, the inclusion of such components may lead to the transition of these products between open decay channels, including channels of their excitation. The inclusion of transitions featuring the excitation of decay products makes it possible to analyze effects associated with the polarization of decay products in the decay process being studied.

An investigation of this problem was performed in [8] by considering the example of a quantum mechanical description of the binary and ternary fission of nuclei on the basis of the formalism of the multiparticle theory of nuclear reactions [11, 12], the unified theory of the nucleus [13], and the theory of open Fermi systems [14]. The objective of the present study is to refine and generalize, within the conceptual framework developed in [11, 12], the results obtained in [8].

2. STRUCTURE OF THE WAVE FUNCTION FOR A DECAY NUCLEAR STATE

The present investigation will be performed for the example where a parent nucleus of mass number A and charge number Z decays to two fragments whose mass and charge numbers are, respectively, A_i and Z_i $(i = 1, 2)$. The wave function Ψ_σ^{JM} describing an isolated quasistationary decaying-nucleus state characterized by a spin J, its projection M onto the z axis of the laboratory frame, other quantum numbers σ, and the total set of intrinsic coordinates ξ satisfies the Schrödinger equation

$$(H_A - \bar{E}_\sigma^J)\Psi_\sigma^{JM}(\xi) = 0, \qquad (1)$$

where H_A is the Hamiltonian for nucleus A in its c.m. frame and $\bar{E}_\sigma^J = (E_\sigma^J - i\Gamma_\sigma^J/2)$ is the complex-valued energy whose real part E_σ^J coincides with the sign-reversed binding energy of the nucleus and whose imaginary part is related to the total width Γ_σ^J with respect to the decay of nucleus A through all open channels. Following the strategies adopted in the unified theory of the nucleus [13] and in the theory of open Fermi systems [14], we can represent the wave function $\Psi_\sigma^{JM}(\xi)$ in the form

$$\Psi_\sigma^{JM}(\xi) = \hat{P}\Psi_\sigma^{JM}(\xi) + \hat{Q}\Psi_\sigma^{JM}(\xi). \qquad (2)$$

The operator $\hat{P}$ projects the states of nucleus A onto the internal (shell) region of the configuration space spanned by the coordinates ξ. In this region, nucleus A is of a simply connected shape and can be described by using an orthonormalized finite basis $\Psi_n^{JM}(\xi)$ of multiparticle shell functions that are constructed with allowance for normal and superfluid nucleon–nucleon correlations and collective modes of motion, the subscript n running through a discrete and a finite set of values. In this case, the operator $\hat{P}$ can be represented as

$$\hat{P} = \sum_n \left|\Psi_n^{JM}\right\rangle \left\langle\Psi_n^{JM}\right|. \qquad (3)$$

The operator $\hat{Q} = 1 - \hat{P}$ projects the decaying-nucleus state onto the configuration-space region (cluster region) where the products of the decay of nucleus A have already been formed. In the cluster

*e-mail: kadmensky@phys.vsu.ru

region, the wave function $\hat{Q}\Psi_\sigma^{JM}$ describing a quasistationary parent-nucleus state for which $\Gamma_\sigma^J \ll E_\sigma^J$ can be represented [13] in the form

$$\hat{Q}\Psi_\sigma^{JM}(\xi) = \langle G^{JM}(\xi,\xi')|\hat{Q}(H_A - E_\sigma^J)\hat{P}|\Psi_\sigma^{JM}(\xi')\rangle, \quad (4)$$

where $G^{JM}(\xi,\xi')$ is the multiparticle Green's function in the cluster region. It satisfies the equation

$$\hat{Q}(H_A - E_\sigma^J)\hat{Q}G^{JM}(\xi,\xi') = \delta(\xi - \xi'). \quad (5)$$

In order to describe the motion of decay fragments in the cluster region, we introduce the relative coordinate $\mathbf{R} = \mathbf{R}_1 - \mathbf{R}_2$ (where $\mathbf{R}_i$ is the coordinate of the center of mass of the ith fragment) and the solid angle $\Omega_\mathbf{R}$ determining the direction of the radius vector $\mathbf{R}$ in the laboratory frame. In the cluster region, one can introduce the channel function $U_\alpha^{JM}(x)$ ($\alpha \equiv cL$, $c = J_1\sigma_1 J_2\sigma_2$) possessing correct transformation properties under time inversion [11],

$$U_\alpha^{JM}(x) = \left\{\left\{\Psi_{\sigma_1}^{J_1M_1}(\xi_1)\Psi_{\sigma_2}^{J_2M_2}(\xi_2)\right\}_{IM_I} i^L Y_{LM_L}(\Omega_\mathbf{R})\right\}_{JM}, \quad (6)$$

where the set of coordinates x includes all of the coordinates ξ apart from the absolute value R of the radius vector $\mathbf{R}$. In formula (6), $\Psi_{\sigma_i}^{J_iM_i}(\xi_i)$ is the intrinsic wave function for the ith fragment [for this function, we can use its shell component $\hat{P}\Psi_{\sigma_i}^{J_iM_i}(\xi_i)$], $Y_{LM_L}(\Omega_\mathbf{R})$ is a spherical harmonic that describes the angular component of the relative motion of decay fragments, and braces denote vector coupling of angular momenta. The energy Q_c of the relative motion of fragments in the α channel is given by $Q_c = E_\sigma^J - E_{\sigma_1}^{J_1} - E_{\sigma_2}^{J_2}$.

In the cluster region, we introduce a complete set of wave functions $\Psi_{\alpha E}^{JM(\pm)}(\xi)$ that are normalized to a delta function of energy and which describe the relative motion of fragments in the continuous-spectrum region. Since the wave functions $\Psi_{\alpha E}^{JM(\pm)}(\xi)$ are orthogonal to the shell functions $\Psi_n^{JM}(\xi)$ of the nucleus, the wave functions $\Psi_{\alpha E}^{JM(\pm)}(\xi)$ cannot take into account multiparticle resonance states of a composite system; they describe only the potential scattering of fragments on each other with allowance for the coupling of various decay channels. The wave functions $\Psi_{\alpha E}^{JM(\pm)}(\xi)$, for which the superscripts $(\pm)$ were defined in [11], satisfy the Schrödinger equation

$$\hat{Q}(H_A - E)\hat{Q}\Psi_{\alpha E}^{JM(\pm)}(\xi) = 0. \quad (7)$$

Equation (7) can be represented in a more convenient form if we use the orthogonal-projection method [15] and replace the operator $\hat{Q}(H_A - E)\hat{Q}$ by the operator $(\tilde{H}_A - E) = (H_A + \chi\hat{P} - E)$, where $\hat{P}$ is the projection operator introduced above and the quantity χ is taken in the limit $\chi \to \infty$, which ensures that the wave functions $\Psi_{\alpha E}^{JM(\pm)}(\xi)$ are orthogonal to the set of shell functions $\Psi_n^{JM}(\xi)$ and, hence, to the decaying-nucleus shell function $\hat{P}\Psi_\sigma^{JM}(\xi)$.

Further, we assume that the interaction of decay fragments does not lead to the rearrangement of their nucleonic content—that is, that A_i and Z_i remain unchanged. In this case, the Hamiltonians H_A and $\tilde{H}_A$ can be represented as

$$H_A = H_A^0 + V, \quad \tilde{H}_A = H_A^0 + V + \chi\hat{P} \equiv H_A^0 + \tilde{V}, \quad (8)$$

where H_A^0 is the Hamiltonian describing noninteracting decay fragments and V is the potential describing the interaction of these fragments. The Green's function $G^{JM}(\xi,\xi')$ (5) can be represented in the form

$$G^{JM}(\xi,\xi') = \sum_\alpha \int \frac{\left|\Psi_{\alpha E}^{JM(+)}(\xi)\right\rangle\left\langle\Psi_{\alpha E}^{JM(-)}(\xi')\right|}{E_\sigma^J - E + i\delta} dE, \quad (9)$$

where the term $(+i\delta)$ in the denominator of the integrand ensures the appearance of diverging spherical waves in all open decay channels.

3. DECAYING-NUCLEUS WAVE FUNCTION IN THE ASYMPTOTIC REGION

In order to find an explicit expression for the Green's function $G^{JM}(\xi,\xi')$ (9), we represent the wave function $\Psi_{\alpha E}^{JM(\pm)}(\xi)$ in the form of an expansion in the channel functions (6) as

$$\Psi_{\alpha E}^{JM(\pm)}(\xi) = \sum_{\alpha'} U_{\alpha'}^{JM}(x)\frac{f_{\alpha'\alpha}^{J(\pm)}(R)}{R}. \quad (10)$$

Substituting formula (10) into Eq. (7), one can obtain a set of coupled equations for the form factors $f_{\alpha'\alpha}^{J(\pm)}(R)$; that is,

$$\left(\frac{d^2}{dR^2} - \frac{L'(L'+1)}{R^2} + k_{c'}^2\right) f_{\alpha'\alpha}^{J(\pm)}(R) - \frac{2M}{\hbar^2}\sum_{\alpha''}\tilde{V}_{\alpha'\alpha''}(R) f_{\alpha''\alpha}^{J(\pm)}(R) = 0, \quad (11)$$

where

$$\tilde{V}_{\alpha'\alpha''}(R) = \left\langle U_{\alpha''}^{JM}\left|\tilde{V}\right|U_{\alpha'}^{JM}\right\rangle, \quad (12)$$

$$k_{c'} = \sqrt{\frac{2M\bar{Q}_{c'}}{\hbar^2}},$$

$\bar{Q}_{c'} = E - E^{J_1}_{\sigma_1} - E^{J_2}_{\sigma_2}$, and M is the reduced mass of the fragments. The form factors $f^{J(+)}_{\alpha'\alpha}(R)$ correspond to the regular solution to the Schrödinger equation (7) and satisfy the boundary conditions

$$f^{J(+)}_{\alpha'\alpha}(R) \to 0 \text{ for } R \to 0; \tag{13}$$

$$f^{J(+)}_{\alpha'\alpha}(R) \to -\frac{1}{2i}\sqrt{\frac{2}{\pi\hbar v_{c'}}} \times \left\{\exp\left[-i\left(k_{c'}R - \frac{L\pi}{2}\right)\right]\delta_{\alpha'\alpha} - S^J_{\alpha'\alpha} \times \exp\left[i\left(k_{c'}R - \frac{L'\pi}{2}\right)\right]\right\} \text{ for } R \to \infty,$$

where $v_{c'} = \hbar k_{c'}/M$ and $S^J_{\alpha'\alpha}$ is an S-matrix element in the representation of the channel functions $U^{JM}_{\alpha}(x)$ (6). The form factor $f^{J(-)}_{\alpha'\alpha}(R)$ is identical to the time-reversed form factor $f^{J(+)}_{\alpha'\alpha}(R)$ and can be written as [11]

$$f^{J(-)}_{\alpha'\alpha}(R) = (-1)^L\left[f^{J(+)}_{\alpha'\alpha}(R)\right]^*. \tag{14}$$

Since the S matrix is unitary and symmetric [11], we can reduce, with the aid of the unitary real orthogonal operator N having the property $NN^+ = 1$, which can be rewritten in the matrix form as

$$\sum_{\beta} N_{\alpha'\beta}(N^+)_{\beta\alpha} = \sum_{\beta} N_{\alpha'\beta}N_{\alpha\beta} = \delta_{\alpha\alpha'}, \tag{15}$$

the S matrix to the diagonal form [11, 12]

$$S^J_{\alpha'\alpha} = \sum_{\beta\beta'} N_{\alpha'\beta}S^J_{\beta\beta'}(N^+)_{\beta'\alpha} = \sum_{\beta\beta'} N_{\alpha'\beta}S^J_{\beta\beta'}N_{\alpha\beta'}, \tag{16}$$

where

$$S^J_{\beta\beta'} = e^{2i\delta^J_\beta}\delta_{\beta\beta'}, \tag{17}$$

δ^J_β being the potential phase shift for decay-product scattering in the channel β. The regular form factor $f^{J(+)}_{\alpha'\alpha}(R)$ can then be expressed in terms of the regular real form factor $\tilde{f}^J_{\alpha'\beta}(R)$, whose asymptotic behavior for $R \to \infty$ is

$$\tilde{f}^J_{\alpha'\beta}(R) \to \sqrt{\frac{2}{\pi\hbar v_{c'}}}\sin\left(k_{c'}R - \frac{L'\pi}{2} + \delta^J_\beta\right). \tag{18}$$

As a result, we obtain [11]

$$f^{J(+)}_{\alpha'\alpha}(R) = \sum_{\beta} e^{i\delta^J_\beta}N_{\alpha'\beta}N_{\alpha\beta}\tilde{f}^J_{\alpha'\beta}(R). \tag{19}$$

We can now introduce the nonregular form factor $\bar{f}^{J(+)}_{\alpha'\alpha}(R)$, which diverges in the limit $R \to 0$ and which is related, by an equation of the type in (19), to the nonregular real form factor $\bar{\tilde{f}}^J_{\alpha'\beta}(R)$, whose asymptotic behavior in the limit $R \to \infty$ is

$$\bar{\tilde{f}}^J_{\alpha'\beta}(R) \to \sqrt{\frac{2}{\pi\hbar v_{c'}}}\cos\left(k_{c'}R - \frac{L'\pi}{2} + \delta^J_\beta\right). \tag{20}$$

Relations (18)–(20) solve the problem of constructing, with allowance for channel coupling, both regular and nonregular solutions to the problem of the scattering of particles having an intrinsic structure.

Using relation (19), we can represent the wave function $\Psi^{JM(+)}_{\alpha E}$ (10) in the form

$$\Psi^{JM(+)}_{\alpha E} = \sum_{\alpha'\beta} U^{JM}_{\alpha'}e^{\delta^J_\beta}N_{\alpha'\beta}N_{\alpha\beta}\frac{\tilde{f}^J_{\alpha'\beta}(R)}{R}. \tag{21}$$

Substituting (21) into the definition (9) of the Green's function and performing integration with respect to the energy E, one can determine the asymptotic behavior of the Green's function (9) in the limit $R \to \infty$. As a result, we have

$$G^{JM}(\xi,\xi') \xrightarrow[R\to\infty]{} \sum_{\alpha\alpha'\beta\alpha''\beta'} \left| U^{JM}_{\alpha'}e^{i\delta^J_\beta}N_{\alpha'\beta}N_{\alpha\beta} \times \frac{\exp\left[i\left(k_{c'}R - \frac{L'\pi}{2} + \delta^J_\beta\right)\right]}{R}\right\rangle \times \left\langle U^{JM}_{\alpha''}e^{i\delta^J_{\beta'}}N_{\alpha''\beta'}N_{\alpha\beta'}\frac{\tilde{f}^J_{\alpha''\beta'}(R')}{R'}\right|. \tag{22}$$

Upon performing summation over α with allowance for the properties of the operator N in (15), redefining the superscripts as $\alpha' \to \alpha$ and $\alpha'' \to \alpha'$, and using relation (19), we can reduce formula (22) to the form

$$G^{JM}(\xi,\xi') \xrightarrow[R\to\infty]{} \sum_{\alpha}\left|U^{JM}_{\alpha}\frac{\exp\left[i\left(k_cR - \frac{L\pi}{2}\right)\right]}{R}\right\rangle \times \sum_{\alpha'}\left\langle U^{JM}_{\alpha'}\frac{f^{J(-)}_{\alpha'\alpha}(R')}{R'}\right|. \tag{23}$$

Employing the definition (4) of the cluster component $\hat{Q}\Psi^{JM}_{\sigma}$ of the decaying-nucleus wave function Ψ^{JM}_{σ} (2) and taking into account the asymptotic expression (23) for the Green's function $G^{JM}(\xi,\xi')$ in the cluster region, one can find that, in the limit $R \to \infty$, the asymptotic behavior of the decaying-nucleus wave function Ψ^{JM}_{σ} is

$$\Psi^{JM}_{\sigma} \to \sum_{\alpha} U^{JM}_{\alpha}\frac{\exp\left[i\left(k_cR - \frac{L\pi}{2}\right)\right]}{R}\sqrt{\Gamma^J_{\sigma\alpha}}, \tag{24}$$

where the quantity $\sqrt{\Gamma^J_{\sigma\alpha}}$, which is complex-valued in general, is defined as

$$\sqrt{\Gamma^J_{\sigma\alpha}} = \sqrt{2\pi} \times \sum_{\alpha'} \left\langle U^{JM}_{\alpha'} \frac{f^{J(-)}_{\alpha\alpha'}(R)}{R} \middle| H_A - E^J_\sigma \middle| \hat{P}\Psi^{JM}_\sigma(\xi') \right\rangle. \quad (25)$$

If use is made of formula (14), the quantity in (25) can be rewritten in terms of the form factors $f^{J(+)}_{\alpha'\alpha}(R)$ as

$$\sqrt{\Gamma^J_{\sigma\alpha}} = \sqrt{2\pi}(-1)^L \times \sum_{\alpha'} \left\langle U^{JM}_{\alpha'} \frac{\left(f^{J(+)}_{\alpha'\alpha}(R)\right)^*}{R} \middle| H_A - E^J_\sigma \middle| \hat{P}\Psi^{JM}_\sigma(\xi') \right\rangle. \quad (26)$$

Since the quantity $\sqrt{\Gamma^J_{\sigma\alpha}}$ (25) is complex-valued in general, it can be represented in the form

$$\sqrt{\Gamma^J_{\sigma\alpha}} = \sqrt{(\Gamma^J_{\sigma\alpha})^0} e^{i\delta^J_\alpha}, \quad (27)$$

where the real quantities $\sqrt{(\Gamma^J_{\sigma\alpha})^0}$ and δ^J_α can be considered as, respectively, the amplitude of the partial decay width and the effective potential phase shift for scattering in the α channel. They are analogous to the corresponding amplitude and phase shift in the R-matrix theory of nuclear reactions [11] and in the unified theory of the nucleus [13], where there is no direct coupling between open decay channels. The phase shift δ^J_α is expressed in terms of a linear combination of the phase shifts δ^J_β for the potential scattering of decay products in the β channels, for which the S matrix (17) has a diagonal form. As a matter of fact, formulas (24)–(27) provide a solution to the problem of taking into account the effect of open-decay-channel coupling on the decay properties of nuclei.

We note that the quantities $\sqrt{(\Gamma^J_{\sigma\alpha})^0}$ can have either a positive or a negative sign. This sign can be determined via a continuous transition to the limiting situation where there is no coupling between decay channels, in which case the sign of the quantity $\sqrt{(\Gamma^J_{\sigma\alpha})^0}$ and the phase shift δ^J_α are determined unambiguously.

Formulas (24) and (25) were derived for the first time in [8] in developing the quantum-mechanical theory of nuclear fission and were used there to validate the results on the angular distributions [7, 9] and on P-odd and P-even asymmetries [10] in the angular distributions obtained for the binary and ternary fission of polarized nuclei.

4. CONCLUSION

In contrast to the integral formulas used previously in [1–5] for deep-subbarrier decays, the integral formulas that have been obtained here for determining the amplitudes of partial decay widths and potential phase shifts appear to be valid for a wide range of nuclear decays of both subbarrier and above-barrier types. These formulas make it possible to take into account the coupling of various open decay channels and effects of decay-fragment polarizability, which are caused by their interaction. The resulting formulas are applicable to describing the decays of not only spherical but also deformed nuclei (this is of greater importance) with the aid of the methods developed for protonic decay [3], alpha decay [16], and the fission of deformed nuclei [6–9]. The formulas obtained above for binary decay channels can easily be generalized, by using the methods developed in the quantum theory of ternary nuclear fission [8, 9], to the case of nuclear-decay channels involving three or more particles. These formulas can play a particular role in developing the theory of the two-proton decay of nuclei, where it is of paramount importance to take into account the interaction (first of all, the Coulomb interaction) of the products of this decay.

ACKNOWLEDGMENTS

I am grateful to V.E. Bunakov for stimulating discussions.

This work was supported in part by the Ministry of Higher Education of the Russian Federation within the program Universities of Russia (project no. UR-02.01.003).

REFERENCES

1. V. P. Bugrov, S. G. Kadmenskiĭ, V. I. Furman, and V. G. Khlebostroev, Yad. Fiz. **41**, 1123 (1985) [Sov. J. Nucl. Phys. **41**, 717 (1985)].
2. S. G. Kadmensky, Yad. Fiz. **63**, 613 (2000) [Phys. At. Nucl. **63**, 551 (2000)].
3. V. P. Bugrov and S. G. Kadmenskiĭ, Yad. Fiz. **49**, 1562 (1989) [Sov. J. Nucl. Phys. **49**, 967 (1989)].
4. S. G. Kadmensky and W. P. Furman, *Alpha Decay and Related Nuclear Reactions* (Énergoatomizdat, Moscow, 1985) [in Russian].
5. S. G. Kadmenskiĭ, V. P. Furman, and Yu. M. Chuvil'skiĭ, Izv. Akad. Nauk SSSR, Ser. Fiz. **50**, 1786 (1986).
6. S. G. Kadmensky, Yad. Fiz. **65**, 1424 (2002) [Phys. At. Nucl. **65**, 1390 (2002)].
7. S. G. Kadmensky and L. V. Rodionova, Yad. Fiz. **66**, 1259 (2003) [Phys. At. Nucl. **66**, 1219 (2003)].
8. S. G. Kadmensky, Yad. Fiz. **67**, 167 (2004) [Phys. At. Nucl. **67**, 170 (2004)].
9. S. G. Kadmensky, Yad. Fiz. **65**, 1833 (2002) [Phys. At. Nucl. **65**, 1785 (2002)].

10. S. G. Kadmensky, Yad. Fiz. **66**, 1739 (2003) [Phys. At. Nucl. **66**, 1691 (2003)]; **67**, 258 (2004) [**67**, 241 (2004)].
11. M. Goldberger and K. Watson, *Collision Theory* (Wiley, New York, 1964; Mir, Moscow, 1967).
12. N. F. Mott and H. S. W. Massey, *Theory of Atomic Collisions* (Clarendon, Oxford, 1965; Mir, Moscow, 1969).
13. K. Wildermuth and Y. C. Tang, *A Unified Theory of the Nucleus* (Vieweg, Braunschweig, 1977; Mir, Moscow, 1980).
14. S. G. Kadmensky, Yad. Fiz. **62**, 236 (1999) [Phys. At. Nucl. **62**, 201 (1999)]; **64**, 478 (2001) [**64**, 423 (2001)].
15. V. I. Kukulin, V. G. Neudatchin, and Yu. F. Smirnov, Fiz. Élem. Chastits At. Yadra **10**, 1236 (1979) [Sov. J. Part. Nucl. **10**, 492 (1979)].
16. S. G. Kadmenskiĭ and V. E. Kalechits, Yad. Fiz. **12**, 70 (1970) [Sov. J. Nucl. Phys. **12**, 37 (1971)].

Translated by A. Isaakyan

Physics of Atomic Nuclei, Vol. 67, No. 12, 2004, pp. 2139–2147. Translated from Yadernaya Fizika, Vol. 67, No. 12, 2004, pp. 2162–2170.
Original Russian Text Copyright © 2004 by Yankauskas.

NUCLEI
Theory

Investigation of Low-Lying Levels of the $^{8}_{4}$Be Nucleus in the Multiquantum Approximation of the Orthogonal Scheme

K. I. Yankauskas*

Klaipeda University, Klaipeda, Lithuania

Received December 11, 2003

Abstract—In the multiquantum approximation of the orthogonal scheme, specific calculations for the energies and radii of the $^{8}_{4}$Be nucleus are performed with allowance for all states characterized by the $\lambda = [44]$ Young diagram, the quantum numbers $K_{\min}$ and $K_{\min} + 2$ of the $O(3(A-1))$ group, and the quantum numbers $E = K + 2N$ ($N \leq 9$) of the $U(3(A-1))$ group. The convergence of the results with respect to the extension of the basis is studied, and the structure of relevant wave functions is revealed. The results of these calculations are compared with the results obtained in the analogous approximation of the unitary scheme. © *2004 MAIK "Nauka/Interperiodica"*.

1. INTRODUCTION

Within the $U(3(A-1))$ scheme of the translation-invariant model of the nucleus, use is made of a few bases characterized by specific chains of subgroups of the $U(3(A-1))$ group. These include the unitary-scheme basis, the orthogonal-scheme basis [1], and some of their modifications [2]. The mathematical formalism of the unitary-scheme model is more elaborate, and this is the main reason why this model is employed much more often than the orthogonal-scheme model. In this connection, it is highly desirable to develop a mathematical formalism for the orthogonal scheme and to reveal the potential of the corresponding basis.

In [3], spectroscopic calculations were performed for the $^{8}_{4}$Be nucleus in the multiquantum approximation of the unitary scheme [it is specified by the following chains of subgroups of the $U(3(A-1))$ group: $U(3(A-1)) \supset SU(3) \times U(A-1)$, $U(A-1) \supset O(A-1) \supset S(A)$, and $SU(3) \supset O^{+}(3)$]. From the calculations performed with semirealistic potentials, it follows that the inclusion of $U(3(\mathrm{A}-1))$ states involving multiquantum excitations improves the results considerably: the binding energy increases by 25–40%, while the electric quadrupole moments and the probabilities of electric quadrupole transitions become severalfold greater.

A number of studies were devoted to examining the properties of light nuclei within the orthogonal scheme (for an overview, see [2]), which is specified by the following chains of subgroups of the $U(3(A-1))$ group: $U(3(A-1)) \supset O(3(A-1)) \supset O(A-1) \times O(3)$ and $O(A-1) \supset S(A)$. In those studies, however, the potential of the orthogonal scheme has not been exhausted, since the calculations there were performed in bases that are coincident with unitary bases if no account is taken of states appearing to be ρ excitations (that is, $E > K$ states—see below). Moreover, no attention has been given to some spectroscopic features of nuclei, such as electric quadrupole moments and the transition probabilities $B(E2)$. In view of the aforesaid, it is advisable to develop a relevant procedure, to perform calculations that would be similar to those in [3] and which would rely on a basis inherent in the orthogonal scheme and different from the unitary-scheme basis substantially, and to compare the results obtained within the unitary and orthogonal schemes.

This is precisely the objective of the present study. Specific calculations for the $^{8}_{4}$Be nucleus are performed here by using the orthogonal-scheme bases that contain all functions labeled with the $\lambda = [44]$ Young diagram and by the quantum numbers $E = K = K_{\min}$ and $K_{\min} + 2$ of the irreducible representations of the $U(3(A-1))$ and $\mathrm{O}(3(\mathrm{A}-1))$ groups ($K_{\min}$ and $K_{\min} + 2$ approximations), and the role of the functions corresponding to different quantum numbers of the $O(3(A-1))$ and $O(A-1)$ groups is examined. Also, calculations are performed in the $K_{\min}$ and $K_{\min} + 2$ bases extended by adding $E > K$ functions (multiquantum approximations), and the role of ρ-excited states is investigated. The calculated quantities include the binding energy and the energies and radii of low-lying $L^{\pi} = 0^{+}$, 2^{+}, 4^{+} and 0^{+}_{1}, 2^{+}_{1}, 4^{+}_{1} levels (rotational bands). The choice of the $^{8}_{4}$Be nucleus for the subject of the calculation and the

*e-mail: fizkat@jtf.ku.lt

use of the same potentials as in [3] were motivated by the desire to compare the available results in the multiquantum approximation of the unitary scheme with the results of the present study in the analogous approximation of the orthogonal scheme and to draw some conclusions on the potential of the orthogonal-scheme basis associated with the $U(3(A-1))$ group.

In the present study, a procedure for taking into account orthogonal-scheme-basis states that involve multiquantum excitations is developed and is applied to the $^{8}_{4}$Be nucleus; also, the extent to which the two bases of the $U(3(A-1))$ model—that of the orthogonal scheme and that of the unitary scheme—are appropriate is revealed. In this connection, it is necessary to touch upon the question of the place that the $U(3(A-1))$ scheme occupies among other methods related to it. It should be noted that the $U(3(A-1))$ scheme is close to the method of K harmonics and the method of multidimensional hyperspherical functions and that it is intimately related to the $Sp(2n, R)$ model—more specifically, it was proven in [2] that some approximations of the $U(3(A-1))$ scheme are equivalent to the aforementioned models. It is more difficult to compare the $U(3(A-1))$ scheme with the multiquantum shell model (also known as the no-core shell model) [4, 5], since studies that would employ a rather wide basis and respective effective interactions have not yet been performed within the $U(3(A-1))$ scheme. The fact that good results were obtained in [4] is likely to be due not only to the choice of basis but also to the application of appropriate effective interactions derived microscopically, which employ realistic phenomenological nucleon–nucleon forces. On the basis of model concepts used in the $U(3(A-1))$ scheme and in the model proposed in [4], one would expect that, for a rather wide basis, the results within the $U(3(A-1))$ scheme will be close to those obtained in [4]. But if we compare the mathematical methods of the $U(3(A-1))$ scheme with those in the model from [4], it should be emphasized that determinants are employed to construct antisymmetric states in the latter case. As a result, there arise difficulties in constructing kinematically correct wave functions [6]—that is, in ensuring translation invariance and a good quantum number J. (In all probability, these problems will be resolved on the basis of the recently developed translation-invariant version of this model [7].) There are no such problems in constructing basis functions of the $U(3(A-1))$ scheme, where one relies on the density-matrix formalism and extensively employs group-theory methods, this formalism being equally applicable to nuclei like ^{4}He and ^{8}Be and to systems of the ^{12}Be type.

Computational methods developed within the $U(3(A-1))$ scheme ($SU(3)$ method of the irreducible density matrix [2] within the unitary scheme and the method of Petrauskas coefficients [8] within the orthogonal scheme) make it possible to take into account quite straightforwardly states involving multiquantum excitations; moreover, there is presently every possibility of performing, for few-nucleon systems, calculations similar to those in [4]. It is planned to do this in the future.

2. BASIS AND BASIC FORMULAS

For a system of A nucleons, we denote the basis function by

$$\Psi(EK\beta\omega_{123}\alpha\lambda L\Gamma_0),$$

where E and K are the symmetric irreducible representations of the $U(3(A-1))$ and the $O(3(A-1))$ group, respectively; $\omega_{123}=(\omega_1\omega_2\omega_3)$ is an irreducible representation of the $O(A-1)$ group; β and α are the repetition indices for the chains $O(3(A-1))\supset O(A-1)\times O^{+}(3)$ and $O(A-1)\supset S(A)$, respectively; λ is a Young diagram for the $S(A)$ group; L is the orbital angular momentum; and Γ_0 stands for the remaining quantum numbers, including the spin–isospin feature.

Specific calculations for the $^{8}_{4}$Be nucleus will be performed by using a basis of functions that is extended step by step, these functions being labeled with the most symmetric Young diagram $\lambda=[44]$ ($S=0, T=0$); the orbital angular momentum taking the values of $L=0$, 2, 4; and the following quantum numbers $EK\beta\omega_{123}\alpha$ associated with irreducible representations of the $U(3(A-1))$, $O(3(A-1))$, and $O(A-1)$ groups:

$$EK\beta\omega_{123}\alpha = E4(400), E6\beta(400), E6(600),$$
$$E6(510), E6(420)\alpha \quad (\text{basis } B_{\max}).$$

For the number E, we have $E=K+2N$, where N assumes the values of $N=0,1,\ldots,9$. For states where there are no repetitions, the indices β and α are not indicated explicitly. At $L=2$, the repetition index β takes the values of $\beta=1$, 2, 3, while, at $L=4$, it is $\beta=1$, 2. For the repetition index α, we have $\alpha=1$, 2. The basis $B_{\max}$ involving functions labeled with the minimum possible value $K_{\min}$ and $N=1$ and functions associated with $K_{\min}+2$ and $N=0$ corresponds to the $K_{\min}+2$ approximation. The basis $B_{\max}$ of the same functions featuring $N>1$ corresponds to the multiquantum approximation.

We will now present basic definitions and relations and discuss the procedure used in the ensuing calculations. We will employ the orthogonal-scheme wave function in the form [2]

$$|EK\Gamma_0\rangle \equiv R_{EK}(\rho)U_K^{\Gamma_0}(\Omega). \qquad (1)$$

Expression (1) is a solution to the harmonic-oscillator problem in the $3(A-1)$-dimensional system of spherical coordinates. In this function, $R(\rho)$ is the radial component, which depends on the multidimensional distance ρ; $U(\Omega)$ stands for the angular and the spin–isospin function, Ω being the corresponding variables; E is the total number of oscillator quanta; K is the multidimensional angular momentum; and Γ_0 denotes the remaining quantum numbers. Functions for which $E > K$ represent radial excitations (also known as ρ excitations) of the $E = K$ state. In expression (1), $U_K^{\Gamma_0}$ is the angular function in the method of K harmonics [2]. First, we will consider the calculation of energy. It is well known that, for states associated with the Young diagram $\lambda = [4\ldots4k]$, where $k = 0, 1, 3$, the total Hamiltonian has the form

$$H = V_C + T + O^{\mathrm{C}}, \tag{2}$$

where V_{C} is the central nucleon–nucleon interaction in the form given by expression (2) in [3], O^{C} is the Coulomb interaction operator, and T is the kinetic-energy operator. By applying the density-matrix formalism, we can represent a matrix element of the operator V_C in the form

$$\langle EK\Gamma_0|V_C|E'K'\Gamma_0'\rangle \tag{3}$$
$$= \sum_{\nu}\sum_{p,\alpha=0}^{N+N'} Q_p^{\nu KK\Gamma_0K'K'\Gamma_0'} D_{p,\alpha}^{NN'l_Kl_{K'}} I_{p+\alpha}^{\nu}.$$

The notation used in (3) is the following: $l_K = K + (3A-6)/2$ (recall that A is the number of nucleons); $N = (E-K)/2$; Q_p^{ν} denotes the reduced density matrices for $E = K$ and $E' = K'$ states; the symbol $\nu =$ W, M, B, or H labels the type of interaction (respectively, Wigner, Majorana, Bartlet, or Heisenberg interaction); $I_{p+\alpha}^{\nu}$ stands for the Talmi integrals of the corresponding functions $V_\nu(r)$ for the operator V_{C} of central nucleon–nucleon interaction {see [3], formula (3)}; and $D_{p,\alpha}$ are the Petrauskas coefficients {see [8], formula (8)}.

We note that, in order to calculate expression (3) in the case of the $[4\ldots4k]$ ($k = 0, 1, 3$), diagrams it is sufficient to know the density matrices Q^{W} and Q^{M} for Wigner and Majorana interactions, since, in this case, we have

$$Q^{\mathrm{B}} = -Q^{\mathrm{H}} = 2(Q^{\mathrm{W}} - Q^{\mathrm{M}})/5. \tag{4}$$

An expression similar to that in (3) can be written for the Coulomb energy operator

$$O^{\mathrm{C}} = \frac{e^2}{16\pi\varepsilon_0}\sum_{i<j}^{A}\frac{(1-2t_0^1(i))(1-2t_0^1(j))}{r_{ij}}, \tag{5}$$

where e is the electron charge, ε_0 is the dielectric constant, $t_0^1(i)$ is the isospin operator for the ith nucleon, and r_{ij} is the distance between the ith and the jth nucleon. We have

$$\langle EK\Gamma_0|O^{\mathrm{C}}|E'K'\Gamma_0'\rangle \tag{6}$$
$$= \sum_{p,\alpha=0}^{N+N'} Q_p^{\mathrm{C}KK\Gamma_0K'K'\Gamma_0'} D_{p,\alpha}^{NN'l_Kl_{K'}} I_{p+a}^{\mathrm{C}}.$$

In (6), Q^{C} is the reduced density matrix for the operator in (5), while the Talmi integrals I_p^{C} are given by

$$I_p^{\mathrm{C}} = \frac{b}{\sqrt{2\pi}r_\Psi}\frac{2^{p+1}p!}{(2p+1)!!}, \quad b = 1.44\ \text{MeV fm}. \tag{7}$$

In expression (8) for this integral in [3], there is a misprint. Employing expression (10) for the root-mean-square radius (see below) and the virial theorem, we find for an element of the kinetic-energy operator that

$$\langle EK\Gamma_0|T|E'K'\Gamma_0'\rangle = \frac{1}{2}\delta(K,K')\delta(\Gamma_0,\Gamma_0') \tag{8}$$
$$\times\{(2N+l_K+3/2)\delta(N,N')$$
$$+[(N+1)(N+l_K+3/2)]^{1/2}\delta(N,N'-1)\}\hbar\omega.$$

In (8), the parameter ω is given by $\omega = \hbar/(mr_\Psi^2)$, where r_Ψ is the scale parameter of the orbital wave function and m is the nucleon mass.

Within the $U(3(A-1))$ scheme, the average of the squares of the distances from the center of mass of a system of A nucleons to its nucleons, $r^2 = \sum r_i^2/A$, is expressed in terms of the multidimensional distance ρ as

$$r^2 = \frac{\rho^2}{A} = \frac{1}{A}\sum_{i=1}^{A-1}\rho_i^2, \tag{9}$$

where ρ_i are normalized Jacobi coordinates [1]. For a matrix element of the operator in (9), we have

$$\langle EK\Gamma_0|r^2|E'K'\Gamma_0'\rangle = \frac{r_\Psi^2}{A}\{(2N+l_K+3/2) \tag{10}$$
$$\times\delta(N,N') - [(N+1)(N+l_K+3/2)]^{1/2}$$
$$\times\delta(N,N'-1)\}\delta(K,K')\delta(\Gamma_0,\Gamma_0').$$

From the above expressions (6), (8), and (10), one can see that, as a matter of fact, the problem of calculating relevant matrix elements for $E > K$ orthogonal-scheme states amounts to calculating the reduced density matrices Q^ν ($\nu =$ W, M) and Q^{C} for the $E = K$ states. The expressions for the density matrices Q^ν and Q^{C} can be obtained by means of respective summation in the general formulas given in [2]. We will now discuss the calculation of these matrices. Since no procedure for directly evaluating

Table 1. Variations in the binding energy (they are given in parentheses) and in the relative energies of levels (in MeV) in response to an extension of the basis

Potential V_4								
	B_0		B_1		B_2		$B_{\max}$	
L^π	$N=0$	$N=9$	$N=0$	$N=9$	$N=0$	$N=9$	$N=0$	$N=9$
0^+	0(−36.41)	0(−37.24)	0(−44.42)	0(−45.11)	0(−45.77)	0(−46.42)	0(−46.04)	0(−46.75)
2^+	2.01	1.94	3.00	2.99	3.17	3.15	3.53	3.48
4^+	6.58	6.26	9.37	9.02	9.69	9.51	10.12	9.79
L^π	$N=1$	$N=9$	$N=1$	$N=9$	$N=1$	$N=9$	$N=1$	$N=9$
0_1^+	21.13	18.92	27.65	19.80	28.92	19.96	29.17	20.05
2_1^+	23.16	20.70	30.00	22.24	31.04	22.64	31.14	22.97
4_1^+	29.95	24.81	32.96	26.94	34.08	27.70	34.55	27.97
Potential V_7								
	B_0		B_1		B_2		$B_{\max}$	
L^π	$N=0$	$N=9$	$N=0$	$N=9$	$N=0$	$N=9$	$N=0$	$N=9$
0^+	0(−53.25)	0(−53.42)	0(−61.23)	0(−61.41)	0(−63.01)	0(−63.42)	0(−63.52)	0(−63.73)
2^+	1.95	1.34	2.14	2.71	2.76	2.79	3.07	3.10
4^+	6.59	4.26	6.70	7.31	8.09	7.74	8.10	7.98
L^π	$N=1$	$N=9$	$N=1$	$N=9$	$N=1$	$N=9$	$N=1$	$N=9$
0_1^+	18.47	17.82	24.65	18.12	26.61	18.38	26.85	18.40
2_1^+	19.94	19.24	26.96	20.45	28.31	20.89	28.31	21.20
4_1^+	23.40	22.48	27.43	24.00	29.45	24.80	29.72	25.08

density matrices has been developed so far, the approach used in the present study is based on determining the transformation bracket B between the bases of the unitary and the orthogonal scheme and on expressing the density matrix in the orthogonal scheme in terms of the readily calculable density matrix in the unitary scheme as

$$Q^O = BQ^U B^{-1}, \tag{11}$$

where Q^O and Q^U are the density matrices in the orthogonal and the unitary scheme, respectively. The transformation bracket is labeled as follow [2]:

$$B^{(E\omega_{123}L)}_{K\beta,E_{123}\delta\kappa}. \tag{12}$$

The columns of B are labeled with the quantum numbers $\mathrm{E}_{123}\delta\kappa$ of the unitary scheme [1]. For the symmetric representations $\omega_{123} = (\omega_1 00)$ and $K = K_{\min} + 2$, the transformation bracket B (12) can be found on the basis of the results reported in [9]. For the $\lambda = [44]$, $E = E_{\min} + 2$ ($E_{\min}$ being the minimum possible value of the number E [1]) states, in which we are interested, the density matrix in the unitary scheme, Q^U, was calculated by the present author in [10].

3. RESULTS OF THE CALCULATIONS AND DISCUSSION

The calculations were performed for bases extended step by step up to the complete set $B_{\max}$, the basis functions being labeled with the quantum numbers $EK\beta\omega_{123}\alpha$; that is,

1) $E4(400)$ (B_0),
2) $E4(400)$, $E6\beta(400)$ (B_1),
3) $E4(400)$, $E6\beta(400)$, $E6(600)$ (B_2),
4) $E4(400)$, $E6\beta(400)$, $E6(600)$, $E6(510)$, $E6(420)\alpha$ $(B_{\max})$,

where $E = K + 2N$ with $N = 0, 1, \ldots, 9$; B_0 is the minimal-approximation ($K_{\min}$) basis; B_1 is the basis formed by all $K_{\min}$ and $K_{\min} + 2$ functions corresponding to $\omega_{123} = (K_{\min}00)$; B_2 is the basis B_1 supplemented with the functions corresponding to the most symmetric representation $\omega_{123} = (K_{\min} + 2\,00)$; and $B_{\max}$ is the complete basis.

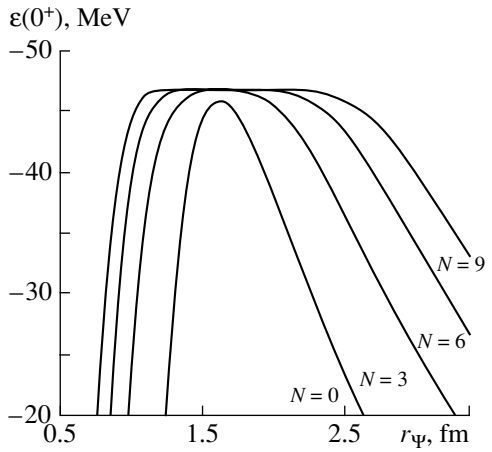

Fig. 1. Energy $\varepsilon(L) = f(r_\Psi)$ of the $L = 0^+$ level for the potential V_4 as a function of the scale parameter according to the calculation that employed the $B_{\max}$ basis.

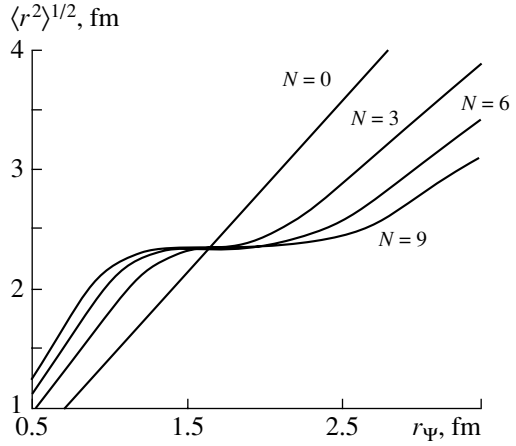

Fig. 2. Root-mean-square radius $\langle r^2(L)\rangle^{1/2} = f(r_\Psi)$ for the $L = 0^+$ level in the potential V_4 as a function of the scale parameter according to the calculation that employed the $B_{\max}$ basis.

The calculated quantities included the energies and the root-mean-square radii of the $L^\pi = 0^+$, 2^+, and 4^+ and 0^+_1, 2^+_1, and 4^+_1 levels. In these calculations, use was made of the same set of semirealistic potentials from [11–13] as in [3]. The numbering of the potentials and their parameters are given in [14] (see Table 1 in that article). The calculations involved diagonalizing matrices of rank up to 80. The present analysis was aimed at exploring changes in the results (a) upon extending the basis with respect to the quantum numbers K and ω_{123} and (b) upon taking into account $E > K$ states.

Basic results of the calculations (for values of the parameter r_ψ that minimize the energy) are quoted in Tables 1 and 2 and in Figs. 1–4. The structure of the wave functions is displayed in Table 3. Given in the B_0, B_1, B_2, and $B_{\max}$ columns of Table 1 are the results obtained in the corresponding bases. Further, the columns $N = 0$ contain the results for the $L^\pi = 0^+, 2^+, 4^+$ band in the corresponding bases for $N = 0$ (that is, without allowance for ρ-excited states) and the results for the $L^\pi = 0^+_1$, 2^+_1, 4^+_1 band in the corresponding bases for $N = 1$ [that is, in the bases supplemented with the 64(400) function, since it is precisely this function that ensures the existence of bound-state solutions]. Presented in the columns $N = 9$ are the results in multiquantum approximations with allowance for multiquantum ρ excitations—that is, the results obtained by taking into account the $E = K + 2N$ $(N = 0, 1, \ldots, 9)$ states. Table 1 does not give the results for all of the quoted potentials, because the results for the potentials V_1, V_2, and V_3 are similar to the results for V_4, while the results for V_7 are similar to the results for V_6, V_8, V_9, and V_{10}.

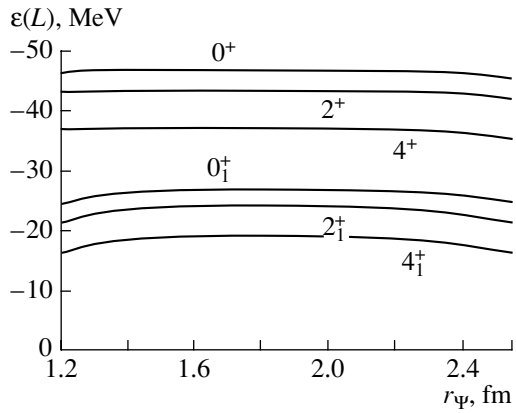

Fig. 3. Dependence $\varepsilon(L) = f(r_\Psi)$ for the potential V_4 according to the calculation that employs the $B_{\max}$, $N = 9$ basis.

For various values of the number N of ρ excitations that are taken into account, Figs. 1 and 2 show, respectively, the energy of the $L = 0^+$ level for the potential V_4 as a function of the scale parameter r_Ψ and the analogous dependence for the corresponding root-mean-square radius. For different values of L and different potentials, the general form of the dependences is similar. Figures 3 and 4 display, on a smaller scale, the dependences $\varepsilon(L) = f(r_\Psi)$ and $\langle r^2(L)\rangle^{1/2} = f(r_\Psi)$ for values of r_Ψ from the plateau region [see item (iv) below].

Formulated immediately below are some conclusions drawn from the present calculations:

(i) Table 1 illustrates variations in the binding energy and in the relative energies of the levels in response to a step-by-step extension of the basis with respect to the quantum numbers K and ω_{123}.

Table 2. Binding energy (in parentheses), relative energies of the levels (in MeV), and the root-mean-square radii (in fm) in the $K_{\min}$ and $K_{\min}+2$ approximations

	V_1		V_3		V_6		V_9		Experiment [15]
	$K_{\min}$ approximation (basis B_0)								
L^π	$N=0$	$N=9$	$N=0$	$N=9$	$N=0$	$N=9$	$N=0$	$N=9$	
0^+	0(−35.83)	0(−36.40)	0(−35.61)	0(−35.98)	0(−54.05)	0(−54.31)	0(−58.97)	0(−59.22)	−56.6
	2.221	2.276	2.289	2.336	2.491	2.532	2.356	2.386	
2^+	2.08	2.05	2.08	2.05	1.49	1.47	1.03	1.00	3.04
	2.221	2.262	2.289	2.322	2.491	2.511	2.356	2.360	
4^+	6.92	6.75	6.82	6.68	4.82	4.75	3.13	3.07	11.4 ± 3
	2.221	2.234	2.289	2.285	2.491	2.495	2.289	2.297	
L^π	$N=1$	$N=9$	$N=1$	$N=9$	$N=1$	$N=9$	$N=1$	$N=9$	
0_1^+	20.82	18.97	21.04	19.54	18.47	17.59	21.12	20.22	20.2
	2.690	2.880	2.773	2.942	2.878	3.010	2.742	2.848	
2_1^+	22.83	20.82	23.01	21.35	20.05	19.12	22.42	21.44	22.2
	2.695	2.883	2.779	2.946	2.890	2.996	2.757	2.827	
4_1^+	27.56	25.09	27.66	25.54	23.82	22.64	25.39	24.19	25.4
	2.705	2.890	2.792	2.955	2.918	2.962	2.682	2.772	
	$K_{\min}+2$ approximation (basis $B_{\max}$)								
L^π	$N=0$	$N=9$	$N=0$	$N=9$	$N=0$	$N=9$	$N=0$	$N=9$	
0^+	0(−46.16)	0(−46.75)	0(−46.42)	0(−46.80)	0(−64.71)	0(−65.01)	0(−66.15)	0(−66.47)	−56.6
	2.432	2.418	2.433	2.490	2.722	2.732	2.571	2.616	
2^+	3.97	3.90	4.16	4.09	3.27	3.24	2.38	2.33	3.04
	2.286	2.419	2.430	2.479	2.720	2.713	2.569	2.581	
4^+	10.54	10.34	10.50	10.30	8.69	8.58	6.38	6.22	11.4 ± 3
	2.287	2.405	2.433	2.459	2.577	2.682	2.422	2.516	
L^π	$N=1$	$N=9$	$N=1$	$N=9$	$N=1$	$N=9$	$N=1$	$N=9$	
0_1^+	29.70	20.45	30.31	21.30	27.32	18.28	25.93	19.76	20.2
	2.999	2.924	3.149	3.007	3.298	3.143	2.999	3.004	
2_1^+	31.69	23.60	32.28	24.47	28.93	21.22	27.13	21.89	22.2
	2.847	2.945	2.999	2.993	2.998	3.131	2.847	2.985	
4_1^+	34.98	28.77	35.20	29.37	30.79	25.59	28.52	24.89	25.4
	2.862	2.960	2.829	3.000	2.979	3.096	2.688	2.905	

Table 3. Structure of the wave functions $\Psi(L)$ in the $B_{\max}$ ($N \leq 9$) basis: coefficients $b(EK\beta\omega_{123}\alpha) \times 10^2$ in expansions in terms of $E = K + 2N$ ($N = 0, 1, \ldots, 4$) basis states (for $N > 4$ basis states, the expansion coefficients are $b(EK\beta\omega_{123}\alpha) \times 10^2 \approx 0$)

				V_4						V_7					
E	K	β	$\omega_{123}\alpha$	$L^\pi = 0^+$	2^+	4^+	0_1^+	2_1^+	4_1^+	0^+	2^+	4^+	0_1^+	2_1^+	4_1^+
4	4		(400)	89	90	90	17	−2	8	89	90	88	4	2	5
6				−8	11	7	75	83	77	3	6	12	85	85	79
8				11	13	14	−30	−13	−16	4	5	8	−15	−12	−4
10				−3	1	1	27	24	26	−2	−1	0	12	13	13
12				1	2	2	−15	−8	−9	0	0	0	−7	−6	−4
14				0	0	0	8	6	8	−1	−1	−1	1	1	1
6	6	1	(400)	37	0	23	−10	0	−25	39	0	24	−19	−1	−35
8				0	0	1	36	0	24	5	0	3	38	0	23
10				5	0	3	−13	0	−11	3	0	2	−3	0	−6
12				−1	0	0	11	0	8	0	0	0	6	0	4
14				0	0	0	−6	0	−5	0	0	0	−2	0	2
6	6	2	(400)	–	30	30	–	−15	−17	–	31	29	–	−15	−23
8				–	6	3	–	30	28	–	6	5	–	32	28
10				–	5	5	–	−4	−9	–	3	3	–	−2	−3
12				–	1	0	–	9	9	–	0	0	–	5	5
14				–	1	1	–	−2	−4	–	0	0	–	−2	−2
6	6	3	(400)	–	19	–	–	−16	–	–	18	–	–	−17	–
8				–	2	–	–	19	–	–	1	–	–	19	–
10				–	3	–	–	−5	–	–	9	–	–	−4	–
12				–	0	–	–	6	–	–	0	–	–	3	–
14				–	0	–	–	−2	–	–	0	–	–	−2	–
6	6		(600)	−16	−15	−13	3	6	3	−20	−20	−18	5	−20	4
8				−1	−4	−3	−16	−14	−11	−5	−5	−6	−20	−5	−16
10				−3	−3	−3	5	1	0	−3	−3	−4	−1	−3	−4
12				0	−1	−1	−6	−5	−4	−1	−1	−1	−4	−1	−4
14				−1	−1	−1	2	0	0	0	0	−1	0	0	−1
6	6		(420)1	−3	−2	−3	1	0	−1	−3	3	−4	−1	2	1
8				0	0	1	−3	0	0	0	−1	−1	−3	0	−3
10				0	−1	1	2	0	0	0	0	−1	0	1	0
12				0	0	0	−1	0	0	0	0	0	0	0	−1
14				0	0	0	1	0	0	0	0	0	0	0	0
6	6		(420)2	7	−6	−8	10	−4	−5	7	−6	−8	0	−5	−5
8				1	−1	−4	6	−2	−1	2	1	2	7	−1	−1
10				1	−2	−1	1	0	−2	1	−3	2	1	−1	1
12				0	0	1	2	−1	0	0	0	1	1	−1	0
14				0	0	0	0	0	0	0	0	0	0	0	0
6	6		(510)	–	0	0	–	−1	1	–	0	1	–	−1	3
8				–	0	0	–	0	0	–	0	0	–	0	0
10				–	0	0	–	0	0	–	0	0	–	0	1

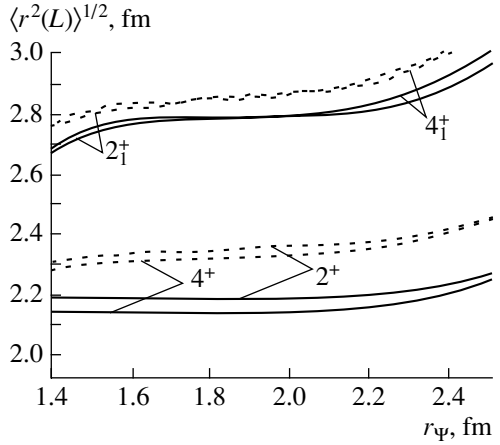

Fig. 4. Dependence $\langle r^2(L)\rangle^{1/2} = f(r_\Psi)$ for the potential V_4 according to the calculation that employs (dashed curves) the $B_{\max}$, $N = 9$ basis or (solid curves) the B_0, $N = 9$ basis.

This table presents typical results for the potentials V_4 and V_7. Comparing the values in the B_0, B_1, B_2, and B_{max} columns, we conclude that, in the extension of the basis, only the functions corresponding to $K_{min} + 2$ and minimal $\omega_{123} = (K_{min}00) \equiv (400)$ play a significant role, these functions ensuring an increase of 8 to 9 MeV in the binding energy. Of the functions characterized by the representation ω_{123} for $\omega_1 + \omega_2 + \omega_3 = K_{min} + 2$, only those that correspond to the most symmetric representation ω_{123}, $\omega_{123} = (K_{min} + 200) \equiv (600)$, deserve particular attention. The role of the functions corresponding to ω_{123} of lower symmetry is insignificant. A similar situation was also observed for the analogous $E_{min} + 2$ approximation within the unitary scheme [3]. Thus, we see that, in the $K_{min} + 2$ approximation, we can restrict ourselves to the B_2 or even the B_1 basis in practical calculations.

(ii) The inclusion of ρ excitations—that is, of $E > K$ states—leads to a modest increase (of less than 0.8 MeV for all potentials) in the binding energy and has virtually no effect on the relative spacing between the levels of the first band, either in the K_{min} or in the $K_{min} + 2$ approximation.

(iii) At the same time, ρ excitations play a leading role in the formation of the second-band levels. The inclusion of ρ excitations shifts the second-band levels by 1.0 to 1.5 MeV in the K_{min} approximation and by 6.0 to 9.0 MeV in the $K_{min} + 2$ approximation. Concurrently, the band becomes narrower by 0.3 to 0.5 MeV in the K_{min} approximation and wider by 2.5 to 3.5 MeV in the $K_{min} + 2$ approximation. The results of the calculations confirm (see also the structure of the wave functions in Table 3) that, within the orthogonal scheme, the levels of the second band can be interpreted as ρ excitations of the first band.

(iv) For the energies of the levels, the results begin to converge—that is, they become independent of N—from $N = 2$ or 3 for the levels of the first band and from $N = 3$ or 4 for the levels of the second band (see Fig. 1). A further extension of the basis via the inclusion of the functions associated with ρ excitations leads to the formation of a horizontal segment in the dependence $\varepsilon(L) = f(r_\Psi)$ (plateau in Figs. 1 and 3). This circumstance makes it possible to change the root-mean-square radius by varying the quantity r_Ψ within the plateau. By way of example, we indicate that, if r_Ψ is taken at the endpoints of the plateau, the root-mean-square radius can change by 0.1 to 0.2 fm (see Fig. 4), depending on the choice of potential. Thus, we see that, in the multiquantum approximation, there arises an additional possibility for fitting theoretical results to experimental data.

(v) It is of interest to compare the structure of the wave functions in the present study (see Table 3) with that in the multiquantum approximation of the unitary scheme (see Table 7 in [3]). Within the orthogonal scheme, the weights of the first ρ excitations ($N \leq 2$) stand out distinctly. For the functions in the multiquantum approximation of the unitary scheme [3], the distribution of weights over excited basis states is smoother, which can be explained by an implicit dependence of the weight coefficients in the unitary-scheme functions on the quantum number K. A multiquantum excitation of the unitary scheme [3] is a superposition of states featuring different $K \geq K_{min}$, this being precisely the circumstance that leads to the aforementioned smoother distribution of weights. The same factor—that is, an implicit inclusion of $K \geq K_{min}$ states—may be responsible for a greater increase in the binding energy within the multiquantum approximation of the unitary scheme [3].

(vi) A comparison of the results of the present study with those reported in [3] suggests that, in describing low-lying levels, at least of the rotational type, the quantum number K of the $O(3(A-1))$ group plays a more important role than the numbers E_{123} of the $U(A-1)$ group in the unitary scheme.

As to the potential of the orthogonal-scheme basis, it can be seen that the $K_{min} + 2$ approximation is virtually equivalent to the $E_{min} + 2$ approximation of the unitary scheme and that the $K_{min} + 2$ multiquantum approximation (that is, that which corresponds to $N \leq 9$) yields results close to those in the multiquantum approximation of the unitary scheme [3], this being so for all quantities, with the exception of the binding energy, which, for the reasons indicated above, is 3 to 5 MeV higher in [3]. It addition, it should be noted that the algorithm for taking into account $U(3(A-1))$ states involving multiquantum excitations is much simpler in the orthogonal than in the unitary scheme.

REFERENCES

1. V. V. Vanagas, *Algebraic Methods in the Theory of the Nucleus* (Mintis, Vilnyus, 1971) [in Russian].
2. K. I. Yankauskas and A. K. Petrauskas, *Density Matrix of Excited $U(3(n-1))$ States of Nuclei and Its Application* (Klaipeda Univ., Klaipeda, 1997) [in Russian].
3. K. Yankauskas, Yad. Fiz. **64**, 238 (2001) [Phys. At. Nucl. **64**, 194 (2001)].
4. P. Navratil and B. R. Barret, Phys. Rev. C **57**, 3119 (1998).
5. P. Navratil and B. R. Barret, Phys. Rev. C **57**, 562 (1998).
6. V. V. Vanagas, *Methods of Group Theory Representations and of Isolation of Collective Degrees of Freedom of a Nucleus* (MIFI, Moscow, 1974).
7. P. Navratil, G. P. Kamuntavicius, and B. R. Barret, Phys. Rev. C **61**, 044001 (2000).
8. K. I. Yankauskas, Yad. Fiz. **65**, 984 (2002) [Phys. At. Nucl. **65**, 953 (2002)].
9. A. K. Petrauskas, K. I. Yankauskas, and V. M. Bondarenko, Available from LII, No. 2540 (Vilnus, 1990).
10. K. I. Yankauskas, Litov. Fiz. Sb. **41**, 23 (2001).
11. A. V. Volkov, Nucl. Phys. **74**, 33 (1965).
12. A. I. Baz', Yu. T. Grin', V. F. Demin, and M. V. Zhukov, Fiz. Élem. Chastits At. Yadra **3**, 275 (1972) [Sov. J. Part. Nucl. **3**, 275 (1972)].
13. D. Gogny, P. Pires, and R. Tourreil, Phys. Lett. A **32A**, 591 (1970).
14. K. I. Yankauskas and A. K. Petrauskas, Litov. Fiz. Sb. **37**, 102 (1997).
15. F. Ajzenberg-Selove, Nucl. Phys. A **227**, 1 (1974).

Translated by A. Isaakyan

Physics of Atomic Nuclei, Vol. 67, No. 12, 2004, pp. 2148–2153. Translated from Yadernaya Fizika, Vol. 67, No. 12, 2004, pp. 2171–2177.
Original Russian Text Copyright © 2004 by Mirabutalybov.

NUCLEI
Theory

Nonrelativistic Description of Nucleon–Nucleus Scattering

M. M. Mirabutalybov

Azerbaijan State Petroleum Academy, pr. Azadlyg 20, Baku, 370010 Azerbaijan

Received December 24, 2003

Abstract—Within the three-dimensional semiclassical approximation, an analytic expression is obtained for the amplitude of proton–nucleus scattering at intermediate energies of incident protons. The method for deriving this amplitude is based on the use of the high-energy approximation with distorted waves. In view of the short-range character of proton–nucleon interaction, the process of proton–nucleus scattering is represented as a series of single scattering events occurring on each individual nucleon. With the aid of the proposed mathematical formalism, a recursion relation is derived that makes it possible to express the nuclear form factor obtained within the distorted-wave method in terms of the sum of an infinite Born series. Parameters that characterize the distributions of protons and neutrons in the spherical nuclei ^{40}Ca, ^{48}Ca, ^{90}Zr, and ^{208}Pb and which include the width of the surface layer of nucleons and the root-mean-square radii of the proton-, neutron-, and nucleon-density distributions are determined from an analysis of the measured cross sections for the elastic scattering of 1-GeV protons, a modified Fermi function being employed for the nucleon-density distribution. © *2004 MAIK "Nauka/Interperiodica"*.

Rapid advances in experimental techniques over the past decade have made it possible to perform numerous experiments devoted to studying proton–nucleus scattering at intermediate projectile energies. It turned out that, if intermediate-energy protons are employed as probing particles, difficulties in interpreting experimental data are much less pronounced than in the case where use is made of particles having lower energies. Some effects that play a significant role in the scattering of low-energy particles and which usually defy all attempts at precisely taking them into account die out at intermediate energies almost completely. As a result, the reaction mechanism becomes quite simple. In the interaction of intermediate-energy nucleons with nuclei, where the projectile-nucleon energy exceeds the Fermi energy and where the energy and momentum transfers are much less than the projectile energy and momentum, the scattering of an intermediate-energy proton on a target nucleus can be considered as a sequence of single collisions with each individual nucleon that the projectile proton encounters on its path. This approach made it possible to develop the theory of multiple nucleon scattering on nuclei [1, 2]. The scattering amplitude obtained in [1, 2] on the basis of the high-energy approximation ($V/E \ll 1$ and $kR \gg 1$, where E is the projectile-nucleon energy, V is the nuclear potential, and R is the region where the potential is operative) within the eikonal approach is valid only at small scattering angles, $\theta \ll (kR)^{-1}$. Calculations performed on the basis of this theory in order to determine the cross sections for proton–nucleus scattering revealed that it is necessary to determine the phase function in the scattered-proton wave functions more precisely.

Schiff [3] proposed an alternative approach where an approximate method for summing an infinite Born series was used to obtain the reaction amplitude that is valid at large scattering angles, $\theta > (kR)^{-1/2}$. However, problems in calculating a large number of phase shifts arise in that case as well.

On the basis of the three-dimensional semiclassical approximation, the scattering amplitudes for dynamical small and large scattering angles were derived in [4] within a unified framework relying on the high-energy approximation. Numerous calculations and a comparison of charge form factors for nuclei [5, 6] showed that the expressions obtained for the scattering amplitudes on the basis of the semiclassical approximation within this framework are always highly accurate.

The objective of the present study is to derive an explicit expression for the scattering amplitude on the basis of the semiclassical approximation and to relate this expression to multiple-scattering theory. Also, we aim here at developing a method for calculating scattering amplitudes.

We begin by writing the differential cross section for the process in question in the general form

$$\frac{d\sigma}{d\Omega} = \frac{1}{2}\left(\frac{k}{E}\right)^2 \frac{2J_f+1}{2J_i+1} \sum_{\sigma_i\sigma_f} \sum_{M_iM_f} |f_{if}(\mathbf{k}_i, \mathbf{k}_f)|^2, \quad (1)$$

1063-7788/04/6712-2148$26.00 © 2004 MAIK "Nauka/Interperiodica"

where $f_{if}(\mathbf{k}_i, \mathbf{k}_f)$ is the amplitude for the process where a nucleon of momentum $\mathbf{k}_i$ and spin projection σ_i is scattered to the final state of momentum $\mathbf{k}_f$ and spin projection σ_f; M_i is the projection of the target-nucleus spin; and M_f is the recoil-nucleus-spin projection, which does not vanish in the case of inelastic scattering. We have

$$f_{if}(\mathbf{k}_i, \mathbf{k}_f) \tag{2}$$
$$= -\frac{m}{2\pi\hbar^2}\left\langle J_f M_f \left| \int d\mathbf{r}\psi_f^{*(-)}(\mathbf{r})V(\mathbf{r}\xi)\psi_i^{(+)}(\mathbf{r}) \right| J_i M_i \right\rangle,$$

where the wave function for the nuclear state $|JM\rangle$ depends on the corresponding coordinates ξ of the internal motion of intranuclear nucleons.

The wave functions describing the relative motion of incident and scattered nucleons can be obtained by solving the Schrödinger equation and are given by

$$\psi^{(\pm)}(\mathbf{k}, \mathbf{r}) = \exp\left\{i[\mathbf{k}\cdot\mathbf{r} \mp \Phi^{(\pm)}(\mathbf{k}, \mathbf{r})]\right\}, \tag{3}$$

where the distorting term in the phase is

$$\Phi^{(\pm)}(\mathbf{k}, \mathbf{r}) = \frac{m}{\hbar^2 k}\int\limits_0^\infty V(\mathbf{r} \mp \hat{k}s)ds. \tag{4}$$

In evaluating expression (4), it is assumed that the trajectories of scattered particles are straight lines. Taking the z axis to be aligned with $\mathbf{k}$ and setting $\mathbf{r} = \boldsymbol{\rho} + \hat{k}z$, where ρ is the impact parameter, we represent the distorting term in the form [7]

$$\Phi^{(\pm)}(\mathbf{k}, \mathbf{r}) = -\frac{m}{\hbar^2 k}\int\limits_0^z V\left(\sqrt{\rho^2 + t^2}\right)dt \tag{5}$$
$$\pm \frac{m}{\hbar^2 k}\int\limits_0^\infty \left[V(t) - V\left(\sqrt{\rho^2 + t^2}\right)\right]dt,$$

which involves two integral terms. In order to calculate the first integral, we expand the nuclear potential V in a Taylor series as

$$V(r) \approx V(0) + ak^3r^2/2, \tag{6}$$

where

$$a = \frac{1}{k^3}\left.\frac{\partial^2 V(r)}{\partial r^2}\right|_{r=0}. \tag{7}$$

The second integral is evaluated by expanding the corresponding integrand in powers of the impact parameter squared (ρ^2). Retaining the terms to the second order inclusive, we obtain

$$\frac{m}{\hbar^2 k}\int\limits_0^\infty \left[V(t) - V\left(\sqrt{\rho^2 + t^2}\right)\right]dt \tag{8}$$
$$= -\frac{m\rho^2}{2\hbar^2 k}\int\limits_0^\infty \frac{1}{t}\frac{\partial V}{\partial t}dt - \frac{m\rho^4}{8\hbar^2 k}$$
$$\times \int\limits_0^\infty \left(\frac{1}{t^2}\frac{\partial^2 V}{\partial t^2} - \frac{1}{t^3}\frac{\partial V}{\partial t}\right)dt \equiv -b(\rho k)^2 + c(\rho k)^4,$$

where

$$b = \frac{m}{2\hbar^2 k^3}\int\limits_0^\infty \frac{1}{t}\frac{\partial V}{\partial t}dt, \tag{9}$$

$$c = -\frac{m}{8\hbar^2 k^5}\int\limits_0^\infty \left(\frac{1}{t^2}\frac{\partial^2 V}{\partial t^2} - \frac{1}{t^3}\frac{\partial V}{\partial t}\right)dt. \tag{10}$$

Thus, the distorting term assumes the form

$$\Phi^{(\pm)}(k, z) = -\frac{m}{\hbar^2 k}V(0)z \tag{11}$$
$$-\frac{ma}{2\hbar^2 k}(k^3\rho^2 z + k^3 z^3/3) \mp b(\rho k)^2 + c(\rho k)^4.$$

Considering that $\mathbf{r} = \boldsymbol{\rho} + \hat{k}z$ and $\boldsymbol{\rho} \perp \mathbf{k}$, we represent expression (11) in a vector form; that is,

$$\Phi^{(\pm)}(\mathbf{k}, \mathbf{r}) = -\frac{m}{\hbar^2 k^2}V(0)(\mathbf{k}\cdot\mathbf{r}) \tag{12}$$
$$-\frac{ma}{2\hbar^2 k}(\mathbf{k}\cdot\mathbf{r})(3k^2r^2 + (\mathbf{k}\cdot\mathbf{r})^2)$$
$$\mp b[\mathbf{r}\times\mathbf{k}]^2 \pm c[\mathbf{r}\times\mathbf{k}]^4.$$

Taking into account the spherical symmetry of the nuclear potential and using the static equation

$$\nabla^2 V(r) - k_0^2 V(r) = 4\pi\gamma\rho(r), \tag{13}$$

we can find the coefficient in the expansion of the potential. The result is

$$a = \left(\frac{4\pi}{3k^3}\right)\gamma\rho(0) + \frac{k_0^2 V(0)}{3k^3}, \tag{14}$$

where $\gamma = f_\pi^2 = 0.08$ is the coupling constant, whose value is determined from experimental data on nucleon–nucleon scattering [8]; $\rho(r)$ is the nucleon-density distribution in the nucleus being considered; and $k_0 = m_\pi c/\hbar$, the inverse of this quantity corresponding to the range of nuclear forces.

In calculating the coefficients $V(0)$, b, and c appearing in the distorting term (12), it is assumed that the distortion occurs in the meson field of a pointlike source (nucleon) in a nucleus—that is, in an attractive potential of the Yukawa type. The nuclear potential then assumes the form

$$V(r\xi) = 4\pi\gamma\left(\frac{1}{r}\int\limits_0^r \rho(x\xi)x^2 e^{-k_0 x}dx\right. \tag{15}$$

$$+\int_r^\infty \rho(x\xi)xe^{-k_0x}dx\Bigg).$$

Disregarding, within the high-energy approximation, the energy loss of the incident nucleon [$\Delta E \ll E$, where $E=\hbar^2k^2/(2m)$] and setting $|\mathbf{k}_i|=|\mathbf{k}_f|=k$, we now have

$$\psi_f^{*(-)}\psi_i^{(+)} = \exp\left[i\mathbf{q}\cdot\mathbf{r}+i\Phi(\mathbf{r})\right], \qquad (16)$$

where $\mathbf{q}=\mathbf{k}_i-\mathbf{k}_f$ is the momentum transfer to the target nucleus and

$$\Phi(\mathbf{r}) = \frac{V(0)}{2E}(\mathbf{k}_f\cdot\mathbf{r}-\mathbf{k}_i\cdot\mathbf{r}) - \frac{ka}{12E} \qquad (17)$$
$$\times\left(3k^2r^2(\mathbf{k}_i\cdot\mathbf{r}-\mathbf{k}_f\cdot\mathbf{r})+2(\mathbf{k}_i\cdot\mathbf{r})^3-2(\mathbf{k}_f\cdot\mathbf{r})^3\right)$$
$$-b\left([\mathbf{r}\times\mathbf{k}_i]^2+[\mathbf{r}\times\mathbf{k}_f]^2\right)+c\left([\mathbf{r}\times\mathbf{k}_i]^4+[\mathbf{r}\times\mathbf{k}_f]^4\right).$$

Further, we can neglect the change in the position of intranuclear nucleons within the time it takes for a fast proton to traverse the nucleus. The scattering in question occurs predominantly at small angles around the forward direction. The scattered nucleon consecutively interacts with a few intranuclear nucleons that it encounters on its path. In view of the short-range character of nucleon–nucleon interaction, the scattering of a nucleon on a nucleus can therefore be represented as a sequence of single scattering events. Taking this into account, we express the nuclear potential in terms of an integral of the components $v(|\mathbf{r}-\mathbf{x}|)$ describing the interaction of the incident particle with individual nucleons of the target nucleus; that is,

$$V(\mathbf{r}\xi) = \int v(|\mathbf{r}-\mathbf{x}|)\rho(\mathbf{x}\xi)d\mathbf{x}. \qquad (18)$$

Since the binding energy of intranuclear nucleons is much less than the incident-proton energy, we can disregard nucleon-binding effects. Therefore, the potential of nucleon–nucleon interaction can be expressed in terms of the amplitudes for scattering on free nucleons. These amplitudes are determined by solving the Schrödinger equation and are given by [1]

$$f_{NN}(\mathbf{k}',\mathbf{k}) = -\frac{\mu_0}{2\pi\hbar^2}\int e^{-i\mathbf{k}'\cdot\mathbf{r}'}v(|\mathbf{r}'|)\psi_k(\mathbf{r}')d\mathbf{r}', \qquad (19)$$

where $\mu_0=m_pm_N/(m_p+m_N)$ is the reduced mass, m_p is the incident-proton mass, and m_N is the nucleon mass in the target nucleus.

The incident-nucleon wave function then has the form

$$\psi_k(\mathbf{r}) = \exp\left[i\mathbf{k}\cdot\mathbf{r}-\frac{im}{\hbar^2k}\int_{-\infty}^{z} v(\boldsymbol{\rho}+\hat{k}z')dz'\right]. \qquad (20)$$

Substituting (20) into (19), we obtain the scattering amplitude in the form

$$f_{NN}(\mathbf{q}') = -\frac{\mu_0}{2\pi\hbar^2}\int e^{i\mathbf{q}'\cdot\mathbf{r}'}v^{\mathrm{dist}}\left(|\mathbf{r}'|\right)d\mathbf{r}', \qquad (21)$$

where $\mathbf{q}'=\mathbf{k}-\mathbf{k}'$ is the momentum transfer from the incident particle to a target nucleon. The distorted nucleon–nucleon potential is then given by

$$v^{\mathrm{dist}}(r) = v(r)\exp\left(-\frac{im}{\hbar^2k}\int_{-\infty}^{z} vdz'\right). \qquad (22)$$

In (18), we further take into account the Fourier transformation of $v(|\mathbf{r}|)$ in (21); for the nuclear potential, we then obtain

$$V(\mathbf{r}\xi) = -\frac{\hbar^2}{(2\pi)^2\mu_0}\int e^{i\mathbf{q}'\cdot(\mathbf{r}-\mathbf{x})}f_{NN}(\mathbf{q}')\rho(\mathbf{x}\xi)d\mathbf{q}'d\mathbf{x}. \qquad (23)$$

For the nucleon–nucleon amplitude, we choose here the parametrization [9, 10]

$$f_{NN}(q') = \frac{ik\sigma}{4\pi}(1-i\varepsilon_0)e^{-\beta^2q'^2}. \qquad (24)$$

Substituting (16) and (23) into (2), making the change of variables $\mathbf{u}=\mathbf{r}-\mathbf{x}$, and expanding the phase function as

$$\Phi(\mathbf{u}+\mathbf{x}) = \Phi(\mathbf{x})+\nabla\Phi(\mathbf{u}+\mathbf{x})_{u=0}\mathbf{u}+\ldots, \qquad (25)$$

we obtain the scattering amplitude in the form

$$f_{if}(\mathbf{q}) = -\frac{\hbar^2}{(2\pi)^2\mu_0}\int e^{i(\mathbf{q}_{\mathrm{eff}}-\mathbf{q}')\cdot\mathbf{u}}f_{NN}(\mathbf{q}') \qquad (26)$$
$$\times e^{i[\mathbf{q}\cdot\mathbf{x}+\Phi(\mathbf{x})]}\langle J_fM_f|\rho(\mathbf{x}\xi)|J_iM_i\rangle d\mathbf{u}d\mathbf{q}'d\mathbf{x},$$

where

$$\mathbf{q}_{\mathrm{eff}} = \mathbf{q}+\nabla\Phi(\mathbf{u}+\mathbf{x})_{u=0}. \qquad (27)$$

Expressing $\rho(\mathbf{x}\xi)$ in terms of the radial transition nuclear density $\rho_L(x)$ as

$$\langle J_fM_f|\rho(\mathbf{x}\xi)|J_iM_i\rangle \qquad (28)$$
$$=\sum_{LM}\rho_L(\mathrm{x})Y^*_{LM}(J_iLM_iM|J_fM_f)$$

and performing relevant integration, we now obtain the differential cross section in the form

$$\frac{d\sigma}{d\Omega} = \left(\frac{k^2}{4\pi E}\right)^2\frac{1}{2}\frac{2J_f+1}{2J_i+1}\sum_{LM}\frac{1}{2L+1}|F_{LM}(\mathbf{q})|^2, \qquad (29)$$

where, for the form factor, we have the expression

$$F_{LM}(\mathbf{q}) = \int e^{i[\mathbf{q}\cdot\mathbf{x}+\Phi(x)]}f_{NN}(\mathbf{q}_{\mathrm{eff}})\rho_L(x)Y^*_{LM}(\hat{x})d\mathbf{x}. \qquad (30)$$

Thus, the problem of determining the cross section reduces to calculating the form factor given by (30).

In the phase shift, we further single out the small parameter γ in the distorting term and rewrite the form factor as

$$F_{LM}(\mathbf{q}) = \frac{ik\sigma(1-i\varepsilon_0)}{4\pi}\int J(\mathbf{q},\mathbf{x})\rho_L(x)Y^*_{LM}(\hat{x})d\mathbf{x}, \tag{31}$$

where

$$J(\mathbf{q},\mathbf{x}) = \exp[i\mathbf{q}\cdot\mathbf{x} - \beta^2\mathbf{q}^2 + i\gamma\chi_1(\mathbf{x}) + \gamma^2\chi_2(\mathbf{x})], \tag{32}$$

$$\chi_1(\mathbf{x}) = (\Phi(\mathbf{x}) + 2i\mathbf{q}\beta^2\nabla\Phi(\mathbf{u}+\mathbf{x})|_{u=0})/\gamma,$$
$$\chi_2(\mathbf{x}) = -\beta^2(\nabla\Phi(\mathbf{u}+\mathbf{x})|_{u=0})^2/\gamma^2.$$

Further, we expand $J(\mathbf{q},\mathbf{x})$ in a power series in $\gamma \ll 1$ as

$$J(\mathbf{q},\mathbf{x}) = \sum_{n=0}^{\infty}\gamma^n J_n(\mathbf{x}). \tag{33}$$

We represent the derivative of expression (32) with respect to γ in the form

$$\frac{\partial J(\mathbf{q},\mathbf{x})}{\partial\gamma} = [i\chi_1(\mathbf{x}) + 2\gamma\chi_2(\mathbf{x})]J(\mathbf{q},\mathbf{x}). \tag{34}$$

At the same time, we expand expression (34) in a power series in γ and compare the result with the derivative of (33) with respect to γ. This yields the recursion relation

$$(n+1)J_{n+1}(\mathbf{x}) = i\chi_1(\mathbf{x})J_n(\mathbf{x}) + 2\chi_2(\mathbf{x})J_{n-1}(\mathbf{x}), \quad n = 1,2,3,\ldots, \tag{35}$$

where

$$J_1(\mathbf{x}) = i\chi_1(\mathbf{x})J_0(\mathbf{x}), \tag{36}$$

with $J_0(\mathbf{x})$ being

$$J_0(\mathbf{x}) = e^{i\mathbf{q}\cdot\mathbf{x}}. \tag{37}$$

This recursion relation makes it possible to express all of the quantities that appear in (33) in terms of the simpler expression for $J_0(\mathbf{x})$.

As a result, the form factor (30) assumes the form

$$F_{LM}(\mathbf{q}) = \frac{ik\sigma(1-i\varepsilon_0)}{4\pi}\int e^{i\mathbf{q}\cdot\mathbf{x}-\beta^2\mathbf{q}^2}\Re(\mathbf{x})\rho_L(x)Y^*_{LM}(\hat{x})d\mathbf{x}, \tag{38}$$

where

$$\Re(\mathbf{x}) = 1 + i\Phi(\mathbf{x}) - 2\beta^2\mathbf{q}\nabla\Phi(\mathbf{u}+\mathbf{x})|_{u=0} - \Phi^2(\mathbf{x})/2 - 2i\beta^2\mathbf{q}\Phi(\mathbf{x})\nabla\Phi(\mathbf{u}+\mathbf{x})|_{u=0} + (2\beta^4\mathbf{q}^2 - \beta^2)(\nabla\Phi(\mathbf{u}+\mathbf{x})|_{u=0})^2.$$

In order to evaluate expression (38), it is necessary to go over from the respective three-dimensional integral to a one-dimensional integral. For this purpose, we choose the coordinate system where the z axis is parallel to $\mathbf{q}$ with $q = |\mathbf{q}| = |\mathbf{k}_i - \mathbf{k}_f| = 2k\alpha$ and $\alpha = \sin(\theta/2)$ and where the x axis is orthogonal to $\mathbf{q}$, in which case $\cos(\mathbf{q}\cdot\mathbf{x}) = \mu$, $\mathbf{x} = \{x\mu\varphi\}$, $d\mathbf{x} = -x^2dxd\mu d\varphi$, $\cos(xk_i) = \mu\alpha + \sqrt{1-\mu^2}\sqrt{1-\alpha^2}\times\cos\varphi$, and $\cos(xk_f) = -\mu\alpha + \sqrt{1-\mu^2}\sqrt{1-\alpha^2}\times\cos\varphi$. Upon integration with respect to the azimuthal angle φ, the integrand $\Re(x\mu\varphi)$ assumes a simpler form, with the result that, for $F_{LM}(q)$, we obtain

$$F_{LM}(q) = -\frac{i}{2}k\sigma(1-i\varepsilon_0)\int_0^{\infty}\int_{-1}^{1}\exp(iqx\mu - q^2\beta^2\mu^2)\Re(x\mu)\rho_L(x)Y^*_{LM}(\hat{x})x^2dxd\mu. \tag{39}$$

Upon integration by parts with respect to μ, we arrive at

$$F_{L0}(q) = -\frac{k\sigma}{2}(1-i\varepsilon_0)e^{-q^2\beta^2} \times \sum_{\varepsilon=\pm1}\varepsilon\int_0^{\infty}\frac{\Re(x\varepsilon)e^{iqx\varepsilon}}{qx + 2iq^2\beta^2\varepsilon}\rho_L(x)Y^*_{L0}(\varepsilon)x^2dx + \ldots. \tag{40}$$

We disregard the second term in the integral because it is much smaller than the first term. Moreover, we can retain, in the calculations for $L \neq 0$, only the $M = 0$ term, since it is precisely this term that makes a dominant contribution to the modulating amplitude.

Thus, the ensuing problem of determining the form factor reduces to calculating one-dimensional integrals of the form in (40). For this purpose, we consider elastic proton scattering on spherical nuclei.

An analysis of respective cross sections in terms of the theory of multiple proton scattering at intermediate energies makes it possible to deduce quite precise information about nucleon distributions in nuclei. It is well known that fast protons show approximately identical sensitivity to intranuclear protons and neutrons. It follows that, from data on proton–nucleus scattering, one can extract information about the isoscalar density—that is, about the sum of the neutron- and proton-density distributions,

$$\rho(r) = \rho_p(r) + \rho_n(r). \tag{41}$$

The proton- and neutron-density distributions are taken in the form of the Fermi functions,

$$\rho_i(r) = \rho_{0i}(1 + e^{(r-c)/b_i})^{-1} = \rho_{0i}\tilde{\rho}(r|b_i), \quad i = \mathrm{p}, n. \tag{42}$$

The form factor in (40) for elastic proton scattering in the case of the Fermi density (42) was calculated on the basis of the pole method developed in [5].

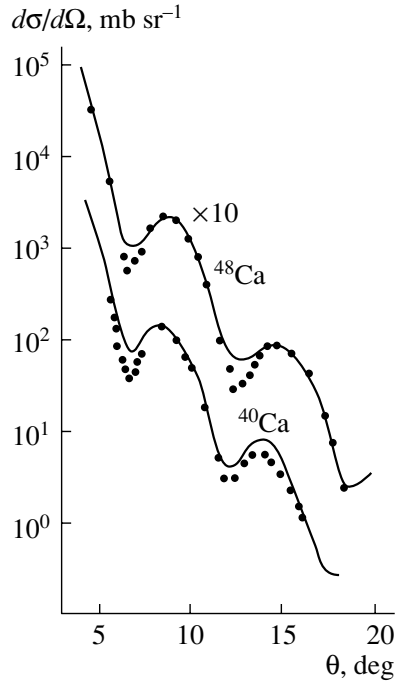

Fig. 1. Differential cross sections for the elastic scattering of 1-GeV protons on ^{40}Ca and ^{48}Ca nuclei: (points) experimental data and (solid curves) cross sections calculated by the distorted-wave method.

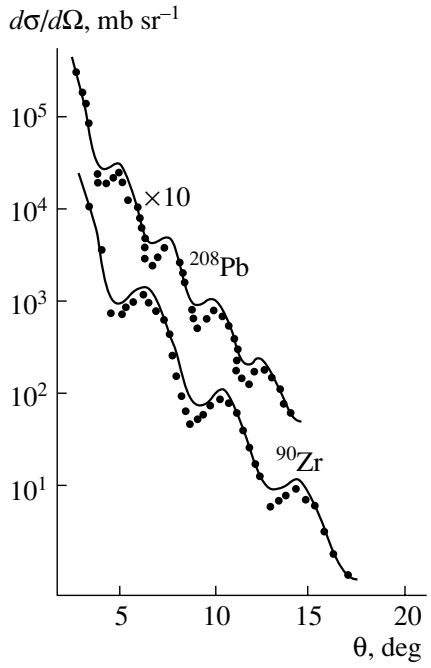

Fig. 2. Differential cross sections for the elastic scattering of 1-GeV protons on ^{90}Zr and ^{208}Pb nuclei. The notation is identical to that in Fig. 1.

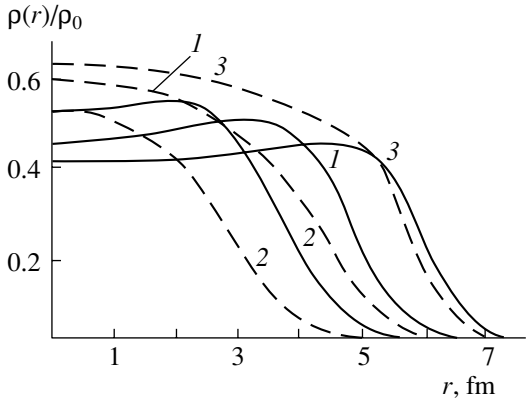

Fig. 3. Distributions of the (solid curves) proton and (dashed curves) neutron densities in nuclei for (*1*) ^{90}Zr, (*2*) ^{40}Ca, and (*3*) ^{208}Pb.

Experimental data on elastic proton scattering by ^{40}Ca, ^{48}Ca, ^{90}Zr, and ^{208}Pb nuclei at an energy of about 1 GeV [11, 12] were analyzed on the basis of multiple-scattering theory within the high-energy approximation by using the distorted-wave method. Figures 1 and 2 illustrate versions where the best agreement between the theoretical cross sections and their experimental counterparts was attained at specific sets of values for parameters that characterize the proton- and neutron-density distributions. The results obtained with these values for the root-mean-square radii of the proton, neutron, and nucleon distributions ($\langle r_p^2\rangle^{1/2}$, $\langle r_n^2\rangle^{1/2}$, and $\langle r_N^2\rangle^{1/2}$, respectively) and for the nuclear-surface-layer thickness $t = b$ are given in the table.

Good agreement for the cross sections was obtained at $b_p = b_n = b$, this implying that, in spherical nuclei, the proton-surface-layer thickness does not differ from the neutron-surface-layer thickness. This is yet another piece of evidence for the inability of fast protons to "feel" a fine structure at the surfaces in spherical nuclei. As is well known, the fine structure in the proton-density distribution is revealed upon taking into account a three-parameter Fermi function in elastic electron scattering on nuclei [13].

For the equality in (41) to hold, we choose the proton- and neutron-density distributions in the form

$$\rho_{p(n)}(r) = \frac{1}{2}[1 \mp \beta(r)]\tilde{\rho}(r), \quad \beta(r) = \alpha_0 - \alpha_1\frac{r^2}{c^2},$$

where the parameter $\alpha_0 = (N - Z)/(N + Z)$ corresponds to the approximation of proportional densities and $\alpha_1 = (Z/A)W$, with W being a variable parameter that characterizes the fine structure of proton-density distributions (it is extracted from data on elastic electron scattering by nuclei) [13].

Thus, the proton- and neutron-density distribu-

Parameters characterizing the proton-, neutron-, and nucleon-density distributions in nuclei

Nucleus	W_p	W_n	$t = 4.4b$, fm	$\langle r_p^2\rangle^{1/2}$, fm	$\langle r_n^2\rangle^{1/2}$, fm	$\langle r_N^2\rangle^{1/2}$, fm	$cA^{-1/3}$, fm
^{40}Ca	0.60	0.60	2.260	3.920	2.662	3.705	1.020
^{48}Ca	0.64	0.43	2.480	3.590	2.754	3.184	1.023
^{90}Zr	0.40	0.32	2.306	4.308	4.207	4.220	1.040
^{208}Pb	0.60	0.39	1.710	5.482	4.982	5.266	1.048

tions in nuclei assume the form

$$\rho_{p(n)}(r) = \rho^0_{0p(n)}\left(1 \pm W_{p(n)}\frac{r^2}{2c^2}\right)\tilde{\rho}(r), \qquad (43)$$

where $\rho^0_{0p} = (Z/A)\rho_0$ (ρ_0 is determined from the normalization condition for the distribution of the intranuclear-nucleon density), $\rho^0_{0n} = (N/A)\rho_0$, and the parameters characterizing the fine structure in the proton- and neutron-density distributions are related by the equations $W_p \equiv W$ and $W_n \equiv (Z/N)^W_p$.

All of the calculations were performed by employing, for the elementary amplitudes in (24), the parameter values determined from a fit to data on elastic nucleon–nucleon scattering [14]. These are $\sigma = 4.4$ fm^2, $\beta^2 = 0.2$ fm^2, and $\varepsilon_0 = 0.25$.

From a comparison of the calculated cross sections with their measured counterparts, one can see that the agreement is good on the right slopes of diffraction peaks, but that the calculated cross sections are somewhat overestimated in the region of diffraction minima and on the left slopes.

Figure 3 shows the proton- and neutron-density distributions. The parameters of these distributions were obtained from a global analysis of experimental cross sections in the high-energy approximation with the distorted waves of proton and electron scattering on the corresponding nuclei [13]. From this figure, one can see that, in contrast to what we have for the neutron distribution, the density of the proton distribution decreases from the surface of a nucleus toward its interior, but this decrease stops as one approaches the center of the nucleus. This shape of the proton density—it is known as the shape of a wine-bottle bottom—was confirmed in experiments that studied the elastic scattering of polarized protons on nuclei [15].

CONCLUSION

On the basis of multiple-scattering theory, an analytic expression for differential cross sections has been obtained in the high-energy approximation with distorted waves. This expression makes it possible to study the structure of nuclei by means of elastic proton scattering. A mathematical formalism has been proposed for calculating the respective form factor in the distorted-wave approximation. With the aid of this formalism, we have derived a recursion relation that makes it possible to obtain a simpler representation for the form factor. The resulting expressions have been used to analyze elastic proton scattering at an energy of about 1 GeV with the aim of determining parameters that characterize the proton- and neutron-density distributions in the spherical nuclei of ^{40}Ca, ^{48}Ca, ^{90}Zr, and ^{208}Pb. The parameters of such distributions in nuclei have been selected in such a way as to ensure the best fit of theoretical cross sections to their experimental counterparts, all of the remaining parameters used being extracted from experimental data. The parameter W characterizing the fine structure in the proton distribution at the nuclear surface has been deduced from the results obtained for electron scattering on the same nuclei in the distorted-wave approximation.

REFERENCES

1. R. J. Glauber, Lect. Theor. Phys. (N.Y.) **1**, 315 (1959).
2. A. G. Sitenko, Ukr. Fiz. Zh. **4**, 152 (1959).
3. L. I. Schiff, Phys. Rev. **103**, 443 (1956).
4. V. K. Luk'yanov, Izv. Akad. Nauk, Ser. Fiz. **58** (1), 8 (1994).
5. V. K. Lukyanov and Yu. S. Pol, Fiz. Élem. Chastits At. Yadra **5**, 955 (1974).
6. A. V. Dzhavadov and M. M. Mirabutalybov, Izv. Akad. Nauk SSSR, Ser. Fiz. **40**, 2156 (1976).
7. D. R. Jennie, F. L. Boss, Jr., and D. G. Ravenhall, Phys. Rev. **137**, B882 (1965).
8. E. Devlin *et al.*, Phys. Rev. Lett. **4**, 242 (1960).
9. J. P. Auger, A. Tellez-Arenas, G. Lazard, and R. J. Lombard, J. Phys. G **12**, 317 (1986).
10. S. B. Dubovichenko and I. I. Strakovsky, Yad. Fiz. **63**, 646 (2000) [Phys. At. Nucl. **63**, 582 (2000)].
11. Markus Simonius, Phys. Rev. Lett. **78**, 4161 (1997).
12. H. F. Arellano, F. A. Brieva, M. Sander, and H. V. von Geramb, Phys. Rev. C **54**, 2570 (1996).
13. A. V. Dzhavadov and M. M. Mirabutalybov, Izv. Akad. Nauk SSSR, Ser. Fiz. **42**, 1869 (1978).
14. T. D. Alkhazov, Izv. Akad. Nauk SSSR, Ser. Fiz. **48**, 1858 (1984).
15. H. O. Meyer, G. L. Moake, and P. P. Singh, Phys. Rev. C **23**, 616 (1981).

Translated by A. Isaakyan

Physics of Atomic Nuclei, Vol. 67, No. 12, 2004, pp. 2154–2165. Translated from Yadernaya Fizika, Vol. 67, No. 12, 2004, pp. 2178–2189.
Original Russian Text Copyright © 2004 by Donchev, Kalachev, Kolesnikov, Tarasov.

NUCLEI
Theory

Carcass Functions in Variational Calculations for Few-Body Systems

A. G. Donchev, S. A. Kalachev, N. N. Kolesnikov, and V. I. Tarasov

Department of Physics, Moscow State University, Vorob'evy gory, Moscow, 119899 Russia

Received March 31, 2003; in final form, November 19, 2003

Abstract—For variational calculations of molecular and nuclear systems involving a few particles, it is proposed to use carcass basis functions that generalize exponential and Gaussian trial functions. It is shown that the matrix elements of the Hamiltonian are expressed in a closed form for a Coulomb potential, as well as for other popular particle-interaction potentials. The use of such carcass functions in two-center Coulomb problems reduces, in relation to other methods, the number of terms in a variational expansion by a few orders of magnitude at a commensurate or even higher accuracy. The efficiency of the method is illustrated by calculations of the three-particle Coulomb systems $\mu\mu e$, ppe, dde, and tte and the four-particle molecular systems H_2 and HeH^+ of various isotopic composition. By considering the example of the ${}^{9}_{\Lambda}$Be hypernucleus, it is shown that the proposed method can be used in calculating nuclear systems as well. © *2004 MAIK "Nauka/Interperiodica"*.

1. INTRODUCTION

Among the presently existing quantum-mechanical methods for calculating nonrelativistic bound systems, the variational method stands out in the following respects: this method is the most universal in the sense that it can be applied both to atomic and molecular and to nuclear problems; moreover, the variational method makes it possible to obtain not only an upper but also a lower bound on respective energies. For systems involving three or more particles, there are examples of variational calculations that are unique in accuracy.

As a rule, the trial function is represented in the form of a superposition of basis functions φ^a,

$$\psi = \sum_{a=1}^{n} c_a \varphi^a, \qquad (1)$$

where c_a are linear coefficients.

Exponential and Gaussian basis functions have been successfully used in calculations of few-body nuclear and Coulomb systems. In the case of zero total orbital angular momentum, such functions for a system of A particles can be represented in the form

$$\varphi^a = \exp\left(-\sum_{i>j=1}^{A} \alpha_{ij}^a R_{ij}^\lambda\right), \qquad (2)$$

where R_{ij} is the distance between the ith and the jth particle, α_{ij}^a are variational parameters, and the exponent λ takes a value of 1 in the case of an exponential basis and a value of 2 in the case of a Gaussian basis.

It was shown in [1] (for more details, see [2]) that, for standard potentials (Coulomb, exponential, Yukawa, Gaussian, square-well potentials), all matrix elements required for obtaining not only an upper but also a lower bound on the relevant energy are expressed in terms of elementary functions, error integrals, and dilogarithms. Functions of exponential and Gaussian bases (along with polynomial functions of the Hylleraas type [3]) ensure the highest accuracy in calculations of not only one-center atomic systems but also systems formed by particles of identical or close masses—for example, electron–positron systems [4]. If, however, the masses of particles differ by an order of magnitude, the presence of two or more heavy particles in addition to light ones results in that the convergence of variational estimates obtained with an exponential or a Gaussian basis deteriorates to such an extent that one cannot attain accuracy beyond three to four decimal places in calculating energies (see [5, 6]). The reason is that the density w of the probability to find two heavy particles at a distance R between them has a sharp maximum at some value of R (the greater the mass ratio between heavy and light particles, the sharper the maximum of this probability density), and it is difficult to approximate such behavior by using exponential or Gaussian functions. This is illustrated in Fig. 1, which shows the results of calculations with exponential functions for the example of the ppe^- system. As the number n of functions in (1) is increased and as, accordingly, the accuracy of the calculation is improved, the maximum becomes narrower; yet, it remains broader than its counterpart in a precise calculation, with carcass functions in the present case (see below).

1063-7788/04/6712-2154$26.00 © 2004 MAIK "Nauka/Interperiodica"

In order to improve the trial function in calculations for two-center (adiabatic) problems, it was proposed to modify an exponential trial function by adding trigonometric functions [7] or, which is equivalent, to use complex-valued nonlinear parameters (exponents) [8]. The use of exponential–trigonometric functions made it possible to improve, for a large number of parameters, the accuracy in calculations for two-center systems nearly up to a value that was achieved within the adiabatic approximation (but which still remains below the accuracy in calculations for one-center systems). The use of trial functions in the form $R_{12}^m \exp(-\alpha R_{12})$ [9], where R_{12} is the distance between heavy particles is yet another way to sidestep difficulties in calculating two-center systems. This made it possible to calculate, at $m = 10$, the H_2^+ energy to a precision of seven significant digits; however, a further improvement of the accuracy requires increasing m up to 30, which complicates the calculations considerably (see [5, 6]). Finally, the Born–Oppenheimer approximation [10, 11] or its modifications (for details, see [12]) are widely used in calculating two-center systems, but the coupling of electron motion to nuclear motion is not always fully taken into account in this case (see [6, 9]).

In the present study, we propose quite an efficient diabatic approach to calculating two-center systems and other systems of the molecular type. This approach, which is based on the use of carcass trial functions, was developed in [13] in connection with a calculation of nuclear systems involving particles whose interaction includes a short-range attracting potential going over to strong repulsion at the shortest distances. Even for a small number of basis functions, the accuracy of the results obtained by using this method is higher than that within other methods.

2. CARCASS BASIS

In those cases where the distances between the particles involved change within narrow intervals (see, for example, Fig. 1), something like a rigid carcass of the system is formed, and the positions of the particles are smeared around this carcass. Upon eliminating the motion of the center of mass of a system consisting of A particles, one can specify its carcass in terms of $A-1$ vectors $\boldsymbol{\rho}_i^a$ $(i = 1, 2, \ldots, A-1)$ measured, for example, from the Ath particle and represent the dependence of a basis function on the coordinate vectors $\boldsymbol{\rho}_i$ in the form

$$\varphi^a = \exp\left(-\sum_{i,j=1}^{A-1}(\boldsymbol{\rho}_i - \boldsymbol{\rho}_i^a)\beta_{ij}^a(\boldsymbol{\rho}_j - \boldsymbol{\rho}_j^a)\right) \qquad (3)$$
$$= \exp(-(\boldsymbol{\rho} - \boldsymbol{\rho}^a)^T\beta^a(\boldsymbol{\rho} - \boldsymbol{\rho}^a)),$$

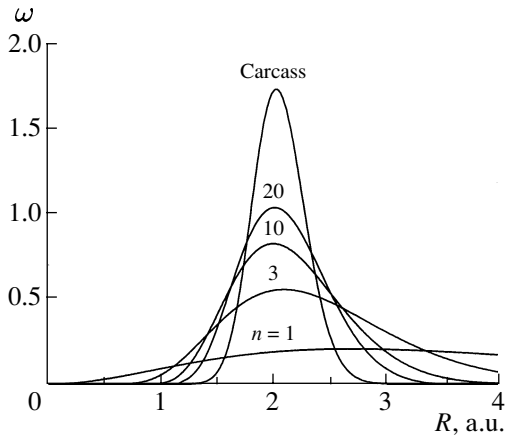

Fig. 1. Density w of the probability to find the protons in the ppe^- system at a distance R in calculations with various numbers n of exponential basis functions $(\int_0^\infty w(R)dR = 1)$.

where $\boldsymbol{\rho}$ and $\boldsymbol{\rho}^a$ are the one-column matrices of the $A-1$ vectors $\boldsymbol{\rho}_i$ and $\boldsymbol{\rho}_i^a$, respectively, while β is a positive definite matrix of dimensions $(A-1)\times(A-1)$ whose elements are considered as variational parameters along with the vectors $\boldsymbol{\rho}_i^a$.

On the other hand, the carcass of a basis function can be specified in terms of the distances R_{ij}^a within each pair (i, j) of particles. In this case, one can represent a carcass basis function in the form

$$\varphi^a = \exp\left(-\sum_{i>j=1}^{A}\alpha_{ij}^a(R_{ij} - R_{ij}^a)^2\right) \qquad (4)$$

and consider α_{ij}^a and R_{ij}^a as variational parameters. The carcass formed by the lengths R_{ij}^a is not associated with the orientation of coordinate axes; in view of this, carcass functions in the form (4) will be referred to as free (unoriented) functions. Obviously, they correspond to zero orbital angular momentum and form a good basis for approximating ground-state functions.

In contrast to functions of the form (4), carcass functions of the form (3) depend on the orientation of cascade vectors, and we will refer to them as vector carcass functions for this reason. They do not correspond to zero orbital angular momentum or any specific value of orbital angular momentum, in general. For example, $\varphi^a = \exp(-\beta^a(\boldsymbol{\rho} - \boldsymbol{\rho}^a)^2)$ in the case of a two-particle system, and the probability density for the relative positions of the particles is explicitly anisotropic, having a maximum in the direction of the carcass vector $\boldsymbol{\rho}^a$.

In order to describe the ground state in terms of the vector carcass functions (3), one can either average

basis functions over the orientations of the carcass vectors or construct combinations of basis functions such that they would ensure an approximate spherical symmetry of the wave function. Finally, vector carcass functions not averaged over angles can be used to a rather high degree of precision in molecular systems, where the rotational energy of the motion of heavy particles is much lower than the total energy.

Returning to a free (unoriented) basis, we note first of all that, apart from a constant factor, the function in (4) can be represented in the form

$$\varphi^a = \exp\left(-\sum_{i\neq j=1}^{A}\left(\alpha_{ij}^a R_{ij}^2 + \beta_{ij}^a R_{ij}\right)\right). \quad (5)$$

Such functions are more general than purely exponential or purely Gaussian trial functions and reduce to them for a special choice of the variational parameters (specifically, to exponential functions at $\alpha = 0$ and to Gaussian functions at $\beta = 0$). It follows that, as an exponential basis, the basis in (5) can equally well be used to calculate one-center systems and systems formed by particles of close masses; however, the latter is able to describe multicenter systems as well, even with a relatively small number of variational parameters.

By way of example, we indicate that, in the case of two-center systems, both terms in the exponent on the right-hand side of (5) are retained only for a single bond (say, that which corresponds to $i = 1$, $j = 2$), only linear or only quadratic terms being selected for other bonds. Accordingly, the functions

$$\varphi^a = \exp\left(-\alpha_{12}(R_{12} - R_{12}^a)^2 - \sum_{\substack{i>j=1\\ \{i,j\}\neq\{1,2\}}}^{A} \beta_{ij}^a R_{ij}\right) \quad (6)$$

and the functions

$$\varphi^a = \exp\left(-\alpha_{12}(R_{12} - R_{12}^a)^2 - \sum_{\substack{i>j=1\\ \{i,j\}\neq\{1,2\}}}^{A} \alpha_{ij}^a R_{ij}^2\right) \quad (7)$$

will be referred to as, respectively, carcass–exponential and carcass–Gaussian functions.

Each of the functions in (6) and (7) has its own domain of applicability. A carcass–exponential basis ensures a very high accuracy in calculating three-particle two-center systems of the ppe^- type even with a small number of functions. In calculating the energy, one such function alone ensures an accuracy of up to three significant digits—that is, an accuracy that requires introducing a hundred conventional exponentials or Gaussian functions. In calculating systems containing more than three particles, there arise, however, difficulties, which are also inherent in the approach employing ordinary exponential bases.

The accuracy in calculating three-particle two-center Coulomb systems with the aid of carcass–Gaussian functions is much lower than the accuracy of the corresponding calculations with carcass–exponential functions, but the former are applicable to calculating two-center systems involving four or more particles—for example, the hydrogen molecule.

With allowance for this, formulas for determining the matrix elements of a Hamiltonian are given in Appendices A and B both for the case of carcass–exponential and for the case of carcass–Gaussian functions.

Unfortunately, the matrix elements of a Hamiltonian cannot be obtained in a closed form for two or more carcass bonds if use is made of free carcass functions. The vector carcass functions (3), which are applicable to multicenter systems involving an arbitrary number of particles, are free from this drawback. For the case of vector carcass functions, the required matrix elements are given in Appendix C.

In calculations, the most serious difficulties arise, as usual, in determining optimum values of nonlinear variational parameters (scale parameters in the exponents and lengths of carcass bonds). Since the potential of deterministic methods is fast exhausted as the number of terms in expansion (1) is increased, a dedicated procedure was employed that combines a step-by-step stochastic search [14] and a deterministic search. First, points in the multidimensional space of nonlinear parameters were chosen at random in accordance with the preselected distribution function, whereupon a coordinate-by-coordinate descent was performed, first, in a stochastic and, then, in a deterministic way. At this stage, we selected points that are the most promising for the ensuing detailed optimization. The aforementioned distribution function was found by means of a procedure that is similar to that described in [15].

3. RESULTS OF NUMERICAL CALCULATIONS

3.1. Three-Particle Systems

As three-particle systems, we considered the two-center Coulomb systems $\mu\mu e$, ppe, dde, and tte and the ${}^{9}_{\Lambda}\mathrm{Be}$ hypernucleus, which is a system of the nuclear type. The calculations for the Coulomb systems were performed with a comparatively small number (not more than 50) of trial functions of the form (6), but the accuracy attained in this case was at the same level as or even higher than that in the best

Table 1. Upper bounds on the energies of two-center three-particle Coulomb systems and of ${}^{9}_{\Lambda}$Be

System	n	E_U, a.u.	Comments
$\mu\mu e$	1	−0.583 356	In [8], the value of $E_U = -0.585\,126\,097\,176$ was obtained by using complex-valued parameters for $n = 500$
	5	−0.585 112 990	
	10	−0.585 125 383 5	
	50	−0.585 126 095 200	
ppe	1	−0.596 426	In [8], the value of $E_U = -0.597\,139\,063\,107\,6$ was obtained for $n = 500$. In [11], the value of $E = -0.597\,139\,063\,123$ was obtained in the Born–Oppenheimer approximation
	5	−0.597 136 342	
	10	−0.597 138 947 7	
	50	−0.597 139 063 059	
dde	1	−0.598 230	In [8], the value of $E_U = -0.598\,788\,783\,890$ was obtained for $n = 500$
	5	−0.598 786 749	
	10	−0.598 788 727 9	
	50	−0.598 788 783 941	
tte	1	−0.599 016	In [8], the value of $E_U = -0.599\,506\,909\,80$ was obtained for $n = 500$
	5	−0.599 504 934	
	10	−0.599 506 864 7	
	50	−0.599 506 909 911	
${}^{9}_{\Lambda}$Be	1	−4.810 9	The energy of ${}^{9}_{\Lambda}$Be is given in MeV; the calculation of ${}^{9}_{\Lambda}$Be was performed with the potential (8)
	5	−6.494 6	
	10	−6.540 1	
	50	−6.546 5	

of the published results. The use of only one basis function in the form (6) makes it possible to calculate the energies of the above two-center systems to a precision of up to three decimal places—that is, to a precision at a level achieved with a hundred exponential or Gaussian functions. Even in relation to an exponential–trigonometric basis, a carcass basis ensures the same accuracy of the calculation with an order of magnitude smaller number of basis functions. This is illustrated in Table 1, which gives the results of the calculations with carcass-exponential functions for the $\mu\mu e$, ppe, dde, and tte Coulomb systems for various numbers of trial functions. Also quoted in this table for the sake of comparison are the currently best results of the calculations with exponential–trigonometric functions [8] and the results of the calculations within the Born–Oppenheimer method [11].

From Table 1, it can be seen that the calculated values of the energy E_U are fast saturated as the number of terms in expansion (1) is increased, especially for a larger mass of heavy particles, the results being in agreement to within 9 to 10 decimal places with those that are presented in [8, 11].

At a fixed number of basis functions, the accuracy of the calculations for singly charged Coulomb systems of the $X^{\pm}X^{\pm}Y^{\mp}$ type becomes higher with increasing particle-mass ratio $\xi = m_X/m_Y$. This can be seen in Fig. 2. The carcass character of the functions manifests itself for $\xi \gtrsim 10$; at smaller values of ξ, the basis degenerates into a purely exponential basis. For $\xi < 0.2$, the accuracy of the calculation is virtually independent of the particle-mass ratio. In the intermediate region $1 < \xi < 10$, the accuracy of the calculation is the poorest.

For the same Coulomb systems, the results of the calculations at $n = 50$ for the mean values of the total, kinetic, and potential energies (E_U, $\langle T\rangle$, and $\langle V\rangle$, respectively); the mean values of the potential energy of interaction between a light and a heavy particle ($\langle V_1\rangle$); the mean values of the potential energy of interaction between heavy particles ($\langle V_3\rangle$); the mean and root-mean-square distances between a light and

Table 2. Some features of two-center three-particle Coulomb systems according to calculations with carcass–exponential basis functions for $n = 50$

	$\mu\mu e$	ppe	dde	tte
m_1/m_3	206.768 262	1836.152 701	3670.483 014	5496.921 58
E_U [a.u.]	−0.585 126 0952	−0.597 139 063 1	−0.598 788 783 9	−0.599 506 909 9
$\langle V_1\rangle$ [a.u.]	−0.820 339 791	−0.842 492 962	−0.845 615 398	−0.846 981 674
$\langle V_3\rangle$ [a.u.]	0.470 427 360	0.490 707 798	0.493 653 238	0.494949 536
$\langle T\rangle$ [a.u.]	0.585 126 126	0.597 139 062	0.598 788 774	0.599 506 903
$\langle V\rangle$ [a.u.]	−1.170 252 220	−1.194 278 126	−1.197 577 558	−1.199 013 814
$\eta \times 10^9$	30	0.7	8	6
$\langle R_1\rangle$ [a.u.]	1.769 302 287	1.692 966 210	1.682 346 558	1.677 707 696
$\sqrt{\langle R_1^2\rangle}$ [a.u.]	1.984 554 669	1.886 477 654	1.872 839 866	1.866 882 152
δ_1 [%]	50.81	49.16	48.92	48.81
$\langle R_3\rangle$ [a.u.]	2.205 214 958	2.063 913 868	2.044 070 059	2.035 386 060
$\sqrt{\langle R_3^2\rangle}$ [a.u.]	2.244 233 456	2.076 845 190	2.053 203 130	2.042 844 719
δ_3 [%]	18.89	11.21	9.46	8.57

a heavy particle ($\langle R_1\rangle$ and $\langle R_1^2\rangle^{1/2}$, respectively); and the mean and root-mean-square distances between heavy particles ($\langle R_3\rangle$ and $\langle R_3^2\rangle^{1/2}$, respectively) are presented in Table 2. Also given in Table 2 is the square root $\delta_{1,3} = \left(\langle R_{1,3}^2\rangle - \langle R_{1,3}\rangle^2\right)^{1/2}/\langle R_{1,3}\rangle$ of the variance in percent, this quantity characterizing deviations from a rigid carcass structure. As might have been expected, δ_3 is much less than δ_1 and decreases fast with increasing heavy-particle mass. Finally, Table 2 displays the deviation of the results of the calculation from the virial theorem, $\eta = |1 + 2\langle T\rangle/\langle V\rangle|$, this quantity correlating with the accuracy of the calculation. We note that, to a precision of up to nine decimal places, the geometric features of the systems being considered agree with the results quoted in [8].

The results of variational calculations for Coulomb systems deteriorate considerably if use is made of Gaussian functions instead of exponential functions. One can see manifestations of this even in the two-body atomic problem, and the trend in question survives in systems involving a larger number of particles. By way of example, we indicate that, in the case of the He atom, the accuracy attained with Gaussian functions is three orders of magnitude lower than that in the calculation with the same number (n) of exponential functions. The use of carcass–Gaussian functions in calculating the ppe^- system at $n = 30$ makes it possible to obtain seven to eight correct significant digits instead of 11 in the case of a carcass–exponential basis. As to vector carcass functions, they ensure only three correct digits if no averaging over the angles of carcass vectors is performed.

For a system of the nuclear type, we took the ${}^{9}_{\Lambda}$Be hypernucleus. For it, the calculation was performed within the $\alpha + \alpha + \Lambda$ cluster model by using hard $\alpha\alpha$ and $\Lambda\alpha$ potentials.[1)] For the $\alpha\alpha$ interaction, use was made of the d_0 version of the Ali–Bodmer potential [17], while, for the $\Lambda\alpha$ interaction, the potential was found with the aid of the most realistic sign-alternating ΛN potential from [18] via averaging over the nucleon-density distribution in alpha particles. In doing this, the nucleon-density distribution in an

[1)] Also, we have considered a version of the soft $\alpha\alpha$ and $\Lambda\alpha$ potentials from [16] that were fitted to the experimental binding energy of ${}^{9}_{\Lambda}$Be ($B_\Lambda = 6.71$ MeV). Our calculations revealed that, in fact, the total energy was strongly overestimated in [16]. Without allowing for Coulomb interaction, the value of $E_U = -10.2425$ MeV was found for an upper variational bound on the energy at $n = 50$. This upper bound was compellingly confirmed by the calculation of a lower bound (according to the computational technique proposed in [15]): $E_L = -10.2427$ MeV. The result obtained upon taking into account the Coulomb interaction of alpha particles treated as pointlike charges is $E_U = -8.3876$ MeV. With allowance for a spatial distribution of the charge in alpha particles, we have $E_U = -8.4586$ MeV.

Table 3. Some features of the ${}^{9}_{\Lambda}$Be hypernucleus that were calculated with $n = 50$ carcass–Gaussian functions

	With allowance for the alpha-particle charge	Without allowance for the alpha-particle charge
E_U [MeV]	−6.5465	−8.2760
$\langle T\rangle$ [MeV]	14.4714	14.8758
$\langle V\rangle$ [MeV]	−21.0179	−23.1518
$\langle V_{\alpha\Lambda}\rangle$ [MeV]	−8.8137	−8.9717
$\langle V_{\alpha\alpha}\rangle$ [MeV]	−3.3905	−5.2084
$\langle V^{\mathrm{Coul}}_{\alpha\alpha}\rangle$ [MeV]	1.7125	0.0000
$\sqrt{\langle R^2_{\alpha\Lambda}\rangle}$ [fm]	3.1244	3.0609
$\sqrt{\langle R^2_{\alpha\alpha}\rangle}$ [fm]	3.7093	3.6160

alpha particle was taken in the form of a Gaussian function of root-mean-square radius 1.5 fm. Upon integration, the $\Lambda\alpha$ potential reduced to the form

$$V_{\Lambda\alpha}(r) = \sum_{i=1}^{3} V_i e^{-\nu_i r^2}, \qquad (8)$$

where the parameter values are $V_1 = 17.77$ MeV, $V_2 = 19.56$ MeV, $V_3 = -83.01$ MeV, $\nu_1 = 0.6491$ fm^{-2}, $\nu_2 = 0.5963$ fm^{-2}, and $\nu_3 = 0.5024$ fm^{-2}. Within the Λ + core model, this potential ensures a correct value of the binding energy for the ${}^{5}_{\Lambda}$He hypernucleus.

The calculations for ${}^{9}_{\Lambda}$Be were performed by using the carcass–Gaussian functions (7). The character of convergence of the results is also illustrated in Table 1. The value found for E_U at $n = 50$ is nearly coincident with the experimental value of B_Λ. Our calculations revealed that the "carcass effect" is weaker for the nuclear system being considered than for typical two-center Coulomb systems. For ${}^{9}_{\Lambda}$Be, the expectation values of the kinetic- and the potential-energy operator and the root-mean-square distances between the particles involved are given in Table 3 according to the calculations at $n = 50$ that were performed either with or without allowance for the Coulomb interaction in this nuclear system.

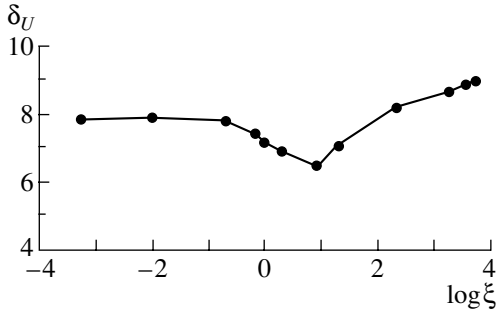

Fig. 2. Number of significant digits in calculating an upper bound on the energy of systems belonging to the $X^{\pm}X^{\pm}Y^{\mp}$ type as a function of the particle-mass ratio $\xi = m_X/m_Y$ for 30 basis functions.

3.2. Four-Particle Coulomb Systems

Calculations for four-particle two-center systems—in particular, for the H_2 molecule—beyond the adiabatic approximation are of interest not only for studying the systems themselves but also for estimating the accuracy of the adiabatic approximation. The method used here makes it possible to estimate isotopic effects in four-particle molecular systems reliably. Our calculations were performed with the cascade–Gaussian functions (7). The hydrogen molecule H_2 and the HeH^+ system of various isotopic composition are considered in detail.

The character of convergence of the energy E_U with increasing number n in expansion (1) is illustrated by the following values (in atomic units): −1.068 at $n = 1$, −1.161 at $n = 10$, −1.1627 at $n = 20$, −1.1635 at $n = 50$, and −1.16401 at $n = 200$. The results for E_U at $n = 200$ for the ppe^-e^- (H_2) system differ from the most precise results obtained in [5, 6] in the last decimal place.

For the hydrogen molecules of various isotopic composition, the results of the calculations for the ground-state energy E_U and for the dissociation energy E_D are presented in Table 4 for the case where use was made of 200 carcass–Gaussian functions. We note that, for the four-particle systems being considered, the deviation from the virial theorem correlates (in just the same way as for the above three-particle systems) with the accuracy in calculating the energy.

As might have been expected, the dissociation energy E_D grows slowly (by a few percent) with increasing mass of the molecule. Our results are at the level of the best results published thus far in the literature.

Along with this, the energy of the first excited S state of the hydrogen molecule was calculated by using the same basis. It proved to be $E_1 = -1.1446$ a.u., which corresponds to the excitation energy of 0.528 eV (to be compared with the experimental value of 0.54 eV). This state corresponds to the first vibrational level in the adiabatic approximation.

The helium hydride positive ion HeH^+, which consists of an alpha particle, a proton, and two electrons, was another molecular system that was considered in detail. This system is of interest for astrophysics,

Table 4. Ground-state and dissociation energies of molecular-hydrogen isotopes according to calculations with $n = 200$ carcass–Gaussian functions

	H_2	D_2	T_2	HD	HT	DT
E_U [a.u.]	−1.1640	−1.1669	−1.1681	−1.1654	−1.1659	−1.1675
E_D [a.u.]	0.1645	0.1672	0.1683	0.1658	0.1663	0.1677

Table 5. Ground-state and dissociation energies of $^nHe^mH^+$ systems according to calculations with $n = 200$ carcass–Gaussian functions

	$^3HeH^+$	$^3HeD^+$	$^3HeT^+$	$^4HeH^+$	$^4HeD^+$	$^4HeT^+$	$^6HeH^+$	$^6HeD^+$	$^6HeT^+$	$^8HeH^+$	$^8HeD^+$	$^8HeT^+$
E_U [a.u.]	−2.9706	−2.9720	−2.9725	−2.9709	−2.9723	−2.9728	−2.9713	−2.9727	−2.9732	−2.9714	−2.9729	−2.9734
E_D [a.u.]	0.0674	0.0688	0.0693	0.0676	0.0690	0.0695	0.0679	0.0693	0.0698	0.0679	0.0694	0.0699

since it is rather copiously produced in interstellar clouds under the effect of ionizing stellar radiation. The experimental observation of this system was reported in [19, 20], and its dissociation energy was estimated at 1.835 eV (0.0674 a.u.). Calculations in the adiabatic approximation without taking into account the kinetic energy of heavy particles were performed in [21–23] for the $^4HeH^+$ system.

For helium hydride ions of various isotopic composition, the total ground-state energies calculated with the aid of the functions in (7) are given in Table 5. Also quoted in this table are the energies of dissociation into respective helium- and hydrogen-ion isotopes. Just as in the case of the hydrogen molecule, the dissociation energy of the helium-hydride ion increases by a few percent with increasing nuclear masses. The results of the calculation for the $^4HeH^+$ system fall between the values published in the literature, $E_U = -2.969$ a.u. [23] and -2.978 a.u. [22], and are close to experimental data. As to the energy of the first excited S state of $^4HeH^+$, it is -2.9560 a.u., which corresponds to the excitation energy of 0.41 eV.

Table 6. Root-mean-square distances (in atomic units) in the ground (g) and the first excited (e) state of various isotopic systems belonging to the $^nH^mH$ type

$n:m$	R_{ee}		R_{ne}		R_{me}		R_{nm}	
	g	e	g	e	g	e	g	e
1 : 1	2.410	2.484	1.774	1.843	1.774	1.843	1.459	1.596
2 : 2	2.401	2.497	1.766	1.855	1.766	1.855	1.445	1.618
3 : 3	2.397	2.502	1.763	1.860	1.763	1.860	1.439	1.626
1 : 2	2.406	2.446	1.771	1.820	1.771	1.810	1.453	1.569
1 : 3	2.405	2.448	1.770	1.822	1.770	1.811	1.452	1.571
2 : 3	2.404	2.453	1.769	1.826	1.768	1.815	1.449	1.580

The root-mean-square distances between the particles in molecular hydrogen $^nH^mH$ of various isotopic composition are presented in Table 6 for the ground and the first excited state—specifically, the distances R_{nm} between the nuclei; the distances R_{ee} between the electrons; and the distances R_{ne} and R_{me} between an electron and the ^nH and ^mH nuclei, respectively.

As can be seen from this table, the root-mean-square distance between the protons is nearly 10% greater in the excited than in the ground state. Also, the excitation leads to an increase of a few percent in the distance between the electrons and in the distance between an electron and a proton.

Table 7 displays the root-mean-square distances between the particles in helium hydride ions of various isotopic composition for the ground and the first excited state—namely, the distances R_{nm} between the nuclei, the distances R_{ee} between the electrons, the distances R_{ne} between the hydrogen nucleus and an electron, and the distances R_{me} between the helium nucleus and an electron. Just as in the hydrogen molecule, the geometry of the molecular ion in question in the first excited state differs significantly from the geometry of the ground state. The distances between the nuclei increase by nearly 16%; the remaining interparticle distances also grow.

In addition to HeH^+, the $He\mu^+$ ($\alpha\mu^+e^-e^-$) system also proved to be bound, its ground-state and dissociation energies being $E_0 = -2.9591$ a.u. and $E_D = 0.0558$ a.u., respectively. Moreover, our analysis reveals that all four-particle systems of the HeX^+ type are bound under the condition $m_X \geq 8m_e$, where m_X is the mass of the X^+ particle and m_e is the electron mass. At smaller values of m_X, the systems

Table 7. Root-mean-square distances (in atomic units) in the ground (g) and the first excited (e) state of various isotopic systems belonging to the $^nHe^mH^+$ type

$n:m$	R_{ee}		R_{ne}		R_{me}		R_{nm}	
	g	e	g	e	g	e	g	e
1 : 3	1.554	1.591	1.088	1.111	1.674	1.895	1.534	1.783
2 : 3	1.552	1.595	1.087	1.113	1.665	1.904	1.524	1.792
3 : 3	1.552	1.596	1.086	1.114	1.661	1.907	1.520	1.795
1 : 4	1.554	1.592	1.088	1.111	1.673	1.897	1.533	1.784
2 : 4	1.552	1.596	1.086	1.114	1.661	1.907	1.520	1.795
3 : 4	1.551	1.596	1.086	1.114	1.660	1.908	1.518	1.797
1 : 6	1.554	1.592	1.087	1.112	1.671	1.898	1.531	1.786
2 : 6	1.552	1.596	1.086	1.114	1.661	1.907	1.520	1.795
3 : 6	1.551	1.597	1.086	1.115	1.658	1.910	1.516	1.798
1 : 8	1.553	1.592	1.087	1.112	1.670	1.899	1.530	1.787
2 : 8	1.551	1.596	1.086	1.114	1.661	1.908	1.519	1.796
3 : 8	1.551	1.597	1.085	1.115	1.657	1.910	1.516	1.799

in question appear to be unstable with respect to breakup into a helium atom and a free particle X^+—in particular, the system consisting of an alpha particle, two electrons, and a positron is unstable.

Only hydrogen and helium can form two-center molecular systems involving two electrons. According to the calculations, the $X^{Z+}e^-e^-p^+$ system cannot be stable at any value of the mass of the X particle if $Z > 2$. In particular, the $Li^{3+}e^-e^-p^+$ system is unstable.

In summary, our analysis has revealed that carcass basis functions (in various versions, free and vector carcass functions) can ensure a high precision in calculating two-center Coulomb systems and nuclear systems. As a further development, one can hope to extend the proposed approach to the case of more complicated multicenter molecular systems, as well as to the case of nuclear cluster systems (for example, ${}^{10}_{\Lambda\Lambda}Be$ or supernuclei), which were not considered here.

Note added in proof. Part of the results of this study was published in a recent article of A.G. Donchev, S.A. Kalachev, N.N. Kolesnikov, and V.A. Tarasov [Phys. Rev. A **69**, 034501 (2004)].

ACKNOWLEDGMENTS

We are grateful to V.B. Belyaev, participants of the seminar at the Bogolyubov Laboratory of Theoretical Physics at the Joint Institute for Nuclear Research (JINR, Dubna), V.I. Kukulin, P.P. Zakharov, and V.S. Rostovsky for discussions on the results of this study and for enlightening comments.

APPENDIX A

Carcass–Exponential Basis

In the presence of one carcass bond (two-center systems), the carcass–exponential basis function for a system of three particles interacting via central forces can be represented in the form

$$\varphi^a = \exp\left(-\sum_{i=1}^{3}\alpha_i^a R_i - \beta^a R_3^2\right), \qquad (A.1)$$

where α_p^a and β^a are nonlinear parameters. Here, we have denoted by R_i the distance between the jth and kth particles, where (i, j, k) is a triplet of numbers (1, 2, 3) or one of their cyclic permutations.

The matrix elements of a Hamiltonian are expressed in terms of integrals of the form

$$I_{klm} = 8\pi^2\int_0^\infty e^{-\alpha_3 R_3-\beta R_3^2}R_3^m dR_3 \qquad (A.2)$$
$$\times\int_0^\infty e^{-\alpha_2 R_2}R_2^l dR_2\int_{|R_3-R_2|}^{R_3+R_2} e^{-\alpha_1 R_1}R_1^k dR_1,$$

which are found by differentiating the basic integral I_{000}:

$$I_{klm} = \left(-\frac{\partial}{\partial\alpha_1}\right)^k\left(-\frac{\partial}{\partial\alpha_2}\right)^l\left(-\frac{\partial}{\partial\alpha_3}\right)^m I_{000}. \qquad (A.3)$$

In turn, the basic integral is expressed in terms of combinations of error integrals; that is,

$$I_{000} = -\frac{16\pi^2}{\sqrt{\beta}(\alpha_1^2-\alpha_2^2)} \qquad (A.4)$$
$$\times\left(F\left(\frac{\alpha_1+\alpha_3}{2\sqrt{\beta}}\right)-F\left(\frac{\alpha_2+\alpha_3}{2\sqrt{\beta}}\right)\right),$$

where $F(z) \equiv e^{z^2}\int_z^\infty e^{-t^2}dt$.

For the representation of the matrix elements of the operators T and V to be convenient, we introduce the notation

$$t_p \equiv \cos\vartheta_p, \quad T_{p0} \equiv \langle a|t_p|b\rangle, \quad T_{p1} \equiv \langle a|t_p R_3|b\rangle,$$
$$G_p \equiv \langle a|R_p^{-1}|b\rangle, \quad N_0 \equiv \langle a|b\rangle, \quad N_1 \equiv \langle a|R_3|b\rangle,$$
$$N_2 \equiv \langle a|R_3^2|b\rangle,$$

where ϑ_p is the angle at the vertex associated with the pth particle in the triangle formed by particles 1, 2, and 3.

For the matrix element of the operator T between the states a and b, we then obtain

$$\langle a|T|b\rangle = \left(\frac{\alpha_1^a\alpha_1^b}{2\mu_{23}} + \frac{\alpha_2^a\alpha_2^b}{2\mu_{31}} + \frac{\alpha_3^a\alpha_3^b}{2\mu_{12}}\right) N_0 \quad \text{(A.5)}$$
$$+ \frac{\alpha_3^a\beta^b}{\mu_{12}} N_1 + 2\frac{\beta^a\beta^b}{\mu_{12}} N_2 + \frac{\alpha_2^a\alpha_3^b + \alpha_3^a\alpha_2^b}{4m_1} T_{10}$$
$$+ \frac{\alpha_3^a\alpha_1^b + \alpha_1^a\alpha_3^b}{4m_2} T_{20} + \frac{\alpha_1^a\alpha_2^b + \alpha_2^a\alpha_1^b}{4m_3} T_{30}$$
$$+ \frac{\alpha_2^a\beta^b + \beta^a\alpha_2^b}{2m_1} T_{11} + \frac{\alpha_3^a\beta^b + \beta^a\alpha_3^b}{2m_2} T_{21},$$

where μ_{ij} is the reduced mass of the ith and jth particle.

In the case of popular potentials, the calculation of the matrix elements of the potential energy reduces to evaluating the same integrals as for the matrix elements of the kinetic-energy operator. In particular, it is sufficient to calculate a matrix element of the form $\langle a|1/R_p|b\rangle = G_p$ for determining the expectation value of the Coulomb interaction.

In the following, the immaterial common numerical factor $16\pi^2$ is omitted in all integrals for the sake of convenience. Upon introducing the notation

$$C = \frac{1}{\alpha_1 + \alpha_2}, \quad a_1 = \frac{\alpha_1 + \alpha_3}{2\sqrt{\beta}}, \quad a_2 = \frac{\alpha_2 + \alpha_3}{2\sqrt{\beta}},$$
$$d = a_1 - a_2, \quad k = \frac{1}{2\sqrt{\beta}},$$

$$S_n = \left[\left(\frac{\partial}{\partial a_1}\right)^{n-1} F(a_1) - \left(\frac{\partial}{\partial a_2}\right)^{n-1} F(a_2)\right]/d,$$
$$Z_n = 2\left[\left(\frac{\partial}{\partial a_1}\right)^{n-2} F(a_1) + \left(\frac{\partial}{\partial a_2}\right)^{n-2} F(a_2) - 2S_{n-2}\right]/d^2,$$

where $\alpha_i \equiv \alpha_i^a + \alpha_i^b$, $\beta \equiv \beta^a + \beta^b$, we obtain $I_{000} = -CS_1/2\beta$. For the normalization factor N_0 and for the functions G_p, N_1, N_2, T_{p0}, and T_{p1} in (A.5), we have

$$G_1 = \frac{C^2}{2\beta} kS_2 - \frac{C}{8\beta} k^2(2S_3 - Z_4 d);$$
$$G_2 = \frac{C^2}{2\beta} kS_2 - \frac{C}{8\beta} k^2(2S_3 + Z_4 d);$$
$$G_3 = -\frac{C^3}{\beta} S_1 + \frac{C^2}{2\beta} kS_2 - \frac{C}{4\beta} k^2 Z_3;$$
$$N_0 = \frac{C^3}{\beta} kS_2 - \frac{C^2}{2\beta} k^2 S_3 + \frac{C}{4\beta} k^3 Z_4;$$
$$N_1 = -\frac{C^3}{\beta} k^2 S_3 + \frac{C^2}{2\beta} k^3 S_4 - \frac{C}{4\beta} k^4 Z_5;$$
$$N_2 = \frac{C^3}{\beta} k^3 S_4 - \frac{C^2}{2\beta} k^4 S_5 + \frac{C}{4\beta} k^5 Z_6;$$
$$T_{10} = -\frac{C^3}{\beta} kZ_3 d - \frac{C^2}{2\beta} k^2(2Z_3 - Z_4 d) + \frac{C}{2\beta} k^3 Z_4;$$
$$T_{20} = \frac{C^3}{\beta} kZ_3 d - \frac{C^2}{2\beta} k^2(2Z_3 + Z_4 d) + \frac{C}{2\beta} k^3 Z_4;$$
$$T_{30} = \frac{2C^3}{\beta} kS_2 - \frac{C^2}{\beta} k^2 S_3 - \frac{C}{2\beta} k^3 Z_4;$$
$$T_{11} = \frac{C^3}{\beta} k^2 Z_4 d + \frac{C^2}{2\beta} k^3(2Z_4 - Z_5 d) - \frac{C}{2\beta} k^4 Z_5;$$
$$T_{21} = -\frac{C^3}{\beta} k^2 Z_4 d + \frac{C^2}{2\beta} k^3(2Z_4 + Z_5 d) - \frac{C}{2\beta} k^4 Z_5.$$

In the case of $|d/a| \ll 1$, where $a = (a_1 + a_2)/2$, it is advisable to use the expansions

$$S_n = \sum_{k=0,2,\ldots}^{\infty} \left(\frac{\partial}{\partial a}\right)^{n+k} F(a) \left(\frac{d}{2}\right)^n \frac{1}{(n+1)!},$$
$$Z_n = \sum_{k=0,2,\ldots}^{\infty} \left(\frac{\partial}{\partial a}\right)^{n+k} F(a) \left(\frac{d}{2}\right)^n \frac{n+2}{(n+3)!}$$

in calculating S_n and Z_n.

The calculation of matrix elements in the case of two or three carcass bonds is much more involved even for a three-particle system (see, for example, [24]).

APPENDIX B

Carcass–Gaussian Basis

The possibility of calculating, with a Gaussian basis, systems that involve an arbitrary number of particles is the main advantage of this type of basis over other variational bases. A carcass modification of Gaussian bases also possesses this remarkable feature. In the case of one carcass bond (for example, between particles A and $A-1$), it is convenient to represent a function that enters into a carcass–Gaussian basis in the form of the difference

$$\varphi^a = \varphi_+^a - \varphi_-^a,$$

where

$$\varphi_\pm^a = \exp\left(-\sum_{p>q=1}^{A} \alpha_{pq}^a R_{pq}^2 \pm \beta^a R_{A-1,A}\right). \quad \text{(A.6)}$$

Here, p and q are particle numbers, while α_{pq}^a and β^a are nonlinear variational parameters.

For the ensuing calculations to be more convenient, we introduce the notation

$$N \equiv \langle a|b\rangle,$$

$$N' \equiv \langle a_+|b_+\rangle + \langle a_+|b_-\rangle + \langle a_-|b_+\rangle + \langle a_-|b_-\rangle,$$
$$G_{pqr} \equiv \langle a|\mathbf{R}_{pq}\cdot\mathbf{R}_{pr}|b\rangle,$$
$$G'_{pqr} \equiv \left\langle a_-\left|\frac{\mathbf{R}_{pq}\cdot\mathbf{R}_{pr}}{R_{A-1,A}}\right|b_-\right\rangle - \left\langle a_+\left|\frac{\mathbf{R}_{pq}\cdot\mathbf{R}_{pr}}{R_{A-1,A}}\right|b_+\right\rangle,$$
$$G''_{pqr} \equiv \left\langle a_-\left|\frac{\mathbf{R}_{pq}\cdot\mathbf{R}_{pr}}{R_{A-1,A}}\right|b_+\right\rangle - \left\langle a_+\left|\frac{\mathbf{R}_{pq}\cdot\mathbf{R}_{pr}}{R_{A-1,A}}\right|b_-\right\rangle.$$

Simple calculations in accordance with the technique developed in [1, 2, 15] lead to the following expression for the matrix element of the kinetic-energy operator T between the states $|a\rangle$ and $|b\rangle$:

$$\langle a|T|b\rangle = 2\sum_{p,q,r=1}^{A}\frac{\alpha^a_{pq}\alpha^b_{pr}}{m_p}G_{pqr} + \left(\frac{1}{2m_{A-1}}+\frac{1}{2m_A}\right)\beta^a\beta^b N' + \sum_{p=1}^{A}\frac{\beta^a\alpha^b_{A-1,p}+\beta^b\alpha^a_{A-1,p}}{m_{A-1}}G'_{A-1,p,A} + \sum_{p=1}^{A}\frac{\beta^a\alpha^b_{pA}+\beta^b\alpha^a_{pA}}{m_A}G'_{A,p,A-1} - \sum_{p=1}^{A}\frac{\beta^a\alpha^b_{A-1,p}-\beta^b\alpha^a_{A-1,p}}{m_{A-1}}G''_{A-1,p,A} - \sum_{p=1}^{A}\frac{\beta^a\alpha^b_{pA}-\beta^b\alpha^a_{pA}}{m_A}G''_{A,p,A-1}. \quad (A.7)$$

In the case of Coulomb potentials, the calculation of matrix elements of the potential energy amounts to evaluating integrals of the form $V_{pq} \equiv \langle a|1/R_{pq}|b\rangle$. The matrix elements of Gaussian potentials of interaction within any pair of particles reduce to the integral N whose arguments differ somewhat from those in the calculation of the overlap integral of basis functions. As to the matrix elements of the exponential and Yukawa potentials of interaction between particles forming a carcass bond, they reduce to the integrals N and $V_{A-1,A}$, respectively, their arguments being also somewhat modified.

The calculation of the integrals N, N', G_{pqr}, G'_{pqr}, G''_{pqr}, and V_{pq}, which are necessary for obtaining an upper variational bound, yields

$$N = \frac{2}{D^{3/2}}\left\{(1+2\xi^2)e^{\xi^2} - (1+2\chi^2)e^{\chi^2}\right\}, \quad (A.8)$$

$$N' = \frac{2}{D^{3/2}}\left\{(1+2\xi^2)e^{\xi^2} + (1+2\chi^2)e^{\chi^2}\right\},$$
$$G_{pqr} = \frac{D_{pq}+D_{pr}-D_{qr}}{2D^{5/2}}\times\left\{(3+12\xi^2+4\xi^4)e^{\xi^2} - (3+12\chi^2+4\chi^4)e^{\chi^2}\right\} - \frac{D_{pq;A,A-1}+D_{pr;A,A-1}-D_{qr;A,A-1}}{D^{3/2}D_{A,A-1}}\times\left\{(3\xi^2+2\xi^4)e^{\xi^2} - (3\chi^2+2\chi^4)e^{\chi^2}\right\},$$
$$G'_{pqr} = -\frac{2\xi}{DD^{1/2}_{A-1,A}}e^{\xi^2}\times\left\{\frac{D_{pq}+D_{pr}-D_{qr}}{2D}(3+2\xi^2) - \frac{D_{pq;A,A-1}+D_{pr;A,A-1}-D_{qr;A,A-1}}{D_{A,A-1}}\xi^2\right\},$$
$$G''_{pqr} = -\frac{2\chi}{DD^{1/2}_{A-1,A}}e^{\chi^2}\times\left\{\frac{D_{pq}+D_{pr}-D_{qr}}{2D}(3+2\chi^2) - \frac{D_{pq;A,A-1}+D_{pr;A,A-1}-D_{qr;A,A-1}}{D_{A,A-1}}\chi^2\right\},$$
$$V_{pq} = \frac{4}{DD^{1/2}_{pq}}\left\{\Omega(\xi;g_{pq;A,A-1}) - \Omega(\chi;g_{pq;A,A-1})\right\},$$

where

$$D_{pq} = \frac{\partial D}{\partial\alpha_{pq}}, \quad D_{pq;rs} = \frac{\partial^2 D}{\partial\alpha_{pq}\partial\alpha_{rs}},$$
$$g^2_{pq;rs} = 1 - \frac{DD_{pq;rs}}{D_{pq}D_{rs}},$$
$$\xi = \frac{\beta^a+\beta^b}{2}\sqrt{\frac{D_{A,A-1}}{D}}, \quad \chi = \frac{\beta^a-\beta^b}{2}\sqrt{\frac{D_{A,A-1}}{D}},$$
$$\Omega(x;g) = e^{(1-g^2)x^2}\left\{\frac{1}{\sqrt{\pi}} + xe^{g^2x^2}\frac{\mathrm{erf}(gx)}{g}\right\}.$$

In these expressions, $D = \det(u^a+u^b)$, where u^a is the $(A-1)\times(A-1)$ matrix whose elements are related to the parameters α^a_{pq} by the equations $u^a_{pp} = \sum_{q=1}^{A}\alpha^a_{pq}$ and $u^a_{pq} = -\alpha^a_{pq}$, $1 \le p, q \le A-1$, $p \ne q$.

It should be noted that exponential and Yukawa potentials along the carcass bond do not generate additional complications in calculating matrix elements of the potential energy; in the case of Gaussian potentials of interparticle interaction, the matrix elements of the potential energy reduce to the normalization integral N.

APPENDIX C

Vector Carcass Functions

The calculation of matrix elements with vector carcass functions is similar to the calculation with Gaussian trial functions (see [1]). In order evaluate the overlap integral of the basis functions φ^a and φ^b, it is convenient to go over in (3) from ρ to the new variables

$$\mathbf{r} = \boldsymbol{\rho} - \mathbf{t}^{ab}, \tag{A.9}$$

where $\mathbf{t}^{ab}$ is a one-column matrix formed by $A-1$ constant vectors. If these vectors are chosen in such a way that

$$\mathbf{t}^{ab} = B^{ab}(\beta^a\boldsymbol{\rho}^a + \beta^b\boldsymbol{\rho}^b), \tag{A.10}$$

$$B^{ab} = (\beta^a + \beta^b)^{-1}, \tag{A.11}$$

the product of the basis functions (3) reduces to the form

$$\varphi_a\varphi_b = \exp\left(-\mathbf{r}^+(\beta^a+\beta^b)\mathbf{r} - \mathrm{tr}(\alpha^{ab}K^{ab})\right), \tag{A.12}$$

where we have introduced the notation

$$\alpha^{ab} \equiv \beta^a B^{ab}\beta^b, \tag{A.13}$$
$$K^{ab} \equiv (\boldsymbol{\rho}^a - \boldsymbol{\rho}^b)\cdot(\boldsymbol{\rho}^a - \boldsymbol{\rho}^b)^+.$$

After that, the overlap integral is calculated in the same way as in [1]. We have

$$\langle a|b\rangle = \frac{\pi^{3(N-1)/2}}{(D^{ab})^{3/2}}\exp\left(-\mathrm{tr}(\alpha^{ab}K^{ab})\right), \tag{A.14}$$

where

$$D^{ab} \equiv \det(\beta^a + \beta^b). \tag{A.15}$$

In terms of the variables $\boldsymbol{\rho}_i$, the kinetic-energy operator has the form

$$T = \frac{1}{2}\hbar^{-2}\mathbf{p}^+M\mathbf{p} = \frac{1}{2}\sum_{i,j=1}^{A-1}T_{ij} \tag{A.16}$$
$$= -\frac{1}{2}\sum_{i,j=1}^{A-1}M_{ij}\cdot\boldsymbol{\nabla}_i\cdot\boldsymbol{\nabla}_j,$$

where

$$M_{ij} \equiv \frac{\hbar^2}{m_A} + \frac{\hbar^2\delta_{ij}}{m_i}, \tag{A.17}$$

m_i being the mass of the ith particle.

In the sum for the kinetic energy, the matrix element of the operators T_{ij} can be represented in the form

$$\langle a|T_{ij}|b\rangle = \langle a| - M_{ij}\boldsymbol{\nabla}_i\cdot\boldsymbol{\nabla}_i|b\rangle \tag{A.18}$$
$$= M_{ij}\left(6\alpha_{ij}^{ab} - 4\sum_{kl}\alpha_{ik}^{ab}K_{kl}^{ab}\alpha_{lj}^{ab}\right)\langle a|b\rangle,$$

so that

$$\langle a|T|b\rangle = \langle a|b\rangle\mathrm{tr}\left(3M\alpha^{ab} - 2M\alpha^{ab}K^{ab}\alpha^{ab}\right). \tag{A.19}$$

The matrix element of the potential energy of interaction between the ith and the jth particle ($i \neq A$, $j \neq A$) reduces to the integral

$$\langle a|V_{ij}(|\boldsymbol{\rho}_i - \boldsymbol{\rho}_j|)|b\rangle \tag{A.20}$$
$$= \frac{\langle a|b\rangle}{\sqrt{\pi}\tau_{ij}^{ab}t_{ij}^{ab}}\int_{-\infty}^{\infty} rdrV_{ij}(r)\exp\left(-\frac{(r-t_{ij}^{ab})^2}{(\tau_{ij}^{ab})^2}\right),$$

where

$$\mathbf{t}_{ij}^{ab} \equiv \mathbf{t}_i^{ab} - \mathbf{t}_j^{ab}, \tag{A.21}$$
$$\tau_{ij}^{ab} \equiv \sqrt{B_{ii}^{ab} + B_{jj}^{ab} - 2B_{ij}^{ab}}.$$

This formula and those that follow can be applied to the case of $i = A$ (or $j = A$) as well; for this, it is necessary to set formally $t_A^{ab} = 0$ and $B_{AA}^{ab} = B_{iA}^{ab} = 0$, $i = 1, \ldots, A-1$.

In particular, it is sufficient to calculate the matrix element

$$\left\langle a\left|\frac{1}{|\boldsymbol{\rho}_i - \boldsymbol{\rho}_j|}\right|b\right\rangle = \frac{\langle a|b\rangle}{t_{ij}^{ab}}\mathrm{erf}\left(\frac{t_{ij}^{ab}}{\tau_{ij}^{ab}}\right), \tag{A.22}$$

where $\mathrm{erf}(x) \equiv 2\pi^{-1/2}\int_0^x\exp(-t^2)dt$, for Coulomb interaction and the matrix element

$$\langle a|e^{-\nu_{ij}(\boldsymbol{\rho}_i-\boldsymbol{\rho}_j)^2}|b\rangle \tag{A.23}$$
$$= \frac{\langle a|b\rangle}{(1+\nu_{ij}(\tau_{ij}^{ab})^2)^{3/2}}\exp\left(-\frac{\nu_{ij}(t_{ij}^{ab})^2}{1+\nu_{ij}(\tau_{ij}^{ab})^2}\right)$$

for the Gaussian potential.

REFERENCES

1. N. N. Kolesnikov and V. I. Tarasov, Yad. Fiz. **35**, 609 (1982) [Sov. J. Nucl. Phys. **35**, 354 (1982)].
2. N. N. Kolesnikov, V. I. Tarasov, and M. I. Starosotnikov, Available from VINITI, No. 3832-80 (1980).
3. E. A. Hylleraas, Z. Phys. **54**, 347 (1929).
4. A. G. Donchev, N. N. Kolesnikov, and V. I. Tarasov, Preprint No. 8/2002, MGU (Moscow State University, Moscow, 2002).
5. J. Zs. Mezei, J. Mitroy, R. G. Loves, and K. Varga, Phys. Rev. A **64**, 032501 (2001).
6. D. B. Kinghorn and I. Adomicz, Phys. Rev. Lett. **83**, 2541 (1999).
7. T. K. Rebane and O. N. Yusupov, Zh. Éksp. Teor. Fiz. **98**, 1870 (1990) [Sov. Phys. JETP **71**, 1050 (1990)].

8. A. M. Frolov, Phys. Rev. A **57**, 2436 (1998); A. M. Frolov and V. H. Smith, Jr., J. Phys. B **28**, L449 (1995).
9. A. K. Bhatia, Phys. Rev. A **58**, 2787 (1998).
10. M. Born and J. R. Oppenheimer, Ann. Phys. **84**, 457 (1927).
11. B. Gremaud, D. Dominique, and N. Billy, J. Phys. B **31**, 383 (1998).
12. S. I. Vinitsky and L. I. Ponomarev, Fiz. Élem. Chastits At. Yadra **13**, 1336 (1982).
13. P. P. Zakharov, N. N. Kolesnikov, and V. I. Tarasov, Vestn. Mos. Gos. Univ., Ser. 3: Fiz., Astron., No. 24, 34 (1983).
14. V. I. Kukulin, Izv. Akad. Nauk SSSR, Ser. Fiz. **39**, 535 (1975).
15. A. G. Donchev, N. N. Kolesnikov, and V. I. Tarasov, Yad. Fiz. **63**, 419 (2000) [Phys. At. Nucl. **63**, 353 (2000)].
16. I. N. Filikhin and S. L. Yakovlev, Yad. Fiz. **63**, 409 (2000) [Phys. At. Nucl. **63**, 343 (2000)].
17. S. Ali and A. R. Bodmer, Nucl. Phys. **80**, 99 (1966).
18. N. N. Kolesnikov and V. A. Kopylov, Izv. Vyssh. Uchebn. Zaved., Fiz., No. 5, 36 (1983); N. N. Kolesnikov and V. I. Tarasov, Izv. Vyssh. Uchebn. Zaved., Fiz. **40** (10), 19 (1997).
19. W. A. Chupka and M. E. Rassel, J. Chem. Phys. **49**, 5426 (1968).
20. D. van Pijkeren, J. van Eok, and A. Niehaus, Chem. Phys. Lett. **96**, 20 (1984).
21. A. A. Evett, J. Chem. Phys. **24**, 150 (1956).
22. L. Wolnievicz, J. Chem. Phys. **43**, 1087 (1965).
23. J. D. Stuart and F. A. Motsen, J. Chem. Phys. **41**, 1646 (1964).
24. A. G. Donchev, N. N. Kolesnikov, and V. I. Tarasov, Izv. Akad. Nauk, Ser. Fiz. **66**, 1519 (2002).

Translated by A. Isaakyan

Physics of Atomic Nuclei, Vol. 67, No. 12, 2004, pp. 2166–2168. Translated from Yadernaya Fizika, Vol. 67, No. 12, 2004, pp. 2190–2192.
Original Russian Text Copyright © 2004 by Egorov, Ryabov.

ELEMENTARY PARTICLES AND FIELDS
Experiment

Experimental Upper Limit on Diffractive Dissociation in Muon-Neutrino Interaction with Photoemulsion Nuclei According to Data of the E-128 Experiment (Protvino)

O. K. Egorov* and **V. A. Ryabov**[1)]

Institute of Theoretical and Experimental Physics,
Bol'shaya Cheremushkinskaya ul. 25, Moscow, 117259 Russia

Received October 28, 2003; in final form, January 16, 2004

Abstract—The phenomenon of diffractive dissociation is experimentally estimated for neutrino interaction with photoemulsion nuclei. The results are based on data obtained in the SCIP experiment performed in a neutrino beam at the U-70 accelerator (Protvino). The data sample subjected to analysis included 670 charged-current events corresponding to neutrino interactions in the vertex detector. Events in which the Bjorken variable was $x = 0$–0.1 were selected from this sample. Upon going over to the variable x', which takes into account the nucleon mass, we set an upper limit of 0.53 ± 0.07 on the diffractive-dissociation contribution to the total charged-current cross section. © *2004 MAIK "Nauka/Interperiodica".*

Analyzing electroproduction processes in muon interaction with xenon nuclei (E-665 experiment, FNAL), a group of theorists headed by N.N. Nikolaev noticed that, at some specific values of kinematical variables, the contribution of diffractive-dissociation processes on heavy nuclei could reach half of the total deep-inelastic cross section [1].

An experimental investigation of diffractive dissociation in photoproduction became possible only after commissioning the HERA electron–proton collider. In particular, a comprehensive study of this phenomenon by the H1 and ZEUS Collaborations is presented in [2, 3].

On the basis of data coming from the E-128 experiment (Protvino) [4], we estimated the cross section for diffractive dissociation in muon-neutrino interaction with heavy photoemulsion nuclei. Among 710 events of neutrino–nucleus interactions that occurred on silver and bromine nuclei, 670 events are the ν_μ charged-current events of the reactions

$$\nu_\mu + A \to \mu^- + X,$$

where A is the target nucleus and X is the final hadron state. To reduce the contributions of background processes to the data sample under study, we required that the muon momentum and the neutrino energy satisfy the following cuts [5]:

$$|p_\mu| > 0.5 \text{ GeV}/c, \quad E_\nu > 3.0 \text{ GeV}.$$

The cut imposed on the muon momentum permitted us to remove background neutrino interactions caused by the neutral current, while the cut on the neutrino energy suppressed the neutron background. These selections leave 531 events. The figure shows their distribution with respect to the Bjorken scaling variable

$$x = Q^2/(2M\nu), \tag{1}$$

where Q^2 is the square of the 3-momentum transfer from the lepton vertex to the hadron system, M is the nucleon mass, and ν is the energy transfer to hadrons.

We determined the energy of hadrons in an event as the sum of the energies of all reconstructed hadrons, taking into account not only corrections for the energy of undetected, neutral, and low-energy particles but also corrections for intranuclear energy losses and for actual experimental conditions. To determine the corrections for the undetected energy, we used the results obtained in [6]. The corrections for the energy expended on nuclear excitation were derived from an analysis of the experimentally measured total energy for "evaporated" particles identified according to tagging in the photoemulsion used. Additionally, we introduced a correction for an incomplete angle of coverage of the kinematically allowed region of secondary-particle emission by the tagging track detector. The total correction value was 20% of the energy of recorded hadrons. In the experiment being discussed, Q^2 ranged between 0.2 and 30 GeV$^2/c^2$. The Q^2 distribution of events that survived the above selections was presented in [5].

[1)]Lebedev Physical Institute, Russian Academy of Sciences, Leninskiĭ pr. 53, Moscow, 117924 Russia.
*e-mail: egorov@itep.ru

1063-7788/04/6712-2166$26.00 © 2004 MAIK "Nauka/Interperiodica"

Preliminary results of the E-128 experiment were reported in [7], where the distributions of events with respect to all kinematical variables were constructed for half of the statistics. Even from that study, it was evident that, for half of the events, the Bjorken scaling variable x had values in the range between 0 and 0.1.

In the x distribution shown in the figure, 235 events fall within the range between 0 and 0.1. The ratio $235/531 = 0.44$ sets an upper limit on the ratio of the diffractive-dissociation cross section to the total deep-inelastic cross section of neutrino–nucleus interactions.

In [5], one can find the distribution of 531 events with respect to the variable x',

$$x' = x/(1 + M^2x^2/Q^2),$$

which, in contrast to the Bjorken scaling variable x, takes into account the fact that the proton mass is nonzero. An analysis of the x' distribution reveals that, upon going over from x to x', the number of events in the range 0–0.1 increases to 281, which yields a value of 0.53 ± 0.07 for the ratio of the diffractive-dissociation cross section to the total deep-inelastic cross section for neutrino–nucleus interaction. The uncertainty indicated in this estimate is purely statistical.

The distributions of events with respect to x and x' were also compared for the data obtained with the SKAT bromine-freon chamber [8]. In that case, the transition from x to x' changes the ratio of the diffractive-dissociation cross section to the total deep-inelastic cross section from 0.17 to 0.21. This estimate disregards corrections for a miscount of events at very low values of x'. We note that there is a similar miscount of events in the E-665 experiment (this was indicated in [1]), which also employed a heavy liquid (xenon).

In the E-128 experiment, virtually no cuts were introduced at the stage of formation of the master signal triggering streamer chambers. Any light charged particle having a momentum in excess of 80 MeV/c and escaping from the photoemulsion vertex detector during the passage of the neutrino beam used could actuate the setup. However, this is a rather stringent constraint for neutron events, since protons, which are predominantly produced in neutron–nucleus interactions, have much higher energy losses in our momentum region. As a consequence, the relationship between neutrino and neutron interactions is much more favorable in the E-128 experiment than, for example, in the E-564 experiment (FNAL) [9].

Our estimates of the ratio of the diffractive-dissociation cross sections to the total deep-inelastic cross sections are upper limits on these ratios. They exceed those that were obtained in [10], where the corresponding ratio was 0.29 ± 0.09. This is because we used a lower energy cut on secondary particles recorded in the track detector, while the vertex detectors used, where ν_μ also interacted with nuclei, were similar in the two experiments. Moreover, the spectrum of charged-current ν_μ events that was obtained in our experiment is softer than that in the E-564 experiment [9].

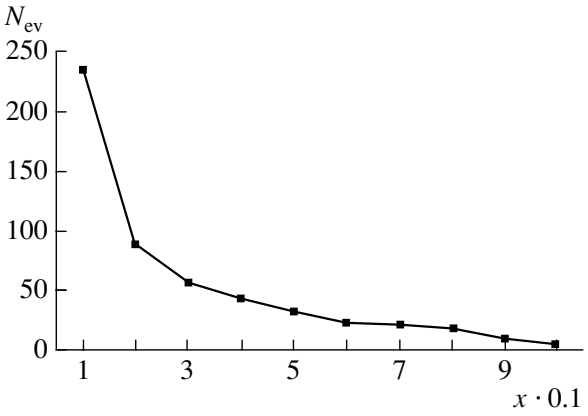

Distribution of events from the E-128 experiment (Protvino) with respect to the Bjorken variable x [the variable x multiplied by 0.1 is plotted along the abscissa (the first point indicates the number of events in the range 0–0.1), and the number of events is plotted along the ordinate].

ACKNOWLEDGMENTS

We are grateful to our colleagues V.V. Ammosov, E.M. Gushchin, A.A. Ivanilov, F.F. Kayumov, A.N. Lebedev, B.N. Lomonosov, V.V. Makeev, L.S. Pervov, P.V. Pitukhin, V.M. Korablev, V.I. Silaev, S.V. Somov, M.K. Timofeev, G.I. Tipografshchik, and I.S. Trostin, who participated in the design and exploitation of the spectrometer in the course of the E-128 experiment. Special thanks are also due to V.R. Zoller, A.B. Kaidalov, and N.N. Nikolaev for stimulating discussions.

REFERENCES

1. N. N. Nikolaev and B. G. Zakharov, Z. Phys. C **49**, 607 (1991); **53**, 331 (1992); N. N. Nikolaev, B. G. Zakharov, and V. R. Zoller, Preprint KFA-IKP(TH) 1994-13 (Julich, 1994); Z. Phys. A **351**, 435 (1995).
2. C. Adloff, S. Aid, M. Anderson, *et al.*, Preprint No. 97-009 (DESY, Hamburg, 1997).
3. J. Breitweg, M. Derrick, D. Krakauer, *et al.*, Phys. Lett. B **421**, 368 (1998).

4. Yu. A. Aleshin, V. V. Ammosov, V. I. Baranov, *et al.,* Prib. Tekh. Éksp., No. 5, 23 (1994).
5. Yu. A. Aleshin, V. V. Ammosov, V. I. Baranov, *et al.,* Zh. Éksp. Teor. Fiz. **109**, 385 (1996) [JETP **83**, 205 (1996)].
6. V. I. Baranov, Yu. A. Batusov, A. A. Bel'kov, *et al.,* Yad. Fiz. **39**, 1425 (1984) [Sov. J. Nucl. Phys. **39**, 900 (1984)].
7. V. A. Ryabov, Preprint No. 29, FIAN (Lebedev Inst. Phys., Russ. Acad. Sci., Moscow, 1992).
8. D. S. Baranov, G. G. Volkov, A. A. Ivanilov, *et al.,* Yad. Fiz. **30**, 146 (1979) [Sov. J. Nucl. Phys. **30**, 75 (1979)].
9. Yu. Batusov, S. Bunyatov, O. Kuznetsov, *et al.*, Z. Phys. C **45**, 557 (1990).
10. O. K. Egorov, Yad. Fiz. **65**, 881 (2002) [Phys. At. Nucl. **65**, 849 (2002)].

Translated by E. Kozlovsky

Physics of Atomic Nuclei, Vol. 67, No. 12, 2004, pp. 2169–2175. Translated from Yadernaya Fizika, Vol. 67, No. 12, 2004, pp. 2193–2199.
Original Russian Text Copyright © 2004 by Vasiliev, Mochalov.

ELEMENTARY PARTICLES AND FIELDS
Experiment

General Features of Single-Spin Asymmetry in Inclusive Pion Production in Fixed-Target Experiments

A. N. Vasiliev and V. V. Mochalov*

Institute for High Energy Physics, Protvino, Moscow oblast, 142980 Russia

Received November 26, 2003

Abstract—The results of various experiments that measured a single-spin asymmetry in inclusive pion production are analyzed in the energy range between 13 and 200 GeV. The experimental fact that the single-spin asymmetry begins increasing at one universal value of the pion energy in the c.m. frame is established.
© *2004 MAIK "Nauka/Interperiodica".*

INTRODUCTION

In the PROZA-M experiment, which was performed at the Institute for High Energy Physics (IHEP, Protvino), the single-spin asymmetry A_N in $\pi^- + p_\uparrow \to \pi^0 + X$ and $\pi^- + d_\uparrow \to \pi^0 + X$ reactions at a beam energy of 40 GeV was measured in the central region for values of the Feynman scaling variable in the range $|x_\mathrm{F}| < 0.15$ [1]. It was found that, at transverse momenta in the region $p_T < 1.6$ GeV/c, the asymmetry in question is compatible with zero, but that, for $p_T > 1.6$ GeV/c, the asymmetry grows linearly in absolute value, reaching -40% at $p_T \approx 2.5$ GeV/c (see Fig. 1, left panel). If the asymmetry is approximated by a linear function, the corresponding straight line intersects the abscissa at a transverse-momentum value of $p_T^0 \approx 1.7$ GeV/c [1]. The asymmetry in $\pi^- + p_\uparrow \to \pi^0 + X$ reactions was also measured in the region of polarized-target fragmentation [2] (see Fig. 1, right panel). It was discovered that, for $-0.8 < x_\mathrm{F} < -0.4$, the asymmetry is significant at p_T values in the range between 1 and 2 GeV/c, but that, at low values of $|x_\mathrm{F}|$ and p_T, the asymmetry is compatible with zero. It turned out that the asymmetry begins growing at a c.m. neutral-pion energy of $E_0^{\mathrm{c.m.}} \approx 1.7$ GeV [2]. In [3], it was found that the asymmetry in $p + p_\uparrow \to \pi^0 + X$ reactions at 70 GeV behaves similarly. Thus, one can assume that the asymmetry does not arise up to a threshold value, whereupon it grows linearly, eventually reaching saturation at some level, if for no other reason than its boundedness (recall that the asymmetry cannot exceed 100%).

On the basis of the aforesaid, the energy dependence of the asymmetry can be described as

$$A_N = \begin{cases} 0 & \text{for } E < E_0, \\ k \cdot (E - E_0) & \text{for } E \geq E_0. \end{cases} \quad (1)$$

where E is the c.m. energy of the product neutral pion and E_0 is the threshold energy. Neutral pions are detected within a rather narrow angle around the beam axis, whence it follows that, in each experiment, the energy dependence of the asymmetry reflects in fact the transverse-momentum (p_T) dependence (an experiment in the central region) or the x_F dependence (an experiment in the region of polarized-target fragmentation). The above saturation can be reached at high values of p_T or x_F, where the experimental errors are rather large, so that these points do not change the result significantly. Since there is no criterion that would make it possible to pinpoint the locus where the asymmetry begins approaching saturation, all of the points were used in the fitting procedure.

For the energy E_0, from which the asymmetry begins growing, a fit on the basis of (1) leads to a value of $E_0^{\mathrm{c.m.}} = 1.67 \pm 0.11$ GeV in the central region and a value of $E_0^{\mathrm{c.m.}} = 1.76 \pm 0.16$ GeV in the region of polarized-target fragmentation. It should be noted that actual experimental errors are somewhat greater since no account was taken of inaccuracies in determining the energy and since integration with respect to the transverse momentum and with respect to x_F is performed for each point. By way of example, we indicate that, at an energy of 200 GeV, a change of 0.01 in the mean value of the variable x_F leads to a change of 0.1 GeV in the position of the cusp.

Thus, we see that, in $\pi^- + p_\uparrow \to \pi^0 + X$ reactions, the asymmetry begins growing at the same value of the c.m. neutral-pion energy in two different kinematical regions. However, this result does not

*e-mail: mochalov@mx.ihep.su

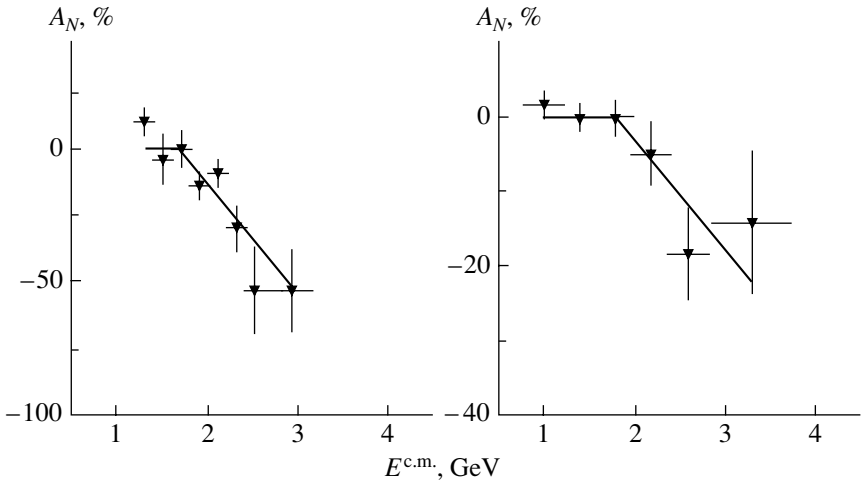

Fig. 1. Asymmetry A_N in $\pi^- + p_\uparrow \to \pi^0 + X$ reactions at a beam energy of 40 GeV as a function of the c.m. neutral-pion energy in (left panel) the central region [1] and (right panel) the target-fragmentation region [2].

provide a solution to the problem of determining the kinematical variable with respect to which the behavior of the asymmetry is universal. The majority of the existing theoretical models consider the asymmetry as a function of x_F or p_T, depending on the kinematical region where the measurements being analyzed were performed.

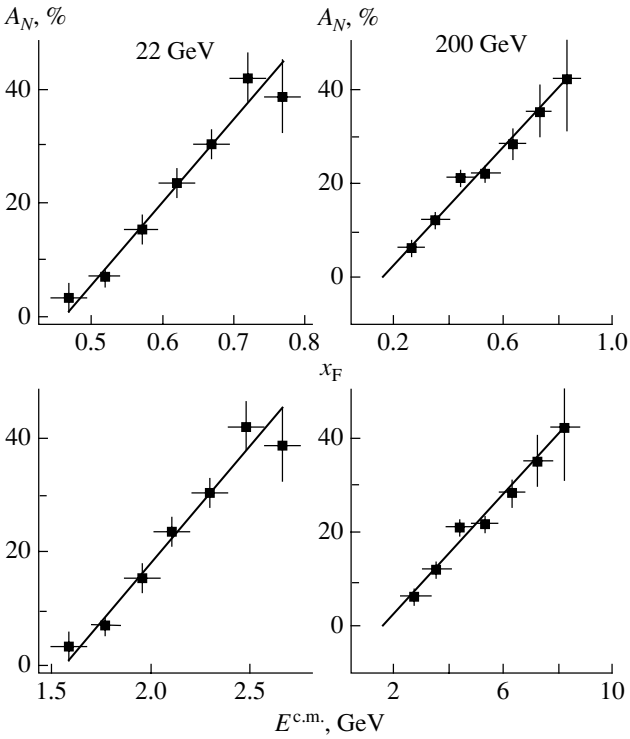

Fig. 2. Single-spin asymmetry A_N as a function of (upper panels) x_F and (lower panels) c.m. energy for the polarized-beam-fragmentation region of $p_\uparrow + p \to \pi^+ + X$ reactions in the (left panels) E925 experiment at 22 GeV [4] and (right panels) E704 experiment at 200 GeV [5].

In the present study, the results obtained by measuring the single-spin asymmetry in inclusive charged- and neutral-pion production in all fixed-target experiments with polarized particles at beam energies between 13 and 200 GeV are analyzed for various kinematical regions subjected to the condition that the transverse momentum p_T is in excess of 0.5 GeV/c.

1. SINGLE-SPIN ASYMMETRIES IN INCLUSIVE PION PRODUCTION

1.1. Single-Spin Asymmetries in the Inclusive Production of Positively Charged Pions

The single-spin asymmetry A_N in the inclusive production of positively charged pions was measured at the Brookhaven National Laboratory (BNL) for beam energies of 13.3, 18.5, and 22 GeV; at IHEP for a beam energy of 40 GeV; and at the Fermi National Accelerator Laboratory (FNAL) for a beam energy of 200 GeV.

For the polarized-beam-fragmentation region of $p_\uparrow + p \to \pi^+ + X$ reactions, we will first analyze the results of two experiments that covered the same region of the kinematical variables p_T and x_F at significantly different beam energies of 22 and 200 GeV (E925 [4] and E704 [5], respectively). In both experiments, the asymmetry in question reaches 40% for $p_T > 0.7$ GeV/c and $x_\mathrm{F} > 0.7$. At the same time, the asymmetry begins growing at markedly different values of the variable x_F. If the experimental data are approximated by formula (1) in terms of the variable x_F, we find that the point at which this occurs is $x_\mathrm{F}^0 =$

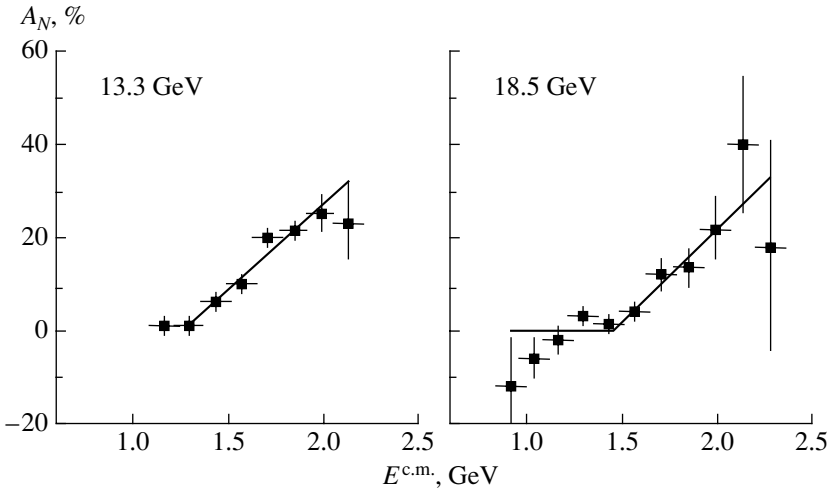

Fig. 3. Single-spin asymmetry A_N as a function of $E^{\text{c.m.}}$ in $p_\uparrow + p \to \pi^+ + X$ reactions at a beam energy of (left panel) 13.3 and (right panel) 18.5 GeV for $x_{\text{F}} \approx 0.2$ [7].

0.46 ± 0.01 in the E925 experiment and $x_{\text{F}}^0 = 0.16 \pm 0.02$ in the E704 experiment (see Fig. 2, upper panels). According to almost all of the existing theoretical models, the asymmetry in the region of polarized-beam fragmentation depends predominantly on x_{F} (see, for example, [6]), but this is at odds with experimental data.

In the Introduction and previously in [2], it was indicated that, in $\pi^- + p_\uparrow \to \pi^0 + X$ reactions, the absolute value of the asymmetry begins growing at the same value of the c.m. neutral-pion energy in two different kinematical regions (specifically, in the region of polarized-particle fragmentation and in the central region at $x_{\text{F}} \approx 0$). For each experiment, we then find the dependence of the asymmetry on the c.m. energy $E^{\text{c.m.}}$ (see Fig. 2, lower panels). The point at which the asymmetry begins growing is $E_0^{\text{c.m.}} = 1.57 \pm 0.04$ GeV for the E925 experiment and $E_0^{\text{c.m.}} = 1.68 \pm 0.22$ GeV for the E704 experiment, these two values being in agreement with each other within the errors. Surprisingly, these results also agree with those that were previously obtained for neutral pions.

For all other experiments, we immediately analyzed the dependence of the asymmetry on the total pion energy in the c.m. frame in terms of the function in (1) (recall that the authors of the original studies examined the asymmetry as a function of the transverse momentum p_T or the Feynman scaling variable x_{F}).

1.1.1.Measurements at BNL for beam energies of 13.3 and 18.5 GeV. In the BNL experiments performed at polarized-proton-beam energies of 13.3 and 18.5 GeV, the asymmetry was studied at $\langle x_{\text{F}} \rangle = 0.2$ as a function of transverse momentum. The respective results, borrowed from [7], are given in Fig. 3. The asymmetry begins growing from the point $E_0^{\text{c.m.}} = 1.26 \pm 0.04$ GeV at 13.3 GeV and from the point $E_0^{\text{c.m.}} = 1.46 \pm 0.08$ GeV at 18.5 GeV.

1.1.2. Measurements at IHEP for 40 GeV. The asymmetry in the inclusive production of positively charged pions was also measured in the FODS experiment (Protvino) [8]. The authors of [8] concluded that, in approximating their data by a straight line, the asymmetry takes zero value at $x_T = 0.37 \pm 0.02$, which, at $x_{\text{F}} \equiv 0$, corresponds to a c.m. energy of $E_0^{\text{c.m.}} = 1.62 \pm 0.10$ GeV ($x_T = 2p_T/\sqrt{s}$). Unfortunately, the values of x_{F} are not given in [8] for each transverse-momentum interval. At the same time, it was indicated there that the mean value of x_{F} changed from 0.02 to 0.1. The value of $x_{\text{F}} = 0.1$ for each longitudinal-momentum interval means the vanishing of the asymmetry at $E_0^{\text{c.m.}} = 1.66$ GeV. To a high precision, we therefore obtain $E_0^{\text{c.m.}} = 1.64 \pm 0.15$ GeV.

1.2. Single-Spin Asymmetries in Inclusive Neutral-Pion Production

The asymmetry in inclusive neutral-pion production was studied at CERN in $pp_\uparrow$ scattering at 24 GeV, at IHEP in $\pi^- + p_\uparrow \to \pi^0 + X$ reactions at 40 GeV and in $p + p_\uparrow \to \pi^0 + X$ reactions at 70 GeV, and at FNAL in $p_\uparrow p$ and $\bar{p}_\uparrow p$ interactions at 200 GeV. The results obtained from an analysis of the asymmetry in $\pi^- + p_\uparrow \to \pi^0 + X$ reactions at 40 GeV are considered below.

1.2.1. Measurements in $p + p_\uparrow \to \pi^0 + X$ reactions. The asymmetry measured in [9] for $p + p_\uparrow \to \pi^0 + X$ reactions at an energy of 24 GeV is displayed

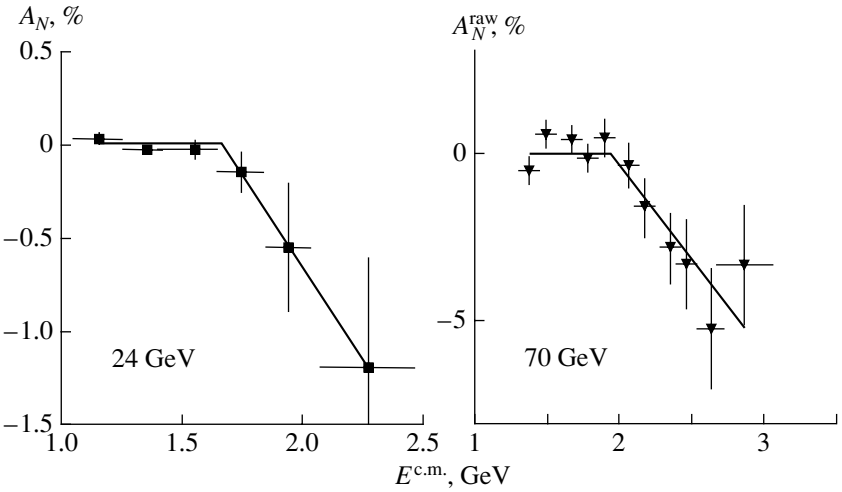

Fig. 4. Single-spin asymmetry A_N in $p + p_\uparrow \to \pi^0 + X$ reactions as a function of $E^{\text{c.m.}}$ in (left panel) the central region at 24 GeV [9] and (right panel) the region of polarized-particle fragmentation at 70 GeV [3].

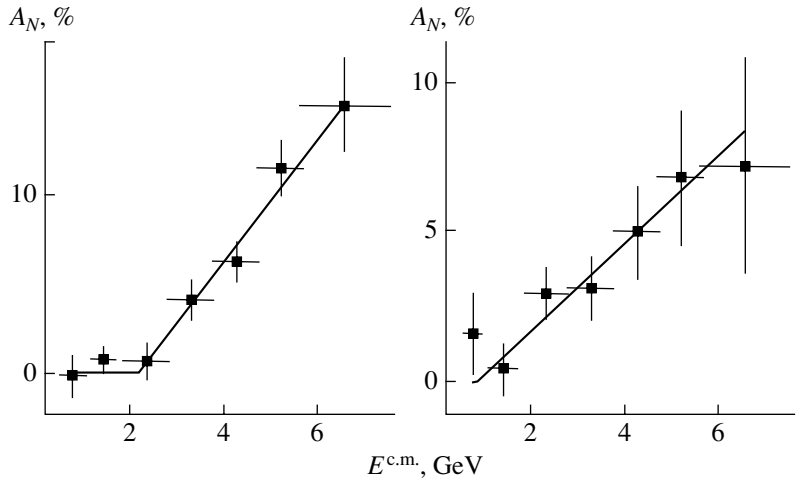

Fig. 5. Single-spin asymmetry A_N for neutral pions from (left panel) $p_\uparrow p$ and (right panel) $\bar{p}_\uparrow p$ interactions at 200 GeV as a function of $E^{\text{c.m.}}$ in the beam-fragmentation region (FNAL) [10].

in Fig. 4 (left panel). The asymmetry in question grows from $E_0^{\text{c.m.}} = 1.70 \pm 0.07$ GeV.

Preliminary experimental results for A_N in $p + p_\uparrow \to \pi^0 + X$ reactions at an energy of 70 GeV were reported in [3]. In the central region, the measured asymmetry is close to zero, whereas, in the target-fragmentation region, the raw asymmetry A_N^{raw} amounted to -3%, which corresponded to a value of -30% for the physically observed asymmetry A_N (see Fig. 4, right panel). The point at which the asymmetry begins growing is $E_0^{\text{c.m.}} = 1.93 \pm 0.12$ GeV.

1.2.2. Measurements in $p_\uparrow(\bar{p}_\uparrow) + p \to \pi^0 + X$ reactions at 200 GeV. The asymmetry A_N in $p_\uparrow(\bar{p}_\uparrow) + p \to \pi^0 + X$ reactions at 200 GeV was measured in the E704 experiment [10] (see Fig. 5). The asymmetry begins growing at $E_0^{\text{c.m.}} = 2.16 \pm 0.26$ GeV in $p_\uparrow + p \to \pi^0 + X$ reactions and at $E_0^{\text{c.m.}} = 0.9 \pm 0.6$ GeV in $\bar{p}_\uparrow + p \to \pi^0 + X$ reactions.

In the central region of $p_\uparrow + p \to \pi^0 + X$ reactions, the asymmetry is compatible with zero over the entire range of the measurements reported in [11].

1.3. Single-Spin Asymmetries in the Inclusive Production of Negatively Charged Pions

Similar investigations were performed for $p_\uparrow + p \to \pi^- + X$ reactions at energies of 22 GeV [4] and 200 GeV [5]. The asymmetry begins growing at $E_0^{\text{c.m.}} = 1.95 \pm 0.02$ GeV in the E925 experiment [4] and at $E_0^{\text{c.m.}} = 2.9 \pm 0.2$ GeV in the E704 experiment [5] (see Fig. 6).

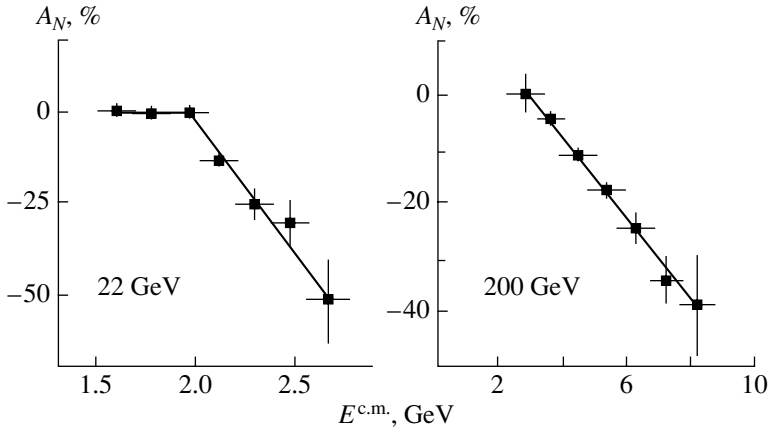

Fig. 6. Single-spin asymmetry A_N as a function of $E^{\text{c.m.}}$ for the target-fragmentation region of $p_\uparrow + p \to \pi^- + X$ reactions at a beam energy of (left panel) 22 GeV [4] or (right panel) 200 GeV [5].

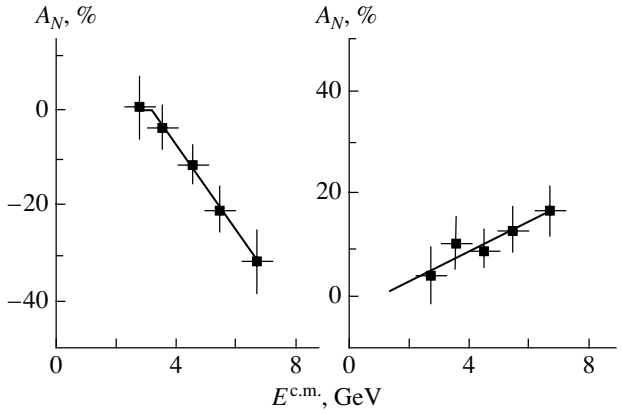

Fig. 7. Single-spin asymmetry A_N for (left panel) positively charged pions and (right panel) negatively charged pions from $\bar{p}_\uparrow p$ interactions at an energy of 200 GeV [12] as a function $E^{\text{c.m.}}$.

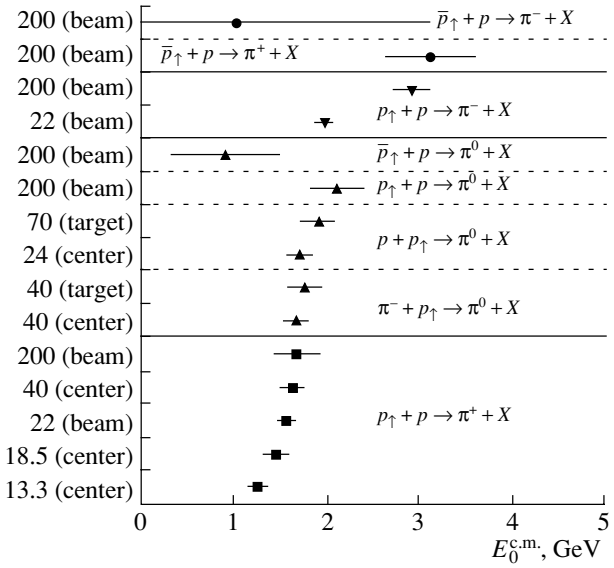

Fig. 8. Points at which there appears an asymmetry: (center) experiments in the central region (at $x_{\text{F}} \approx 0$), (target) experiments in the target-fragmentation region, and (beam) experiments in the beam-fragmentation region. The respective energies are given in GeV.

In all of the experiments performed for beam energies of 13.3 and 18.5 GeV at BNL [7] and 40 GeV at IHEP [8], the asymmetry for negatively charged pions from $p_\uparrow + p \to \pi^- + X$ reactions is compatible with zero in the central region.

1.4. Single-Spin Asymmetries in $\bar{p}_\uparrow + p \to \pi^\pm + X$ Reactions at 200 GeV

The asymmetry A_N in $\bar{p}_\uparrow + p \to \pi^\pm + X$ reactions at 200 GeV is given in Fig. 7. For positively and negatively charged pions, the points at which the asymmetry begins growing are $E_0^{\text{c.m.}} = 3.1 \pm 0.5$ GeV and $E_0^{\text{c.m.}} = 1.0 \pm 2.2$ GeV, respectively; however, the measurement errors are large.

2. DISCUSSION OF THE RESULTS

The entire body of the results discussed above is summarized in the table and in Fig. 8. Both the fitting-procedure uncertainties and the resolution in kinematical variables are taken into account in the errors. Also given in the table are χ^2/N values and the slope of $k \cdot (\sqrt{s} - E_0^{\text{c.m.}})$, this slope characterizing the asymptotic asymmetry at the phase-space boundary if it is still described by a linear function and if there is no saturation. The results of experiments that yielded zero asymmetry are not quoted in the table.

We note that, in the inclusive production of neutral and negatively charged pions in $p_\uparrow p$ interactions, the asymmetry is zero in the central region. This circumstance can be explained as follows. In the beam-fragmentation region, a negatively charged

Compendium of the results for the point $E_0^{\text{c.m.}}$ at which the asymmetry begins growing in various experiments ($E_{\max}^{\text{c.m.}} = \sqrt{s}/2$; for experiments with a polarized target, the asymmetry is taken with the opposite sign)

Reaction	Energy, GeV	$E_0^{\text{c.m.}}$, GeV	χ^2/N	$k \cdot (E_{\max}^{\text{c.m.}} - E_0^{\text{c.m.}})$, %	References
$p_\uparrow + p \to \pi^+ + X$	13.3	1.26 ± 0.1	0.9	52 ± 6	[7]
$p_\uparrow + p \to \pi^+ + X$	18.5	1.46 ± 0.15	0.85	63 ± 16	[7]
$p_\uparrow + p \to \pi^+ + X$	21.92	1.57 ± 0.1	0.9	68 ± 6	[4]
$p_\uparrow + p \to \pi^+ + X$	40	1.64 ± 0.15			[8]
$p_\uparrow + p \to \pi^+ + X$	200	1.68 ± 0.25	1.1	52 ± 5	[5]
$\pi^- + p_\uparrow \to \pi^0 + X$	40	1.67 ± 0.15	1.5	107 ± 26	[1]
$\pi^- + p_\uparrow \to \pi^0 + X$	40	1.76 ± 0.2	0.7	36 ± 14	[2]
$p + p_\uparrow \to \pi^0 + X$	24	1.7 ± 0.15	0.6	334 ± 165	[9]
$p + p_\uparrow \to \pi^0 + X$	70	1.9 ± 0.2	0.85	208 ± 70	[3]
$p_\uparrow + p \to \pi^0 + X$	200	2.1 ± 0.3	0.5	26 ± 5	[10]
$\bar{p}_\uparrow + p \to \pi^0 + X$	200	0.9 ± 0.6	0.5	13 ± 4	[10]
$p_\uparrow + p \to \pi^- + X$	21.92	1.95 ± 0.1	0.5	-87 ± 11	[4]
$p_\uparrow + p \to \pi^- + X$	200	2.9 ± 0.2	<0.1	-51 ± 6	[5]
$\bar{p}_\uparrow + p \to \pi^+ + X$	200	3.1 ± 0.5	<0.1	-59 ± 16	[12]
$\bar{p}_\uparrow + p \to \pi^- + X$	200	1.0 ± 2.2	0.1	25 ± 15	[12]

pion is produced predominantly from a valence d quark, whose polarization direction is assumed to be opposite to the proton and u-quark polarization direction {this follows from $SU(6)$ symmetry and from data on the structure functions for a longitudinally polarized proton—see, for example, [13]}, while, in the central region, the production of a negatively charged pion also proceeds via different channels featuring different polarizations of quarks and gluons. It follows that, in the region of polarized-particle fragmentation, the sign of the asymmetry for a negatively charged pion, which originates from a d quark, is opposite to the sign of the asymmetry for a positively charged pion, which originates from a u quark, whereas, in the central region, the asymmetry for a negatively charged pion is smeared because, in the proton, there are one valence d quark and two valence u quarks. In the case of $\pi^- p_\uparrow$ interaction, a large anisotropy for a neutral pion can arise via the formation of such a pion from the valence $\bar{u}$ antiquark of the incident negatively charged pion and a valence u quark of a polarized proton, the contribution of the valence d quark of the proton at high transverse momenta being significantly suppressed in this case with respect to the contribution mentioned immediately above.

The asymmetry in the inclusive production of positively charged pions begins growing at the same value of $E_0^{\text{c.m.}}$ in the range from about 1.5 to 2.0 GeV. The same behavior is observed for neutral pions. However, this is not so for negatively charged pions. This may be due to the fact that positively charged pions are produced from valence u quarks, whose polarization is coincident with the polarization of the proton involved and whose number is greater than the number of other quarks. Recall that we consider only the data for $p_T > 0.5$ GeV/c. As was indicated above, other channels may contribute to the production of negatively charged pions, the relationship between the channel contributions being in principle dependent on x_R ($x_R = 2E^{\text{c.m.}}/\sqrt{s}$)—that is, not only on the c.m. secondary-particle energy, but also on the total energy $\sqrt{s}$ in the c.m. frame. It follows that, in all cases, the asymmetry for a negatively charged pion in $p_\uparrow p$ interaction begins growing at $E^{\text{c.m.}}$ values greater than those for positively charged pions, and this leads to different values at different energies for the point of the emergence of an asymmetry for negatively charged pions. If the above assumption is valid, the asymmetries for positively and negatively charged pions from $\bar{p}_\uparrow p$ interaction must be interchanged with respect to $p_\uparrow p$ interaction. This is precisely the behavior that is actually observed—the asymmetry for a positively charged pion begins growing at the same value of $E_0^{\text{c.m.}}$ as the asymmetry for a negatively charged pion in $p_\uparrow p$ interaction, and the behavior of the asymmetry

in $\bar{p}_\uparrow + p \to \pi^- + X$ reactions is similar to the behavior of the asymmetry in $p_\uparrow + p \to \pi^+ + X$ reactions.

We also note that, in eight experiments in the region of polarized-particle fragmentation that were devoted to measuring the asymmetry for charged pions, the values of $k \cdot (E_{\max}^{\text{c.m.}} - E_0^{\text{c.m.}})$ were close.

CONCLUSIONS

Data on the single-spin asymmetry in inclusive pion production in fixed-target experiments have been analyzed for beam energies in the range between 13 and 200 GeV. The following experimental fact has been discovered: for a pion that originates from quarks whose number in the hadron involved is greater than the number of quarks belonging to a different sort and whose polarization coincides with the polarization of the hadron, the asymmetry begins growing at the same value of the c.m. pion energy $E_0^{\text{c.m.}}$ and is independent of the primary beam energy.

ACKNOWLEDGMENTS

We are grateful to Yu.A. Matulenko, L.V. Nogach, P.A. Semenov, L.F. Solov'ev, and K.E. Shestermanov for stimulating discussions. We are also indebted to A.M. Zaitsev and V.V. Kiselev for enlightening comments.

This work was supported by the Russian Foundation for Basic Research (project no. 03-02-16919).

REFERENCES

1. N. S. Amaglobeli, V. D. Apokin, Yu. I. Arestov, *et al.,* Yad. Fiz. **50**, 695 (1989) [Sov. J. Nucl. Phys. **50**, 432 (1989)]; V. D. Apokin *et al.*, Phys. Lett. B **243**, 461 (1990).
2. A. N. Vasiliev *et al.,* Preprint No. 2003-21, IFVÉ (Inst. for High Energy Phys., Protvino, 2003); Yad. Fiz. **67**, 1520 (2004).
3. N. I. Belikov *et al.*, Preprint No. 97-51, IHEP (Inst. for High Energy Phys., Protvino, 1997); in *Procedings of the 13th International Symposium on High-Energy Spin Physics (SPIN 98), Protvino, 1998*, p. 465.
4. C. E. Allgower *et al.*, Phys. Rev. D **65**, 092008 (2002).
5. D. L. Adams *et al.*, Phys. Lett. B **264**, 462 (1991).
6. M. Anselmino and F. Murgia, Phys. Lett. B **442**, 470 (1998); hep-ph/9808426.
7. S. Heppelmann *et al.*, in *Proceedings of the 8th International Symposium on High-Energy Spin Physics, Minneapolis, 1988*, Vol. 1, p. 157.
8. V. V. Abramov *et al.*, Preprint No. 96-82, IHEP (Inst. for High Energy Phys., Protvino, 1996); Nucl. Phys. B **492**, 3 (1997); hep-ex/0110011.
9. J. Antille *et al.*, Phys. Lett. B **94B**, 523 (1980).
10. D. L. Adams *et al.*, Preprint No. 91-014-E, Fermilab (1991); Preprint No. 91-50, IHEP (Inst. for High Energy Phys., Protvino, 1991); Phys. Lett. B **276**, 531 (1992).
11. D. L. Adams *et al.*, Preprint No. 91-49, IHEP (Inst. for High Energy Phys., Protvino, 1991); Z. Phys. C **56**, 181 (1992).
12. A. Bravar *et al.*, Phys. Rev. D **55**, 1159 (1997).
13. D. Adams *et al.* (Spin Muon Collab.), CERN-PPE-97-022; CERN-PPE-97-22; DAPNIA-SPHN-97-27; Phys. Rev. D **56**, 5330 (1997); hep-ex/9702005.

Translated by A. Isaakyan

Physics of Atomic Nuclei, Vol. 67, No. 12, 2004, pp. 2176–2182. Translated from Yadernaya Fizika, Vol. 67, No. 12, 2004, pp. 2200–2206.
Original Russian Text Copyright © 2004 by Podorozhnyi, Rapoport, Turundaevsky.

ELEMENTARY PARTICLES AND FIELDS
Experiment

Properties of Backscattered Particles Produced by Protons of Energy above 1 TeV in an Iron Absorber

D. M. Podorozhnyi, I. D. Rapoport, and A. N. Turundaevsky*

Institute of Nuclear Physics, Moscow State University, Vorob'evy gory, Moscow, 119899 Russia
Received July 11, 2003; in final form, October 21, 2003

Abstract—Backscattered-particle production is studied by means of a detailed simulation of cascade processes in a dense medium. The energy dependence of the albedo and the spatial and angular distributions of various components of this flux are analyzed. © *2004 MAIK "Nauka/Interperiodica".*

Investigation of cosmic rays makes it possible to obtain data that are of importance for understanding processes of the production, acceleration, and propagation of charged particles in the Galaxy. In such studies, it is desirable to derive detailed information both about the energy distribution of cosmic rays and about their chemical composition. In view of this, recording arrays traditionally involve two main parts, an energy spectrometer and a charge detector.

The ionization-calorimeter method [1], which is based on recording hadronic showers in an absorbing medium, is the most popular method of energy measurements for cosmic-ray particles in the region of high energies (above 1 TeV). Since the absorber mass is quite large, thin ionization calorimeters have come into use, in which case only part of a shower initiated by the primary particle is recorded in a limited absorber volume [2]. Physical processes in showers are described by means of a mathematical simulation based on various codes (GEANT [3] among them).

Some secondary particles of the recorded shower are inevitably scattered outside the calorimeter in various directions, including the arrival direction of incoming primary particles. The flux of backscattered particles is referred to as the albedo. Investigation of the properties and the magnitude of the albedo is of paramount importance, since albedo particles can generate spurious signals in charge detectors intended for recording primary particles. These signals can distort the results of measurements considerably [4, 5]. In developing equipment, it is necessary to take into account special features of the detector response and the detector sensitivity to various particles. The problems of charge-detector optimization were considered in the proposal of the new experiment described in [6].

As a rule, detectors recording particle ionization losses or Cherenkov light are used to determine charges. Therefore, the distortion caused by albedo particles is the greatest in recording protons and He nuclei. The features of backscattered particles in calorimeter facilities were studied by means of a mathematical simulation of showers in an iron absorber of total thickness 90 cm that were initiated by 0.5-, 2-, 8-, and 32-TeV protons. The arrival direction of incident particles was assumed to be orthogonal to the absorber, and secondary particles escaping through the top surface of the absorber were recorded. These conditions are the most stringent for recording protons [7].

In our simulation, we relied on the GEANT 3.21 code [3], describing high-energy and low-energy hadron interactions (up to 50 GeV) on the basis of the QGSJET [8, 9] and FLUKA [3] generators, respectively. The backscattered-particle flux receives contributions both from the interactions of a high-energy primary particle and from the interactions of secondary particles, which have relatively low energies. In inelastic interactions, some product particles travel in the direction opposite to the incident-particle momentum. As a rule, the intranuclear cascade is taken into account in order to describe adequately particle production in the target-fragmentation region [10, 11]. In a number of studies [8, 9, 12], the applicability of the models for describing hadron interactions was confirmed through a comparison with experimental data. In particular, the model was found to agree with experimental data on the emission of low-energy protons from a nucleus [12]. Hence, the emission of neutrons is also described adequately. One can therefore expect that a simulation of the neutron component within the above models will provide results close to their experimental counterparts. The energy dependence of the inelastic-interaction cross sections and of the multiplicity of

*e-mail: ant1@fromru.com

1063-7788/04/6712-2176$26.00 © 2004 MAIK "Nauka/Interperiodica"

Table 1. Mean multiplicities of backscattered particles

E, TeV	γ	e^+e^-	n	$\pi^+\pi^-$
0.5	43.8 ± 2.9	1.2 ± 0.10	178.9 ± 5.7	0.5 ± 0.05
2.0	76.0 ± 4.9	1.8 ± 0.16	411.8 ± 12.7	0.8 ± 0.07
8.0	174.0 ± 11.5	4.1 ± 0.29	1032.6 ± 32.7	1.6 ± 0.14
32.0	406.3 ± 30.2	10.5 ± 1.7	2597.3 ± 84.8	3.2 ± 0.21

Table 2. Mean distances of backscattered particles to the shower axis (in cm)

E, TeV	γ	e^+e^-	n	$\pi^+\pi^-$
0.5	11.16 ± 0.07	10.38 ± 0.45	23.46 ± 0.05	6.27 ± 0.40
2.0	12.18 ± 0.06	10.99 ± 0.39	24.35 ± 0.03	8.16 ± 0.44
8.0	12.66 ± 0.04	11.55 ± 0.27	24.83 ± 0.02	7.77 ± 0.30
32.0	12.76 ± 0.03	10.33 ± 0.18	25.20 ± 0.01	8.46 ± 0.21

secondary particles within the QGSJET model is in agreement with experimental data from experiments with colliding beams [9, 13]. This gives sufficient grounds for employing the model in the region of high energies. The problem of the dependence on the choice of model in describing the initial part of the hadronic shower—the backscattered-particle flux, in particular—was studied in [14]. It appeared that different models yield close results in simulating a shower near the point of the first inelastic interaction; therefore, the model dependence of the description of the backscattered-particle flux must be insignificant.

Our simulation permitted us to estimate various components of the backscattered-particle flux, including photons, electrons and positrons, neutrons, and charged pions. Various approaches can be used to analyze these data. On one hand, the backscattered-particle flux can be separated into an electromagnetic and a nuclear component. On the other hand, it is reasonable at the preparatory stage of experiments to consider individually all backscattered charged particles that initiate a pulse in a charge detector. Both approaches are used in our study. It should be noted that there are very few charged pions in the backscattered-particle flux. Therefore, only their mean properties can be assessed.

The resulting mean multiplicities of backscattered particles are given in Table 1. These data reveal a strong energy dependence of the multiplicity for all types of backscattered particles. The number of backscattered electrons is small because of high ionization losses. The yield of backscattered photons and the backscattered-neutron flux are detectable, the latter increasing fast with incident-particle energy. We note that neutron interactions can distort substantially the results of measurements performed with detectors of thickness above a few g/cm^2 units, but the probability of errors in charge measurements because of neutron interactions is low for finely segmented detectors [15].

The lateral distribution of various backscattered particles is of special interest. The lateral density dN/dS of various backscattered particles versus the distance to the shower axis is shown in Fig. 1 at the top surface of the absorber. The lateral distribution of neutrons is wider than that of the electromagnetic component. One can also trace this effect in Table 2, which gives the mean distances from the tracks of various backscattered particles to the shower axis at the surface of the absorber top. Neutral pions from hadron interactions in the initial part of the shower make the main contribution to the electromagnetic component because of a strong absorption of other particles. At the same time, neutrons emitted at the maximum of the shower can reach the top surface of the absorber.

The angular distribution of backscattered particles is nearly isotropic in the production regions, but there arises anisotropy at the top surface of the absorber, because some components are absorbed. This effect is especially typical of charged pions. Figure 2 displays the $\cos^2\theta$ distributions, where θ is the angle between the particle track and the normal to the absorber. Table 3 gives the mean cosines of backscattered-particle emission angles, $\langle\cos\theta\rangle$. For the strictly isotropic emission of particles into the upper hemisphere, we have $dN/d\cos^2\theta = \text{const}$ and $\langle\cos\theta\rangle = 2/3$.

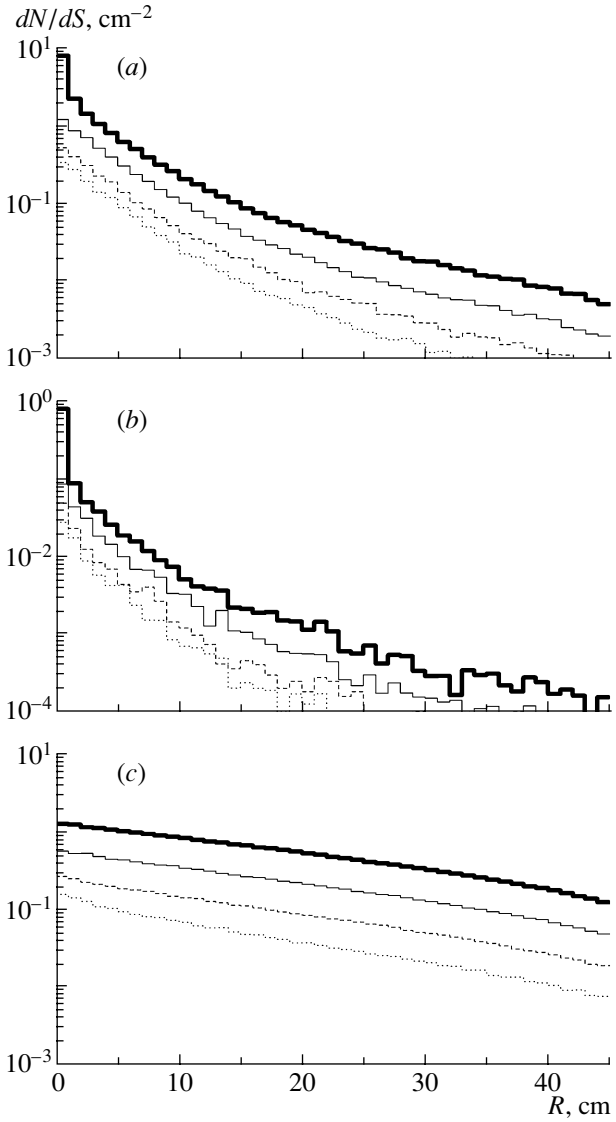

Fig. 1. Lateral distributions of (*a*) backscattered photons, (*b*) all backscattered charged particles, and (*c*) backscattered neutrons at incident-proton energies of (dotted-line histogram) 0.5, (dashed-line histogram) 2, (thin-solid-line histogram) 8, and (thick-solid-line histogram) 32 TeV.

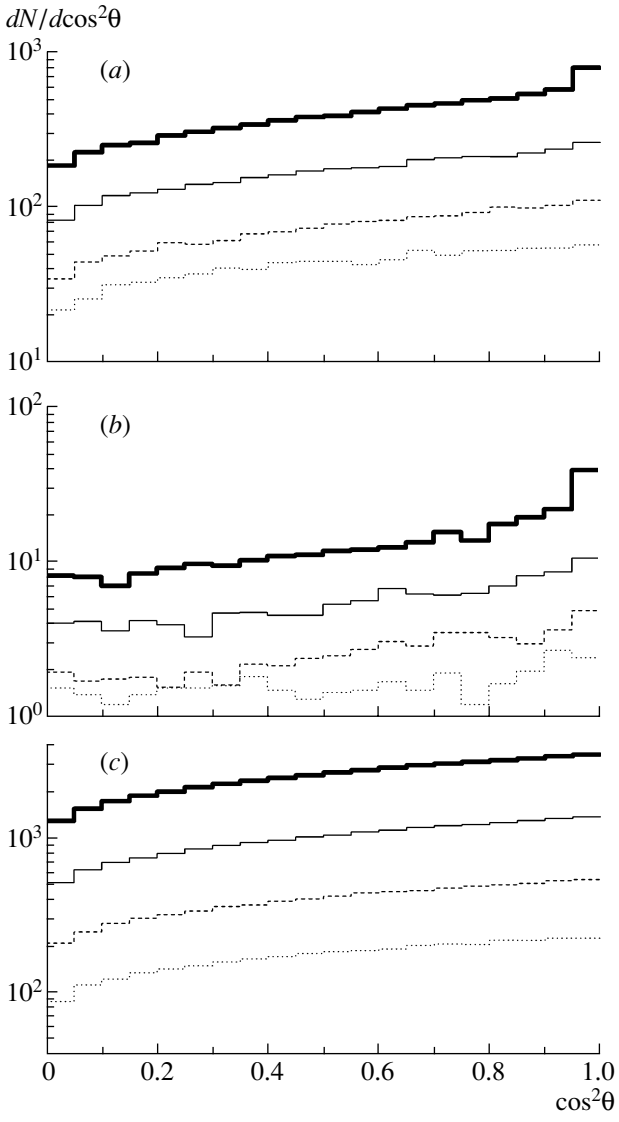

Fig. 2. Angular distributions of backscattered particles for various incident-proton energies. The notation is identical to that in Fig. 1.

Figure 3 shows the energy distributions of backscattered particles. The energies of the main fraction of the particles lie in the region of a few MeV, but the distribution extends to a few GeV. With increasing incident-particle energy, the flux of low-energy neutrons from the hadronic-shower maximum increases by and large, while the mean kinetic energy of backscattered neutrons decreases concurrently. The mean kinetic energies of backscattered particles are given in Table 4. We note relatively high energies of backscattered charged pions produced in hadron–nucleus interactions.

Since the shower maximum occurs at a depth not exceeding some 30 cm in an iron absorber for the energies being considered, the backscattered-particle flux can be suppressed by a time cutoff if the actuation time is bounded by a value not greater than some 10 ns. In this case, one rejects neutrons of kinetic energy up to about 5 MeV.

The number of backscattered particles fluctuates widely. Figure 4 shows the corresponding distributions, which indicate that there can occur events where the backscattered-particle yield exceeds the mean values considerably (Table 1).

There is a correlation between the fluxes of different components of the backscattered-particle flux. Figure 5 shows the numbers of electrons and positrons, neutrons, and all charged particles versus the

Table 3. Mean cosines of the backscattered-particle emission angles, $\langle\cos\theta\rangle$

E, TeV	γ	e^+e^-	n	$\pi^+\pi^-$
0.5	0.7194 ± 0.0016	0.6786 ± 0.0109	0.7191 ± 0.0008	0.7433 ± 0.0151
2.0	0.7317 ± 0.0012	0.7104 ± 0.0086	0.7217 ± 0.0005	0.7768 ± 0.0112
8.0	0.7289 ± 0.0008	0.7061 ± 0.0059	0.7231 ± 0.0003	0.7910 ± 0.0078
32.0	0.7409 ± 0.0005	0.7406 ± 0.0036	0.7243 ± 0.0002	0.8010 ± 0.0051

Table 4. Mean kinetic energies of backscattered particles (in MeV)

E, TeV	γ	e^+e^-	n	$\pi^+\pi^-$
0.5	2.87 ± 0.08	14.04 ± 1.45	3.15 ± 0.04	193 ± 13
2.0	2.87 ± 0.07	14.42 ± 1.02	2.81 ± 0.03	312 ± 63
8.0	2.90 ± 0.07	15.73 ± 0.89	2.65 ± 0.02	620 ± 191
32.0	3.44 ± 0.08	26.41 ± 1.39	2.48 ± 0.01	513 ± 82

Table 5. Parameters in the approximation of the number of backscattered particles as a function of the depth of the first inelastic interaction: $N(X_{\text{int}}) = N_0\exp(-X_{\text{int}}/L_{\text{abs}})$, where N_0 is the albedo for the interaction at the top surface of the absorber, L_{abs} is the absorption, and χ^2/ν characterizes the quality of the approximation

E, TeV	N_0	L_{abs}, g/cm^2	χ^2/ν	N_0	L_{abs}, g/cm^2	χ^2/ν
	γ			e^+e^-		
0.5	118 ± 4	54 ± 3	1.8	4.1 ± 0.3	36 ± 4	1.2
2.0	223 ± 8	56 ± 2	2.2	5.7 ± 0.4	47 ± 4	1.2
8.0	384 ± 12	67 ± 3	3.6	11.0 ± 0.6	57 ± 4	0.7
32.0	839 ± 26	64 ± 3	2.3	18.8 ± 1.1	62 ± 5	0.9
	n			All charged particles		
0.5	303 ± 6	153 ± 8	0.8	5.6 ± 0.4	41 ± 5	0.8
2.0	727 ± 15	154 ± 7	2.5	8.7 ± 0.6	51 ± 4	0.6
8.0	1748 ± 35	162 ± 8	1.0	15.6 ± 0.8	59 ± 4	0.6
32.0	4397 ± 87	150 ± 7	1.0	34.3 ± 2.0	55 ± 4	0.5

number of photons. Within the statistical uncertainties, the dependence $\bar{N}_e(\bar{N}_\gamma)$ is unified for the electromagnetic component at different incident-proton energies. However, the neutron flux increases faster with increasing incident-particle energy than the photon and electron fluxes. This effect is explained by a long range of neutrons in matter, whereby a considerable portion of the hadronic shower contributes to the backscattered-particle flux, whereas the electromagnetic component is absorbed substantially. The corresponding correlation dependence for all charged particles differs only slightly from the electron curve because of a small flux of charged pions.

The dependences of the numbers of backscattered particles on the depth of the first inelastic interactions

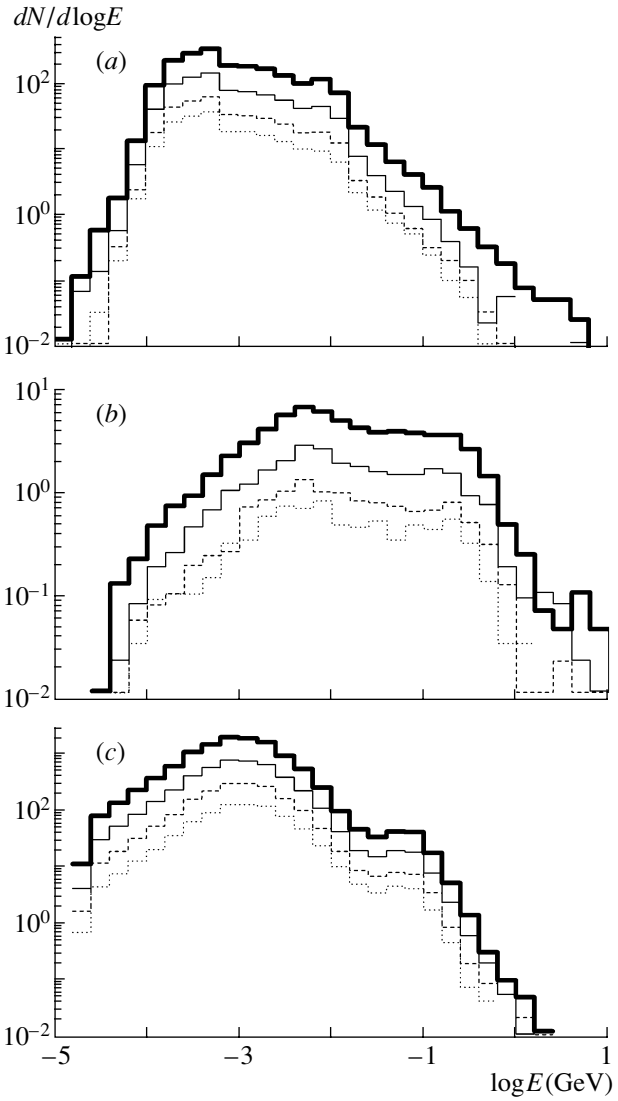

Fig. 3. Energy distributions of backscattered particles at various incident-proton energies. The notation is identical to that in Fig. 1.

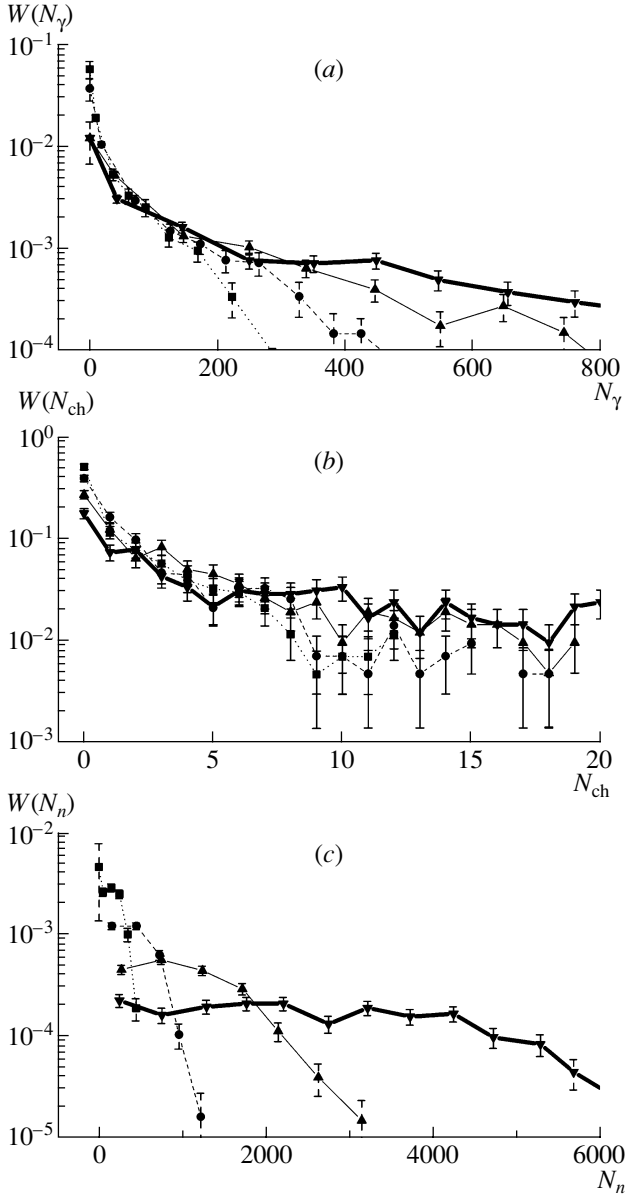

Fig. 4. Distributions versus the number of (*a*) backscattered photons, (*b*) all backscattered charged particles, and (*c*) backscattered neutrons for incident-proton energies of (■ and dotted curve) 0.5, (● and dashed curve) 2, (▲ and thin solid curve) 8, and (▼ and thick solid curve) 32 TeV.

have a shape that is also determined by the absorption length of the corresponding component. Figure 6 shows these dependences for photons, all charged particles, and neutrons. It is evident that the dependence in question is noticeably less pronounced for neutrons than for the electromagnetic component. In the case of the exponential approximation $N(X_{\rm int}) = N_0\exp(-X_{\rm int}/L_{\rm abs})$, the absorption lengths for the electromagnetic component are substantially shorter than the absorption length for neutrons. The numerical values of the adjustable parameters N_0 and $L_{\rm abs}$ are given in Table 5 for the various components along with the corresponding χ^2 values per degree of freedom. Rather large values of χ^2/ν indicate that backscattered-particle absorption deviates from a strictly exponential behavior. This can be explained by the dependence of the absorption length on the backscattered-particle energy. We note that the $L_{\rm abs}$ values for the electron–positron component are compatible with the value obtained for the backscattered-particle flux in the Sokol-2 experiment [7].

The above analysis permits us to single out the main features of the backscattered-particle flux from hadronic showers. Neutrons of energy between 0.1 MeV and 1 GeV constitute a considerable fraction of the backscattered-particle flux. The simulation

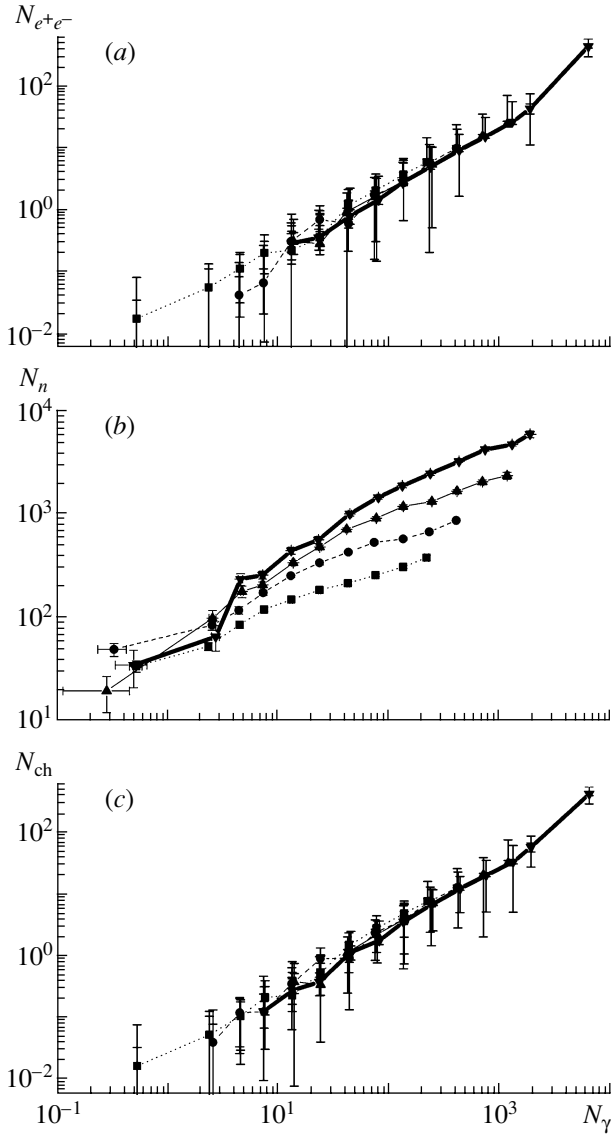

Fig. 5. Numbers of (*a*) electrons and positrons, (*b*) neutrons, and (*c*) all charged particles in the albedo versus the number of photons at various incident-proton energies. The notation is identical to that in Fig. 4.

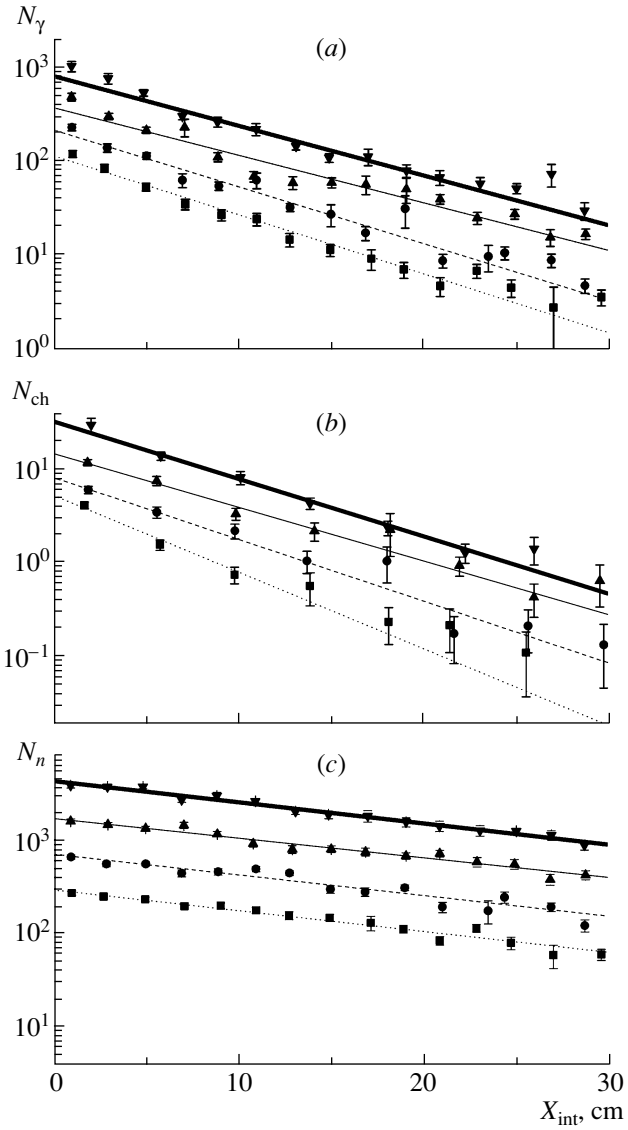

Fig. 6. Number of (*a*) backscattered photons, (*b*) all backscattered charged particles, and (*c*) backscattered neutrons versus the depth of the first inelastic interaction for (■ and dotted curve) 0.5, (● and dashed curve) 2, (▲ and thin solid curve) 8, and (▼ and thick solid curve) 32 TeV (at all energy values, the curves represent the results of an exponential approximation).

has demonstrated a substantial energy dependence of the backscattered-particle flux. A comparison of the lateral distributions of the electron–photon and neutron components of the backscattered-particle flux shows that the electromagnetic component originates predominantly from the initial part of the hadronic shower, while the bulk of neutrons come from the shower maximum. The above data on the properties of the backscattered-particle flux can be used to optimize charge detectors for new experiments.

ACKNOWLEDGMENTS

This work was supported by the Russian Foundation for Basic Research (project no. 03-02-16272).

REFERENCES

1. N. L. Grigorov, V. S. Murzin, and I. D. Rapoport, Zh. Éksp. Teor. Fiz. **34**, 506 (1958) [Sov. Phys. JETP **7**, 348 (1958)].
2. I. P. Ivanenko, D. M. Podorozhnyi, I. D. Rapoport, *et al., Cascade Theory of Showers* (MGU, Moscow, 1996) [in Russian], p. 102.

3. *GEANT User's Guide,* CERN DD/EE/83/1 (Geneva, 1983).
4. R. W. Ellsworth, J. A. Goodman, A. Ito, *et al.*, Nucl. Instrum. Methods **203**, 167 (1982).
5. V. I. Zatsepin, J. H. Adams, H. S. Ahn, *et al.*, in *Proceedings of the 28th ICRC, Tsukuba, Japan*, 2003, p. 1861.
6. A. N. Turundaevsky, D. M. Podorozhnyi, E. B. Postnikov, *et al.*, in *Proceedings of the 28th ICRC, Tsukuba, Japan*, 2003, p. 2213.
7. V. Ya. Shestoperov, I. D. Rapoport, Yu. V. Basina, *et al.,* Yad. Fiz. **57**, 858 (1994) [Phys. At. Nucl. **57**, 804 (1994)].
8. N. N. Kalmykov and S. S. Ostapchenko, Preprint No. 98-36/537, NIIYaF MGU (Inst. Nucl. Phys., Moscow State Univ., Moscow, 1998).
9. N. N. Kalmykov, S. S. Ostapchenko, and A. I. Pavlov, Nucl. Phys. B (Proc. Suppl.) **52**, 17 (1997).
10. J. Ranft, Preprint SSC-143 (1987).
11. N. S. Amelin, K. K. Gudima, S. Yu. Sivoklokov, and V. D. Toneev, Yad. Fiz. **52**, 272 (1990) [Sov. J. Nucl. Phys. **52**, 172 (1990)].
12. I. D. Rapoport, A. N. Turundaevsky, and V. Ya. Shestoperov, Yad. Fiz. **65**, 176 (2002) [Phys. At. Nucl. **65**, 170 (2002)].
13. J. Knapp, D. Heck, and G. Schatz, Preprint No. 5828, FZKA (Institut für Kernphysik, Karlsruhe, 1996).
14. I. D. Rapoport, A. N. Turundaevsky, V. Ya. Shestoperov, and I. V. Yashin, Yad. Fiz. **62,** 1026 (1999) [Phys. At. Nucl. **62,** 959 (1999)].
15. J. H. Adams, Jr., G. L. Bashindzhagyan, V. I. Zatsepin, *et al.,* Prib. Tekh. Éksp., No. 4, 38 (2001).

Translated by E. Kozlovsky

Physics of Atomic Nuclei, Vol. 67, No. 12, 2004, pp. 2183–2187. Translated from Yadernaya Fizika, Vol. 67, No. 12, 2004, pp. 2207–2211.
Original Russian Text Copyright © 2004 by Bazarov, Glagolev, Gulamov, Lugovoy, Lutpullaev, Olimov, Turumov, A. Yuldashev, B. Yuldashev.

ELEMENTARY PARTICLES AND FIELDS
Experiment

Contribution of Excited Nuclei $^{12}C^*$ to the Channel of Three-Alpha-Particle Production in ^{16}Op Collisions at a Momentum of 3.25 GeV/c per Nucleon

E. Kh. Bazarov, V. V. Glagolev[1)], K. G. Gulamov, V. V. Lugovoy, S. L. Lutpullaev, K. Olimov[*], E. Turumov, A. A. Yuldashev, and B. S. Yuldashev[2)]

Institute for Physics and Technology, Fizika–Solntse Research and Production Association, Uzbek Academy of Sciences, ul. G. Mavlyanova 2b, Tashkent, 700084 Republic of Uzbekistan

Received March 20, 2003; in final form, December 5, 2003

Abstract—A phenomenological analysis of the channel involving the production of three alpha particles in collisions of relativistic oxygen nuclei with protons is performed for the first time. It is shown that one-third of it is saturated by the decay of an excited nucleus $^{12}C^*$, while the remaining part is due to direct Fermi breakup or the quasielastic knockout of one alpha-particle cluster from a loosely bound residual nucleus consisting of three alpha particles. The results obtained by simulating the decay of the excited system involving three alpha particles for an isotropic phase space describe experimental data satisfactorily at moderate values of the excitation energy ($\Delta E^* < 15$ MeV). © *2004 MAIK "Nauka/Interperiodica".*

From a comparative analysis of the channels involving the production of three alpha particles and ^{12}C nuclei in ^{16}Op collisions at a momentum of 3.25 GeV/c per nucleon, it was deduced [1] that the mean multiplicities and the mean momentum features of secondary fragments and charged particles produced in these two channels agree within the statistical uncertainties. Also, it was found that the yield cross sections for these channels are very close. All of this indicates that the two channels in question are realized under similar physical conditions. On the basis of a comparison of the results reported in [1] with the predictions of the cascade–fragmentation–evaporation model [2], which treats a nucleus as a perfect Fermi gas, it was concluded that the alpha-cluster structure of the ^{16}O nucleus plays an important role in the fragmentation of this nucleus.

The present study is a continuation of that which was reported in [1]; it is based on the same set of experimental data and is devoted to a further analysis of the channel involving the production of three alpha particles in the reaction

$$^{16}O + p \to 3\alpha + X, \qquad (1)$$

where X may be a singly or a doubly charged fragment of mass number in the region $A \leq 3$. In addition, charged pions and a recoil proton may also be present here unless the latter has suffered inelastic charge-exchange transformation into a neutron and a positively charged pion. The experimental-data set in question was obtained with the aid of a 1-m hydrogen bubble chamber exposed to a beam of oxygen nuclei accelerated to a momentum of 3.25 GeV/c per nucleon at the synchrophasotron of the Laboratory of High Energies at the Joint Institute for Nuclear Research (JINR, Dubna) and is based on an analysis of more than 11 000 inelastic ^{16}Op interactions. We note that the use of a hydrogen bubble chamber in a magnetic field proved to be a highly efficient method for analyzing many features of fragmentation under conditions of 4π coverage and makes it possible to separate light fragments in mass with a high reliability. The procedure used to identify charged secondaries and fragments of oxygen nuclei was described in [1, 3, 4]. Just as in [1], we consider here fragments for which the length of the track measured over the fiducial volume of the chamber satisfies the condition $L > 35$ cm, this being necessary for a reliable mass identification of the fragments.

The objective of the present study was to establish the origin of alpha-particle production in reaction (1). If the ^{16}O nucleus does indeed possess an alpha-cluster structure, the primary interaction event is that of target-proton interaction with one of the alpha-particle clusters (or with its nucleon). Depending on the excitation energy acquired in this interaction by the residual nucleus of mass number $A = 12$, it either

[1)]Joint Institute for Nuclear Research, Dubna, Moscow oblast, 141980 Russia.
[2)]Institute of Nuclear Physics, Uzbek Academy of Sciences, pos. Ulughbek, Tashkent, 702132 Republic of Uzbekistan.
[*]E-mail: olimov@uzsci.net

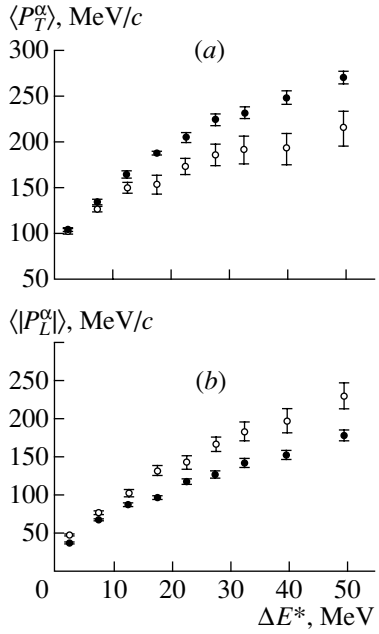

Fig. 1. (*a*) Mean transverse momentum and (*b*) mean absolute value of the longitudinal momentum of alpha particles versus the excitation energy ΔE^*: (open circles) experimental data and (closed circles) results of a Monte Carlo simulation.

survives as ^{12}C or breaks up into three alpha particles. However, it is not clear whether the three alpha particles in reaction (1) are products of the decay of an excited residual having quantum numbers of three alpha particles (that is, ^{12}C*) or whether each of them originated from the prompt multifragment breakup of the oxygen nucleus ^{16}O, bypassing the formation of an excited nucleus ^{12}C*. Since either mechanism of alpha-particle production is possible, there arises the problem of assessing the fractions of alpha particles generated by the two mechanisms in question. In order to clarify relevant questions, we performed a Monte Carlo simulation of the formation of three alpha particles in reaction (1), relying on the isotropic-phase-space model (see Appendix). It was assumed that, in the rest frame of the excited nucleus ^{12}C*, its prompt decay $^{12}\mathrm{C}^* \to 3\alpha$ and the cascade decay $^{12}\mathrm{C}^* \to {}^8\mathrm{Be}^* + \alpha \to 3\alpha$ are isotropic. Thus, our calculation takes into account the following two channels of the decay of the ^{12}C* nucleus:

$$^{16}\mathrm{O} + p \to {}^{12}\mathrm{C}^* + X \to 3\alpha + X \qquad (2)$$
$$\text{with a probability of } W = 0.4,$$

$$^{16}\mathrm{O} + p \to {}^{12}\mathrm{C}^* + X \to {}^8\mathrm{Be}^* + \alpha + X \qquad (3)$$
$$\to 3\alpha + X \text{ with a probability of } W = 0.6.$$

In reaction (3), the decay of the unstable nucleus ^{8}Be* into two alpha particles was generated with a probability of $W(0^+) = 0.67$ for the ground state ($J^P = 0^+$) at an energy of $\Delta E^* = 0.1$ MeV and with a probability of $W(2^+) = 0.33$ for the first excited state ($J^P = 2^+$) at an energy of $\Delta E^* = 3.04$ MeV [5]. In order to determine the fractions of the prompt and cascade channels of the decay of the ^{12}C* nucleus and the probabilities $W(0^+)$ and $W(2^+)$ of the decays of the unstable nucleus ^{8}Be* into two alpha particles, the distribution of the angle $\Delta\vartheta_{\alpha\alpha}$ between the momenta of two alpha particles in reaction (1) was analyzed by the method developed in [6].

Figure 1*a* shows the experimental and calculated values of the mean transverse momentum of alpha particles $\langle P_T^\alpha \rangle$ versus the excitation energy ΔE^* defined as

$$\Delta E^* = M_{3\alpha} - 3M_\alpha,$$

where $M_{3\alpha}$ is the invariant mass of three alpha particles, while $3M_\alpha$ is their total mass.

The experimental mean transverse momentum $\langle P_T^\alpha \rangle$ as a function of ΔE^* grows linearly at low excitation energies ($\Delta E^* < 15$ MeV); however, the rate of its growth decreases in the energy region $\Delta E^* > 15$ MeV. It is likely to suggest that, in the region $\Delta E^* > 15$ MeV, there occurs either a quasielastic knockout of one alpha-particle cluster from a loosely bound residual nucleus consisting of three alpha-particle clusters or a prompt decay of the residual nucleus into three alpha particles, with the result that the formation of an excited nucleus ^{12}C* becomes impossible. These are the circumstances that lead to weak correlations between $\langle P_T^\alpha \rangle$ and ΔE^*.

The dependence of $\langle P_T^\alpha \rangle$ on ΔE^* is stronger in the theoretical Monte Carlo calculation than in the experimental data; that is, the experimental results show a deviation from an isotropic decay of the system, and this can be due to a simultaneous increase in the mean longitudinal momentum of an alpha particle with increasing excitation energy ΔE^*. This assumption is confirmed by the ΔE^* dependences of the mean absolute values of the longitudinal momenta of alpha particles (in the reference frame where the longitudinal momentum of the nuclear fragment ^{12}C* is zero), $\langle P_T^\alpha \rangle$, in the Monte Carlo calculation and in the experiment (see Fig. 1*b*). It is interesting to note that, in Figs. 1*a* and 1*b*, the difference $\Delta P_T^\alpha = \langle P_T^\alpha \rangle_{\mathrm{MC}} - \langle P_T^\alpha \rangle_{\mathrm{expt}}$ is approximately equal to the sign-reversed difference $\Delta P_L^\alpha = \langle P_L^\alpha \rangle_{\mathrm{MC}} - \langle P_L^\alpha \rangle_{\mathrm{expt}}$ at each fixed value of ΔE^*; that is, there is an approximate kinematical compensation: $\Delta P_T^\alpha \approx \Delta P_L^\alpha$.

From Figs. 1*a* and 1*b*, we can also see that, at excitation energies in the region $\Delta E^* < 15$ MeV, the experimental data agree with the results of the

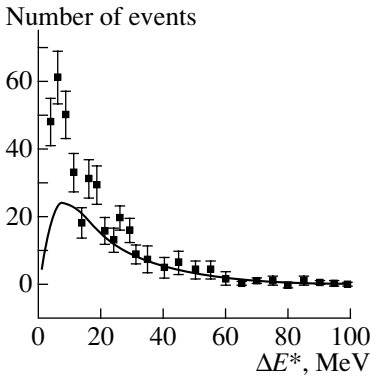

Fig. 2. Distribution of events with respect to the excitation energy ΔE^*. The solid curve represents the background distribution.

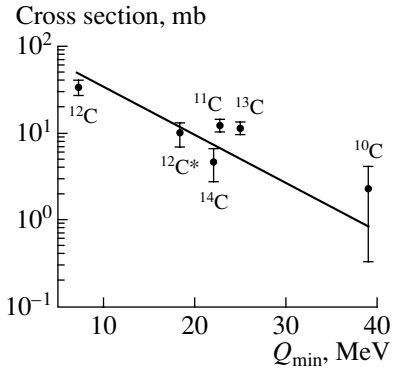

Fig. 3. Inclusive cross sections for the yields of carbon isotopes and of excited nuclei $^{12}C^*$ versus Q_{min}. The solid line represents the predictions of the model proposed in [7].

Monte Carlo calculations within the statistical uncertainties. One can assume that, in this excitation-energy region, the channel involving the production of three alpha particles receives a significant contribution from the prompt and cascade decays of $^{12}C^*$ to three alpha particles via reactions (2) and (3), which can proceed isotropically. In order to determine this contribution to the channel in (1), we consider the distribution of events with respect to the quantity ΔE^* (it is equivalent to the invariant-mass spectrum of three alpha particles). This distribution is shown in Fig. 2, along with the analogous distribution for background events (solid curve). The background distribution was constructed for an artificial set of events that was composed by means of a random choice of one alpha particle from each experimental event. In the breakup of an excited nucleus $^{12}C^*$, there can arise purely kinematical effects that lead to azimuthal correlations. In order to take these effects into account, the transverse components of the alpha-particle momenta were preliminarily determined with respect to their total transverse momentum in each event.

The experimental and the background distribution were normalized in the region $\Delta E^* > 35$ MeV. One can see that, in this region, the background describes the experimental excitation-energy spectrum (effective-mass spectrum) satisfactorily. The experimental spectrum with respect to ΔE^* exhibits peaks at the excitation-energy values of 6.25, 17.5, and 26.5 MeV. It can easily be seen (Fig. 2) that, in the region $\Delta E^* < 15$ MeV, half of the events of reaction (1) are associated with the decay of an excited nucleus $^{12}C^*$ to three alpha particles. The total number of excess events above the background spectrum proved to be 151. Taking into account the loss of events because of alpha-particle interaction with the working liquid of the chamber, we find that, at a distance of $L = 35$ cm, the number of $^{12}C^*$ nuclei is 215, which corresponds to a cross section of 9.8 ± 0.9 mb, this value being $(38.0 \pm 0.8)\%$ of the total cross section for reaction (1). Naturally, there arises the question of whether this result is plausible. In order to test it, the yields of carbon isotopes and of $^{12}C^*$ nuclei are contrasted against the predictions of the model proposed in [7], where it is assumed that the excitation of the primary nucleus is peripheral and that its decay is statistical.

In Fig. 3, the inclusive cross sections for the yields of carbon isotopes and of excited nuclei $^{12}C^*$ are shown according to our experimental data versus Q_{min}—that is, versus the excitation energy required for the formation of a given isotope. The straight line, which represents an exponential dependence, was taken from Fig. 1 in [7] and was drawn in accordance with the normalization of the theoretical results to the experimental data by means of the least squares method. The value of Q_{min} for $^{12}C^*$ nuclei was determined as

$$Q_{min} = \langle \Delta E^* \rangle + 7.3 \text{ MeV},$$

where $\langle \Delta E^* \rangle$ is the quantity that was calculated on the basis of the ΔE^* distribution of experimental events above the background spectrum and 7.3 MeV is the minimum energy required for the breakup of the $^{12}C^*$ nucleus into three alpha particles. One can see that, by and large, there is a general trend toward a decrease in the cross section with increasing Q_{min} and that the experimental point for $^{12}C^*$ is compatible with this trend. However, there is no satisfactory agreement between the model results and the experimental data. In all probability, this is partly due to the fact that some of the channels involving the production of carbon isotopes cannot be associated with peripheral interactions, where all fragments of the primary nucleus are products originating from the

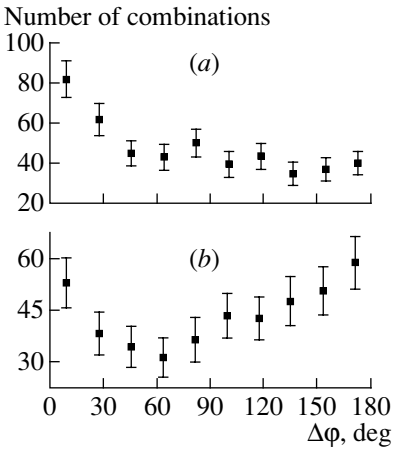

Fig. 4. Distribution with respect to the azimuthal-angle difference $\Delta\varphi$ between the alpha particle having $\vartheta_{\max}$ and the remaining alpha particles in an event for (*a*) $\Delta E^* < 15$ MeV and (*b*) $\Delta E^* > 15$ MeV.

breakup of an intermediate excited oxygen nucleus. It should be noted that the model proposed in [7] describes satisfactorily the dependence of the cross sections for the (26), (2222), and (224) channels (the figures in parentheses indicate the charge of multiply charged fragments) on the mean value of $Q_{\min}$ [8]. The mean value of $Q_{\min}$ was calculated with allowance for the experimental probability of the realization of each channel featuring a specific isotopic composition of fragments for a given topology.

It was indicated above that, for $\Delta E^* > 15$ MeV, there can also occur a quasielastic knockout of an alpha-particle cluster. It is natural to assume that, on average, the knock-on alpha particle will have the largest polar emission angle $\vartheta_{\max}$ and that the knockout process itself will lead to a violation of azimuthal isotropy and to a trend toward the emission of these particles in opposite directions in the azimuthal plane. Therefore, it is of interest to consider, for two excitation-energy regions, $\Delta E^* < 15$ MeV and $\Delta E^* > 15$ MeV, the distribution with respect to the azimuthal-angle difference $\Delta\varphi$ between the alpha particle having $\vartheta_{\max}$ and the other alpha particles from the same event.

The deviation of the $\Delta\varphi$ distribution from an isotropic distribution in Fig. 4*a* (a peak in the region $\Delta\varphi \leq 36^\circ$) may be due to the following mechanisms: the cascade decay of a $^{12}C^*$ nucleus to three alpha particles ($^{12}C^* \rightarrow {}^8Be^* + \alpha$, $^8Be^* \rightarrow 2\alpha$), dynamical mechanisms associated with final-state interaction in a pair of alpha particles, and identity effects.

In Fig. 4*b*, the distribution with respect to $\Delta\varphi$ has two maxima, one in the region $\Delta\varphi \leq 36^\circ$ and the other at $\Delta\varphi \approx 180^\circ$. The former is caused by the aforementioned reasons, while the latter is associated with the trend toward alpha-particle emission in opposite directions in the azimuthal plane at large values of $\Delta\varphi$, this trend being due to a quasielastic knockout of one of the alpha-particle clusters contained in the residual nucleus. The fact that the second maximum is rather small can be explained by an arbitrary direction of the Fermi momentum of this alpha-particle cluster in its collision with a secondary particle.

If the quasielastic knockout of an alpha-particle cluster from a loosely bound residual nucleus does indeed occur for $\Delta E^* < 15$ MeV, then the mean multiplicity of charged pions produced in such events must be identical to their mean multiplicity in events for $\Delta E^* > 15$ MeV. In order to test this conjecture, we determined the mean multiplicities of charged pions in events occurring for $\Delta E^* < 15$ MeV and $\Delta E^* > 15$ MeV, and they proved to be 0.82 ± 0.05 and 0.84 ± 0.05, respectively, these values being in agreement within the statistical errors.

Thus, we can conclude that one-third of the events of reaction (1) proceed via the decay of an excited nucleus $^{12}C^*$, the remaining two-thirds of the events being due to prompt Fermi breakup or a quasielastic knockout of one alpha-particle cluster from a loosely bound residual nucleus, which contains three alpha particles. The results obtained by simulating the decay of our excited system on the basis of the isotropic-phase-space model describe the experimental data satisfactorily at low excitation energies ($\Delta E^* < 15$ MeV).

APPENDIX

Monte Carlo Simulation

It is assumed that three alpha particles are formed upon the decay of an excited nucleus $^{12}C^*$. The invariant-mass ($M_{3\alpha}$) distribution of $^{12}C^*$ and the distribution with respect to its momentum components P_x, P_y, and P_z were generated in accordance with the analogous experimental spectra for the system of three alpha particles from reaction (1). In order to take into account here the possible correlations between P_x, P_y, and P_z and the excitation energy ΔE^*, the components of the momentum of the system of three alpha particles were generated individually for each interval ΔE^* of the corresponding experimental distribution. Within our Monte Carlo calculations, we generated first the invariant mass of three alpha particles and then the projections P_x, P_y, and P_z of the vector sum of the momenta of three alpha particles. In the rest frame of the oxygen nucleus (K_0 reference frame), the vector sum of the momenta of three alpha particles is the momentum vector $\mathbf{P}_0$ of the nuclear

fragment $^{12}C^*$; that is, $P_0 = \sqrt{P_x^2 + P_y^2 + P_z^2}$. In this reference frame, the energy E_0 of the nuclear fragment $^{12}C^*$ is $E_0 = \sqrt{P_0^2 + M_{3\alpha}^2}$.

Decay of a $^{12}C^*$ Nucleus to Three Alpha Particles

The decay of the nuclear fragment $^{12}C^*$ to three alpha particles in (2) was generated in its rest frame. In order to go over from the K_0 reference frame to the rest frame of the nuclear fragment $^{12}C^*$, we rotate the K_0 reference frame in such a way as to align the z^* and y^* axes with, respectively, the momentum $\mathbf{P}_0$ of the nuclear fragment $^{12}C^*$ and the vector product $\mathbf{z}^* \times \mathbf{z}_0$. We denote this new reference frame by K^*. Suppose that the K^* reference frame moves at the velocity $\boldsymbol{\beta}_0 = \mathbf{P}_0/E_0$. In this way, we arrive at the rest frame K of the nuclear fragment $^{12}C^*$.

The decay of the nuclear fragment $^{12}C^*$ to three alpha particles in (2) was generated on the basis of the isotropic-phase-space model; that is,

$$d^5W \propto \Phi(M_{12})\frac{p_3^2}{\varepsilon_3}dp_3 \sin\theta_3 d\theta_3 d\phi_3 \sin\theta_1' d\theta_1' d\phi_1',$$

where p_3 and ε_3 are, respectively, the momentum and the energy of α_3 in the rest frame of the nuclear fragment; M_{12} is the invariant mass of the $\alpha_1\alpha_2$ system; Φ is its phase space; θ_3 and ϕ_3 are, respectively, the polar and the azimuthal angle of α_3 emission in the rest frame of the nuclear fragment $^{12}C^*$; and θ_1' and ϕ_1' are, respectively, the polar and the azimuthal angle of α_1 emission in the c.m. frame of the $\alpha_1\alpha_2$ system (the choice of the $\alpha_1\alpha_2$ c.m. frame in the rest frame of the nuclear fragment $^{12}C^*$ is similar to the choice of the rest frame of the nuclear fragment $^{12}C^*$ in the K_0 reference frame).

After the Lorentz transformation from the K to the K^* reference frame, the projections of the momentum vectors of the α_1, α_2, and α_3 particles were transformed from the K^* to the K_0 reference frame according to the formulas

$$p_{xi}^0 = -p_{xi}^* \cos\theta \cos\varphi - p_{yi}^* \sin\varphi - p_{zi}^* \sin\theta \cos\varphi,$$
$$p_{zi}^0 = p_{xi}^* \sin\theta - p_{zi}^* \cos\theta,$$
$$p_{yi}^0 = -p_{xi}^* \cos\theta \sin\varphi + p_{yi}^* \cos\varphi - p_{zi}^* \sin\theta \sin\varphi,$$

where p_{xi}^*, p_{yi}^*, and p_{zi}^* are the projections of the momentum of the ith alpha particle (in the K^* reference frame) and the angles θ and φ are defined by the relations

$$\cos\theta' = -P_z/\sqrt{P_x^2 + P_y^2 + P_z^2},$$
$$\cos\varphi' = -P_x/\sqrt{P_x^2 + P_y^2},$$
$$\sin\varphi' = -P_y/\sqrt{P_x^2 + P_y^2},$$

with P_x, P_y, and P_z being the projections of the momentum of the nuclear fragment $^{12}C^*$.

Decay of the $^{12}C^*$ Nucleus through the Channel $^{12}C^* \rightarrow {}^8Be + \alpha \rightarrow 3\alpha$

The decay in (3) of an excited nucleus $^{12}C^*$ to a nucleus having the ^{8}Be quantum numbers and the α_1 particle was generated with a probability of 0.6. In this decay, the α_1-particle emission angles θ_1' and φ_1' in the rest frame of the nuclear fragment $^{12}C^*$ were generated in accordance with an isotropic angular distribution. The z' axis of the rest frame of the nuclear fragment $^{12}C^*$ is parallel to its momentum in the K_0 reference frame, while the y' axis is aligned with the vector product $\mathbf{z}^* \times \mathbf{z}_0$. The projections of the α_1 and ^{8}Be momenta were transformed from the rest frame of the nuclear fragment $^{12}C^*$ to the K_0 rest frame. The same method was used to generate the decay of ^{8}Be to two alpha particles.

REFERENCES

1. M. A. Belov, K. G. Gulamov, V. V. Lugovoĭ, *et al.,* Yad. Fiz. **65**, 990 (2002) [Phys. At. Nucl. **65**, 959 (2002)].
2. A. S. Botvina, A. S. Iljinov, and I. N. Mishustin, Nucl. Phys. A **507**, 649 (1990); A. S. Botvina *et al.,* Preprint No. 626, IYaI AN SSSR (Inst. for Nucl. Res., Acad. Sci. USSR, Moscow, 1989).
3. S. Botvina, W. Wislicki, Sh. Gaitinov, *et al.*, Z. Phys. A **345**, 413 (1993).
4. V. V. Glagolev, K. G. Gulamov, M. Yu. Kratenko, *et al.,* Pis'ma Zh. Éksp. Teor. Fiz. **58**, 497 (1993); **59**, 316 (1994) [JETP Lett. **59**, 336 (1994)].
5. F. Ajzenberg-Selove, Nucl. Phys. A **490**, 1 (1988).
6. V. V. Glagolev, K. G. Gulamov, M. Yu. Kratenko, *et al.,* Yad. Fiz. **58**, 2005 (1995) [Phys. At. Nucl. **58**, 1896 (1995)].
7. V. K. Lukyanov and A. I. Titov, Phys. Lett. B **57B**, 10 (1975).
8. M. A. Belov, É. Kh. Bazarov, V. D. Lipin, *et al.,* Dokl. Akad. Nauk Resp. Uzb., No. 3, 16 (2002).

Translated by A. Isaakyan

Physics of Atomic Nuclei, Vol. 67, No. 12, 2004, pp. 2188–2199. From Yadernaya Fizika, Vol. 67, No. 12, 2004, pp. 2212–2224.
Original English Text Copyright © 2004 by Ivanov, Zupnik.

ELEMENTARY PARTICLES AND FIELDS
Theory

New Approach to Nonlinear Electrodynamics: Dualities as Symmetries of Interaction*

E. A. Ivanov and B. M. Zupnik

Joint Institute for Nuclear Research, Dubna, Moscow oblast, 141980 Russia

Received March 25, 2003; in final form, November 12, 2003

Abstract—The duality-symmetric nonlinear electrodynamics in a new formulation with auxiliary tensor fields is considered. The Maxwell field strength appears only in bilinear terms of the corresponding generic Lagrangian, while the self-interaction is represented by a function E depending on the auxiliary fields. Two types of dualities inherent in the nonlinear electrodynamics admit a simple off-shell characterization as symmetry properties of this function. In the standard formulation, the continuous $U(1)$ duality symmetry is nonlinearly realized on the Maxwell field strength. In the new setting, the same symmetry acts as linear $U(1)$ transformations of the auxiliary field variables. The nonlinear $U(1)$ duality condition proves to be equivalent to the $U(1)$ invariance of the self-interaction E. The discrete self-duality (or self-duality by Legendre transformation) amounts to a weaker reflection symmetry of E. For a class of duality-symmetric Lagrangians, an alternative representation with the auxiliary scalar field is introduced and new explicit examples of such systems are found. © *2004 MAIK "Nauka/Interperiodica".*

1. INTRODUCTION

It is well known that the on-shell $SO(2)$ ($U(1)$) duality symmetry (or self-duality) of Maxwell equations can be generalized to the whole class of models of nonlinear electrodynamics, including the famous Born–Infeld (BI) theory. The condition of $SO(2)$ duality can be formulated as a nonlinear differential constraint on the Lagrangians of these models [1–3]. Using a nonanalytic change of basic field variables of the Lagrangian, the $SO(2)$ duality condition can be transformed to the well-known Courant–Hilbert equation [4–6]. Recently, it has been observed that the requirement of analyticity of the initial Lagrangian implies an additional algebraic constraint which selects the proper subclass of solutions of this Courant–Hilbert equation [7].

In this paper, we elaborate on another approach to the $U(1)$ duality-symmetric Lagrangians, in which the manifest analyticity is guaranteed at each step.[1)] It makes use of the auxiliary tensor fields. The starting point is the generic Lagrangian of the nonlinear electrodynamics

$$L(F^2,\bar F^2) = -\frac{1}{2}(F^2+\bar F^2) + L^{\rm int}(F^2,\bar F^2), \quad (1.1)$$

where $F^2 = F_{\alpha\beta}F^{\alpha\beta}$, $\bar F^2 = \bar F_{\dot\alpha\dot\beta}\bar F^{\dot\alpha\dot\beta}$, $F_{\alpha\beta}$, $\bar F_{\dot\alpha\dot\beta}$ are the mutually conjugated $(1,0)$ and $(0,1)$ components of the Maxwell field strength in a two-component spinor notation, and $L^{\rm int}$ is the nonlinear interaction. The new representation of the nonlinear Lagrangian involves, apart from the Maxwell field strength, also unconstrained auxiliary symmetric bispinor (tensor) fields $V_{\alpha\beta}, \bar V_{\dot\alpha\dot\beta}$ and their squares $V^2 \equiv \nu$ and $\bar V^2 \equiv \bar\nu$:

$$\mathcal{L}(F,V) = \frac{1}{2}(F^2+\bar F^2) + (\nu+\bar\nu) - 2(V\cdot F + \bar V\cdot\bar F) + E(\nu,\bar\nu), \quad (1.2)$$

where $E(\nu,\bar\nu)$ codifies the entire self-interaction. The generic Lagrangian (1.1) is recovered as a result of eliminating the auxiliary fields in (1.2) with the help of their algebraic equations of motion (see Section 3). The basic advantage of this novel representation for $U(1)$ duality-symmetric systems is related to its following remarkable feature. In contradistinction to nonlinear $U(1)$ duality transformations of F^2, $\bar F^2$, the transformations of the new auxiliary variables are linear. As a consequence, the $SO(2)$ duality condition is linearized and can be explicitly solved in this new setting. The general Lagrangian solving this constraint is specified by the interaction term $E^{\rm ds}(\nu,\bar\nu) = \mathcal{E}(\nu\bar\nu)$ which includes only the $U(1)$-invariant scalar combination of the auxiliary fields $\nu\bar\nu = V^2\bar V^2$ as an argument. More general nonlinear Lagrangians respecting the so-called discrete self-duality (or duality by Legendre transformation) also admit a simple off-shell characterization in terms of the function E. In

*This article was submitted by the authors in English.

[1)] A preliminary version of this approach was presented in [8, 9].

1063-7788/04/6712-2188$26.00 © 2004 MAIK "Nauka/Interperiodica"

this case, it should be even, $E(\nu,\bar\nu) = E(-\nu,-\bar\nu)$, and arbitrary otherwise.

The paper is organized as follows. In Section 2, we give a brief account of the continuous and "discrete" dualities in nonlinear electrodynamics in the conventional approach. A novel representation of the appropriate Lagrangians via bispinor auxiliary fields is discussed in Section 3. An explicit solution of the algebraic equations of motion relating the initial and auxiliary variables can be immediately found only for a restricted class of interaction functions $\mathcal{E}(\nu\bar\nu)$, e.g., for the textbook case of BI theory (though their perturbative solution always exists). In order to construct new explicit examples of duality-symmetric models, we introduce, in Section 4, an alternative representation for the important subclass of interactions $L^{\rm int}(F^2,\bar F^2)$, namely, those containing terms of the fourth order in the field strengths. This representation makes use of a different linearly transforming auxiliary scalar variable μ which is related to the variable $\nu = V^2$ by a sort of Legendre transformation. The ansatz for the appropriate class of solutions of the $U(1)$ duality condition contains an invariant analytic function $I(\mu\bar\mu)$, and the expression for the corresponding Lagrangians in the μ representation is parametrized by this function. The algebraic equation for the auxiliary variable μ can be explicitly solved in terms of the initial variables F^2, $\bar F^2$ for a wide class of the functions $I(\mu\bar\mu)$. Explicit examples of duality-symmetric analytic Lagrangians, including the BI Lagrangian and some new ones constructed here for the first time, are collected in Section 5. The main results are summarized in the Conclusions.

2. DUALITIES IN NONLINEAR ELECTRODYNAMICS

We start by recapitulating the basic facts about models of nonlinear $4D$ electrodynamics which reveal duality properties and include the free Maxwell theory and BI theory as particular cases. Detailed motivations why such models are of interest to study can be found, e.g., in [3].

2.1. Continuous On-Shell SO(2) Duality

In the two-component spinor notation, the Maxwell field strengths are defined by

$$F_\alpha^\beta(A) \equiv \frac{1}{4}(\sigma^m)_{\alpha\dot\beta}(\bar\sigma^n)^{\dot\beta\beta}F_{mn} \qquad (2.1)$$
$$= \frac{1}{4}\big(\partial_\alpha^{\dot\beta}A_{\beta\dot\beta} + \partial_\beta^{\dot\beta}A_{\alpha\dot\beta}\big),$$
$$\bar F_{\dot\alpha}^{\dot\beta}(A) \equiv \overline{F_\alpha^\beta(A)},$$
$$F_{mn} = \partial_m A_n - \partial_n A_m,$$

where σ^m and $\bar\sigma^n$ are the Weyl matrices of the group $SL(2,C)$, $\partial_{\alpha\dot\beta} = (\sigma^m)_{\alpha\dot\beta}\partial_m$, and $A_{\alpha\dot\beta} = (\sigma^m)_{\alpha\dot\beta}A_m$ is the corresponding vector gauge potential. Below, we shall sometimes treat $F_{\alpha\beta}$ ($\bar F_{\dot\alpha\dot\beta}$) as independent variables, without assuming them to be expressed through A_m.

Let us introduce the Lorentz-invariant complex variables

$$\varphi \equiv F^2 = F^{\alpha\beta}F_{\alpha\beta}, \quad \bar\varphi = \bar F^2 = \bar F^{\dot\alpha\dot\beta}\bar F_{\dot\alpha\dot\beta}. \quad (2.2)$$

Two independent real invariants, which one can construct out of the Maxwell field strength in the standard vector notation, take the following form in these complex variables:

$$F^{mn}F_{mn} = 2(\varphi+\bar\varphi), \qquad (2.3)$$
$$\frac{1}{2}\varepsilon^{mnpq}F_{mn}F_{pq} = -2i(\varphi-\bar\varphi).$$

It will be convenient to deal with dimensionless $F_{\alpha\beta}$, $\bar F_{\dot\alpha\dot\beta}$ and φ, $\bar\varphi$, introducing a coupling constant f, $[f]=2$. Then the generic nonlinear Lagrangian can be represented as

$$f^{-2}L(\varphi,\bar\varphi),$$

where

$$L(\varphi,\bar\varphi) = -\frac{1}{2}(\varphi+\bar\varphi) + L^{\rm int}(\varphi,\bar\varphi) \qquad (2.4)$$

and the real analytic self-interaction $L^{\rm int}(\varphi,\bar\varphi)$ collects all possible higher order terms $\varphi^k\bar\varphi^m$, $(k+m)\geq 2$. This analyticity requirement rules out, for instance, terms with radicals of the type $\sqrt{\varphi}$ or $\sqrt{\varphi\pm\bar\varphi}$.

We shall use the following notation for the derivatives of the Lagrangian $L(\varphi,\bar\varphi)$:[2)]

$$P_{\alpha\beta}(F) \equiv i\partial L/\partial F^{\alpha\beta} = 2iF_{\alpha\beta}L_\varphi, \qquad (2.5)$$
$$L_\varphi = \partial L/\partial\varphi, \quad L_{\bar\varphi} = \partial L/\partial\bar\varphi,$$

and for the bilinear combinations of them:

$$\pi \equiv P^2 = P^{\alpha\beta}P_{\alpha\beta} = -4\varphi(L_\varphi)^2, \qquad (2.6)$$
$$\bar\pi = \bar P^2 = \bar P^{\dot\alpha\dot\beta}\bar P_{\dot\alpha\dot\beta} = -4\bar\varphi(L_{\bar\varphi})^2.$$

In the vector notation, the same quantities read

$$\widetilde P^{mn} \equiv \frac{1}{2}\varepsilon^{mnpq}P_{pq} = 2\partial L/\partial F_{mn},$$
$$\frac{i}{2}P_{mn}\widetilde P^{mn} = \pi - \bar\pi.$$

[2)] In these and some subsequent relations, it is assumed that the functional argument F stands for both $F_{\alpha\beta}$ and $\bar F_{\dot\alpha\dot\beta}$; we hope that this shorthand notation will not give rise to any confusion.

The nonlinear equations of motion have the following form in the spinor notation:

$$\partial^{\dot\beta}_{\alpha}\bar P_{\dot\alpha\dot\beta}(F) - \partial^{\beta}_{\dot\alpha}P_{\alpha\beta}(F) = 0. \qquad (2.7)$$

These equations, together with the Bianchi identities

$$\partial^{\dot\beta}_{\alpha}\bar F_{\dot\alpha\dot\beta} - \partial^{\beta}_{\dot\alpha}F_{\alpha\beta} = 0, \qquad (2.8)$$

constitute a set of first-order equations in which one can treat $F_{\alpha\beta}$ and $\bar F_{\dot\alpha\dot\beta}$ as unconstrained conjugated variables.

This set is said to be duality-symmetric if the Lagrangian $L(\varphi,\bar\varphi)$ satisfies a certain nonlinear condition [1–3]. The precise form of this $SO(2)$ duality condition is as follows:

$$F^2 + P^2 - \bar F^2 - \bar P^2 \equiv \frac{i}{4}\varepsilon^{mnpq}(F_{mn}F_{pq} + P_{mn}P_{pq}) = \varphi + \pi - \bar\varphi - \bar\pi = \varphi - \bar\varphi - 4[\varphi(L_\varphi)^2 - \bar\varphi(L_{\bar\varphi})^2] = 0. \qquad (2.9)$$

To clarify the meaning of (2.9), let us define the nonlinear transformation

$$\delta_\omega F_{\alpha\beta} = \omega P_{\alpha\beta}(F) = 2i\omega F_{\alpha\beta}L_\varphi \qquad (2.10)$$

and the corresponding transformation of the scalar (2.2)

$$\delta_\omega\varphi = 4i\omega\varphi L_\varphi, \qquad (2.11)$$

where ω is a real parameter. Then Eq. (2.9) ensures that this transformation constitutes a nonlinear realization of the $SO(2)$ group. Indeed, given (2.9), $F_{\alpha\beta}$ and $P_{\alpha\beta}(F)$ form an $SO(2)$ vector

$$\delta_\omega P_{\alpha\beta}(F) = -\omega F_{\alpha\beta}. \qquad (2.12)$$

The set of Eqs. (2.7), (2.8) and the constraint (2.9) itself are clearly invariant under this transformation. Thus, (2.10) is an obvious generalization of the $SO(2)$ duality transformation in the Maxwell theory,

$$\delta_\omega F_{\alpha\beta} = -i\omega F_{\alpha\beta}, \quad \delta_\omega\bar F_{\dot\alpha\dot\beta} = i\omega\bar F_{\dot\alpha\dot\beta},$$

which is a symmetry of the vacuum Maxwell equation $\partial^{\beta}_{\dot\alpha}F_{\alpha\beta} = 0$.

With (2.9), the following important relations can be derived:

$$\delta_\omega L = i\omega(\varphi - \bar\varphi), \quad \delta_\omega L_\varphi = \frac{i}{2}\omega - 2i\omega L_\varphi^2. \qquad (2.13)$$

It should be pointed out that these transformations make sense only on the mass shell defined by Eqs. (2.7), (2.8).

The general solution of the $SO(2)$ duality condition (2.9) has been considered earlier in [2, 4–7]. Using the nonanalytic change of variables

$$p = \frac{1}{4}(\varphi+\bar\varphi) + \frac{1}{2}\sqrt{\varphi\bar\varphi}, \quad q = \frac{1}{4}(\varphi+\bar\varphi) - \frac{1}{2}\sqrt{\varphi\bar\varphi}, \qquad (2.14)$$

one can cast Eq. (2.9) in the form of the well-known Courant–Hilbert equation

$$\mathcal{L}_p\mathcal{L}_q = 1. \qquad (2.15)$$

The general solution of this equation is parametrized by a real analytic function $v(s)$

$$L(p,q) = v(s) + \frac{2p}{v'(s)}, \quad q = s + \frac{p}{[v'(s)]^2},$$

and it is completely specified by an algebraic equation for the auxiliary variable s. The authors of [7] have shown that the natural requirement of analyticity of the Lagrangian with respect to the initial variables $\varphi,\bar\varphi$ can be rephrased as the additional constraint on the function $\Psi(s) = -s[v'(s)]^2$:

$$\Psi[\Psi(s)] = s. \qquad (2.16)$$

The perturbative analysis shows that the whole class of duality-symmetric analytic solutions $L[p(\varphi,\bar\varphi), q(\varphi,\bar\varphi)]$ exists. However, the only solution explicitly worked out so far is the familiar BI example. Nonphysical solutions of Eq. (2.15) contain nonanalytic terms $\sqrt{\varphi\bar\varphi}$ (see, e.g., [6]).

In Sections 3 and 4, we shall discuss two complementary approaches to solving the $SO(2)$ duality equation which guarantee analyticity and covariance of solutions at each stage of calculations. Based on this, in Section 5, we shall present several new examples of duality-symmetric Lagrangians which meet the analyticity criterion.

It is worth pointing out once more that the $SO(2)$ duality transformations in the standard setting described above cannot be realized on the vector potential A_m; they provide a symmetry between the equations of motion and the Bianchi identity and as such define on-shell symmetry. The manifestly $SO(2)$ duality-invariant off-shell Lagrangians can be constructed in the formalism with additional vector and auxiliary fields [10]. We are planning to discuss a relation to this extended formalism elsewhere.

The Lagrangian $L(\varphi,\bar\varphi)$ satisfying (2.9) is not invariant with respect to transformation (2.10). Yet one can construct, out of φ and $\bar\varphi$, the $SO(2)$ invariant function

$$I(\varphi,\bar\varphi) \equiv L + \frac{i}{2}(F\cdot P - \bar F\cdot\bar P) = L - \varphi L_\varphi - \bar\varphi L_{\bar\varphi}, \qquad (2.17)$$

where $F\cdot P = F^{\alpha\beta}P_{\alpha\beta}$. However, $I(\varphi,\bar\varphi)$ starts with the fourth-order term $\varphi\bar\varphi$, so this invariant cannot be interpreted as a Lagrangian.

Finally, note that, given some $L^{\rm ds}(\varphi,\bar\varphi)$ obeying (2.9), the following Lagrangian related to $L^{\rm ds}$ by the simple rescaling

$$L^{\rm ds}(\varphi,\bar\varphi) \Rightarrow rL^{\rm ds}(r^{-1}\varphi, r^{-1}\bar\varphi), \qquad (2.18)$$

with $r \neq 0$ being an arbitrary real number, also obeys (2.9) and so yields a duality-symmetric model. Clearly, rescaling the coupling constant as $f^2 \to |r|f^2$ and properly rescaling $F_{\alpha\beta}$, $\bar{F}_{\dot{\alpha}\dot{\beta}}$, one can always choose $|r| = 1$, so only the sign of r actually matters in (2.18). Thus,

$$L^{(-)}(\varphi, \bar{\varphi}) = -L^{\mathrm{ds}}(-\varphi, -\bar{\varphi}) \tag{2.19}$$

gives a nonequivalent duality-symmetric Lagrangian for each given L^{ds}. In Section 5, we shall consider this transformation for the Lagrangian of the BI theory.

2.2. Self-Duality by Legendre Transformation

To explain what "discrete duality" means, we will need a first-order representation of the action corresponding to the Lagrangian (2.4). It is such that the Bianchi identities (2.8) are implemented in the action with the Lagrange multiplier and so $F_{\alpha\beta}$, $\bar{F}_{\dot{\alpha}\dot{\beta}}$ are unconstrained complex variables off shell. This form of the action is given by

$$\frac{1}{f^2}\int d^4x L^D(F, F^D) \tag{2.20}$$
$$= \frac{1}{f^2}\int d^4x [L(\varphi, \bar{\varphi}) + i(F \cdot F^D - \bar{F} \cdot \bar{F}^D)],$$

where

$$F^D_{\alpha\beta} \equiv \frac{1}{4}(\partial^{\dot{\beta}}_{\alpha} A^D_{\beta\dot{\beta}} + \partial^{\dot{\beta}}_{\beta} A^D_{\alpha\dot{\beta}}). \tag{2.21}$$

Varying with respect to the Lagrange multiplier $A^D_{\alpha\dot{\beta}}$, one obtains just the Bianchi identities for $F_{\alpha\beta}$, $\bar{F}_{\dot{\alpha}\dot{\beta}}$ (2.8). Solving them in terms of the gauge potential $A_{\alpha\dot{\beta}}$ and substituting the result into (2.20), we come back to (2.4). On the other hand, the multiplier $A^D_{\alpha\dot{\beta}}$ is defined up to the standard Abelian gauge transformation, which suggests interpreting $A^D_{\alpha\dot{\beta}}$ and $F^D_{\alpha\beta}$ as the dual gauge potential and gauge field strength, respectively. Using the algebraic equations of motion for the variables $F_{\alpha\beta}$, $\bar{F}_{\dot{\alpha}\dot{\beta}}$, one can express the action (2.20) in terms of $F^D_{\alpha\beta}$, $\bar{F}^D_{\dot{\alpha}\dot{\beta}}$. If the resulting action has the same form as the original one in terms of $F_{\alpha\beta}(A)$, $\bar{F}_{\dot{\alpha}\dot{\beta}}(A)$, the corresponding model is said to enjoy discrete duality. This sort of duality should not be confused with the on-shell continuous $SO(2)$ duality discussed earlier. However, as we shall see soon, any $L(\varphi, \bar{\varphi})$ solving the constraint (2.9) defines a system possessing discrete duality. The inverse statement is not generally true, so the class of nonlinear electrodynamics actions admitting $SO(2)$ duality of equations of motion forms a subclass in the variety of actions which are duality-symmetric in the "discrete" sense.

Let us elaborate on this in some detail. The dual picture is achieved by varying (2.20) with respect to the independent variables $F_{\alpha\beta}$, $\bar{F}_{\dot{\alpha}\dot{\beta}}$, which yields the equation

$$F^D_{\alpha\beta} = i\partial L/\partial F^{\alpha\beta} \equiv P_{\alpha\beta}(F) = 2iF_{\alpha\beta}L_{\varphi}, \tag{2.22}$$

where $P_{\alpha\beta}(F)$ is the same as in (2.5). Substituting the solution of this algebraic equation, $F_{\alpha\beta} = F_{\alpha\beta}(F^D)$, into (2.20) gives us the dual Lagrangian $L'(F^D)$:

$$L'(\varphi^D, \bar{\varphi}^D) \equiv L^D[F(F^D), F^D], \tag{2.23}$$

where $\varphi^D \equiv F^{D\alpha\beta}F^D_{\alpha\beta} = \pi(F)$ and π, $\bar{\pi}$ were defined in (2.6). Then the discrete self-duality defined above amounts to the condition

$$L'(\varphi^D, \bar{\varphi}^D) = L(\varphi^D, \bar{\varphi}^D), \tag{2.24}$$

or, equivalently, to

$$L'(\pi, \bar{\pi}) = L(\pi, \bar{\pi}). \tag{2.25}$$

Using (2.22) and its conjugate, as well as the definitions (2.20), (2.23), one can explicitly check the property

$$F_{\alpha\beta} = -i\partial L'(\varphi^D, \bar{\varphi}^D)/\partial F^{D\alpha\beta}. \tag{2.26}$$

Due to this relation and keeping in mind the inverse one (2.22), one can treat the equation

$$L'(P^2, \bar{P}^2) = L(F^2, \bar{F}^2) \tag{2.27}$$
$$+ i(F \cdot P - \bar{F} \cdot \bar{P}) = L(\varphi, \bar{\varphi}) - 2\varphi L_{\varphi} - 2\bar{\varphi}L_{\bar{\varphi}}$$

as setting the Legendre transforms $L \leftrightarrow L'$ between two functions of complex variables. Thus, the discrete duality (2.24), (2.25) can be equivalently called "self-duality by Legendre transformation."

On the level of equations of motion (2.7) and (2.8), the discrete self-duality (2.25) can be equivalently defined as their invariance with respect to the special finite $SO(2)$ transformation Λ:

$$F_{\alpha\beta} \to \Lambda F_{\alpha\beta} = P_{\alpha\beta}, \quad P_{\alpha\beta} \to \Lambda P_{\alpha\beta} = -F_{\alpha\beta}. \tag{2.28}$$

This invariance is manifested in the following on-shell transformation properties of the Lagrangian and its derivative:

$$\Lambda L(\varphi, \bar{\varphi}) = L(\varphi, \bar{\varphi}) + iP \cdot F - i\bar{P} \cdot \bar{F} \equiv L(\pi, \bar{\pi}), \tag{2.29}$$

$$\Lambda L_{\varphi} = \frac{1}{4}L^{-1}_{\varphi}.$$

Let us show that the $SO(2)$ duality condition (2.9) indeed guarantees discrete duality (2.25). The simplest proof of this statement (see, e.g., [3]) makes use of the special $SO(2)$ transformation Λ, Eq. (2.28), and the invariance of function (2.17) under the global version of the general $SO(2)$ transformations (2.10)

$$\Lambda I(\varphi,\bar\varphi)\equiv L(\pi,\bar\pi)-\frac{i}{2}F\cdot P+\frac{i}{2}\bar F\cdot\bar P=I(\varphi,\bar\varphi). \tag{2.30}$$

Comparing this relation with (2.27), we arrive at the condition (2.25). Clearly, the Λ invariance of $I(\varphi,\bar\varphi)$ is a weaker condition than its $SO(2)$ invariance, so the Lagrangians revealing the property of $SO(2)$ duality form a subclass of those which are self-dual in the discrete sense.

3. NONLINEAR ELECTRODYNAMICS AND DUALITIES REVISITED

3.1. A New Setting for Lagrangians of Nonlinear Electrodynamics

The recently constructed $N=3$ supersymmetric extension of the BI theory [8] suggests a new representation for the actions of nonlinear electrodynamics discussed in the previous section.

The infinite-dimensional off-shell $N=3$ vector multiplet contains gauge field strengths (2.1) and auxiliary fields $V_{\alpha\beta}$ and $\bar V_{\dot\alpha\dot\beta}$.

The gauge field part of the off-shell super $N=3$ Maxwell component Lagrangian is[3)]

$$\mathcal{L}_2(V,F)=\nu+\bar\nu-2(V\cdot F+\bar V\cdot\bar F)+\frac{1}{2}(\varphi+\bar\varphi), \tag{3.1}$$

where

$$\nu\equiv V^2=V^{\alpha\beta}V_{\alpha\beta},\quad \bar\nu\equiv\bar V^2=\bar V^{\dot\alpha\dot\beta}\bar V_{\dot\alpha\dot\beta}, \tag{3.2}$$
$$V\cdot F\equiv V^{\alpha\beta}F_{\alpha\beta},\quad \bar V\cdot\bar F\equiv\bar V^{\dot\alpha\dot\beta}\bar F_{\dot\alpha\dot\beta}.$$

Eliminating $V^{\alpha\beta}$ by its algebraic equation of motion,

$$V^{\alpha\beta}=F^{\alpha\beta},\quad \bar V^{\dot\alpha\dot\beta}=\bar F^{\dot\alpha\dot\beta}, \tag{3.3}$$

we arrive at the free Maxwell Lagrangian

$$L_2(F)=-\frac{1}{2}(\varphi+\bar\varphi). \tag{3.4}$$

Our aim will be to find a nonlinear extension of the free Lagrangian (3.1) such that this extension becomes the generic nonlinear Lagrangian $L(F^2,\bar F^2)$, Eq. (2.4), upon eliminating the auxiliary fields $V_{\alpha\beta}$, $\bar V_{\dot\alpha\dot\beta}$ by their algebraic (nonlinear) equations of motion.

By Lorentz covariance, the off-shell (F,V) representation of the nonlinear Lagrangian (2.4) has the following general form:

$$\mathcal{L}[V,F(A)]=\mathcal{L}_2[V,F(A)]+E(\nu,\bar\nu), \tag{3.5}$$

where E is a real analytic function of two variables which encodes self-interaction. Varying the action with respect to $V_{\alpha\beta}$, we derive the analytic relation between V and $F(A)$ in this formalism

$$F_{\alpha\beta}(A)=V_{\alpha\beta}(1+E_\nu) \tag{3.6}$$

(and the complex conjugate relation), where $E_\nu\equiv\partial E(\nu,\bar\nu)/\partial\nu$. The corresponding algebraic relations between the scalar functions are

$$\varphi=\nu(1+E_\nu)^2,\quad F\cdot V=\nu(1+E_\nu). \tag{3.7}$$

Relation (3.6) can be used to eliminate the auxiliary variable $V_{\alpha\beta}$, which can be expressed in terms of $F_{\alpha\beta}$ and $\bar F_{\dot\alpha\dot\beta}$, $V_{\alpha\beta}\Rightarrow V_{\alpha\beta}[F(A)]$ [see Eq. (3.11) below]. The natural restrictions on the interaction function $E(\nu,\bar\nu)$ are

$$E(0,0)=0,\quad E_\nu(0,0)=E_{\bar\nu}(0,0)=0. \tag{3.8}$$

They mean that the $(\nu,\bar\nu)$ expansion of $E(\nu,\bar\nu)$ does not contain constant and linear terms. Clearly, given some analytic interaction Lagrangian $L^{\rm int}(\varphi,\bar\varphi)$ in (2.4), one can pick up the appropriate function $E(\nu,\bar\nu)$ such that the elimination of $V_{\alpha\beta}$, $\bar V_{\dot\alpha\dot\beta}$ by (3.6) yields just this self-interaction. Thus, Eq. (3.5) with an arbitrary (nonsingular) interaction function E is an alternative form of generic nonlinear electrodynamics Lagrangian (2.4) (see also Section 4). The second equation of motion in this representation, obtained by varying (3.5) with respect to $A_{\alpha\dot\alpha}$, has the form

$$\partial^\beta_{\dot\alpha}[F_{\alpha\beta}(A)-2V_{\alpha\beta}]+\text{c.c.}=0. \tag{3.9}$$

After substituting $V_{\alpha\beta}=V_{\alpha\beta}[F(A)]$ from (3.6), Eq. (3.9) becomes the dynamical equation for $F_{\alpha\beta}(A),\bar F_{\dot\alpha\dot\beta}(A)$ corresponding to the generic Lagrangian (2.4). Comparing (3.9) with (2.7) yields the important relation

$$P_{\alpha\beta}(F)=i\left[F_{\alpha\beta}-2V_{\alpha\beta}(F)\right], \tag{3.10}$$

where $P_{\alpha\beta}(F)$ was defined in (2.5).

Let us elaborate in more detail on how the (F,V) representation of the nonlinear electrodynamics Lagrangians is related to the original "minimal" one (2.4). The general solution of the algebraic equation (3.6) for $V_{\alpha\beta}$ can be written as

$$V_{\alpha\beta}(F)=F_{\alpha\beta}G(\varphi,\bar\varphi). \tag{3.11}$$

[3)] In the rest of the paper, we set the overall coupling constant f equal to 1.

The relation of the transition functions $G, \bar{G}$ to $E(\nu, \bar{\nu})$ follows from Eq. (3.6):

$$G^{-1} = 1 + E_\nu, \quad \bar{G}^{-1} = 1 + E_{\bar{\nu}}. \tag{3.12}$$

Equation (3.11) gives us the relations

$$\nu = \varphi G^2, \quad \bar{\nu} = \bar{\varphi}\bar{G}^2, \tag{3.13}$$

$$V(F) \cdot F = \varphi G, \quad \bar{V}(F) \cdot \bar{F} = \bar{\varphi}\bar{G}, \tag{3.14}$$

which, taking into account (3.12), coincide with (3.7).

The transition function $G(\varphi, \bar{\varphi})$ can be found from the basic requirement that (3.5) coincides with the initial nonlinear action after eliminating $V_{\alpha\beta}$, $\bar{V}_{\dot{\alpha}\dot{\beta}}$,

$$\mathcal{L}[V(F), F] = L(\varphi, \bar{\varphi}). \tag{3.15}$$

Using Eqs. (3.10), (3.14) and the definition (2.5), it is easy to obtain the simple expression for the transition function in terms of the derivative of the Lagrangian (2.4)

$$G(\varphi, \bar{\varphi}) = \frac{1}{2} - L_\varphi. \tag{3.16}$$

A useful corollary of this formula and of Eqs. (3.12), (3.13) is

$$\nu E_\nu = \frac{1}{4}\varphi(1 - 4L_\varphi^2). \tag{3.17}$$

Given a fixed $L(\varphi, \bar{\varphi})$, one can express $\varphi, \bar{\varphi}$ (and then G, $\bar{G}$) in terms of $\nu, \bar{\nu}$ from Eqs. (3.13), (3.16) and restore the explicit form of $E(\nu, \bar{\nu})$ from (3.1), (3.5),

$$E = L(\varphi, \bar{\varphi}) - \frac{1}{2}(\varphi + \bar{\varphi}) - \nu - \bar{\nu} + 2(\varphi G + \bar{\varphi}\bar{G}), \tag{3.18}$$

via the substitution $\varphi, \bar{\varphi} \to \varphi(\nu, \bar{\nu}), \bar{\varphi}(\nu, \bar{\nu})$. Conversely, given $E(\nu, \bar{\nu})$, one can restore $L(\varphi, \bar{\varphi})$ by expressing ν through $\varphi, \bar{\varphi}$ from the first of Eqs. (3.7). In practice, finding such explicit relations is a rather complicated task (see Section 5).

3.2. Duality Symmetries as Invariance of Self-Interaction

So far, we have not discussed dualities in the (F, V) representation. A link with the consideration in the previous section is established by Eq. (3.10), which relates the functions $P_{\alpha\beta}(F)$ and $V_{\alpha\beta}(F)$.

With this identification, the realization of the $SO(2)$ (or $U(1)$) duality transformations (2.10), (2.12) on independent variables $F_{\alpha\beta}$ and $V_{\alpha\beta}$ is easily found to be

$$\delta_\omega V_{\alpha\beta} = -i\omega V_{\alpha\beta}, \tag{3.19}$$
$$\delta_\omega F_{\alpha\beta} = i\omega[F_{\alpha\beta} - 2V_{\alpha\beta}].$$

We see that, before effecting the algebraic equation (3.6), which expresses $V_{\alpha\beta}$ in terms of $F_{\alpha\beta}$ and $\bar{F}_{\dot{\alpha}\dot{\beta}}$, $SO(2)$ duality symmetry is realized linearly.

Next, substituting (3.10) into the $SO(2)$ duality condition (2.9) and making use of Eq. (3.17), we find

$$\frac{1}{4}\varphi(1 - 4L_\varphi^2) - \frac{1}{4}\bar{\varphi}(1 - 4L_{\bar{\varphi}}^2) = \nu E_\nu - \bar{\nu}E_{\bar{\nu}} = 0. \tag{3.20}$$

Thus, passing to the (F, V) representation allows one to rewrite the nonlinear differential equation (2.9) as a linear differential equation for the function $E(\nu, \bar{\nu})$. It is important to emphasize that the new form (3.20) of the constraint (2.9) admits a transparent interpretation as the condition of invariance of $E(\nu, \bar{\nu})$ under the $U(1)$ transformations (3.19)

$$\delta_\omega E = 2i\omega(\bar{\nu}E_{\bar{\nu}} - \nu E_\nu) = 0. \tag{3.21}$$

The general solution of (3.20) is an analytic function $\mathcal{E}(a)$ depending on the single real $U(1)$ invariant variable $a = \nu\bar{\nu} = V^2\bar{V}^2$, which is quartic in the auxiliary bispinor fields

$$E^{\mathrm{ds}}(\nu, \bar{\nu}) = \mathcal{E}(a) = \mathcal{E}(\nu\bar{\nu}), \quad \mathcal{E}(0) = 0. \tag{3.22}$$

We come to the notable result that, in the representation (3.5), the whole class of nonlinear extensions of the Maxwell action admitting the on-shell $SO(2)$ duality is parametrized by an arbitrary $SO(2)$-invariant real function of one argument, $E^{\mathrm{ds}} = \mathcal{E}(\nu\bar{\nu})$. A remarkable property of E^{ds} is that its power expansion collects only terms $\sim \nu^n\bar{\nu}^n$, i.e., those of fourth order in the fields. Below, we shall present this expansion for a few examples, including the notorious case of BI theory.

It is evident that the bilinear part of the duality-symmetric Lagrangian in the (F, V) representation (3.1) is not invariant,

$$\delta_\omega\mathcal{L}_2(F, V) = -2\mathrm{Im}(F^2 + 2V^2 - 2F \cdot V) = i\omega(\varphi - \bar{\varphi}). \tag{3.23}$$

Thus, the continuous $SO(2)$ duality in the (F, V) representation amounts to a "partial" $SO(2)$ symmetry of the entire Lagrangian: it is a symmetry of its interaction part $E^{\mathrm{ds}}(\nu, \bar{\nu})$. It should be pointed out that the auxiliary field $V_{\alpha\beta}$, $\bar{V}_{\dot{\alpha}\dot{\beta}}$ is not subjected off shell to any constraint (as distinct from the Maxwell field strength, which is subjected to the Bianchi identity), so the characterization of the $SO(2)$ duality-symmetric systems in the (F, V) representation as those with the $SO(2)$-invariant self-interaction is valid off shell.

Let us consider the general $U(1)$-invariant interaction $\mathcal{E}(\nu\bar{\nu})$. In order to construct the corresponding

Lagrangian $L(\varphi,\bar\varphi)$, one should solve the algebraic equations for $V_{\alpha\beta}(F)$ or $[V(F)]^2=\nu(\varphi,\bar\varphi)$:

$$F_{\alpha\beta}=V_{\alpha\beta}(1+\bar\nu\mathcal{E}_a) \qquad (3.24)$$
$$\Rightarrow \varphi=\nu(1+\bar\nu\mathcal{E}_a)^2,$$

where $\mathcal{E}_a=d\mathcal{E}/da$. Using Eq. (3.24), one can derive the general equations relating the auxiliary variables ν and $a=\nu\bar\nu$ to the original variables φ, $\bar\varphi$

$$\nu(1-a^2\mathcal{E}_a^4)=\varphi-\bar\varphi a\mathcal{E}_a^2+2a\mathcal{E}_a(a\mathcal{E}_a^2-1),$$
$$(1+a\mathcal{E}_a^2)^2\varphi\bar\varphi=a[\mathcal{E}_a(\varphi+\bar\varphi)+(1-a\mathcal{E}_a^2)^2]^2.$$

Note that it is not easy to find examples of the function $\mathcal{E}(a)$ for which the algebraic equation for $\nu(\varphi,\bar\varphi)$ becomes explicitly solvable. In the next section, we shall consider an alternative choice of the auxiliary scalar variables which simplifies the explicit construction of duality-symmetric Lagrangians.

Finally, let us examine which restrictions on the interaction Lagrangian $E(\nu,\bar\nu)$ are imposed by the requirement of discrete self-duality with respect to the exchange $F(A)\leftrightarrow F^D(A^D)$. We shall do this in two ways.

We shall need a first-order representation of the Lagrangian (3.5) analogous to (2.20). Let us treat $\mathcal{L}(V,F)$ in Eq. (3.5) as a function of two independent complex variables $V_{\alpha\beta}$, $F_{\alpha\beta}$ and implement the Bianchi identities for $F_{\alpha\beta}$, $\bar F_{\dot\alpha\dot\beta}$ [amounting to the expressions (2.1)] in the Lagrangian via the dual field strength $F^D_{\alpha\beta}(A^D)$ (2.21):

$$\widetilde{\mathcal{L}}[V,F,F^D]\equiv\mathcal{L}(V,F)+iF^D\cdot F-i\bar F^D\cdot\bar F. \qquad (3.25)$$

The algebraic equation of motion for $V^{\alpha\beta}$, i.e., $\partial\widetilde L/\partial V^{\alpha\beta}=0$, is just relation (3.6). On the other hand, since $F_{\alpha\beta}$, $\bar F_{\dot\alpha\dot\beta}$ enter only the bilinear part of the full Lagrangian in (3.25), varying (3.25) with respect to $F_{\alpha\beta}$ (keeping $V_{\alpha\beta}$, $\bar V_{\dot\alpha\dot\beta}$ off shell) yields the exact linear relation

$$F_{\alpha\beta}-2V_{\alpha\beta}=-iF^D_{\alpha\beta}(A^D) \qquad (3.26)$$

(and c.c.) as the corresponding equation of motion. As a result, one can explicitly find the dual form of (3.25) in terms of $F^D_{\alpha\beta}$, $\bar F^D_{\dot\alpha\dot\beta}$ and $V_{\alpha\beta}$, $\bar V_{\dot\alpha\dot\beta}$, expressing $F_{\alpha\beta}$ and $\bar F_{\dot\alpha\dot\beta}$ from Eq. (3.26):

$$\widetilde{\mathcal{L}}[V,F(V,F^D),F^D]\equiv\widetilde{\mathcal{L}}(U,F^D) \qquad (3.27)$$
$$=\mathcal{L}_2(U,F^D)+E(-u,-\bar u),$$

where

$$U_{\alpha\beta}\equiv\Lambda V_{\alpha\beta}=-iV_{\alpha\beta},\quad u=U^{\alpha\beta}U_{\alpha\beta}.$$

The discrete self-duality now amounts to the requirement that the Lagrangian (3.27) should have the same form in the variables U,F^D as the original Lagrangian $\mathcal{L}(V,F)$ has in terms of V,F. Comparing the dual Lagrangian (3.27) with the original one (3.5), one firstly observes that $\mathcal{L}_2$ in (3.27) looks the same in terms of the variables U,F^D as the original $\mathcal{L}_2$, Eq. (3.1), in terms of V,F. Then the necessary and sufficient condition of the discrete self-duality is the following simple restriction on the interaction function E [8]:

$$E(\nu,\bar\nu)=E(-\nu,-\bar\nu). \qquad (3.28)$$

Another proof is an analog of the on-shell consideration based on Eqs. (2.28)–(2.30) in the standard formulation. Let us consider the transformation of $\mathcal{L}(V,F)$ (3.5) with respect to a discrete version of the $U(1)$ transformations (3.19)

$$\Lambda F_{\alpha\beta}=i(F_{\alpha\beta}-2V_{\alpha\beta})=P_{\alpha\beta}, \qquad (3.29)$$
$$\Lambda V_{\alpha\beta}=-iV_{\alpha\beta},$$
$$\Lambda\mathcal{L}(V,F)=\mathcal{L}_2(V,F)+E(-\nu,-\bar\nu) \qquad (3.30)$$
$$+iP\cdot F-i\bar P\cdot\bar F.$$

By analogy with the condition (2.30), the requirement of discrete self-duality in the (F,V) representation can now be reformulated as the Λ invariance of the following function:

$$I(F,V)=\mathcal{L}(F,V)+\frac{i}{2}P\cdot F-\frac{i}{2}\bar P\cdot\bar F. \qquad (3.31)$$

We end up with the same condition (3.28) for $E(\nu,\bar\nu)$.

Obviously, an arbitrary $SO(2)$-invariant function $E^{\rm ds}(\nu,\bar\nu)=\mathcal{E}(\nu\bar\nu)$ corresponding to a $SO(2)$ duality-symmetric system automatically satisfies the discrete self-duality condition (3.28). This elementary consideration provides us with a simple proof of the fact (mentioned in Section 2) that the $SO(2)$ duality-symmetric systems constitute a subclass in the set of those revealing the discrete self-duality.

4. AN ALTERNATIVE AUXILIARY FIELD REPRESENTATION

Equation (3.6) [or Eqs. (3.7)] can be treated as an algebraic relation between the independent variables of the function $\mathcal{L}(F,V)$ (3.5). Eliminating variables $F_{\alpha\beta}$ in this function, one can define an on-shell ν representation of the general nonlinear Lagrangian

$$L[\varphi(\nu,\bar\nu),\bar\varphi(\nu,\bar\nu)]\equiv\hat L(\nu,\bar\nu) \qquad (4.1)$$
$$=E+\frac{1}{2}\nu(E_\nu^2-2E_\nu-1)+\frac{1}{2}\bar\nu(E_{\bar\nu}^2-2E_{\bar\nu}-1).$$

However, this representation with $E = \mathcal{E}(a)$ is not very helpful for finding explicit examples of Lagrangians $L^{\rm ds}(\varphi, \bar\varphi)$ in terms of the initial variables (2.2). It proves useful to define an alternative representation for the duality-symmetric Lagrangians

$$\tilde L(\mu, \bar\mu) \equiv \hat L[\nu(\mu, \bar\mu), \bar\nu(\mu, \bar\mu)],$$

introducing new scalar auxiliary variables μ, $\bar\mu$. Basic quantities of this μ representation are related to the corresponding quantities of the ν representation via the Legendre transformation. In Section 5, we shall see that the defining algebraic equation of this μ representation is more convenient for constructing explicit solutions of the $U(1)$ duality condition than the analogous one in the ν representation.

Let us introduce new complex scalar fields

$$\mu(\nu, \bar\nu) = E_\nu, \quad \bar\mu(\nu, \bar\nu) = E_{\bar\nu} \tag{4.2}$$

and consider the complex Legendre transformation $E(\nu, \bar\nu) \to H(\mu, \bar\mu)$:

$$E(\nu, \bar\nu) - \nu E_\nu - \bar\nu E_{\bar\nu} = H(\mu, \bar\mu). \tag{4.3}$$

The corresponding inverse transformation is

$$E(\nu, \bar\nu) = H(\mu, \bar\mu) - \mu H_\mu - \bar\mu H_{\bar\mu} \tag{4.4}$$

and

$$\nu(\mu, \bar\mu) = -H_\mu, \quad \bar\nu(\mu, \bar\mu) = -H_{\bar\mu}. \tag{4.5}$$

Note that the standard conditions (3.8) for the function $E(\nu, \bar\nu)$ do not imply any restriction on the second derivatives of this function. However, for the transformed function $H(\mu, \bar\mu)$ to be analytic at the origin and, respectively, for relations (4.2), (4.5) to be invertible, one is led to impose the following subsidiary condition on the Jacobian $J(\nu, \bar\nu) \equiv |E_{\nu\nu}|^2 - |E_{\nu\bar\nu}|^2$ of the Legendre transformation:

$$J(0, 0) \neq 0. \tag{4.6}$$

It implies an analogous condition for $H(\mu, \bar\mu)$ and selects those $L^{\rm int}(\varphi, \bar\varphi)$ the $(\varphi, \bar\varphi)$ expansion of which starts with a nondegenerate second-order term. Below, we shall limit our study to such analytic functions $H(\mu, \bar\mu)$.

Using Eqs. (3.12), (3.16), and (4.2), one can find how μ is mapped on the derivative L_φ:

$$\mu(L_\varphi) = \frac{1 + 2L_\varphi}{1 - 2L_\varphi} = G^{-1} - 1, \tag{4.7}$$

$$L_\varphi = \frac{\mu - 1}{2(\mu + 1)}.$$

The basic algebraic relation of the ν representation (3.7) can be transformed as follows:

$$\varphi = -(1 + \mu)^2 H_\mu \tag{4.8}$$

(and c.c.). In order to find the corresponding Lagrangian $L(\varphi, \bar\varphi)$, one should treat this basic relation as an equation for the function $\mu(\varphi, \bar\varphi)$. This function can be analyzed perturbatively for any real analytic function E (or H). However, explicit solutions can be found only for some special cases.

Performing the Legendre transformation $E \leftrightarrow H$ in the Lagrangian (4.1) [with the condition (4.6) imposed], one can cast it in the μ representation

$$\tilde L(\mu, \bar\mu) = \hat L[\nu(\mu, \bar\mu), \bar\nu(\mu, \bar\mu)] \tag{4.9}$$
$$= \frac{1}{2}(1 - \mu^2) H_\mu + \frac{1}{2}(1 - \bar\mu^2) H_{\bar\mu} + H(\mu, \bar\mu).$$

It is interesting to note that this Lagrangian and relation (4.8) can be reproduced from an off-shell Lagrangian with μ as an independent complex auxiliary field

$$\tilde{\mathcal{L}}(\varphi, \mu) = \frac{\varphi(\mu - 1)}{2(1 + \mu)} + \frac{\bar\varphi(\bar\mu - 1)}{2(1 + \bar\mu)} + H(\mu, \bar\mu). \tag{4.10}$$

Indeed, varying (4.10) with respect to μ, one obtains just Eq. (4.8). Substituting the latter back into (4.10), one recovers the on-shell representation $\tilde L(\mu, \bar\mu)$, Eq. (4.9). The off-shell Lagrangian (4.10) is an analog of the auxiliary-field reformulations of the BI Lagrangian [11, 12] (see Section 5).

Since the auxiliary fields ν and μ are related via the Legendre transform (4.3), (4.4), a similar off-shell Lagrangian should also exist for the on-shell ν representation (4.1), with relation (3.7) arising as the appropriate algebraic equation of motion for ν. However, the derivation of such a Lagrangian is not so straightforward.

Let us turn to duality issues in the μ representation. Using Eq. (4.7) and formula (2.13) for the variation $\delta_\omega L_\varphi$, one can show that the $SO(2)$ duality group acts on μ as a linear $U(1)$ transformation

$$\delta_\omega \mu = 2i\omega\mu. \tag{4.11}$$

Equation (3.17) implies the relation

$$\frac{1}{4}\varphi(1 - 4L_\varphi^2) = E_\nu \nu = -\mu H_\mu. \tag{4.12}$$

Then the $U(1)$ duality condition (2.9) in the μ representation is equivalent to the condition of $U(1)$ invariance of $H(\mu, \bar\mu)$:

$$\delta_\omega H = 2i\omega(\mu H_\mu - \bar\mu H_{\bar\mu}) = 0 \tag{4.13}$$
$$\Rightarrow H^{\rm ds}(\mu, \bar\mu) = I(b),$$

where $I(b)$ is a real function of the invariant argument $b = \mu\bar\mu$. The Jacobian condition (4.6) now amounts to the one-dimensional relations

$$\mathcal{E}_a(0) \neq 0 \quad \Leftrightarrow \quad I_b(0) = \frac{dI}{db}(0) \neq 0. \tag{4.14}$$

Thus, the solution of the $U(1)$ duality condition has the following form in the μ representation:

$$\nu(\mu,\bar\mu) = -\bar\mu I_b, \quad \varphi = -(1+\mu)^2\bar\mu I_b. \tag{4.15}$$

This solution is easily checked to provide the correct transformation rule for φ

$$\delta_\omega\varphi = 2i\omega\varphi\frac{\mu-1}{\mu+1} = 4i\omega\varphi L_\varphi. \tag{4.16}$$

From the definition of μ and relations (4.15), it is straightforward to derive

$$a \equiv \nu\bar\nu = bI_b^2, \tag{4.17}$$

$$\mu = \bar\nu\mathcal{E}_a \Rightarrow \frac{d\mathcal{E}(a)}{da} = -\left(\frac{dI(b)}{db}\right)^{-1}. \tag{4.18}$$

The one-dimensional Legendre transform (4.3), (4.4) for the $U(1)$-invariant functions in the ν and μ representations reads

$$\mathcal{E}(a) = I(b) - 2bI_b, \quad I(b) = \mathcal{E}(a) - 2a\mathcal{E}_a. \tag{4.19}$$

Relations (4.17), (4.18) can be directly derived from (4.19).

The general expression for the μ representation of the $U(1)$ duality-symmetric Lagrangian follows by substituting $I(b)$ for $H(\mu,\bar\mu)$ into $\tilde L(\mu,\bar\mu)$ defined by Eq. (4.9):

$$\tilde L^{\rm ds}(\mu,\bar\mu) = \frac{1}{2}(\mu+\bar\mu)(1-b)I_b + I(b). \tag{4.20}$$

It possesses the correct $U(1)$ transformation properties

$$\delta_\omega\tilde L^{\rm ds} = i\omega(\mu-\bar\mu)(1-b)I_b = i\omega(\varphi-\bar\varphi), \tag{4.21}$$
$$\delta_\omega(\varphi-\bar\varphi) = 4i\omega(\tilde L^{\rm ds} - I).$$

Equation (4.10) with the substitution $H \to I(b)$ provides an off-shell description of the considered restricted class of the $U(1)$ duality-symmetric theories in the μ representation. Using Eqs. (4.7) and (4.15), one can find

$$\varphi L_\varphi + \bar\varphi L_{\bar\varphi} = \frac{1}{2}(\mu+\bar\mu)(1-\mu\bar\mu)I_b \tag{4.22}$$

and, substituting this into (4.20), show that the analytic functions $I(b)$ satisfying the condition (4.14) constitute a particular class of the invariant functions $I(\varphi,\bar\varphi)$ defined in (2.17):

$$I[b(\varphi,\bar\varphi)] = L(\varphi,\bar\varphi) - \varphi L_\varphi - \bar\varphi L_{\bar\varphi} \equiv I(\varphi,\bar\varphi).$$

This class of functions $I(\varphi,\bar\varphi)$ is characterized by the presence of a nonzero term of fourth order in Maxwell field strength in their $(\varphi,\bar\varphi)$ expansion, $I(\varphi,\bar\varphi) = I_b(0)\varphi\bar\varphi + \ldots$.

Note that the general rescaling (2.18) which preserves the $SO(2)$ duality corresponds in the μ representation to the rescaling $I(b) \to rI(b)$. In particular, (2.19) corresponds to the reflection $I(b) \to -I(b)$. In Section 5, we shall consider the impact of this reflection on the Lagrangian of the BI theory.

The basic algebraic problem of the μ representation is to restore the function $\mu(\varphi,\bar\varphi)$ and then $b(\varphi,\bar\varphi)$ by the given inverse function $\varphi(\mu,\bar\mu)$ in (4.15). Once the latter function is analytic, the analyticity of $\mu(\varphi,\bar\varphi)$ is guaranteed by the implicit function theorem. The basic algebraic equation for the function $b(\varphi,\bar\varphi)$

$$(b+1)^2\varphi\bar\varphi = b[(\varphi+\bar\varphi) - I_b(b-1)^2]^2 \tag{4.23}$$

and the corresponding representation for $\mu(\varphi,\bar\varphi)$,

$$\mu = -\frac{\bar\varphi - b\varphi - 2b(b-1)I_b}{I_b(1-b^2)}, \tag{4.24}$$

follow from Eqs. (4.15). In the next section, we shall see that the relations (4.23) and (4.24) are helpful in seeking the explicit solutions of the $SO(2)$ duality constraint.

Finally, let us analyze the discrete duality of $\tilde L(\mu,\bar\mu)$ (4.9). In the μ representation, the appropriate discrete transformations are

$$\Lambda\mu(\nu,\bar\nu) \equiv \mu(-\nu,-\bar\nu) = -\mu(\nu,\bar\nu). \tag{4.25}$$

The discrete self-duality of $\tilde L(\mu,\bar\mu)$ is then equivalent to the symmetry

$$\Lambda H(\mu,\bar\mu) \equiv H(-\mu,-\bar\mu) = H(\mu,\bar\mu), \tag{4.26}$$

which guarantees the correct Λ transformation (2.29) of the full Lagrangian (4.9).

5. EXAMPLES OF DUALITY-SYMMETRIC SYSTEMS

5.1. Born–Infeld Theory

The Lagrangian of the BI theory has the following form in terms of complex invariants (2.2):

$$L(\varphi,\bar\varphi) = [1 - Q(\varphi,\bar\varphi)], \tag{5.1}$$

where

$$Q(\varphi,\bar\varphi) = \sqrt{1+X}, \tag{5.2}$$
$$X(\varphi,\bar\varphi) \equiv (\varphi+\bar\varphi) + (1/4)(\varphi-\bar\varphi)^2.$$

The power expansion of the BI Lagrangian is

$$L = -\frac{1}{2}(\varphi+\bar\varphi) + \frac{1}{2}\varphi\bar\varphi - \frac{1}{4}\varphi\bar\varphi(\varphi+\bar\varphi) \tag{5.3}$$
$$+ \frac{1}{8}\varphi\bar\varphi(3\varphi\bar\varphi + \varphi^2 + \bar\varphi^2) + O(\varphi^5).$$

In the BI theory, the function (2.5) has the following explicit form:

$$P_{\alpha\beta}(F) = i\partial L/\partial F^{\alpha\beta} \tag{5.4}$$

$$= -iF_{\alpha\beta}Q^{-1}(\varphi,\bar\varphi)\left[1+\frac{1}{2}(\varphi-\bar\varphi)\right];$$

and the basic $U(1)$ transformation of the scalar variable is

$$\delta_\omega\varphi = -2i\omega\frac{\varphi\left[1+\frac{1}{2}(\varphi-\bar\varphi)\right]}{Q}. \qquad (5.5)$$

The function $G(\varphi,\bar\varphi)$, relating the variables $V_{\alpha\beta}$ and $F_{\alpha\beta}$ and defined by Eq. (3.16), is given by the expression

$$G = \frac{1}{2}\left\{1+Q^{-1}\left[1+\frac{1}{2}(\varphi-\bar\varphi)\right]\right\}. \qquad (5.6)$$

Let us first discuss the μ representation of BI theory. It is easy to find the relations

$$\varphi = \frac{2\bar\mu(1+\mu)^2}{(1-\mu\bar\mu)^2}, \quad \bar\varphi = \frac{2\mu(1+\bar\mu)^2}{(1-\mu\bar\mu)^2} \qquad (5.7)$$

which correspond to the following choice of the invariant function in the μ representation (4.15):

$$I(b) = \frac{2b}{b-1}, \quad I_b = -\frac{2}{(b-1)^2} \qquad (5.8)$$

(with $b=\mu\bar\mu$). Using this choice of the auxiliary function in (4.23), we obtain the quadratic equation for the invariant variable b

$$\varphi\bar\varphi b^2 + [2\varphi\bar\varphi - (\varphi+\bar\varphi+2)^2]b + \varphi\bar\varphi = 0. \qquad (5.9)$$

The invariant and linearly transforming functions b and μ obtained by solving (5.9) and using the general formulas (4.7) or (4.24) are given by the expressions

$$b = \frac{\varphi\bar\varphi}{\left[1+Q+\frac{1}{2}(\varphi+\bar\varphi)\right]^2}, \qquad (5.10)$$

$$\mu = G^{-1}-1 = \frac{Q-1-\frac{1}{2}(\varphi-\bar\varphi)}{Q+1+\frac{1}{2}(\varphi-\bar\varphi)}.$$

The corresponding representations for the off- and on-shell BI Lagrangian read

$$\tilde{\mathcal{L}}(\varphi,\mu) = \frac{2b}{b-1} + \frac{\varphi(\mu-1)}{2(1+\mu)} + \frac{\bar\varphi(\bar\mu-1)}{2(1+\bar\mu)}, \qquad (5.11)$$

$$\tilde L(\mu,\bar\mu) = \frac{\mu+\bar\mu+2b}{b-1}.$$

Note that the authors of [11] considered a polynomial off-shell representation of the BI Lagrangian with two complex auxiliary fields. The basic auxiliary field χ of this representation is related to our fields φ,μ, and $b=\mu\bar\mu$ as follows:

$$\chi + \frac{1}{2}\chi\bar\chi = \varphi, \quad \chi = \frac{2(\mu+b)}{b-1}, \qquad (5.12)$$

$$\tilde L(\mu,\bar\mu) = -\frac{1}{2}(\chi+\bar\chi).$$

Let us also study the original (F,V) representation for the BI case. Our aim is to find $\mathcal{E}(a)$ as a function of the variable

$$a \equiv \nu\bar\nu = \frac{4b}{(b-1)^4} \qquad (5.13)$$

[recall Eq. (4.17)]. Introducing $t\equiv(b-1)^{-1}$, one finds that t satisfies the following quartic equation:

$$t^4 + t^3 - \frac{1}{4}\nu\bar\nu = 0, \quad t(\nu=\varphi=0) = -1. \qquad (5.14)$$

It allows one to express t in terms of $a\equiv\nu\bar\nu$:

$$t(a) = -1 - \frac{a}{4} + \frac{3a^2}{16} - \frac{15a^3}{64} + \dots. \qquad (5.15)$$

One can easily write a closed expression for $t(a)$ as the proper solution of (5.14), but we do not present it here.

Now we are ready to find the invariant self-interaction $\mathcal{E}(\nu\bar\nu)$ for this case. Taking into account Eqs. (4.19) and (5.8), we find a simple expression for the self-interaction through the real variables b or $t(a)$ (see also [8])

$$\mathcal{E}_{\rm BI}[a(b)] = \frac{2b(1+b)}{(1-b)^2} = 2[2t^2(a) \qquad (5.16)$$

$$+ 3t(a) + 1] = \frac{a}{2} - \frac{a^2}{8} + \frac{3a^3}{32} + \dots.$$

It is easy to show that (4.23) is reduced to a quadratic equation only for the one-parameter family of functions

$$I_b = -2r/(b-1)^2, \qquad (5.17)$$

which corresponds to performing the transformation (2.18) on the BI Lagrangian (5.1). A new duality-symmetric Lagrangian is obtained in the case $r=-1$:

$$L^{(-)} = -1 + \sqrt{1-\varphi-\bar\varphi+\frac{1}{4}(\varphi-\bar\varphi)^2} \qquad (5.18)$$

$$= -1 + \sqrt{1+\mathbf{E}^2-\mathbf{B}^2-(\mathbf{E}\cdot\mathbf{B})^2},$$

where $\mathbf{E}$ and $\mathbf{B}$ are electric and magnetic fields, respectively. This Lagrangian is obtained from the BI one (5.1) by changing its overall sign and making the replacement $F_{mn}\to\tilde F_{mn} = \frac{1}{2}\epsilon^{mnkl}F_{kl}$, or

$$\mathbf{E}\to\mathbf{B}, \quad \mathbf{B}\to-\mathbf{E}. \qquad (5.19)$$

It would be interesting to find out the physical meaning and implications of this "magnetic" counterpart of the BI theory.

5.2. Exact Duality-Symmetric Lagrangians Corresponding to Solvable Algebraic Equations

The initial data for restoring Lagrangians $L^{\rm ds}(\varphi,\bar\varphi)$ by the known function $I(b)$ in the μ representation is Eq. (4.23) for b and the following representation for the Lagrangian (4.20),

$$\tilde L^{\rm ds} = -\frac{1}{2}\left(\frac{1-b}{1+b}\right)[\varphi+\bar\varphi+4bI_b(b)] + I(b), \tag{5.20}$$

which is obtained by substituting expression (4.24) for μ into (4.20). The key idea of finding out new explicit examples of duality-symmetric models is to pick up those $I(b)$ for which the basic equation (4.23) is simplified as much as possible. Below, we analyze several examples of the function $I(b)$ which turn (4.23) into solvable algebraic equations for $b(\varphi,\bar\varphi)$.

As was already mentioned, the quadratic equation is obtained only in the case of BI theory (5.8) and its "magnetic" counterpart (5.17) (with $r=-1$).

Next in complexity is the following ansatz for I_b:

$$I_b = -\frac{2-cb}{(1-b)^2} \tag{5.21}$$
$$\Rightarrow I(b) = (c-2)\frac{b}{1-b} + c\ln(1-b),$$

where c is some constant and we employed the conditions $I(0)=0$, $I_b(0)=-2$. Being substituted into (4.23), this ansatz gives the cubic algebraic equation for the unknown $b(\varphi,\bar\varphi)$

$$c^2b^3 - b^2[4c+2c(\varphi+\bar\varphi)+\varphi\bar\varphi] \tag{5.22}$$
$$+ b[(\varphi+\bar\varphi+2)^2 - 2\varphi\bar\varphi] - \varphi\bar\varphi = 0.$$

It is straightforward to write the explicit solution of this equation for $b(\varphi,\bar\varphi)$ as the appropriate analytic function of $\varphi,\bar\varphi$ (vanishing at $\varphi=\bar\varphi=0$) and to find the precise expression for the related $SO(2)$ duality-symmetric Lagrangian by substituting this solution into (5.20).

The case $c=0$ yields the BI theory, while for any other value of c we obtain new examples of duality-invariant systems. In the special case $c=2$, I_b and I in Eq. (5.21) are simplified to $I_b=-2(1-b)^{-1}$, $I(b)=2\ln(1-b)$. With this choice, the relation between different auxiliary-field representations is also simplified:

$$a = \frac{4b}{(b-1)^2}, \quad b(a) = \frac{a+2-2\sqrt{1+a}}{a}, \tag{5.23}$$
$$\mathcal{E}(a) = 2(\sqrt{1+a}-1) - 2\ln\frac{1}{2}(1+\sqrt{1+a}).$$

A different ansatz for I_b, also leading to a comparatively simple algebraic equation for b, is as follows:

$$I_b = -\frac{2\sqrt{1-cb}}{(b-1)^2}. \tag{5.24}$$

Equation (4.23) is reduced to

$$(b+1)^2\varphi\bar\varphi - b(\varphi+\bar\varphi)^2 - 4b(1-cb) \tag{5.25}$$
$$= 4(\varphi+\bar\varphi)b\sqrt{1-cb},$$

which is equivalent to a fourth-order equation. In the limit $c\to 0$, Eq. (5.25) becomes quadratic and one recovers the BI theory.

One more solvable ansatz for I_b is

$$I_b = -2\frac{1}{(1-cb)(b-1)^2}. \tag{5.26}$$

It reduces (4.23) to the following equation:

$$(1-cb)^2(b+1)^2\varphi\bar\varphi = b[(1-cb)(\varphi+\bar\varphi)+2]^2.$$

5.3. Discrete-Duality Examples

Let us firstly consider, directly in the original $\varphi,\bar\varphi$ representation, two simple examples of Lagrangians exhibiting discrete self-duality.

The first example is the Lagrangian which depends on a single real variable $\phi=\varphi+\bar\varphi$

$$L = 1-\sqrt{1+\phi}. \tag{5.27}$$

The second example is the holomorphic nonlinear Lagrangian

$$L_h(\varphi,\bar\varphi) = l(\varphi)+\bar l(\bar\varphi), \quad l(\varphi) = 1-\sqrt{1+\varphi}. \tag{5.28}$$

It is a straightforward exercise to check that both these Lagrangians respect self-duality under Legendre transformation as was defined in Section 2.2. At the same time, they are not $SO(2)$ duality-symmetric.

Two other examples of systems with a discrete duality can be introduced in the framework of ν representation. The first one corresponds to the choice

$$E = \frac{1}{2}M^2, \quad M = \nu+\bar\nu; \tag{5.29}$$

then, after eliminating auxiliary fields, the final Lagrangian $L(\varphi,\bar\varphi)$ is a function of the single real variable $\phi=\varphi+\bar\varphi$. The basic algebraic equation is cubic,

$$\phi = M(1+M)^2, \tag{5.30}$$

and it can be solved in radicals

$$M(\phi) = -\frac{2}{3} + A_+(\phi) + A_-(\phi) \tag{5.31}$$
$$= \phi - 2\phi^2 + 7\phi^3 - 24\phi^4 + \ldots,$$

$$A_{\pm}(\phi) = \sqrt[3]{\frac{1}{27} + \frac{\phi}{2} \pm \sqrt{B(\phi)}},$$
$$B(\phi) = \frac{1}{27}\phi + \frac{1}{4}\phi^2.$$

Despite the presence of radical $\sqrt{B(\phi)}$ in $A_{\pm}(\phi)$, the function $M(\phi)$ is analytic.

A more complicated Lagrangian corresponds to the following choice of the even self-interaction function $E(\nu, \bar{\nu}) = E(-\nu, -\bar{\nu})$:

$$E(\nu, \bar{\nu}) = \frac{1}{2}(\nu^2 + \bar{\nu}^2), \quad E_\nu = \nu = \mu, \qquad (5.32)$$
$$L^{\text{int}}(\varphi, \bar{\varphi}) = \frac{1}{2}(\nu^2 + \bar{\nu}^2) + \nu^3 + \bar{\nu}^3.$$

The holomorphic algebraic equation

$$\varphi = \nu + 2\nu^2 + \nu^3 \qquad (5.33)$$

can be explicitly solved similarly to Eq. (5.30). The corresponding Lagrangian $L(\varphi, \bar{\varphi})$ is holomorphic like (5.28).

6. CONCLUSIONS

We introduced a new (F, V) representation for the Lagrangians of nonlinear electrodynamics and showed that it provides a simple description of systems with $U(1)$ duality or/and discrete self-duality in terms of the real function of auxiliary bispinor complex fields $E(V, \bar{V})$. This function encodes the entire self-interaction in the (F, V) representation. The duality properties prove to be related to some linear off-shell symmetries of this general function E. We also defined an alternative μ representation and demonstrated its convenience and efficiency for constructing new explicit examples of duality-symmetric Lagrangians.

The auxiliary linearly transforming variables have also been used to construct the general solution of the $U(n)$ duality constraint for the interaction of n Abelian gauge fields in [9]. The generalization to the $U(n)$ case is a straightforward extension of the formalism described above, so we do not present it here and refer the interested reader to [9].

It is an interesting task to extend our consideration to the case of $N = 1$ and $N = 2$ supersymmetric extensions of nonlinear electrodynamics [3] in order to obtain a general characterization of the corresponding duality-symmetric systems. One more urgent problem is to define an analog (if existing) of the (F, V) representation for non-Abelian BI theory and its supersymmetric extensions. It could shed more light on the structure of these theories, which have deep implications in string theory and still remain to be completely understood.

ACKNOWLEDGMENTS

This work was partially supported by INTAS (grant no. 00-254), the Russian Foundation for Basic Research (RFBR) (project no. 03-02-17440), RFBR-DFG grant no. 02-02-04002, grant DFG 436 RUS 113/669, and a grant from the Heisenberg–Landau Program.

REFERENCES

1. M. K. Gaillard and B. Zumino, Nucl. Phys. B **193**, 221 (1981).
2. G. W. Gibbons and D. A. Rasheed, Nucl. Phys. B **454**, 185 (1995); hep-th/9506035.
3. S. M. Kuzenko and S. Theisen, Fortschr. Phys. **49**, 273 (2001); hep-th/0007231.
4. M. Perry and J. H. Schwarz, Nucl. Phys. B **489**, 47 (1997); hep-th/9611065.
5. M. K. Gaillard and B. Zumino, in *Duality and Supersymmetric Theories*, Ed. by D. I. Olive and P. C. West (Cambridge Univ. Press, Cambridge, 1999), p. 33; hep-th/9712103.
6. M. Hatsuda, K. Kamimura, and S. Sekia, Nucl. Phys. B **561**, 341 (1999); hep-th/9906103.
7. X. Bekaert and S. Cucu, Nucl. Phys. B **610**, 433 (2001); hep-th/0104048.
8. E. A. Ivanov and B. M. Zupnik, Nucl. Phys. B **618**, 3 (2001); hep-th/0110074.
9. E. A. Ivanov and B. M. Zupnik, in *Supersymmetries and Quantum Symmetries,* Ed. by E. Ivanov *et al.* (Dubna, 2002), p. 235; hep-th/0202203.
10. P. Pasti, D. Sorokin, and M. Tonin, Phys. Rev. D **52**, R4277 (1995); hep-th/9506109; A. Nurmagambetov, Phys. Lett. B **436**, 289 (1998); hep-th/9804157; N. Berkovits, Phys. Lett. B **395**, 28 (1997); hep-th/9610134.
11. M. Roček and A. Tseytlin, Phys. Rev. D **59**, 106001 (1999); hep-th/9811232.
12. A. A. Tseytlin, in *The Many Faces of Superworld, Yu. Golfand Memorial Volume*, Ed. by M. A. Shifman (World Sci., Singapore, 2000), p. 417; hep-th/9908105.

Physics of Atomic Nuclei, Vol. 67, No. 12, 2004, pp. 2200–2208. Translated from Yadernaya Fizika, Vol. 67, No. 12, 2004, pp. 2225–2233.
Original Russian Text Copyright © 2004 by Gaponov.

ELEMENTARY PARTICLES AND FIELDS
Theory

Induced Double-Beta Processes in Electron Fluxes as Resonance Reactions in Weak Interaction

Yu. V. Gaponov*

Russian Research Centre Kurchatov Institute, pl. Kurchatova 1, Moscow, 123098 Russia

Received January 13, 2004; in final form, June 2, 2004

Abstract—A theory of induced double-beta processes in electron beams is developed. It is shown that a resonance mechanism of the excitation of the ground state of an intermediate nucleus is realized in them, this mechanism being described in the single-state-dominance approximation, where the process in question is broken down into two stages, the excitation of a dominant state and its decay. This approximation is valid irrespective of the features of this state, both for allowed (for a 1^+ state of the intermediate nucleus) and for forbidden transitions. An analysis of the resonance mechanism reveals that its inclusion in double-beta-decay processes requires introducing additional diagrams that describe the gamma decay of virtual intermediate states. The inclusion of such corrections may lead to a decrease in the expected half-life and to a change in the beta spectrum. Effects associated with the interference between the two stages of a double-beta process are estimated, and it is shown that their influence can be significant if the time interval between these stages is less than or on the order of the lifetime of the dominant state.
© 2004 MAIK "Nauka/Interperiodica".

At the present time, experimental and theoretical investigation of the double-beta decay of nuclei is one of the main lines of research into neutrino physics that are aimed at searches for effects beyond the standard model of electroweak interaction. The discovery of oscillations in solar- and reactor-neutrino fluxes became a first signal from physics beyond the Standard Model [1, 2]. It is obvious that a comprehensive investigation of these realms should involve exploring all possible channels of double-beta processes, including induced reactions that proceed via the excitation of nuclear states in inverse-beta-decay reactions and their subsequent decay to a final nucleus. As one of the versions of reactions inverse to processes of spontaneous double-beta decay, such reactions may contain important information about fine details of the mechanisms that are operative not only in standard double-beta nuclear transitions, where the lepton charge is conserved, but also in their nonstandard lepton-charge-violating counterparts.

The first results reported in the articles of our group in the late 1990s, where we attracted the attention of researchers to this line of investigation for the first time, concerned the development of the theory of double-beta processes induced in neutrino and antineutrino fluxes [3–5]. It was shown that, in reactions that are inverse to two-neutrino processes and which are realized in such fluxes, a mechanism of resonance excitation of the ground state of intermediate nuclei is operative, this mechanism being described in the single-state-dominance approximation, where the double-beta process in question proceeds in two stages. The excitation of the 1^+ ground state of an intermediate nucleus $A(N+1, Z-1)$ (if any) at the first stage is followed by its spontaneous decay through one of the two possible beta channels, to an $A(N-2, Z+2)$ or an $A(N, Z)$ nucleus, at the second stage. Among other things, it was indicated that the degree to which these two sequential states are independent of each other depends on the degree of violation of coherence of electron-emission processes, this coherence being due to their interplay that formally follows from the antisymmetrization operation. This approach was developed and formally applied to investigating some specific neutrino reactions in reactor and neutrino physics [6, 7].

However, induced weak processes may proceed not only in neutrino but also in electron fluxes [8]. In the latter case, they correspond to the inverse two-neutrino and neutrinoless reactions

$$e^- + A(N, Z) \to A(N+2, Z-2) + e^+ + 2\nu, \quad (1)$$

$$e^- + A(N, Z) \to A(N+2, Z-2) + e^+. \quad (2)$$

It should be emphasized that the above reactions in electron fluxes have two special features of great importance: the possibility of obtaining high-density fluxes and the possibility of obtaining monoenergetic fluxes whose time properties can be determined to a

*e-mail: gaponov@imp.kiae.ru

high precision, this enabling one to implement experiments that have no analogs in the neutrino case. We also note that reactions (1) and (2) are reactions inverse to the positron-type double-beta-decay processes

$$A(N,Z) \to A(N+2,Z-2) + 2e^+ + 2\nu, \qquad (3)$$

$$A(N,Z) \to A(N+2,Z-2) + 2e^+, \qquad (4)$$

which have not yet been observed experimentally even in the standard mode of two-neutrino double-beta decay. The number of nuclides capable of undergoing positron-type double-beta decay is rather small, so that a transition to electron-induced processes makes it possible to extend the number of objects appropriate for studying the special features of such processes.

We will now develop the theory of electron-induced weak reactions first of all for the case of two-neutrino double-beta processes [reactions of the type in (1)] and compare the results obtained in this way with their counterparts for the case of neutrino-induced double-beta transitions, which was considered in [3]. As is well known, the double-beta-process amplitude $T_{2\beta}$ is generally described by four diagrams and is given by [9]

$$\begin{aligned}
&(2\pi)^4\delta^4\left(\sum p_f - \sum p_i\right) T_{2\beta} \qquad (5)\\
&= i\frac{G_\beta^2}{2}\sum_m \int d^4x' d^4x''\\
&\times \left[\langle \nu_1|l^\mu(x'')|e_1\rangle\langle \nu_2\bar{e}_2|l^\nu(x')|0\rangle\right.\\
&\times \langle m|h_\mu^+(x'')|i\rangle\langle f|h_\nu^+(x')|m\rangle\\
&- \langle \nu_2|l^\mu(x'')|e_1\rangle\langle \nu_1\bar{e}_2|l^\nu(x')|0\rangle\\
&\times \langle m|h_\mu^+(x'')|i\rangle\langle f|h_\nu^+(x')|m\rangle\\
&- \langle \nu_1\bar{e}_2|l^\mu(x'')|0\rangle\langle \nu_2|l^\nu(x')|e_1\rangle\\
&\times \langle m|h_\mu^+(x'')|i\rangle\langle f|h_\nu^+(x')|m\rangle\\
&+ \langle \nu_2\bar{e}_2|l^\mu(x'')|0\rangle\langle \nu_1|l^\nu(x')|e_1\rangle\\
&\left.\times \langle m|h_\mu^+(x'')|i\rangle\langle f|h_\nu^+(x')|m\rangle\right],
\end{aligned}$$

where $l(x)$ and $h(x)$ are, respectively, the leptonic and hadronic components of the weak current; G_β is the beta-decay current; and summation is performed over all states m of the intermediate nucleus $A(N+1,Z-1)$. The differential cross section for the electron-induced process proceeding in a flux where the energy E_{e_1} is fixed is calculated by a standard method. The result is

$$\begin{aligned}
\frac{d\sigma(E_{e_1})}{dE_{\nu_1}dE_{\nu_2}dE_{\bar{e}_2}} &= \frac{G_\beta^4\lambda^4}{32\pi^5}F(-Z,E_{e_1}) \qquad (6)\\
&\times F(-Z+2,E_{\bar{e}_2})E_{\nu_1}^2E_{\nu_2}^2p_{\bar{e}_2}E_{\bar{e}_2}\\
&\times \delta(\Delta_{if} - 2m_e + E_{e_1} - E_{\nu_1} - E_{\nu_2} - E_{\bar{e}_2})\\
&\times \int \frac{dO_{\nu_1}}{4\pi}\frac{dO_{\nu_2}}{4\pi}\frac{dO_{\bar{e}_2}}{4\pi}|M_{2\beta}|^2,
\end{aligned}$$

where E_{ν_1} and E_{ν_2} are the energies of product neutrinos; $p_{\bar{e}_2}$ and $E_{\bar{e}_2}$ are, respectively, the momentum and the energy of the product positron; $(\Delta_{if} - 2m_e)$ is the energy threshold for the double-beta process being studied [it is determined by the masses of the initial (i) and the final (f) nuclide involved in the reaction and by the electron mass m_e]; $F(-Z,E_{e_1})$ and $F(-Z+2,E_{\bar{e}_2})$ are, respectively, the incident-electron and the emitted-positron Fermi function; λ is the ratio of the Gamow–Teller and the Fermi beta-decay constant; and the integral is taken over all angles of the emitted-neutrino (dO_{ν_1} and dO_{ν_2}) and emitted-positron ($dO_{\bar{e}_2}$) momenta. The quantity $|M_{2\beta}|^2$ involves the double-beta-transition matrix elements, energy factors that are associated with the inclusion of intermediate states, and correlation parameters depending on the neutrino and positron emission angles. Its general form can be found, for example, in [3]. If, however, we restrict our consideration to calculating cross sections for induced processes, where this quantity is integrated over all angles, it assumes a simple form,

$$\begin{aligned}
|M_{2\beta}|^2 &= (4)\sum_{m,m'}\langle f|\sigma\tau|m\rangle^+\langle m|\sigma\tau|i\rangle \qquad (7)\\
&\times \langle f|\sigma\tau|m'\rangle^+\langle m'|\sigma\tau|i\rangle\\
&\times \left\{K_m^+K_{m'} + L_m^+L_{m'} + \frac{1}{2}(K_m^+L_{m'} + L_m^+K_{m'})\right\}.
\end{aligned}$$

Here, $\langle f|\sigma\tau|m\rangle$ and $\langle m|\sigma\tau|i\rangle$ are the reduced matrix elements of the Gamow–Teller type that describe, respectively, the beta transition from the state m of the intermediate nucleus to the final state f and the beta transition from the initial state i to the state m of the intermediate nucleus, while the quantities K^+K, L^+L, and $K^+L + L^+K$ take into account the contributions of various intermediate states of the nucleus $A(N+1,Z-1)$ and, as a matter of fact, determine the mechanism of the reaction being studied. Investigation of neutrino-induced weak processes revealed that, in the particular case where the ground state of the intermediate nucleus has a spin–parity of 1^+, this mechanism is of a resonance character and that the state in question plays a dominant role in this mechanism [3]. This result was obtained in the approximation where the correlation between the basis functions for the stages of our beta process—excitation of the ground state of the intermediate nucleus and its subsequent decay—was disregarded, so that these stages were assumed to be independent.

All these features of the induced-reaction mechanism are directly related to the form of the quantities K_0 and L_0 describing transitions that involve the

ground state of the intermediate nucleus, which are determined by the structure of the factors K and L usually introduced in the theory of double-beta decay (see, for example, [9, 10]). In considering the case of electron-induced reactions in the present study, we will not follow, however, this standard way and will analyze the possibility of exploring, in double-beta processes, additional properties that depend on the width of the time interval within which the physical process in question occurs. In order to take these properties into account, we introduce the quantities K and L in a somewhat modified form that includes this dependence. As is well known, the factors in question arise upon integrating, with respect to time, ordinary energy features associated with the matrix elements for the two subsequent stages of the induced reaction that proceed at the time instants, t'' and t',

$$I = \lim_{A\to\infty} \int_{-A}^{A} dt' \int_{-T}^{0} d(t''-t') e^{-i\alpha t'} e^{-i\beta t''}, \qquad (8)$$

where α and β are parameters that, in general, describe these energy features including the energies of the states involved in these stages at, respectively, the instant t'' and the instant t' [10]. Assuming that the time interval within which there occur the production and the decay of the intermediate nucleus (that is, the interval between the two basic stages of the induced reaction) is bounded by the quantity T, one can show [10] that the integral I (8) has the form

$$I = 2\pi i\delta(\alpha+\beta)\frac{1-e^{i\beta T}}{\beta}. \qquad (9)$$

With the aid of such relations, the quantities K and L for electron-induced processes can be represented in the following modified form:

$$\begin{aligned} K = {} & \sum_m \langle f|\sigma\tau|m\rangle\langle m|\sigma\tau|i\rangle \qquad (10)\\ & \times [(E_{\nu_1} - E_{e_1} + E_m - E_i)^{-1} \\ & \times (1 - e^{i(E_{\nu_1} - E_{e_1} + E_m - E_i)T}) \\ & + (E_{\nu_1} + E_m - E_i + E_{\bar{e}_2})^{-1} \\ & \times (1 - e^{i(E_{\nu_1} + E_m - E_i + E_{\bar{e}_2})T})], \end{aligned}$$

$$\begin{aligned} L = {} & \sum_m \langle f|\sigma\tau|m\rangle\langle m|\sigma\tau|i\rangle \qquad (11)\\ & \times [(E_{\nu_2} - E_{e_1} + E_m - E_i)^{-1} \\ & \times (1 - e^{i(E_{\nu_2} - E_{e_1} + E_m - E_i)T}) \\ & + (E_{\nu_2} + E_m - E_i + E_{\bar{e}_2})^{-1} \\ & \times (1 - e^{i(E_{\nu_2} + E_m - E_i + E_{\bar{e}_2})T})]. \end{aligned}$$

In the limit $T \to \infty$, these expressions reduce to a standard form that is used in the literature [9, 10].

That the dependence on the parameter T, which has the meaning of the time interval within which there occur the interaction of the incident electron with the target nucleus at the first reaction stage and positron emission at the second stage, is introduced in these quantities is a radically new point in the approach developed here. In calculating double-beta-decay processes, this parameter is usually made to tend to infinity, this corresponding to the use of an experimental procedure where one observes the very fact of decay, irrespective of the instant of electron-pair production. In the case of our electron-induced process, however, a drastically different experimental situation is possible in principle, that where this interval is fixed experimentally. It turns out that this modification makes it possible to study the effect of the correlation of the sequential reaction stages and their interference (which arises for a specific choice of parameters that characterize the process in question) on the cross section for this process. Taking this circumstance into account, we will not use the $T \to \infty$ approximation in our investigation from the outset; instead, we will find out how the results depend on the parameter T, and one can in principle test this dependence experimentally.

We would like to emphasize yet another important feature of the modification associated with introducing T-dependent time features in the theory. Within this theoretical framework, the concept of the cross section $\sigma_{2\beta}$ for the inverse-beta-transition reaction

$$e^- + A(N,Z) \to e^+ + 2\nu + A(N+2, Z-2)$$

remains physically meaningful only in the limit $T \to \infty$. In the remaining cases, it is necessary to introduce a quantity that, by analogy with its counterpart in reaction kinetics, can be referred to as the effective time-dependent constant of the rate of the double-beta process that, via the reaction of electrons with nuclei $A(N,Z)$, produces, in the final state, an ensemble that includes two neutrinos, a positron, and a nucleus $A(N+2, Z-2)$. This quantity, which determines the relative rate of the production of the final ensemble of particles at the instant T, coincides, after the completion of all reaction stages over a time smaller than or equal to T, with the quantity $\dfrac{dN(T)}{N_0 dT}$, where $N(T)$ is the number of product nuclei $A(N+2, Z-2)$ in the final state and N_0 is the initial number of nuclei $A(N,Z)$; that is,

$$\lambda(T) = \frac{1}{N_0}\frac{dN(T)}{dT}. \qquad (12)$$

In the limiting case of $T \to \infty$, this quantity is related to the total cross section for the induced double-beta

process by the equation

$$\lim_{T\to\infty}\lambda(T)=\lim_{T\to\infty}\frac{1}{N_0}\frac{dN(T)}{dT}=\sigma_{2\beta}I(e), \quad (13)$$

where $I(e)$ is the incident-electron-flux intensity, which, in our case, is assumed to be independent of time. By analogy with [13], we introduce the effective constant of the rate of the double-beta process at a fixed energy E_{e_1} of incident particles, $\lambda(T,E_{e_1})$, and its corresponding differential characteristic additionally dependent on the emitted-particle energy E_{e_2},

$$\lambda(T,E_{e_1})=\sigma_{2\beta}(T,E_{e_1})I(E_{e_1}), \quad (14)$$
$$\frac{d\lambda(T,E_{e_1},E_{e_2})}{dE_{e_2}}=\frac{d\sigma_{2\beta}(T,E_{e_1},E_{e_2})}{dE_{e_2}}I(E_{e_1}),$$

where $I(E_{e_1})$ is the flux of particles having the above energy. In the following, these quantities will be used instead of the corresponding total and differential cross sections in the case where we will study the dependence on the parameter T; in contrast to the cross sections, they are dependent on the incident-particle flux. It should be emphasized that effective decay-rate constants have a limited application; in general, it is necessary to go over from the diagram technique to time-dependent perturbation theory by using Heitler's classical procedure [11].

Induced processes possess an important special feature that determines the reaction mechanism. In the calculation of the differential cross section by formula (6), the quantities K and L appear in the matrix element $|M_{2\beta}|^2$ in combinations of the form K^+K, L^+L, or K^+L+L^+K that involve sums over all pairs of possible intermediate states of the nucleus $A(N+1,Z-1)$. At energies of the incident electron flux in excess of the threshold energy for the excitation of the ground state of the intermediate nucleus $A(N+1,Z-1)$, some of the reaction channels prove to be open and to be in the physical region, with the result that there occurs a real production of some excited states of the intermediate nucleus. In studying double-beta processes that include two sequential beta decays, one must take into account, however, only those channels in which the width of product excited states with respect to decay through the beta channel associated with the second reaction stage exceeds the decay widths with respect to other channels. At the same time, the gamma-decay widths of real excited nuclear states are, as a rule, orders of magnitude larger than their beta-decay widths; this suggests that, following its formation, an excited state will go over, with a high probability, to low-lying states of the intermediate nucleus via photon emission and, only after that, to a final nucleus $A(N+2,Z-2)$ via beta decay. Only a small fraction of excited states go over to a final nucleus directly via a prompt beta decay, but it is precisely this fraction that corresponds to the double-beta process in question. It is obvious that the ratio of the probabilities of the first and the second decay path is proportional to the ratio of the widths of the excited state in question with respect to gamma and beta decays. The ground state m_0 of the intermediate nucleus $A(N+1,Z-1)$ is the only exclusion from this general rule: there are no transitions from this state to other states of this nucleus, so that only the decay through the beta channel to a final nucleus $A(N+2,Z-2)$ is possible for it. It follows that, among the entire set of possible pairs of intermediate states contributing to the double-beta process, only one term, that which is associated with the excitation and decay of the ground state m_0 of the $A(N+1,Z-1)$ nucleus, its total beta-decay width being γ_0, survives in the combinations K^+K, L^+L, and K^+L+L^+K. As a result, it is legitimate to describe induced double-beta processes within the single-level approximation, where K^+K, L^+L, and $\frac{1}{2}(K^+L+L^+K)$ are approximated by the quantities $|K_0|^2$, $|L_0|^2$, and $\mathrm{Re}(K_0^+L_0)$. It should be emphasized that, according to the above argument, this approximation, which is referred to as the single-level-dominance approximation, where the ground-state level of the $A(N+1,Z-1)$ nucleus is dominant, must be valid for any features of the dominant state. If the spin–parity of the ground state is 1^+, the approximation in question corresponds to the allowed type of beta transitions connecting the initial and final states to the ground state of the intermediate nucleus [5]. If we now retain only the leading singularities in $|K_0|^2$, $|L_0|^2$, and $\mathrm{Re}(K_0^+L_0)$, then these quantities assume the form

$$|K_0|^2\approx|\langle f|\sigma\tau|m_0\rangle|^2|\langle m_0|\sigma\tau|i\rangle|^2 \quad (15)$$
$$\times\frac{1}{(E_{\nu_1}-E_r)^2+\gamma_0^2/4}(1+e^{-\gamma_0T}$$
$$-2\cos((E_{\nu_1}-E_r)T)e^{-\gamma_0T/2}),$$

$$|L_0|^2\approx|\langle f|\sigma\tau|m_0\rangle|^2|\langle m_0|\sigma\tau|i\rangle|^2$$
$$\times\frac{1}{(E_{\nu_2}-E_r)^2+\gamma_0^2/4}$$
$$\times(1+e^{-\gamma_0T}-2\cos((E_{\nu_2}-E_r)T)e^{-\gamma_0T/2}),$$

$$\mathrm{Re}(K_0^+L_0)\approx|\langle f|\sigma\tau|m_0\rangle|^2|\langle m_0|\sigma\tau|i\rangle|^2$$
$$\times\frac{1}{(E_{\nu_1}-E_r)^2+\gamma_0^2/4}\frac{1}{(E_{\nu_2}-E_r)^{-1}+\gamma_0^2/4}$$
$$\times\left\{[(E_{\nu_1}-E_r)(E_{\nu_2}-E_r)+\gamma_0^2/4]\right.$$
$$\left.\times[1+\cos((E_{\nu_1}-E_{\nu_2})T)e^{-\gamma_0T}\right.$$

$$- (\cos((E_{\nu_1} - E_r)T) + \cos((E_{\nu_2} - E_r)T))e^{-\gamma_0 T/2}] + \frac{\gamma_0}{2}(E_{\nu_1} - E_{\nu_2})[(\sin((E_{\nu_1} - E_r)T) - \sin((E_{\nu_2} - E_r)T))e^{-\gamma_0 T/2} + \sin((E_{\nu_1} - E_{\nu_2})T)e^{-\gamma_0 T}]\Bigg\},$$

$$E_r = E_{e_1} - E_{m_0} + E_i.$$

All of these quantities involve pole terms describing the process where the incident electron excites resonantly the ground state of the intermediate nucleus $A(N+1, Z-1)$. The last relation introduces the convenient quantity E_r, which corresponds to the excess of the electron energy above the threshold for the excitation of this state.

We note that this resonance mechanism of an induced double-beta process has a rather general character and also describes the case where the spin–parity of the ground state of the $A(N+1, Z-1)$ nucleus is different from 1^+. In this case, processes involving the induced excitation and decay of this state correspond to forbidden beta transitions, so that formula (6) for the cross section must be modified with allowance for this circumstance. However, this is not of crucial importance for the mechanism of induced transitions—its resonance character, which corresponds to the single-level-dominance approximation, will survive in the case of forbidden transitions as well.

Let us now consider the differential effective constant (14) of the rate of the induced double-beta transition being studied. For this, we multiply expression (6) by the flux of electrons having a specific energy, $I(E_{e_1})$; take into account the T dependence of K_0 and L_0, which follows from (15); and integrate this expression with respect to the energies of emitted neutrinos. As a result, we obtain

$$\frac{d\lambda(T, E_{e_1})}{dE_{\bar{e}_2}} \approx \frac{G_\beta^4 \lambda^4}{4\pi^4 \gamma_0} I(E_{e_1}) F(-Z, E_{e_1}) p_{\bar{e}_2} \quad (16)$$
$$\times E_{\bar{e}_2} F(-Z+2, E_{\bar{e}_2}) |\langle f|\sigma\tau|m_0\rangle|^2 \times (E_{e1} - E_m + E_i)^2 (E_{e2} - E_m + E_f)^2 \times |\langle m_0|\sigma\tau|i\rangle|^2 J(T),$$

$$J(T) = \frac{\gamma_0}{2\pi} \int dE_{\nu_1} dE_{\nu_2} \delta(\Delta_{if} - 2m_e - E_{\nu_1} - E_{\nu_2} + E_{e_1} - E_{\bar{e}_2}) \Bigg\{ \frac{1}{(E_{\nu_1} - E_r)^2 + \gamma_0^2/4} \times (1 + e^{-\gamma_0 T} - 2\cos((E_{\nu_1} - E_r)T)e^{-\gamma_0 T/2}) + \frac{1}{(E_{\nu_2} - E_r)^2 + \gamma_0^2/4}(1 + e^{-\gamma_0 T} - 2\cos((E_{\nu_2} - E_r)T)e^{-\gamma_0 T/2}) + \frac{1}{E_{\nu_1} + E_{\nu_2} - 2E_r} \times \Bigg[\Bigg(\frac{E_{\nu_1} - E_r}{(E_{\nu_1} - E_r)^2 + \gamma_0^2/4} + \frac{E_{\nu_2} - E_r}{(E_{\nu_2} - E_r)^2 + \gamma_0^2/4}\Bigg)(1 + \cos((E_{\nu_1} - E_{\nu_2})T)e^{-\gamma_0 T} - (\cos((E_{\nu_1} - E_r)T) + \cos((E_{\nu_2} - E_r)T))e^{-\gamma_0 T/2}) + \frac{\gamma_0}{2}\Bigg(\frac{1}{(E_{\nu_1} - E_r)^2 + \gamma_0^2/4} - \frac{1}{(E_{\nu_2} - E_r)^2 + \gamma_0^2/4}\Bigg) \times ((\sin((E_{\nu_1} - E_r)T) - \sin((E_{\nu_2} - E_r)T))e^{-\gamma_0 T/2} + \sin((E_{\nu_1} - E_{\nu_2})T)e^{-\gamma_0 T})\Bigg]\Bigg\}.$$

In the limit $T \to \infty$, expression (16) describes the differential cross section for the double-beta process being considered. If we retain only the first and the second term in the expression for $J(T \to \infty)$, the differential cross section for the electron-induced process assumes the form

$$\frac{d\sigma_{2\beta}(E_{e_1}, E_{\bar{e}_2})}{dE_{\bar{e}_2}} \approx \frac{G_\beta^4 \lambda^4}{4\pi^4 \gamma_0} |\langle f|\sigma\tau|m_0\rangle|^2 \quad (17)$$
$$\times (\Delta_{mf} - m_e - E_{\bar{e}_2})^2 p_{\bar{e}_2} E_{\bar{e}_2} F(-Z+2, E_{\bar{e}_2}) \times 2F(-Z, E_{e_1}) |\langle m_0|\sigma\tau|i\rangle|^2 J(T \to \infty)$$
$$\approx \frac{G_\beta^2 \lambda^2}{\pi} |\langle m_0|\sigma\tau|i\rangle|^2 F(-Z, E_{e_1})(E_{e_1} - E_{m_0} + E_i)^2 \frac{G_\beta^2 \lambda^2}{2\pi^3 \gamma_0} |\langle f|\sigma\tau|m_0\rangle|^2$$
$$\times (\Delta_{mf} - m_e - E_{\bar{e}_2})^2 p_{\bar{e}_2} E_{\bar{e}_2} F(-Z+2, E_{\bar{e}_2}),$$

$$J(T \to \infty) = \frac{1}{2\pi} \int dE_\nu \frac{\gamma_0}{(E_\nu - E_r)^2 + \gamma_0^2/4} = 1.$$

In (17), the factor proportional to $|\langle m_0|\sigma\tau|i\rangle|^2$ describes the cross section $\sigma_\beta(E_{e_1})$ for the excitation of the ground state m_0 of the intermediate nucleus $A(N+1, Z-1)$ by an incident electron with allowance for the Coulomb field of the nucleus $A(N, Z)$, whereas the second factor, which is proportional to $|\langle f|\sigma\tau|m_0\rangle|^2$, is the well-known expression for the differential spectrum of positrons from the β^+ decay of this state to the final state of the $A(N+2, Z-2)$ nucleus, this expression being normalized to the total width of the ground state of the intermediate nucleus with respect to all decay modes, including the decays through both the β^- and the β^+ channel.

The quantity $(\Delta_{mf} - m_e)$ is the energy threshold for the excitation of the ground state of the intermediate nucleus. Accordingly, the total cross section for the electron-induced process is given by

$$\sigma_{2\beta}(E_{e_1}) \approx \frac{G_\beta^2\lambda^2}{\pi}F(-Z, E_{e_1}) \times |\langle m_0|\sigma\tau|i\rangle|^2(E_{e_1} - E_{m_0} + E_i)^2 \times \frac{G_\beta^2\lambda^2}{2\pi^3\gamma_0}\int dE_{\bar{e}_2}|\langle f|\sigma\tau|m_0\rangle|^2 \times (\Delta_{mf} - m_e - E_{\bar{e}_2})^2 p_{\bar{e}_2}E_{\bar{e}_2}F(-Z+2, E_{\bar{e}_2}) \approx \sigma_\beta(E_{e_1})\frac{\gamma_{\beta^+}}{\gamma_0}, \quad (18)$$

where γ_{β^+} is the width of the ground state of the $A(N+1, Z-1)$ nucleus with respect to decay through the β^+ channel. This expression is similar to the formula for resonance-reaction cross sections, which is well known for the case of gamma rays. The result obtained for electron-induced processes is analogous to the corresponding result for neutrino-induced reactions that was previously obtained in [3] and shows that induced double-beta processes can indeed be considered as resonance processes in weak-interaction physics.

We will now return to expression (16) and investigate it for the case where the quantity T has specific values. Physically, this means that we take into account correlations between the first and the second reaction stage, fixing the time interval T within which these stages proceed. The dependence on this interval is determined by the integral $J(T)$. As can be seen from (16), the quantity $J(T)$ involves three terms. As a matter of fact, the first and the second term are similar, differing only by a change of variables in the integrand, and require, for their transformation, taking the standard integral that is given in (17) and which can straightforwardly be evaluated if one considers that, at the extremal point $E_\nu = E_r$, the integrand reaches the value $4/\gamma_0$ for an extremal-region width of about γ_0. As was shown above, these terms lead to the well-known expression for the cross section $\sigma_\beta(E_{e_1})$ describing the induced excitation of the ground state of the intermediate nucleus $A(N+1, Z-1)$ in an electron flux. Physically, they correspond to the resonance mechanism of the induced-process part that is not sensitive to the interference between the two sequential reaction stages. On the contrary, the third term is a direct consequence of the interference between the first and the second subprocess. By estimating these three terms, it can be shown that their contributions are controlled by the quantity $\gamma_0 T/2$, the third, interference, term being responsible for the main contribution to the integral $J(T)$ for $\gamma_0 T/2 \ll 1$ if, in addition, the condition $E_{\nu_1} \approx E_{\nu_2}$ is satisfied. This is possible if $0 < E_r < \Delta_{mf}$ ($\Delta_{mf} = E_m - E_f + m_e$), which physically corresponds to the region where the energy of the neutrino produced at the first stage of the process is close to the energy of the neutrino produced at the second stage. Here, the interference effect formally arises as a consequence of antisymmetrizing the amplitude of the process in the neutrino variables. The size of the region where the energies E_{ν_1} and E_{ν_2} overlap—this quantity is of importance for the manifestation of the above interference—is again determined by the width γ_0, which is extremely small for beta-decay processes (at a level of 10^{-16} to 10^{-12} eV or even below this), this corresponding to long lifetimes of the intermediate state (accordingly, 10^{-4} to 1 s or even more). An analysis reveals that interference effects are the most pronounced in the case where the parameter T, which specifies the time interval between electron interaction and positron production, is much less than $1/\gamma_0$, which is the lifetime of the intermediate state m_0. (Obviously, this time is not very long, since the coherence of the two sequential reaction stages can also be violated for some other reasons—for example, because of atomic collisions of the intermediate nucleus in a medium.) In this case, the integral $J(T)$ has the form

$$J(T) \approx \frac{1}{\pi}[2(1 - \cos((2E_m - E_{e_1} - E_{\bar{e}_2} - E_i - E_f)T) + ((2E_m - E_{e_1} - E_{\bar{e}_2} - E_i - E_f)T)\sin((2E_m - E_{e_1} - E_{\bar{e}_2} - E_i - E_f)T))] \quad (19)$$

and tends to zero at small values of the parameter T. Physically, this means that, if the time interval is much shorter than the lifetime of the intermediate nucleus, the number of nuclei that have passed the two reaction stages—production and decay—is small; therefore, the rate of production of positrons associated with the final stage of the induced double-beta process tends to zero. In the case of $\gamma_0 T/2 \geq 1$, the integral $J(T)$ becomes $J(T) \approx 3/4$ and is virtually independent of the parameter T (as in the limit $T \to \infty$), with the result that this case can be interpreted in terms of the differential cross section for the induced double-beta process via a comparison of it with expression (17). Expression (16) can then be represented in the form

$$\frac{d\lambda(T \geq 2/\gamma_0, E_{e_1}, E_{\bar{e}_2})}{dE_{\bar{e}_2}} \approx \frac{G_\beta^4\lambda^4}{8\pi^5}I(E_{e_1})|\langle f|\sigma\tau|m_0\rangle|^2 \times (\Delta_{mf} - m_e - E_{\bar{e}_2})^2 p_{\bar{e}_2}E_{\bar{e}_2}F(-Z+2, E_{\bar{e}_2}) \quad (20)$$

$$\times 2F(-Z,E_{e_1})\frac{3\pi}{\gamma_0}(E_{e_1}-E_m+E_i)^2$$

$$\times (E_{\bar{e}_2}-E_m+E_f)^2 \approx \frac{d\sigma_{2\beta}(E_{e_1},E_{\bar{e}_2})}{dE_{\bar{e}_2}}I(E_{e_1})$$

$$\approx \sigma_{2\beta}(E_{e_1})\frac{3}{4}I(E_{e_1})$$

$$\times \frac{G_\beta^2\lambda^2}{2\pi^3\gamma_0}|\langle f|\sigma\tau|m_0\rangle|^2(\Delta_{mf}-m_e-E_{\bar{e}_2})^2 p_{\bar{e}_2}$$

$$\times E_{\bar{e}_2}F(-Z+2,E_{\bar{e}_2});$$

$$\sigma_{2\beta}(T\geq 2/\gamma_0,E_{e_1}) \approx \frac{3}{4}\sigma_\beta(E_{e_1})\frac{\gamma_{\beta^+}}{\gamma_0}.$$

It is of importance that, in this case, one can employ the concept of the cross section for a double-beta process, thereby estimating the effect of the interference between the two reaction stages on this cross section, which proves to be reduced approximately by one-fourth. If interference effects are disregarded, a further growth of the parameter $\gamma_0 T/2$ leads to a gradual approach of $J(T)$ to the value of $J(T)=1$, which corresponds to the limiting case of large T [see Eq. (17) above]. This makes it possible to draw the interesting conclusion that, in induced double-beta processes, effects associated with the coherence of the two reaction stages and with their interference may prove to be significant for $T\geq 2/\gamma_0$. A more detailed investigation of this circumstance can be performed on the basis of the procedure developed in [12] for resonance gamma processes.

Thus, the investigation of induced double-beta processes proceeding owing to weak interaction in electron or neutrino fluxes revealed that, in these cases, a resonance-type mechanism is realized if incident-lepton energies are in excess of the energy threshold for the excitation of the ground state of the intermediate nucleus. According to this mechanism, a resonance excitation of states of the intermediate nucleus $A(N+1,Z-1)$ at the first stage is followed by their beta decay at the second stage. However, excited states of intermediate nuclei usually have large widths with respect to decay through gamma-transition channels. It follows that only those states for which gamma transitions are either forbidden or suppressed to an extremely high degree for one reason or another can actually contribute to double-beta processes. Since the decay width of the ground state of an intermediate nucleus is determined exclusively by beta processes, it is the state that satisfies this condition.

In all other cases associated with taking into account excited states of intermediate nuclei, there occur processes that involve photons and which, strictly speaking, are not double-beta processes. As a rule, such processes are disregarded in calculations. This means that, in the case of induced double-beta processes, it is necessary to exclude artificially excited states of the $A(N+1,Z-1)$ nucleus from the total set of intermediate states and this is the way in which the single-level-dominance approximation is realized in the induced processes being discussed. It is precisely this pattern that one observes experimentally, separating two independent stages of an induced double-beta process: the formation of an intermediate nucleus and its subsequent beta decay.

An analysis reveals that the single-level-dominance approximation, which has so far been employed only in the cases where the ground state of the intermediate nucleus has a spin–parity of 1^+, so that allowed beta transitions to the initial and the final state are realized, can in fact be applied to other cases featuring forbidden transitions. Naturally, expression (6) for the differential cross section must be appropriately modified in this case.

At the same time, such an analysis makes it possible to inquire into the consequences of taking into account this mechanism in double-beta-decay processes where there does not occur a direct excitation of intermediate states. The distinction between induced reactions and double-beta-decay processes stems from the fact that, in the former, some intermediate states are in open channels, while, in the latter, all transitions through intermediate-nucleus states are virtual, proceeding in an unphysical domain of energy variables. Further, we note that, in existing theoretical models, the calculations of double-beta decay that allow for transitions to all possible intermediate states disregard the widths of those states. Therefore, the above mechanism is not taken into account. This means that, in such models, the limiting transition to induced processes cannot lead to the single-level-dominance approximation, unless one introduces it via a special additional condition.

However, such a transition becomes possible if, in these models, one introduces additional assumptions adequate to the mechanism studied above. From the physical picture of the mechanism, it is clear that this mechanism can be associated with additional diagrams that, along with the generally accepted two-stage pattern of the virtual excitation and subsequent beta decay of $A(N+1,Z-1)$ nuclear states, introduce a three-stage process that involves a virtual excitation of an arbitrary nuclear level, its gamma decay to other states of the intermediate nucleus, and a subsequent beta decay of these extra states to the final nucleus $A(N+2,Z-2)$. Since the ground state of the intermediate nucleus stands out in the sense that it can undergo decay only through the beta channels, transitions to it will be dominant above others. It is obvious that the introduction of such diagrams precisely corresponds to the above mechanism, which,

for induced processes, has led us to the single-level approximation. Thus, additional corrections associated with the contribution of diagrams corresponding to transitions between virtual states via photon emission must be included in the theory in order to take into account the above mechanism in double-beta-decay processes. Naturally, experimental data must be analyzed with allowance for such corrections, which have been disregarded thus far. The example of induced transitions where the single-level approximation can be realized only within such a mechanism shows that their role can prove to be significant in double-beta-decay processes as well.

Moreover, a qualitative description of effects that are associated with taking into account such corrections can now be given on the basis of the above physical pattern. Suppose that double-beta-decay processes proceed via transitions occurring from the initially formed excited states of the intermediate nucleus to its other states and involving the emission of photons, which are not detected in present-day experiments. Their contribution will manifest itself in the effective reduction of the experimental double-beta-transition lifetime in relation to that which is expected according to the generally accepted two-stage scheme. Concurrently, the spectrum of electrons (positrons) formed in such additional channels will be enriched in low-energy electrons (positrons) from decay processes of the last stage, its shape being modified owing to a shift toward that which is described by the single-level-dominance approximation. It is interesting to note that, in the NEMO-3 experiments with ^{100}Mo nuclei, the electron spectrum in the soft region corresponds to the single-level approximation [13].

In summary, the present investigation of weak induced double-beta transitions of the electron type and their comparison with the analogous processes of the neutrino type, which were studied previously, lead to the following conclusions:

(i) A resonance mechanism of the excitation of intermediate-nucleus states is realized in induced weak processes occurring in lepton (neutrino and electron) fluxes.

(ii) The contribution to induced double-beta processes from excited states of the intermediate nucleus that are formed as the result of weak interaction is much smaller than the contribution from its ground state since the gamma-decay widths of excited nuclear states are much larger than their beta-decay widths, so that they predominantly decay to low-lying states through gamma channels.

(iii) The main contribution is associated with the excitation and subsequent beta decay of the ground state of the intermediate nucleus, so that the single-level-dominance approximation is realized in induced weak processes, the ground state of the intermediate nucleus being dominant.

(iv) This approximation must be valid irrespective of the spin–parity of this ground state: in the case of $1^+(0^+)$, it corresponds to allowed-type single-level dominance; otherwise, there arises forbidden-type single-state dominance.

(v) In the approximation where the 1^+ ground state of the intermediate nucleus is dominant, an induced double-beta process is broken down into two stages, the excitation of the dominant state and its decay; the degree to which these stages are correlated is controlled by their interference, which depends on the relationship between the parameter T (which characterizes the time interval between these stages) and the lifetime of the dominant stage.

(vi) The qualitative estimates constructed above reveal that effects associated with the interference between the two sequential stages of a double-beta process are dominant in the region $T \ll 2/\gamma_0$, which must be described on the basis of time-dependent perturbation theory, but they are operative in the region $T \geq 2/\gamma_0$ as well, where the application of the diagram technique seems legitimate. A detailed analysis of such effects must include the influence of atomic processes in a medium, which violate the coherence of the stages in question.

(vii) In the case of double-beta decay, where the states of the intermediate nucleus contribute owing to virtual processes that occur in an unphysical domain, the mechanism being studied must lead to a suppression of contributions from excited states and to the realization of the single-level-dominance approximation, with the ground state of the intermediate nucleus being dominant, and this is indeed observed experimentally.

(viii) In order to take rigorously into account this mechanism in two-neutrino and neutrinoless double-beta decays, it is necessary to introduce, in the theory of double-beta processes, additional diagrams that describe the excitation of states of the intermediate nucleus $A(N \pm 1, Z \mp 1)$, their decays through gamma channels, and subsequent beta decay to the final state.

(ix) A qualitative pattern of the expected results shows that the inclusion of such corrections may lead to the growth of the expected cross sections for double-beta processes and to a change in their beta spectrum toward that which corresponds to the spectrum in the approximation where the ground state is dominant.

In the present study, attention has been given primarily to clarifying those special features of the mechanism of weak induced processes that are of importance for precisely describing them. A detailed analysis of corrections that the inclusion of this mechanism

introduces in the standard theory of double-beta processes will be given elsewhere.

ACKNOWLEDGMENTS

I am grateful to V.V. Lomonosov, S.V. Semenov, and V.V. Khrushchev for stimulating discussions.

This work was supported by the Russian Foundation for Basic Research (project no. 03-02-17266) and by a 2003–2004 grant from the Russian Research Centre Kurchatov Institute for fundamental investigations (no. 14).

REFERENCES

1. SNO Collab., Phys. Rev. Lett. **89**, 011301 (2002).
2. KamLAND Collab., Phys. Rev. Lett. **90**, 021802 (2003).
3. S. V. Semenov, Yu. V. Gaponov, and R. U. Khafizov, Yad. Fiz. **61**, 1379 (1998) [Phys. At. Nucl. **61**, 1277 (1998)].
4. S. V. Semenov, Yu. V. Gaponov, and L. V. Inzhechik, Izv. Akad. Nauk, Ser. Fiz. **64**, 38 (2000).
5. S. V. Semenov, Yu. V. Gaponov, F. Šimkovic, and P. Domin, Yad. Fiz. **65**, 2247 (2002) [Phys. At. Nucl. **65**, 2184 (2002)].
6. L. V. Inzhechik, Yu. V. Gaponov, and S. V. Semenov, Yad. Fiz. **61**, 1384 (1998) [Phys. At. Nucl. **61**, 1282 (1998)].
7. H. Ejiri *et al.*, Phys. Rev. Lett. **85**, 2931 (2000).
8. K. Muto, Czech. J. Phys. **48**, 197 (1998).
9. M. Doi, T. Kotani, and E. Takasugi, Prog. Theor. Phys. Suppl. **83**, 1 (1985).
10. K. Grotz and H. V. Klapdor-Kleingrothaus, *Die Schwache Wechselwirkung in Kern-, Teilchen- und Astrophysik* (Teubner, Stutgart, 1989; Mir, Moscow, 1992).
11. W. Heitler, *The Quantum Theory of Radiation* (Clarendon, Oxford, 1954; Inostr. Lit., Moscow, 1956).
12. V. V. Lomonosov and S. B. Sazonov, Zh. Éksp. Teor. Fiz. **107**, 86 (1993) [JETP **80**, 45 (1993)].
13. O. I. Kochetov, Yad. Fiz. **67**, 2018 (2004) [Phys. At. Nucl. **67**, 1995 (2004)].

Translated by A. Isaakyan

Physics of Atomic Nuclei, Vol. 67, No. 12, 2004, pp. 2209–2215. Translated from Yadernaya Fizika, Vol. 67, No. 12, 2004, pp. 2234–2240.
Original Russian Text Copyright © 2004 by Anipko, Ginzburg, Pak.

ELEMENTARY PARTICLES AND FIELDS
Theory

Study of Anomalous Couplings of Gauge Bosons in the Reaction $e^-\gamma \to W^-\nu \to \ell\bar{\nu}\nu$

D. A. Anipko*, I. F. Ginzburg, and A. V. Pak*****

Sobolev Institute of Mathematics, Siberian Division, RAS, pr. Koptyuga 4, Novosibirsk, 630090 Russia
Novosibirsk State University, ul. Pirogova 2, Novosibirsk, 630090 Russia

Received May 22, 2003; in final form, August 15, 2003

Abstract—The possibility of observing an anomaly in triple interactions of a W boson and a photon in the process $e\gamma \to W\nu$ is considered in the leptonic mode of W-boson decay. It is shown that, in some cases, the use of a bounded phase-space domain instead of the total phase space improves upper limits on the anomalous couplings. The estimates obtained in the above mode under conditions of the TESLA project are poorer than analogous current estimates for all modes of the e^+e^- channel. © *2004 MAIK "Nauka/Interperiodica".*

1. INTRODUCTION

The search for signals from new physics (that is, physics beyond the Standard Model) is the most important problem for future high-energy colliders. It may turn out that new physics will manifest itself either through the production of new particles or through a dramatic change in the character of interactions between known particles at energies somewhat higher than currently available energies. However, a completely different type of situation may occur if the energy scale of new physics, Λ, far exceeds energies accessible to colliders of this generation. In order to seek new-physics effects, one would then have to analyze deviations of interactions between particles from the predictions of the Standard Model—that is, anomalous interactions associated with terms absent in the Standard Model Lagrangian. As long as such deviations from the predictions of the Standard Model are small, corrections to the Standard Model Lagrangian that correspond to anomalous interactions can be expanded in powers of $1/\Lambda$. In this expansion, it is then natural to study only a few leading terms associated with operators of the lowest dimension (4 and 6). Since gauge bosons (W and Z) play a particular role in the Standard Model, the interactions of the gauge bosons with one another and with photons are the most promising processes for studying the anomalies in question. The search for the anomalous interactions of gauge bosons in e^+e^-, $e\gamma$, and $\gamma\gamma$ collisions is an important part of the physics program for e^+e^- linear colliders and photon colliders [1, 2].

Within the program of investigations into anomalous interactions, the discovery potential of e^+e^- colliders was explored in detail [3]. The process $e\gamma \to W\nu$ at a photon collider was first considered in 1984 [4]. The anomalous interactions of gauge bosons in the reactions $ee \to WW$, $\gamma\gamma \to WW$, and $e\gamma \to W\nu$ were studied in [5, 6] without taking into account the contribution of background processes or individual channels of W-boson decay. Besides, spectra, polarizations, or collider luminosities used there were not those that are characteristic of present-day experiments.

In the present study, we consider the process $e\gamma \to W\nu$ in the leptonic mode of W-boson decay. We begin by listing the main features of this process that distinguish it from the process $e^+e^- \to WW$:

(i) large cross section [over the energy range under consideration, $\sigma(e\gamma \to W\nu) \gg \sigma(e^+e^- \to WW)$; in contrast to what occurs in e^+e^- scattering, the cross section $\sigma(e\gamma \to W\nu)$ does not decrease with increasing energy, in which case the contribution of anomalous interactions does increase];

(ii) absence of alien contributions (the process $e\gamma \to W\nu$ involves only γWW anomalies, whereas the amplitude of the process $e^+e^- \to WW$ receives contributions from ZWW interactions as well; to take the latter interactions into account, it is necessary to perform a more intricate data analysis);

(iii) loss of information (the use of the leptonic decay mode alone simplifies the analysis, but one loses some information, considering only one final-state particle, with the result that the analysis becomes less sensitive).

Obviously a comprehensive analysis must also include the quark modes of W-boson decay [7].

*e-mail: dmitry.anipko@tec-no.biz
**e-mail: ginzburg@math.nsc.ru
***e-mail: alexey_pak@ngs.ru

2. AMPLITUDES AND REACTION CHANNELS

It is assumed that the anomalous interactions under study give rise to only small corrections to the predictions of the Standard Model. For this reason, only operators of lowest dimensions (4 and 6) are retained in the effective Lagrangian for anomalous interactions of gauge bosons (anomalous interactions between the gauge bosons and matter are neglected). Here, we use a conventional parametrization of the effective Lagrangian in terms of the anomalous magnetic moment $\Delta\varkappa$ and the quadrupole moment λ of the W boson:

$$\mathcal{L}_{WW\gamma} = ie[W^{\dagger}{}_{\mu\nu}W^{\mu}F^{\nu} - W^{\dagger}{}_{\mu}F_{\nu}W^{\mu\nu} \quad (1)$$
$$+ (1+\Delta\varkappa)W^{\dagger}{}_{\mu}W_{\nu}F^{\mu\nu} + \frac{\lambda}{M_W^2}W^{\dagger}{}_{\lambda\mu}W^{\mu}_{\nu}F^{\nu\lambda}].$$

The cross sections and helicity amplitudes for the reaction $e\gamma \to W\nu$ in terms of variables describing "observed" W bosons in the c.m. frame of colliding particles have the form

$$d\sigma_{\lambda_\gamma} = \sigma_0(1-2\lambda_e)\sum_{\lambda_W}\left|M_{\lambda_\gamma\lambda_W}\right|^2 d\cos\theta, \quad (2)$$
$$\sigma_0 = \frac{\pi\alpha^2}{M^2\sin\theta_{\mathrm{W}}^2} \approx 47\ \mathrm{pb},$$

$$M_{ab} = \frac{M\sqrt{s-M^2}}{2\sqrt{2}s(M^2+s+(M^2-s)\cos\theta)}T_{ab}, \quad (3)$$
$$T_{++} = 4(s-M^2)\cos(\theta/2)$$
$$+ (\lambda s + \Delta\varkappa(2s-M^2))\sin\theta\sin(\theta/2),$$
$$T_{+-} = (\lambda s + \Delta\varkappa M^2)\frac{s}{M^2}\sin\theta\sin(\theta/2),$$
$$T_{--} = 4s\cos^3(\theta/2),$$
$$T_{+0} = -\frac{\sqrt{2}s^{3/2}}{M}(\lambda+\Delta\varkappa)\sin(\theta/2)\cos\theta,$$
$$T_{-+} = \left[-2M^2\right.$$
$$\left. + \frac{s-M^2}{M^2}(\lambda s + \Delta\varkappa M^2)\right]\sin\theta\sin(\theta/2),$$
$$T_{-0} = \left[2M\sqrt{2s}\right.$$
$$\left. - \frac{\sqrt{s}(s-M^2)}{\sqrt{2}M}(\lambda+\Delta\varkappa)\right]\sin\theta\cos(\theta/2),$$

where θ is the angle between the photon and W-boson momenta; M is the W-boson mass; and λ_e, λ_γ, and λ_W are the helicities of the respective particles ($\lambda_\gamma = \pm 1$ and $\lambda_W = 0, \pm 1$).

Let us discuss these expressions.

(i) According to the law of angular-momentum conservation, the helicity-flip amplitudes vanish as the angle θ tends to zero, $T \propto (\sin(\theta/2))^{|\lambda_\gamma - \lambda_W|}$, whereas the non-helicity-flip amplitudes vanish for backward scattering, $\theta \approx \pi$.

(ii) Since, within the Standard Model, $We\nu$ interaction involves only left-handed fermion currents, the cross section is proportional to $(1-2\lambda_e)$, where λ_e is the longitudinal electron polarization. By varying the mean helicity of electrons in the beam, the admixture of right-handed currents in this interaction can be determined in a previously inaccessible region of W-boson virtualities (that is, the possible deviation from the Standard Model in W-boson interaction with matter), irrespective of the contribution of anomalous interactions of gauge bosons [4].

(iii) In the problem of searches for anomalous effects, it is assumed that these effects are small—that is, the respective correction to the cross section is linear in $\Delta\varkappa$ and λ. Relations (3) show that, both in the case of left- and in the case of right-hand photon polarization, each anomaly contributes to the cross section. However, the terms that are linear in λ cancel each other in the case of unpolarized photons. For this reason, circular polarization of photons must be taken into consideration, in contrast to the conclusions drawn in [6].

An analysis of a particular observed final state associated with some specific mode of W-boson decay does not reduce to a convolution of the above amplitudes with the distributions of particles produced in W-boson decay (even with allowance for W-boson polarization).

In the case under study, a complete set of tree diagrams includes, in addition to the "resonance" diagrams in Figs. 1*a* and 1*b*, the diagram describing interaction of the incident photon with a muon (Fig. 1*c*). The first two diagrams yield a cross section proportional to $(\alpha^2/M_W^2)\mathrm{Br}(W \to \mu\nu)$, whereas the contribution of the "nonresonance" diagram (and its interference with the "resonance" diagrams) is proportional to (α^3/M_W^2)—that is, it amounts to about one-tenth of the cross section;[1)] therefore, it must be taken into account. Since neutrinos are undetectable experimentally, the muon momentum can take arbitrary values within the allowed kinematical domain.

[1)] In the case of quark modes, a complete set of diagrams must similarly include those that describe photon interactions with any charged particle formed by quarks. However, we are unaware of any computational algorithm taking this into account. A limitation on the effective mass of quark jets reduces the contribution of such "nonresonance" effects, this rendering its ultimate estimate difficult. There is the same ambiguity in studying W-boson production in other reactions, for example, in e^+e^- collisions.

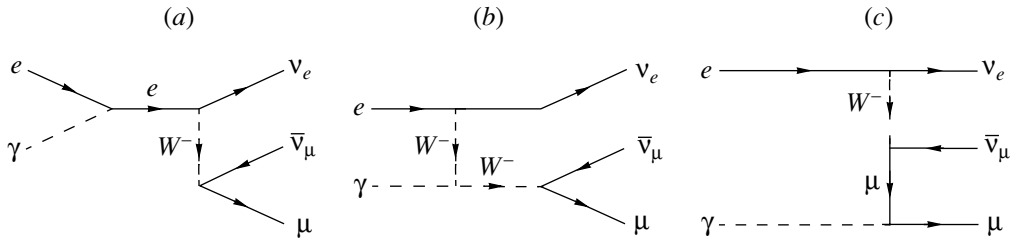

Fig. 1. Tree diagrams for the process $e\gamma \to \mu\nu\bar{\nu}$.

Reaction channels. The channels of the reaction $e\gamma \to W\nu$ are naturally classified by the observed particle and its origin (see table).

We consider only the first two reaction channels featuring one observed particle (muon or electron). For the sake of definiteness, we will discuss predominantly only the muon channel.

3. EVENT SELECTION AND BACKGROUND PROCESSES

We analyze only those events where the muon emission angle in the laboratory frame, $\tilde{\theta}$, is bounded and impose a cut on the muon transverse momentum. We consider rather optimistic cuts on these variables, in accordance with the design parameters of the TESLA detector:

$$\pi - \theta_0 \geq \tilde{\theta} \geq \theta_0 = 10 \text{ mrad}, \qquad (4)$$
$$p_\perp > p_{\perp 0} = 10 \text{ GeV}.$$

For the TESLA 500 project (which is the foremost project today), this cut on the muon transverse momentum means that we in fact use the value of $\theta_0 = 40$ mrad.[2)] Small variations in θ_0 and $p_{\perp 0}$ have but a slight effect on our results.

3.1. Background Processes

For the above selection criteria, events involving only one recorded μ^- meson can be attributed not only to the reaction $e\gamma \to W\nu$ but also to a number of background processes in which either a muon is the only detectable particle in principle, or other charged particles are not detected because of their small emission angles. The background processes are as follows:

(1) processes in which all final-state particles are detectable (a hard photon may be present in their final state):

$$e\gamma \to e\mu^+\mu^-(\gamma); \qquad (5)$$

(2) processes involving final-state neutrinos (and at least one decay $W \to \mu\bar{\nu}$ per each event of W-boson production):

$$\begin{array}{rl} e\gamma \to & e\bar{\tau}\tau, \\ & \downarrow \\ & \nu\bar{\nu}\mu \end{array} \qquad (6a)$$

$$\begin{array}{rl} e\gamma \to & eZZ, \\ & \downarrow\ \downarrow \\ & \bar{\mu}\mu\ \nu\bar{\nu} \end{array} \qquad (6b)$$

$$\begin{array}{rl} e\gamma \to & \nu WZ, \\ & \downarrow \\ & \nu\bar{\nu} \end{array} \qquad (6c)$$

$$\begin{array}{rl} e\gamma \to & eW^-W^+; \\ & \downarrow \\ & \bar{\ell}\nu \end{array} \qquad (6d)$$

(3) processes due to admixtures to the initial state that result from $e \to \gamma$ conversion:

$$e^-e^- \to \nu W^-e^-, \qquad (7a)$$
$$\gamma\gamma \to W^-W^+, \qquad (7b)$$
$$e\gamma \to W\nu. \qquad (7c)$$

A collision of an electron from a high-energy beam with a residual electron from the photon beam is responsible for the process in (7a). The process in (7b) is due to a collision of a high-energy photon and a low-energy photon accompanying the electron beam (beamsstrahlung) and arising upon focusing in the last lens. The process in (7c) corresponds to a collision of an electron from the high-energy beam with a low-energy photon originating either from primary conversion or from secondary collisions between electrons that already lost their energy and laser photons. The contribution of the last background process was

[2)] According to the TESLA technical design project, the respective bound will range to 400 mrad. However, this value is still under discussion (it depends on the arrangement of the conversion device). It should be emphasized that our results depend only weakly on the respective cut.

Modes of the W-boson decay

Muon (electron) mode		τ mode	Quark mode
1	2		
	$e\gamma \to W^-\nu_e$	$e\gamma \to W^-\nu_e$	
$e\gamma \to W^-\nu_e$	$\downarrow$	$\downarrow$	$e\gamma \to W^-\nu_e$
$\downarrow$	$\tau\bar{\nu}_\tau$	$\tau\bar{\nu}_\tau$	$\downarrow$
$\mu(e)\bar{\nu}_{\mu(e)}$	$\downarrow$	$\downarrow$	$q\bar{q}$
	$\mu(e)\bar{\nu}_{\mu(e)}\nu_\tau$	ν_τ + hadrons	

taken into account through the effective spectrum of initial-state photons.

For the above selection criteria (4) and for $\sqrt{s_{e\gamma}} < 1$ TeV, the law of transverse-momentum conservation forbids the processes in (5). For the TESLA 500 facility, this is valid up to $\theta_0 = 40$ mrad.

In order to decide on whether the processes in (6) and (7) can also be ignored, it is necessary to perform an analysis that is more sophisticated than that for the process in (5). First of all, we note that the cross sections for the processes in (6) and (7a) are α times smaller than the cross section for the process being studied. Their inclusion is necessary only in studying loop corrections. Moreover, the processes in (6a), (6b), (6d), and (7b) involve the production of antimuons or hadron jets. The contribution of these processes can be strongly suppressed by imposing additional selection conditions; however, such conditions may affect results somewhat.

As is shown below, events where the muon momentum $\mathbf{p}$ is close to the kinematical limits are of primary importance for studying anomalous interactions. At the same time, the maximum energies and transverse momenta of muons observed in reactions (6b)–(6d), (7a), and (7b) are substantially lower than the respective values in the reaction being studied. The reason is that each of the above background processes involves the production of additional heavy particles; moreover, the total initial-state energy in the c.m. frame is much lower in all of the processes in (7) than in the process being studied. Therefore, the contribution of the processes in (6b)–(6d), (7a), and (7b) is small in the domain where one hopes to observe anomalies. In our simulations, we consider the most "dangerous" process (7c)—muon production via the reaction $e\gamma \to W\nu$ in collisions of electrons with low-energy photons.

4. SIMULATION

4.1. Basic Parameters

Our analysis is performed for primary electron beams of energy 250 GeV. In accordance with [3], we assume that the electrons have left-hand polarization whose average degree is $2\lambda_e = -0.85$. The luminosity of the $e\gamma$ collider is taken to be $\int \mathcal{L}_{e\gamma}dt = (1/4)\int \mathcal{L}_{e^+e^-}dt = 125$ fb^{-1} [2].

We need an adequate description of the spectrum of incident photons because undetectable final-state neutrinos prevent the reconstruction of the momenta of initial-state particles. (In the case of the quark mode, the photon momentum can be reconstructed if the initial-state radiation is neglected.)

In calculating the photon spectrum, it was assumed that the basic parameter of $e \to \gamma$ conversion is $x = 4E\omega_0/m_e^2 = 4.8$. The shape of the photon spectrum in the high-energy region depends only weakly on the beam size, the conversion mechanism, and the laser-flash energy (provided that this energy is not very high); however, it depends on the distance between the conversion and collision points, which is described in terms of the dimensionless parameter ρ. At energies higher than 70% of the maximum possible energy, the photon spectrum was represented by the expressions from [8, 9] at $\rho = 1$. The computations were performed for two opposite circular polarizations of a primary photon; the polarization of high-energy photons was calculated by the formulas from [1] (the average polarization degree was ± 0.95 in this case). On the contrary, the shape of the spectrum in the low-energy region depends crucially on the details of the conversion mechanism, which are expected to change in the course of design and construction. Anyway, the average polarization of low-energy photons will obviously be negligible. Therefore, one can use any plausible curve for this part of the spectrum if it should turn out that photons from this part of the spectrum contribute insignificantly to the ultimate results. To simulate the photon spectrum at energies below 70% of the maximum possible energy, we took the low-energy spectrum of unpolarized photons from [1] at $\rho = 0$ (that is, at the conversion point). We have performed numerical computations for several model configurations (Fig. 2), each trial

curve deviating from the initially prescribed spectrum within 10% at each point. These computations indicate that low-energy photons (3*C* background) have only a little effect on the ultimate results: the Standard Model prediction for the number of events changes within one standard deviation.

Prior to undergoing a collision with a photon from the beam, an electron may lose energy by emitting a photon (so-called initial-state radiation). For this reason, the electron spectrum is not monochromatic. In our calculations, we employed the spectrum from [10, 11].

4.2. Simulation

The calculation of the cross sections and the simulation of events were based on the CompHEP package [12]; in the version used, all powers of the anomalous coupling constants higher than one were set to zero.[3)]

The momentum and emission-angle distributions of muons, $\partial^2\sigma/(\partial p\partial\cos\theta)$, in the region specified by (4) have been calculated both within the Standard Model and with allowance for anomalous contributions. The whole domain expanded to a rectangle was broken down into rectangular cells, and the number of events in each cell was evaluated at a given luminosity. Since the precision of such estimates depends on the size of a cell, the optimum size was determined by the trial-and-error method in order to minimize the time of computations at the required level of accuracy.

Since the mode $\mu\,2$ involves five final-state particles, it is difficult to apply the CompHEP package directly. For this reason, we employed the following procedure. First, we obtained the distributions with respect to the components of the τ-lepton momentum (in just the same way as in the case of the mode $\mu\,1$). After that, we constructed the convolution of the resulting distributions with the distribution of muons produced in the decay of an unpolarized τ lepton. The latter distribution was calculated analytically (integration with respect to the neutrino momenta was performed), the branching fraction for the muon mode of τ decay being estimated at 17%. Since the τ-lepton width is small, our computations are quite accurate.

A deviation of the cross section computed with allowance for the anomalous interactions (anomalous cross section, which is to be observed, according to our assumption) from the Standard Model cross section,

$$\Delta\sigma^{\mathrm{sig}} = \sigma^{\mathrm{obs}} - \sigma^{\mathrm{SM}}, \qquad (8)$$

[3)]We are grateful to A. Pukhov from the Institute of Nuclear Research, Moscow State University, for placing the respective program at our disposal.

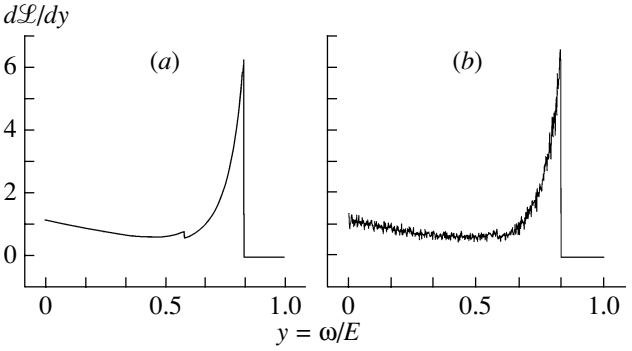

Fig. 2. (*a*) Energy spectrum of photons and (*b*) trial deviations from it.

was considered as a signal from new physics.

The statistical significance of the results for each individual cell of the phase space was estimated on the basis of the distributions calculated both within the Standard Model and with allowance for the anomalous interactions. Under the assumption that the signal is small, we define the statistical significance as

$$SS = \frac{N_{(\mathrm{SM+anom})} - N_{\mathrm{SM}}}{\sqrt{N_{\mathrm{SM}}}}. \qquad (9)$$

Various definitions of statistical significance are discussed in [13].

Since the expressions used here for the cross section are linear in λ and $\Delta\varkappa$, it is convenient to perform simulations of the anomalous cross section at comparatively large values of these parameters. It should be recalled that, in the CompHEP version used here, all powers of the anomalous parameters higher than one are set to zero; in other words, only deviations linear in the anomalous parameters are retained. Owing to this, one can use comparatively large values of the anomalous parameters, thereby rendering the effects of random ($\sim\sqrt{N}$) deviations of the number of events in some cells insignificant. In our simulations, we took the values of $\lambda = \lambda_{\mathrm{sim}} = 0.1$ and $\Delta\varkappa = \Delta\varkappa_{\mathrm{sim}} = 0.1$. The statistical significance was evaluated for each cell.

A typical distribution of the statistical significance is shown in Fig. 3.

It is important that the distribution of the statistical significance is highly nonuniform. It is natural to expect that the best statistical significance is achieved in the domain that combines cells surrounding maxima of the distribution. An integration of adjacent domains characterized by equal values of the statistical significance must also improve it.

To find the domain ensuring the best estimates, we employed the following procedure:

(i) An arbitrary cell of the phase space is chosen.

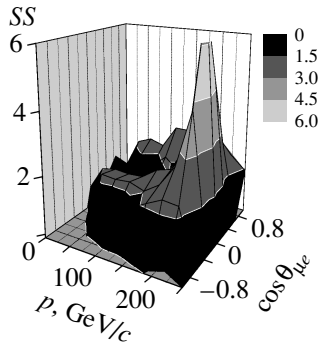

Fig. 3. Distribution of the statistical significance with respect to p and $\cos\theta_{\mu e}$ at $\sqrt{s_{e^+e^-}} = 500$ GeV, $\lambda_\gamma = -1$, $\Delta\varkappa = 0$, and $\lambda = 0.1$.

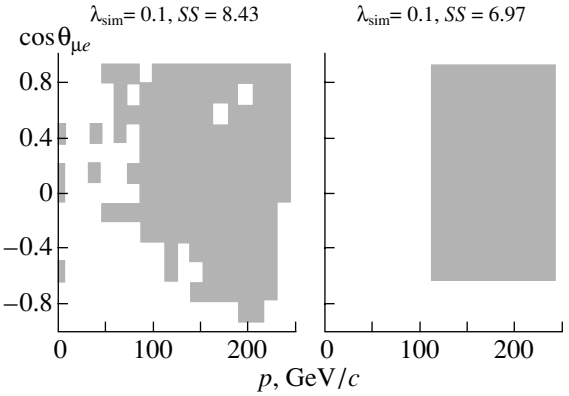

Fig. 4. Domain of the highest statistical significance of the signal and "equivalent" rectangular domain.

(ii) For a domain found in some way, the statistical significance is calculated upon adding the chosen cell (if it is absent from this domain) or removing it (if it is present there).

(iii) If the statistical significance increases after such a change, then the change is accepted—that is the domain is modified.

(iv) The above steps are repeated until the result remains unchanged after a preassigned number of such iterations.

The procedure is performed for each sign of the mean photon polarization and for each anomalous coefficient, λ and $\Delta\varkappa$; the cells characterized by positive deviations from the Standard Model are treated separately from the cells where the deviations from the Standard Model are negative. The result consists in selecting the domain where the results are the best.[4)]

The shapes of the resulting domains and the respective statistical-significance values depend on the photon helicity. The domains appropriate for determining λ are comparatively small.[5)] The greatest value of the statistical significance for the parameter λ, $SS^{\lambda}_{\max} = 12.2$, is obtained in the case of left-hand photon polarization[6)] for the domain shown in Fig. 4. In addition to the domain found by means of the above procedure, one can also indicate a rectangular domain that yields a somewhat smaller statistical-significance value, which is, however, significantly greater than the value corresponding to the whole kinematically allowed domain.

[4)]Such an analysis can be considered as the simplest realization of the method of quasioptimal observables [14], where the function of an observable can only take the value of 0 or 1.

[5)]The domains are blank where the signal is less than the statistical scatter within the Standard Model.

[6)]The entire kinematically allowed domain yields the value of $SS = 2.12$, which is substantially smaller.

In contrast, the optimum domain for the parameter $\Delta\varkappa$ nearly coincides with the kinematically allowed domain.

5. RESULTS

Let $SS_{\rm ob}$ be a preset ratio of the signal to the statistical noise. The smallest measurable value of the anomalous parameter is then given by

$$\lambda_{\rm meas} = \frac{SS_{\rm ob}}{SS^{\lambda}_{\max}}\lambda_{\rm sim}. \qquad (10)$$

For a reliable extraction of the effect, it is necessary that $SS_{\rm ob} > 3$–5. The values of the moments given in [3] correspond to $SS_{\rm ob} = 1$:

$$\Delta\varkappa = 3.3 \times 10^{-4}, \qquad (11)$$
$$\lambda = 5.9 \times 10^{-4} \quad (e^+e^- \text{ mode}).$$

Electron mode. In the case of the e mode, there are additional background processes. However, their effect is insignificant in the domains appropriate for seeking anomalous interactions. Thus, the electron channel can be taken into account by multiplying the estimates for the muon channel by a factor of $\sqrt{2}$. For a comparison with the results presented in [3], we use the value of $SS_{\rm ob} = 1$. For the TESLA 500 project, we obtain

$$\Delta\varkappa = 1 \times 10^{-3}, \qquad (12)$$
$$\lambda = 5.8 \times 10^{-3} \quad (e\gamma \to W\nu \to \ell\nu\nu \text{ mode}).$$

If the momentum distribution of W bosons produced in the process $e\gamma \to W\nu$ is studied by using the quark mode of W decay, the loss of information is less than that in the leptonic mode; consequently, the quark mode is more sensitive to anomalous interactions [7]:

$$\Delta\varkappa = 5 \times 10^{-4}, \qquad (13)$$

$\lambda = 1.5 \times 10^{-3}$ $(e\gamma \to W\nu \to q\bar{q}\nu$ mode, $p_W)$.

Additional information can be obtained by studying the relative motion of quark jets in this reaction.

ACKNOWLEDGMENTS

We are grateful to A. Djouadi, P. Heuer, F. Kapusta, M. Krawczyk, K. Mönig, E. Boos, V. Serbo, and V. Tel'nov for stimulating discussions.

This work was supported in part by the Russian Foundation for Basic Research (project nos. 02-02-17884 and 00-15-96691), by the International Association for the Promotion of Cooperation with Scientists from the Independent States of the Former Soviet Union (grant no. INTAS-00-00679), and by the program "Russian Universities" (grant no. RU.02.01.005).

REFERENCES

1. I. F. Ginzburg, G. L. Kotkin, V. G. Serbo, and V. I. Telnov, Nucl. Instrum. Methods Phys. Res. **205**, 47 (1983); I. F. Ginzburg, G. L. Kotkin, S. L. Panfil, *et al.*, Nucl. Instrum. Methods Phys. Res. A **219**, 5 (1984); Zeroth-Order Design Report for the NLC, SLAC Report 474 (1996); R. Brinkmann *et al.*, Nucl. Instrum. Methods Phys. Res. A **406**, 13 (1998).
2. T. Behnke *et al.*, TESLA Technical Design Report, DESY 2001-011, Part IV.
3. R. D. Heuer *et al.*, TESLA Report 2001-23, TESLA FEL 2001-05, Part III.
4. I. F. Ginzburg, G. L. Kotkin, S. L. Panfil, and V. G. Serbo, Nucl. Phys. B **228**, 285 (1983); **243**, 550(E) (1984).
5. E. Yehudai, Phys. Rev. D **41**, 33 (1990).
6. S. Y. Choi and F. Schrempp, Phys. Lett. B **272**, 149 (1991).
7. K. Mönig *et al.*, *Measurement of W Couplings at a $\gamma\gamma$ and $e\gamma$ Collider,* Report at LCWS'2002.
8. I. F. Ginzburg and G. L. Kotkin, Eur. Phys. J. C **13**, 295 (2000).
9. I. F. Ginzburg, V. A. Ilyin, A. E. Pukhov, *et al.*, Yad. Fiz. **56** (11), 57 (1993) [Phys. At. Nucl. **56**, 1481 (1993)].
10. É. A. Kuraev and V. S. Fadin, Yad. Fiz. **41**, 733 (1985) [Sov. J. Nucl. Phys. **41**, 466 (1985)].
11. M. Skrzypek and S. Jadach, Z. Phys. C **49**, 577 (1991).
12. A. E. Pukhov and A. P. Kryukov, *CompHEP Package Documentation* (NIIYaF MGU, Moscow, 1999) [in Russian].
13. S. I. Bityukov and N. V. Krasnikov, hep-ph/0204326.
14. F. V. Tkachov, hep-ph/0210116.

Translated by R. Rogalyov

Physics of Atomic Nuclei, Vol. 67, No. 12, 2004, pp. 2216–2226. Translated from Yadernaya Fizika, Vol. 67, No. 12, 2004, pp. 2241–2251.
Original Russian Text Copyright © 2004 by Petrukhin, Timashkov.

ELEMENTARY PARTICLES AND FIELDS
Theory

Proton Structure Functions over the Entire Kinematical Region

A. A. Petrukhin and D. A. Timashkov*

Moscow Engineering Physics Institute (State University), Kashirskoe sh. 31, Moscow, 115409 Russia

Received March 18, 2003; in final form, October 17, 2003

Abstract—A new approach to describing inelastic charged-lepton scattering on a proton is proposed. The approach is based on combining the results obtained by theoretically studying the limiting cases of this process. The proton structure function is obtained in an analytic form that involves virtually no free parameters and which is in good agreement with experimental data over the entire kinematical region.
© *2004 MAIK "Nauka/Interperiodica".*

1. INTRODUCTION

The processes of inelastic interaction between charged leptons (electrons, muons) and a proton are of great importance both for obtaining deeper insight into electromagnetic interactions and for investigating the internal structure of the proton (in view of a tight relation to strong interaction). Moreover, the cross sections for such interactions are necessary for solving a number of practical problems that require taking into account inclusive lepton–proton scattering.

The inelastic-scattering cross section in question depends on two structure functions, which entirely determine the dynamics of inelastic interaction. Methods proposed in the past few decades for describing structure functions can be classed by convention as those that rely on models considering a virtual photon and those that rely on models considering the proton and its structure. The first group includes the family of vector-meson-dominance models [1], which were intensively developed in the 1970s. The second group embraces a quark–parton description of the proton; in its modern version, it employs QCD as the theory of interaction [2]. In studying the region of high energies, use is often made of a Regge analysis, which makes it possible to establish the asymptotic behavior of structure functions at small values of the Bjorken scaling variable [3].

Presently, the use of quark distributions in the proton that satisfy the evolution equations [4] is a standard way to describe structure functions in the perturbative region. For initial conditions, one takes either various approximations of experimental data—for example, the Martin–Roberts–Stirling–Thorne fit (MRST group [5]) or the fit proposed by the CTEQ group [6]—or phenomenological models describing the nonperturbative region [7, 8].

In considering a number of questions that arise in practical applications of inelastic-scattering cross sections, it is not necessary, however, to calculate parton distributions, since the cross sections in question involve only structure functions. In those cases, the application of standard computational schemes that employ quark distributions is often inconvenient and inefficient; moreover, this is impossible in the nonperturbative region.

In solving various practical problems, use is usually made of phenomenological formulas involving a large number (up to 20) of parameters that are determined from a fit to experimental data (see, for example, [9]). But as new experimental data appear, the values of these free parameters must be changed significantly, sometimes severalfold. One of the reasons for this is that, as a rule, the structure-function behavior in the different limiting kinematical regions is not taken into account in fitting.

In the present study, we apply a new approach to calculating the proton structure functions. This approach is based on thoroughly studying the structure-function behavior at the boundaries of the kinematical region. On the basis of the results obtained in [10, 11] by investigating quasielastic scattering and the photoproduction limit, we propose a procedure that combines the formulas derived in these limiting cases, thereby making it possible to describe the intermediate region. Further, we investigate in detail the structure-function behavior in the region of high energy transfers. On the basis of the dependences derived in this way, a unified analytic expression is constructed that describes the proton structure function over the entire kinematically allowed region. Preliminary results obtained on the basis of this approach were discussed at the X International Workshop on Deep-Inelastic Scattering (Cracow, 2002) [12].

* e-mail: timashkov@nevod.mephi.ru

1063-7788/04/6712-2216$26.00 © 2004 MAIK "Nauka/Interperiodica"

In the Appendix, we consider the relationship between various scaling variables that are used to describe inelastic interactions.

2. BASIC NOTATION AND FORMULAS

In the approximation of one-photon exchange, the cross section for the inelastic scattering of a charged lepton on a proton can be expressed in terms of two structure functions depending on energy and momentum transfers [13],[1)]

$$\frac{d\sigma_{\rm in}}{d\nu dQ^2} = \frac{2\pi\alpha_e^2}{Q^4E^2\nu} \times \left\{\left(2EE' - Q^2/2\right)F_2 + \frac{\nu}{M}\left(Q^2 - 2m_l^2\right)F_1\right\}, \quad (1)$$

where α_e is the fine-structure constant and m_l is the lepton mass. The rest of the notation is given in Fig. 1.

Instead of the structure function F_1, use is often made of the longitudinal structure function F_L [14],[2)]

$$\frac{d\sigma_{\rm in}}{dx_{\rm B}dQ^2} = \frac{2\pi\alpha_e^2}{Q^4x_{\rm B}}Y_+\left\{F_2 - \frac{y^2}{Y_+}F_L\right\}, \quad (2)$$

$$Y_+ = 1 + (1-y)^2 + \frac{Mx_{\rm B}y}{E}, \quad (3)$$

where

$$x_{\rm B} = Q^2/(2M\nu) \quad (4)$$

is the Bjorken variable and $y = \nu/E$ is the energy-transfer fraction. The function F_L is defined as

$$F_L = \left(1 + \frac{Q^2}{\nu^2}\right)F_2 - 2x_{\rm B}F_1. \quad (5)$$

It follows from (2) that the effect of the longitudinal structure function F_L becomes sizable at high energy transfers (commensurate with the initial lepton energy). Within the quark–parton model, the longitudinal structure function vanishes in the first order in α_s. In the second order, the structure functions F_2 and F_L are related by the equation [14]

$$F_L = \frac{4\alpha_s}{3\pi}x_{\rm B}^2\left\{\int\limits_{x_{\rm B}}^1 \frac{dz}{z^3}F_2\left(z,Q^2\right) + \int\limits_{x_{\rm B}}^1 \frac{dz}{z^3}\left(1 - \frac{x_{\rm B}}{z}\right)zg\left(z,Q^2\right)\right\}, \quad (6)$$

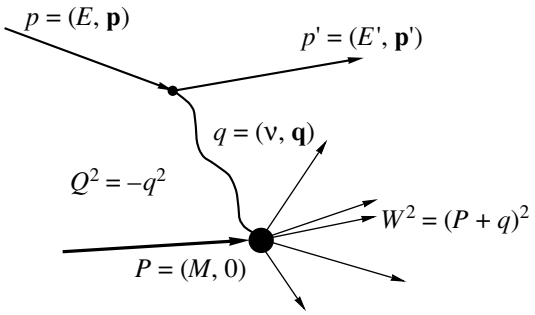

Fig. 1. Feynman diagram for the inelastic scattering of a charged lepton on a proton.

where $x_{\rm B}g\left(x_{\rm B},Q^2\right)$ is the momentum distribution of gluons. At small $x_{\rm B}$, it is proportional to the derivatives of F_2; that is,

$$x_{\rm B}g\left(x_{\rm B},Q^2\right) = \frac{9\pi}{2\alpha_s}\frac{\partial F_2\left(x_{\rm B},Q^2\right)}{\partial\ln Q^2}. \quad (7)$$

In deriving formulas (1)–(3), we have not invoked information about the interaction mechanism in the hadron vertex. Only Feynman rules and conservation laws are required for this. The dynamical mechanism of the interaction between a virtual photon and a proton is described in terms of structure functions (inelastic form factors).

As was mentioned above, a reliable and stable description of inelastic form factors over the entire kinematical region cannot be obtained without precise information about the structure-function behavior in limiting cases. For inelastic scattering, one can single out three limiting cases (see Fig. 2):

(1) photoproduction ($Q^2 \to 0$, $\nu \to E_\gamma$),

(2) quasielastic scattering ($Q^2 \to 2M\nu$, $x_{\rm B} \to 1$), and

(3) small-$x_{\rm B}$ limit ($x_{\rm B} \to 0$, $\nu \to \infty$).

For each of these regions,[3)] there exist approaches that make it possible to derive the limiting expressions for the structure functions. These are the generalized vector-meson-dominance model [1] and the standard Dokshitzer–Gribov–Lipatov–Altarelli–Parisi evolution equations [4] for, respectively, photoproduction and quasielastic scattering. An anomalous growth of F_2 in the small-$x_{\rm B}$ region is generally described within the Pomeron concept [3, 15].

Two limiting cases of quasielastic scattering and photoproduction were previously investigated in [10,

[1)] If the contribution of the diagram corresponding to Z^0-boson exchange is disregarded ($Q^2 < M_Z^2$).

[2)] Expressions (2) and (3) are valid in the region $Q^2 > 2m_l^2$.

[3)] We note that the limit $Q^2 \to \infty$ cannot be considered as an analogous limiting region since, as Q^2 increases, additional diagrams—for example, Z^0-boson exchange for $Q^2 \gtrsim M_Z^2$ (see [8])—must be taken into account and since new, as-yet-unknown, interaction mechanisms can come into play there.

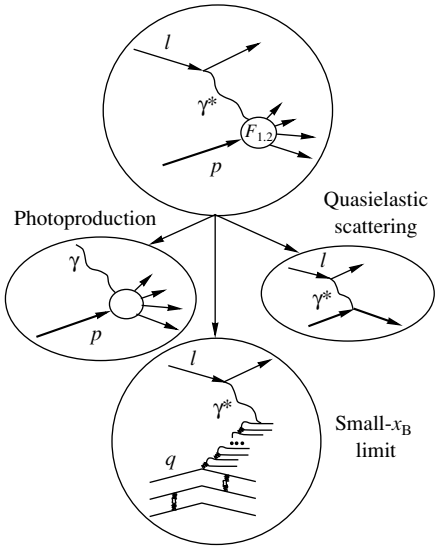

Fig. 2. Diagrams for limiting cases of inelastic scattering.

11], and formulas were obtained there for describing the structure-function behavior in these limiting regions of inelastic scattering ($x_B \to 1$ and $Q^2 \to 0$, respectively).

3. TWO LIMITING CASES

In the quasielastic limit, an exact solution to the evolution equation for the nonsinglet component of the structure function (this is the valence-quark distribution) was found in [10]. For $x_B \to 1$, the main contribution to the structure function comes precisely from the sum of the distributions of three valence quarks in the proton; therefore, the aforementioned solution describes the evolution of the structure function with increasing Q^2 in the limit $x_B \to 1$. If the boundary condition is known to be $F_2(x_B, Q_0^2) \approx (1-x_B)^{n_0}$, the Q^2 dependence of the structure function has the form

$$F_2^{\text{quasiel}}(x_B, Q^2) = F_2(x_B, Q_0^2)(1-x_F)^{4t/3} G_0(t), \quad (8)$$

where

$$t = \frac{12}{33-2n_f}\ln\frac{\ln(Q^2/\Lambda^2)}{\ln(Q_0^2/\Lambda^2)}, \quad (9)$$

$$G_0(t) = \frac{\Gamma(n_0+1)}{\Gamma(n_0+1+4t/3)} e^{(1-4\gamma/3)t}. \quad (10)$$

Here, $n_0 = 3$ and $Q_0^2 = 4\ \text{GeV}^2$ are parameters that are generally used in solving the evolution equations [10], $\Lambda \approx 230$ MeV is a QCD parameter, γ is the Euler constant, and n_f is the number of flavors (which was taken to be equal to three[4)]). The Feynman variable x_F is related to the Bjorken variable x_B by the equation [10]

$$x_F = \frac{2x_B}{1+\sqrt{1+4M^2x_B^2/Q^2}}, \quad (11)$$

which takes explicitly into account the correction for target recoil.[5)]

In the photoproduction limit, the formula for the structure function F_2 was obtained in [11] within the generalized vector-meson-dominance model and Regge theory. The result is

$$F_2^{\text{photo}}(x_B, Q^2) = \frac{\pi}{4} x_T \int_{u_0}^{\infty} \frac{u^{1-\alpha(u)}du}{(u+x_T)^2}, \quad (12)$$

$$u_0 = x_T \frac{m_0^2}{Q^2}.$$

Here, we have used the notation introduced in [11]: $m_0^2 = (m_\rho - \Gamma_\rho/2) = 0.483\ \text{GeV}^2$ is the boundary of the mass spectrum of vector mesons to which a virtual photon can go over, and x_T is a new scaling variable that is related to x_B by the equation

$$x_T = \frac{x_B}{1+x_BM^2/Q^2} = \frac{Q^2}{M^2+2M\nu}. \quad (13)$$

In the case of photoproduction, we have

$$x_T = \frac{Q^2}{M^2+2ME_\gamma} = \frac{Q^2}{s}, \quad (14)$$

where s is the square of energy in the photon–proton reference frame.

The effective intercept $\alpha(u)$ is given by

$$\alpha(u) = \frac{\alpha_R + \alpha_P f(u)}{1+f(u)}, \quad (15)$$

$$f(u) = \ln\sqrt{1+u^{-1}(1-M^2/W^2)},$$

where $W^2 = M^2 + 2M\nu - Q^2$ is the square of energy in the reference frame of the system formed by the virtual photon and the proton. In the photoproduction limit, we have $W^2 = s$. The Reggeon intercept is $\alpha_R = 1/2$, while the quantity α_P is given by

$$\alpha_P = 1 + \Delta = 1 + k_0\sqrt{\ln(s/M^2)}, \quad (16)$$

[4)] This solution can also describe the cases of four or five flavors if one uses the standard scheme for implementing a transition of $\sqrt{Q^2}$ beyond the masses of c and b quarks, where α_s is continuous and Λ is different for different values of n_f.

[5)] Relation (11) was derived in [16] and is sometimes referred to as the Nachtmann variable.

where Δ describes the contribution of multi-Pomeron exchanges and is an addition to the pure-Pomeron intercept, which, within the original Regge theory, is equal to unity, and $k_0 \sim 0.03$. It should be noted that this constant also appears in the expression for the photoproduction cross section [11],

$$\sigma_{\gamma p}(s) = \frac{\pi^3 \alpha_e}{s} \int\limits_{u_0}^{\infty} \frac{du}{u^{1+\alpha(u)}}, \qquad (17)$$

where $\alpha(u)$ is given by formula (15) at $Q^2 = 0$. It was shown in [11] that, in order to describe the entire body of data on photoproduction with allowance for the results of the ZEUS Collaboration [17] for the energy range 0.1–10 TeV, k_0 must be set to a value of 0.028.

The above dependences of the structure functions for two limiting cases determine the behavior of F_2 at the boundaries of the kinematical region.

4. INTERMEDIATE REGION

At first glance, the expression obtained for the proton structure function in the photoproduction limit—that is, at small Q^2—is a natural boundary condition for solving the evolution equation in the quasielastic limit. However, a transition from the region of quasielastic scattering to the photoproduction limit involves some difficulties and requires a more detailed consideration. In comparing expressions (8) and (12), one can single out three main difficulties that prevent a direct use of F_2^{photo} as the initial condition for F_2^{quasiel} [the absence of the factor $(1 - x_{\text{F}})$ at small Q^2 can be explained trivially since, in this case, x_{B} and, accordingly, x_{F} tend to zero].

First, the functions F_2^{photo} and F_2^{quasiel} depend, in fact, on the different variables (11) and (13), which do not reduce to each other directly. Moreover, the variable x_{T} was determined in [11] under the condition $Q^2 \ll M^2 + 2M\nu$—naturally, this condition is violated at high values of Q^2. Second, the expression for F_2^{quasiel} involves the function $G_0(t)$, which does not appear in the formula for F_2^{photo}, the quantity t not being defined for $Q^2 < \Lambda^2$. Third, the structure function in the photoproduction limit, where x_{B} is small by definition, is proportional to the sea-quark distribution, but it is the valence-quark distribution that is required as the initial condition for the evolution equation. The ways to overcome these difficulties are based on the main idea of the proposed approach—the possibility of deriving unified functional dependences for describing the inelastic interactions of charged leptons.

The problem of the different scaling variables can be solved if we assume that, in just the same way as F_2^{photo} and F_2^{quasiel} are the limiting cases of the unified structure function, x_{T} and x_{F} are the limiting cases of some unified scaling variable. For this variable, we proposed the function [12]

$$x_{\text{P}} = \frac{2x_{\text{B}}}{1 + \sqrt{1 + 4M^2 x_{\text{B}}^{1+x_{\text{B}}}/Q^2}}, \qquad (18)$$

which, in the small-Q^2 region and in the large-x_{B} region, reduces to x_{T} and x_{F}, respectively, and which thereby ensures the matching of not only the scaling variables but also their derivatives. The choice of the function in (18) for the unified variable is validated in the Appendix.

Let us consider the second problem: the use of the function $G_0(t)$ and of the variable t at low Q^2. From the definition (10) of the function $G_0(t)$, one can see that, at the boundary of the perturbative region at $Q^2 = Q_0^2\,(t = 0)$, we have $G_0(t) = 1$. We will transfer this point by regularizing the variable t as

$$t = \frac{12}{33 - 2n_f} \ln \frac{\ln\left((Q^2 + Q_0^2)/\Lambda^2\right)}{\ln Q_0^2/\Lambda^2}. \qquad (19)$$

We now have $t = 0$ at $Q^2 = 0$. At $Q^2 = Q_0^2$, we accordingly have $t = 0.07$, while the value of the function G_0 is 1.06. At high values of Q^2, the distinction between the old and the new definition of t becomes very insignificant.

In order to solve the third problem, we will consider that the structure function F_2^{photo}, which is treated as the initial condition, includes the contributions of all quark distributions and that, owing to the effective intercept in (15), the integral in (12) describes simultaneously the Regge dependence on x_{B} (energy) both for the sea- and for valence-quark distributions. Since the solution to the evolution equation describes the evolution of only the valence component of F_2 and since it is sea quarks that make the main contribution to the structure function at small x_{B}, it is necessary that the t dependence in F_2^{quasiel} disappear for $x_{\text{B}} \to 0$. Below (see Section 5), the Q^2 evolution of sea quarks will be described within the Pomeron concept without solving the evolution equations. In order to go over from the $x_{\text{B}} \sim 1$ region to the small-x_{B} region, we introduce a joining function $G(x_{\text{B}}, t)$ that must satisfy the conditions

$$G(x_{\text{B}}, t) \xrightarrow[x_{\text{B}} \to 0]{} 1, \qquad (20)$$

$$G(x_{\text{B}}, t) \xrightarrow[x_{\text{B}} \to 1]{} G_0(t)(1 - x_{\text{P}})^{4t/3}.$$

This definition makes it possible to reduce, in the region where the role of valence quarks is insignificant, the effect of the t dependence appearing in formula (8). Naturally, there exist a variety of functions

that satisfy the conditions in (20). As a matter of fact, we specify an initial condition at $Q^2 = Q_0^2$. Calculations revealed that even the choice of the simplest linear form for $G(x_B, t)$,

$$G(x_B, t) = x_B G_0(t)(1 - x_P)^{4t/3} + 1 - x_B, \quad (21)$$

leads to good agreement with experimental data (see [12]).

In choosing a joining function, it is more reasonable, however, to take into account the relationship between the proton structure function F_2 and the distributions of valence quarks (u^{val}, d^{val}) and sea quarks S ($S = 2\bar{u} + 2\bar{d} + 2\bar{s}$). It is well known that, within the quark–parton model, the structure function F_2 is equal to the sum of the quark and antiquark momentum distributions ($x_B q_i$ and $x_B \bar{q}_i$, respectively) weighted with the squares of their electric charges. Under the assumption that sea quarks and antiquarks are symmetric ($\bar{u} = \bar{d} = 2\bar{s}$), the structure function takes the form

$$F_2(x_B) = \frac{4}{9} x_B u^{val}(x_B) + \frac{1}{9} x_B d^{val}(x_B) + \frac{11}{45} x_B S(x_B). \quad (22)$$

From an investigation of the quark distributions in the intermediate region, it follows [5, 6] that, in the limit $x_B \to 1$, the function d^{val} decreases faster than u^{val}, while the function S decreases faster than d^{val}. By using this conclusion, the values of the weight coefficients of the quark distributions in (22), and the conditions in (20), we can recast the joining function into the form

$$G(x_B, t) = \frac{45}{11}\left(x_B G_0(t)(1 - x_P)^{4t/3} \times \left(\frac{4}{9} + \frac{1}{9}(1 - x_B) \right) + \frac{11}{45}(1 - x_B)^2 \right)$$

or

$$G(x_B, t) = x_B G_0(t)(1 - x_P)^{4t/3} \times \left(\frac{20}{11} + \frac{5}{11}(1 - x_B) \right) + (1 - x_B)^2. \quad (23)$$

The above choice of $G(x_B, t)$ improves agreement with experimental data.[6)]

[6)]It should be emphasized that, in contrast to what was done for relation (22), one should not identify the individual terms in (23) with the valence- or sea-quark distributions. As was indicated above, the common integral factor in (12) involves the contributions from both valence and sea quarks; therefore, the structure function (12) cannot be represented as the sum of quark distributions that is analogous to that in (22). The individual terms in (23) only reflect the difference in the behavior of the parton distributions for $x_B \to 1$.

Upon combining the above results [formulas (8)–(10), (12), (18), and (23)], we obtain the proton structure function in the form

$$F_2(x_B, Q^2) = \frac{\pi}{4} G(x_B, t) \times (1 - x_P)^{n_0} x_P \int_{u_0}^{\infty} \frac{u^{1-\alpha(u)} du}{(u + x_P)^2}, \quad (24)$$

where

$$u_0 = x_P \frac{m_0^2}{Q^2}.$$

This result relates the solution for quasielastic scattering to the solution in the photoproduction limit. In order to use it over the entire kinematical region, it is necessary to consider the small-x_B limit.

5. SMALL-x_B REGION

In contrast to what we have had in dealing with the various limiting regions considered above, the description of the small-x_B region requires employing different approaches for different regions of Q^2. By the small-x_B region, one usually means the region of rather high Q^2 for $\nu \to \infty$ (perturbative region). This makes it possible to use QCD in describing the dynamics of inelastic interaction. At low x_B, however, the use of the Dokshitzer–Gribov–Lipatov–Altarelli–Parisi evolution equations is not quite correct since the derivation of these equations was based on taking into account only those diagrams that are proportional to the highest powers of $\ln(Q^2/Q_0^2)$, the terms proportional to the same powers of $\ln(1/x_B)$ being discarded. It is more reasonable to employ here the Balitsky–Fadin–Kuraev–Lipatov equation [18] for the unintegrated gluon distribution $f(x_B, k_\perp^2)$. This equation was obtained by summing diagrams that are proportional to just the highest powers of $\ln(1/x_B)$. The usual momentum distribution of gluons, $x_B g$, is expressed in terms of f as

$$x_B g(x_B, Q^2) = \int_{}^{Q^2} \frac{dk_\perp^2}{k_\perp^2} f(x_B, k_\perp^2), \quad (25)$$

where $k_\perp^2$ is the square of the transverse momentum of the gluon in the proton. If we neglect the Q^2 dependence of the running coupling constant α_s [that is, if we set $\alpha_s(Q^2) \equiv \bar{\alpha}$], the solution to the Balitsky–Fadin–Kuraev–Lipatov equation has the form [19]

$$x_B g \sim \frac{x_B^{-\Delta_{BFKL}}}{\sqrt{\ln(1/x_B)}}, \quad (26)$$

where Δ_{BFKL} characterizes the intercept of the so-called Balitsky–Fadin–Kuraev–Lipatov Pomeron,

$$\alpha_{\mathrm{P}}^{\mathrm{BFKL}} = 1 + \Delta_{\mathrm{BFKL}} = 1 + \frac{12\bar{\alpha}}{\pi}\ln 2. \qquad (27)$$

Since, at low values of x_{B}, the main contribution to the structure function comes from the sea-quark momentum distributions $x_{\mathrm{B}}S(x_{\mathrm{B}})$, which are proportional to the gluon distributions [20], the x_{B} dependence of F_2 in the perturbative region has a form similar to that in (26),

$$F_2 \sim x_{\mathrm{B}}S(x_{\mathrm{B}}) \sim x_{\mathrm{B}}g \sim \frac{x_{\mathrm{B}}^{-\Delta_{\mathrm{BFKL}}}}{\sqrt{\ln(1/x_{\mathrm{B}})}}. \qquad (28)$$

However, low values of x_{B} can also be obtained in the limit $Q^2 \to 0$ in the nonperturbative region, this corresponding to the photoproduction limit. In this limit, the structure function is described by formula (12), which, in the region $Q^2 < m_0^2$, assumes the form

$$F_2 = \frac{\pi}{4}x_{\mathrm{T}}\int\limits_{u_0}^{\infty}\frac{du}{u^{1+\alpha(u)}}. \qquad (29)$$

Since the small-u region makes a dominant contribution to the integral in (29), one can substitute [see formula (15)] the Pomeron intercept α_{P} for the effective intercept $\alpha(u)$. In this case, the integral can be taken analytically, whereupon the structure function is written as

$$F_2 = \frac{\pi}{4}\left(\frac{Q^2}{m_0^2}\right)^{\alpha_{\mathrm{P}}}\frac{x_{\mathrm{T}}^{-\Delta}}{\alpha_{\mathrm{P}}}. \qquad (30)$$

In order to describe experimental data in the intermediate region at Q^2 of about a few GeV^2 units, use is made of the double logarithmic dependence [21, 22]

$$F_2 \sim 0.5\log\left(1 + Q^2/Q_{\mathrm{tr}}^2\right)\log(x_0/x_{\mathrm{B}}), \qquad (31)$$

where Q_{tr}^2 and x_0 are free parameters.

A comparison of formulas (28) and (30) with (31) shows that, in all probability, a unified expression for describing the small-x_{B} limit at any Q^2 can be found by individually considering the x_{B} and Q^2 dependences.

Let us first consider the x_{B} dependence. Taking into account expression (16) and going over to the limit of high energies, where $x_{\mathrm{T}} \approx x_{\mathrm{B}}$, we can recast expression (30) into the form

$$F_2 \sim \frac{x_{\mathrm{B}}^{-\Delta}}{\sqrt{\ln(s/M^2)}}. \qquad (32)$$

In order to ensure a continuous transition from the logarithm in (32) to the logarithm of $1/x_{\mathrm{B}}$ in formula (28), we change the argument of the logarithm in (16) [and, accordingly, in (32)] as

$$\ln(s/M^2) \to \ln\left(\frac{W^2+Q^2}{M^2+Q^2}\right). \qquad (33)$$

This expression is equivalent to $\ln(s/M^2)$ in the photoproduction limit ($Q^2 \to 0$) and reduces to $\ln(1/x_{\mathrm{B}})$ for $Q^2 \gg M^2$ and $\nu \gg M$. In terms of the variables x_{B} and Q^2, the right-hand side of (33) assumes the form

$$\ln\left(1 + \frac{1-x_{\mathrm{B}}}{x_{\mathrm{B}}}\frac{Q^2}{Q^2+M^2}\right). \qquad (34)$$

With allowance for (33), the x_{B} dependence of the structure function in the nonperturbative region of the low-x_{B} limit takes the form

$$F_2 \sim \frac{x_{\mathrm{B}}^{-\Delta}}{\sqrt{\ln(1/x_{\mathrm{B}})}}, \qquad (35)$$

where Δ depends on x_{B} according to the formula

$$\Delta = k_0\sqrt{\ln(1/x_{\mathrm{B}})}. \qquad (36)$$

Expression (35) reproduces the functional dependence of the solution in (28) to the Balitsky–Fadin–Kuraev–Lipatov equation. Thus, the x_{B} dependence obtained in the photoproduction limit for the high-energy region is similar to the solution to the Balitsky–Fadin–Kuraev–Lipatov equation for the perturbative region. Hence, expression (12) can be used as a boundary condition both for quasielastic scattering and in the low-x_{B} limit, while the solution in (28) reflects the x_{B} dependence of the structure function at small Q^2 in the nonperturbative region.

In the intermediate region of Q^2, the power-law behavior of the structure function (35) is analogous to the logarithmic growth in (31). Indeed, we consider the behavior of F_2 in the region where $\Delta \ll 1$. In this case, the numerator of the expression for the structure function (35) can be expanded in a power series,

$$F_2 \sim \frac{1 + \Delta\ln(1/x_{\mathrm{B}})}{\sqrt{\ln(1/x_{\mathrm{B}})}}. \qquad (37)$$

Substituting the quantity Δ in a form similar to that in (36) into expression (37), we find that, in the intermediate region of the low-x_{B} limit, the x_{B} dependence of the structure function has a form close to that in (31); that is,

$$F_2 \simeq k(Q^2)\ln(1/x_{\mathrm{B}}), \qquad (38)$$

where k is a function of Q^2. This function cannot be determined from any evolution equations, since the

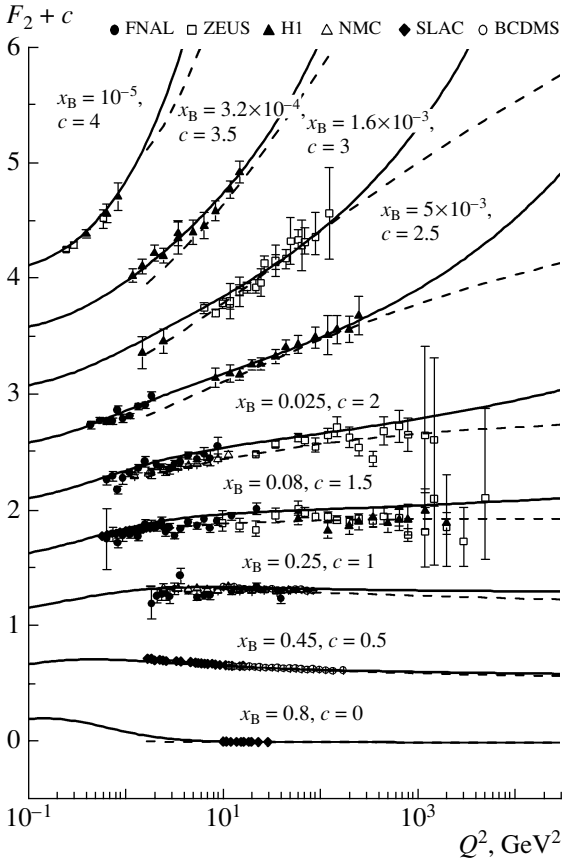

Fig. 3. Proton structure function over the entire kinematical region: (solid curves) calculations by formula (24) and (dashed curves) numerical solution to the Dokshitzer–Gribov–Lipatov–Altarelli–Parisi equations with the CTEQ6 initial parton distributions [6]. The displayed experimental data were borrowed from [26–28].

high-Q^2 and small-x_B region is beyond the applicability range of the Dokshitzer–Gribov–Lipatov–Altarelli–Parisi and Balitsky–Fadin–Kuraev–Lipatov equations. In order to obtain this function, we will employ different approaches.

As was shown in [3, 11], the multi-Pomeron mechanism of interaction plays a dominant role in the high-energy region, the number of Pomerons depending on the energy of the process. This fact is reflected by the quantity Δ, which grows logarithmically with energy. In inelastic scattering, however, the contribution from multi-Pomeron exchange can depend on Q^2 (see [7, 23, 24]). It can be seen from (37) that, in the intermediate region, the structure function is proportional to Δ. Since the Q^2 dependence of F_2 is logarithmic in this region [see (31)], it is obvious from a comparison of expressions (31), (37), and (38) that the Q^2 dependence of the quantity k has a form similar to that in (31); that is,

$$k(Q^2) \sim \ln\sqrt{1 + Q^2/Q_{tr}^2}. \qquad (39)$$

At small Q^2, the logarithmic dependence in (39) reduces to a linear one. With allowance for expression (38), this leads to a linear dependence of F_2 on Q^2 that is analogous to that in (30), the relation $Q_{tr}^2 \simeq m_0^2$ being valid. The final expression for the function k can be found by using expression (16) as a boundary condition for $Q^2 \to 0$. The result is

$$k(Q^2) = k_0\left(1 + \ln\sqrt{1 + Q^2/m_0^2}\right). \qquad (40)$$

Although the choice of m_0^2 for Q_{tr}^2 was motivated by the fact that it ensures a correct transition to the photoproduction limit, the quantity m_0^2 is a good scale that bounds the characteristic domains of applicability of vector-meson-dominance models and perturbative QCD. The correctness of this choice is corroborated by the fact that, in [21, 22, 24, 25], a value of $Q_{tr}^2 \sim 0.5$ GeV^2, which is close to m_0^2, was used to describe experimental data.

The final expression for $\Delta = \alpha_P - 1$ for the entire kinematical region with allowance for (16), (40), (33), and (34) takes the form

$$\Delta\left(x_B, Q^2\right) = k_0\left(1 + \ln\sqrt{1 + Q^2/m_0^2}\right) \times \sqrt{\ln\left(1 + \frac{1 - x_B}{x_B}\frac{Q^2}{M^2 + Q^2}\right)}. \qquad (41)$$

We note that, in contrast to the expression presented in [12] for the case of $x_B \ll 1$, formula (41) involves the factor $1 - x_B$ in the argument of the logarithm, and this factor leads to the relation $\Delta(x_B = 1) = 0$—that is, the Pomeron intercept for elastic scattering becomes equal to unity.

6. PROTON STRUCTURE FUNCTIONS

In order to calculate the proton structure function over the entire kinematical region, we can now use expression (24), where the effective intercept α is determined by formula (15) and where the contribution Δ of multi-Pomeron exchanges to the Pomeron intercept α_P is taken into account by formula (41).

Experimental data from [26–28] on the proton structure function are presented in Fig. 3, along with the results of the calculation with the joining function in (23). As might have been expected, formula (24) describes best of all the boundaries of the kinematical region, but, even in the intermediate region, the deviation from the experimental data does not exceed 10–15%. In the low-x_B region, there is good agreement with the latest experimental data obtained at the HERA collider by both (closed triangles in

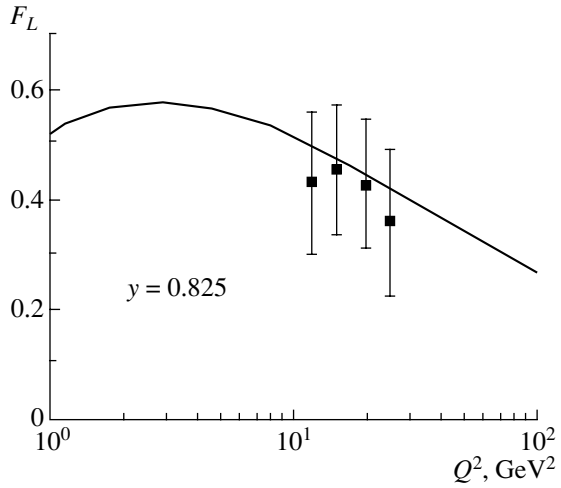

Fig. 4. Longitudinal proton structure function. The displayed experimental data were obtained by the H1 Collaboration [27].

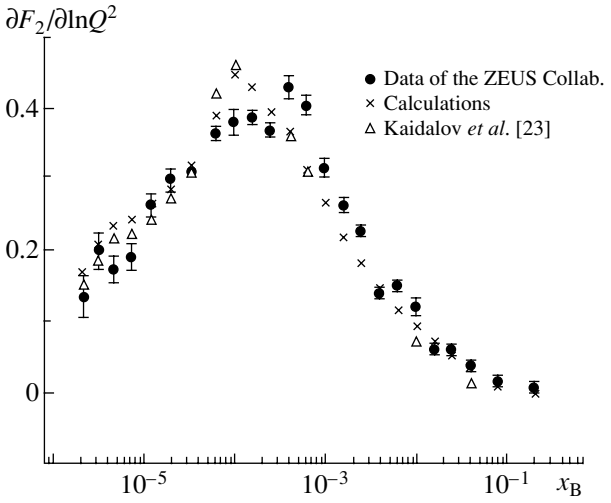

Fig. 5. $\partial F_2/\partial \ln Q^2$ as a function of x_B. The displayed experimental data were obtained by the ZEUS Collaboration [29].

Fig. 3) the H1 Collaboration [27] and (open boxes there) the ZEUS Collaboration [28]. For the sake of comparison, the graphs of the proton structure function obtained on the basis of the solution to the Dokshitzer–Gribov–Lipatov–Altarelli–Parisi evolution equations with the initial parton distributions proposed by the CTEQ [6] group (the CTEQ6 fit depicted by the dashed curves)[7)] are also displayed in Fig. 3. One can see that the numerical solutions obtained in [6] and the analytic formula derived in the present study are in good agreement over the entire experimentally studied domain of the variables x_B and Q^2. As for the deviations at small x_B and large Q^2, they are due to the fact that the numerical calculations relied on the Dokshitzer–Gribov–Lipatov–Altarelli–Parisi equations, while our calculations employed formulas that were obtained from the solution to the Balitsky–Fadin–Kuraev–Lipatov equation. Only future experiments can show which of these approaches is more correct.

With the aid of formula (6), one can obtain the longitudinal structure function. The results of the calculations at the energy-transfer fraction of $y = 0.825$ are given in Fig. 4.

Along with the proton structure function F_2, its logarithmic derivatives with respect to x_B and Q^2 have been vigorously investigated in recent years. The quantity $\partial F_2/\partial \ln Q^2$ describes the gluon momentum distribution (7) at low values of the Bjorken variable. Figure 5 presents the dependence of this derivative on x_B according to data of the ZEUS Collaboration [29].

[7)]The use of another fit, MRST01, that was proposed by the MPCT group [5] changes the results of calculations only slightly.

These results were derived by fitting the structure function in terms of the expression $F_2 \sim a + b \ln Q^2$. Each point was obtained at an averaged (for each x_B) value of Q^2, increasing from left to right from 0.1 to 400 GeV^2. The graph demonstrates explicitly a transition from the perturbative part of the low-x_B limit, where one observes an anomalous growth of the structure functions, to the nonperturbative part of the low-x_B limit. Figure 5 also displays the results obtained by calculating, at relevant values of Q^2, the derivative of formula (24) with respect to Q^2. It can readily be seen from this figure that expression (24) faithfully reproduces not only the structure function but also its derivative $\partial F_2/\partial \ln Q^2$.

Figure 6 gives the values of another derivative of the proton structure function, $\partial \ln F_2/\partial \ln(1/x_B)$. It has also been actively investigated in recent years. These values were obtained by fitting the measured structure function in terms of the relation $F_2 \sim x_B^{-\lambda}$. A comparison of experimental data with the results of the calculation by formula (24) shows that the results of the calculation reproduce the logarithmic growth of the derivative with increasing Q^2. The logarithmic dependence of the quantity Δ on Q^2 is the main reason behind this growth. By analogy with Fig. 5, each point was calculated at the corresponding value of x_B, the values changing from 3×10^{-6} to 8×10^{-3}.

It should be noted that procedures used to analyze experimental data can lead to an ambiguous interpretation of the results. For example, it was indicated in [23] that the values obtained for the derivatives of F_2 at the HERA collider are in fact the coefficients

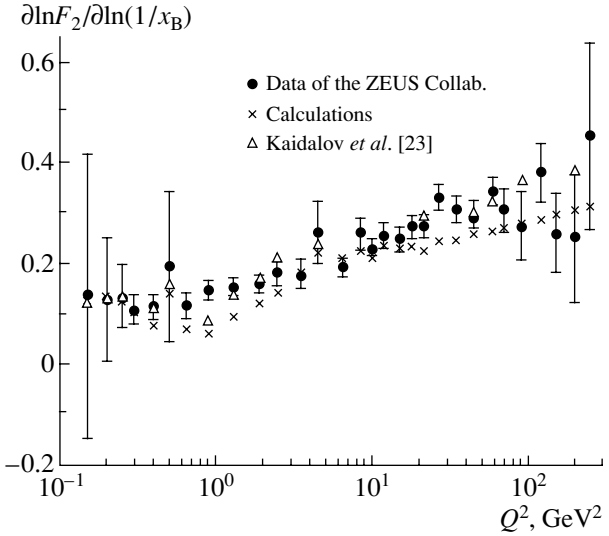

Fig. 6. $\partial \ln F_2/\partial \ln(1/x_B)$ as a function of Q^2. The displayed experimental data were obtained by the ZEUS Collaboration [29].

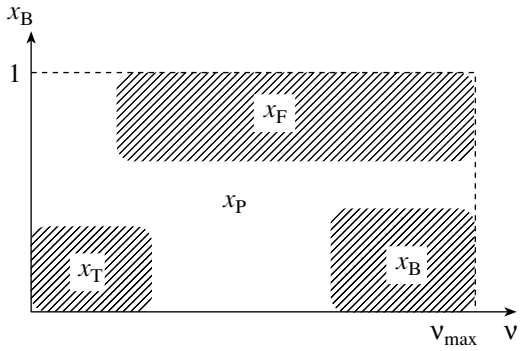

Fig. 7. Regions where different scaling variables are dominant in inelastic scattering.

of fitting functions and can differ from the derivatives calculated on the basis of analytic formulas. The results of our calculations agree with the results of the calculations performed in [23], sharp deviations from the experimental values in the two studies being consistent (see Fig. 5, 6). This can indicate that a methodological difference may exist between the analytic and experimental approaches to analyzing the derivatives of the structure functions.

7. CONCLUSION

The phenomenological approach proposed here for describing the proton structure function on the basis of combining the results of different theoretical models for the limiting cases of inelastic scattering has made it possible to construct a unified analytic expression that describes well the structure function F_2, its derivatives, and the longitudinal structure function. The resulting formulas can be used in various practical calculations where it is necessary to know the inclusive cross sections for inelastic lepton–proton scattering—specifically, in analytic calculations concerning muon propagation through matter and in calculations of various effects induced by inelastic muon scattering. Our formula for the proton structure function will be useful for packages of codes applied in simulating various processes.

It should be emphasized that our expression for the structure function involves virtually no free parameters and that it has been obtained without invoking standard fitting procedures. The majority of the parameters (m_0, α_R, n_f, Q_0^2, Λ, and so on) that we used here are the parameters of the models that describe the corresponding limiting cases. Only one parameter was actually determined from experimental data—the coefficient k_0— but it is not an ordinary free parameter because its value found on the basis of data on the photoproduction cross section (nonperturbative region) also describes the high-momentum-transfer region in the limit of low x_B (perturbative region).

It should also be noted that the description of the limiting case of low x_B at high energy transfers requires further investigations. The multi-Pomeron-exchange concept, which has been widely discussed in recent years (see, for example, [3, 15] or [30]), is not yet a closed theory describing the high-energy region. Although the quantity Δ, which we have used here to describe the contribution of multi-Pomeron exchanges and which depends logarithmically on the energy and momentum transfers, gave good agreement with experimental data, it is quite possible that, in the region of very high energies, the Regge behavior of F_2 goes over to a weaker dependence. It should be noted, however, that a power-law growth of the structure function with energy is compatible with the Froissart condition [31], since, in inelastic scattering, a virtual photon is not on the mass shell (see [32]).

Although the results described above do not enable us to calculate cross sections for exclusive inelastic processes, the proposed procedures will undoubtedly be useful for analyzing the quark and gluon distributions in the proton as well. We also hope that the very fact of obtaining the above simple formula describing a rather complicated process of inelastic charged-lepton scattering over the entire kinematical region of variables will give impetus to theoretical developments aimed at clarifying the physics behind the dependences found here and at refining them further.

APPENDIX

Dimensionless quantities composed of independent variables describing some physical process and

parameters that affect the course of this process under given conditions are widely used in various branches of physics (for example, the Reynolds, Nusselt, and Prandtl numbers in fluid dynamics and thermal physics). Their introduction is based on the simple idea that each problem must be considered in terms of variables that are peculiar to this very problem; the use of such variables makes it possible to reduce the number of arguments in investigating various functional dependences for the physical process under consideration. In similarity theory describing general regularities of applicability of such dimensionless variables, they are also known as similarity numbers, complexes, parameters, and even criteria.

In high-energy physics, this approach is referred to as the scaling-invariance (scaling) approach, the corresponding dimensionless quantities being known as scaling variables. In describing inelastic charged-lepton interactions, use is usually made of two such variables, the Bjorken variable x_B and the Feynman variable x_F. They are related by Eq. (11),

$$x_F = \frac{2x_B}{1+\sqrt{1+4M^2x_B^2/Q^2}}.$$

It follows from [10] that, in describing quasielastic scattering (for $x_B \to 1$), it is necessary to use x_F rather than x_B.

In [11], it was shown that, in the photoproduction limit (at small Q^2), the structure function F_2 and, hence, the cross section for inelastic scattering depend not on x_B or x_F but on some new variable x_T[8] related to x_B by Eq. (13),

$$x_T = \frac{x_B}{1+x_BM^2/Q^2}.$$

Thus, we can see that, in proceeding to analyze the intermediate region, one must address the problem of choosing a variable that would reduce to the variables given by (11) and (13) in, respectively, the limit $x_B \to 1$ and the limit $Q^2 \to 0$ (see Fig. 7). In order to obtain an expression for a generic scaling variable, it is necessary to investigate the behavior of the quantities x_F and x_T as one goes over from one limiting region to another. For this, we consider the limit of expression (11) at small Q^2 and the limit of expression (13) for $x_B \to 1$.

At low momentum transfers, the Feynman variable x_F takes the form

$$x_F \xrightarrow[Q^2\to 0]{} \frac{x_B}{1+x_BM/2\nu}.$$

[8]The subscript on it corresponds to the surname of one of the present authors.

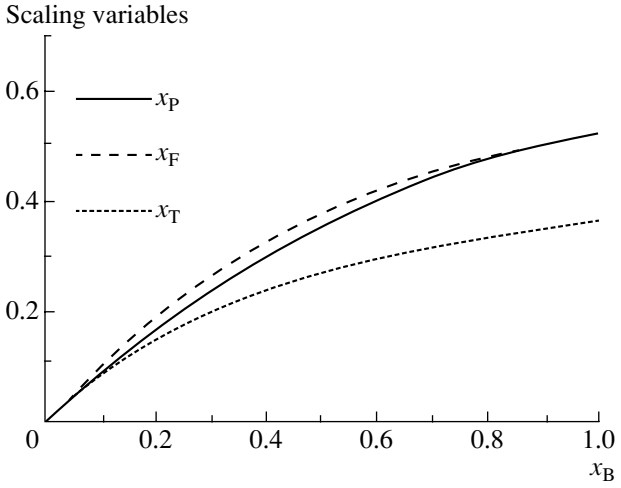

Fig. 8. Relationship between different scaling variables versus x_B at $Q^2 = 0.5$ GeV^2.

If we consider that x_F was defined only in the region around $x_B \approx 1$, we find for x_F that, in the small-Q^2 region, the following relation holds:

$$x_F \xrightarrow[Q^2\to 0]{} \frac{x_B}{1+M/2\nu}. \qquad (A.1)$$

Another scaling variable can easily be extrapolated to the high-x_B region—for this, it is sufficient to recast (13) into the form

$$x_T = \frac{x_B}{1+x_BM^2/Q^2} = \frac{x_B}{1+M/2\nu},$$

which coincides with (A.1). Thus, the variable x_T in the form (13) is a scaling variable at small Q^2 for any x_B. In turn, the variable x_F is a scaling variable for $x_B \to 1$ for any Q^2. In the small-Q^2 and high-x_B region, the two variables coincide.

At low values of x_B, the Feynman variable does not nevertheless reduce to x_T because of an extra power of x_B in the radicand. In order to solve this problem, we proposed, in [12], a new variable x_P[8] [see formula (18) above],

$$x_P = \frac{2x_B}{1+\sqrt{1+4M^2x_B^{1+x_B}/Q^2}},$$

which coincides with the Feynman variable in the region around $x_B \sim 1$ and which, at the same time, ensures a correct transition to x_T in the limit of small Q^2.

Figure 8 displays the three scaling variables versus x_B at $Q^2 = 0.5$ GeV^2. With increasing Q^2, the three scaling variables approach each other, but the qualitative dependence and their interrelations remain unchanged. In the limit of low x_B at fixed Q^2, all

three variables depicted in Fig. 8 reduce to the original scaling variable x_B.

In conclusion, we note that the variable x_B changes from 0 to 1. At the same time, the variables x_F, x_T, and x_P can reach unity, according to (11), (13), and (18), only in the limit $Q^2 \to \infty$. Therefore, it is the variable x_B, whose boundary values correspond to the above limits, that is used in formulas (21) and (23) for the interpolating function in order to link smoothly the two limiting cases in (20).

REFERENCES

1. G. Cvetic, D. Schildknecht, and A. Shoshi, hep-ph/9910379.
2. G. Altarelli, Phys. Rep. **81**, 1 (1982).
3. A. B. Kaidalov, hep-ph/0103011.
4. V. N. Gribov and L. N. Lipatov, Yad. Fiz. **15**, 781 (1972) [Sov. J. Nucl. Phys. **15**, 438 (1972)]; L. N. Lipatov, Yad. Fiz. **20**, 181 (1974) [Sov. J. Nucl. Phys. **20**, 94 (1975)]; G. Altarelli and G. Parisi, Nucl. Phys. B **126**, 298 (1977); Yu. L. Dokshitser, Zh. Éksp. Teor. Fiz. **73**, 1216 (1977) [Sov. Phys. JETP **46**, 641 (1977)].
5. A. D. Martin, R. G. Roberts, W. S. Stirling, and R. S. Thorne, Eur. Phys. J. C **23**, 73 (2002).
6. CTEQ Collab. (J. Pumplin *et al.*), hep-ph/0201195.
7. A. Capella, A. B. Kaidalov, C. Merino, and J. Tran Than Van, Phys. Lett. B **337**, 358 (1994).
8. E. V. Bugaev and Yu. V. Shlemin, Phys. Rev. D **67**, 034027 (2003).
9. H. Abramowicz and A. Levy, hep-ph/9712415.
10. S. R. Kelner and D. A. Timashkov, Yad. Fiz. **64**, 1802 (2001) [Phys. At. Nucl. **64**, 1722 (2001)].
11. A. A. Petrukhin and D. A. Timashkov, Yad. Fiz. **66**, 199 (2003) [Phys. At. Nucl. **66**, 195 (2003)].
12. A. A. Petrukhin and D. A. Timashkov, Acta Phys. Pol. B **33**, 3033 (2002).
13. F. Halzen and A. Martin, *Quarks and Leptons: An Introductory Course in Modern Particle Physics* (Wiley, New York, 1984; Mir, Moscow, 1987).
14. A. M. Cooper-Sarcar, R. C. E. Devenish, and A. de Roeck, hep-ph/9712301.
15. E. Levin, hep-ph/9808486.
16. A. de Rujula *et al.*, Ann. Phys. (N.Y.) **103**, 315 (1977).
17. C. Amelung, Nucl. Phys. B (Proc. Suppl.) **79**, 176 (1999).
18. L. N. Lipatov, Yad. Fiz. **23**, 642 (1976) [Sov. J. Nucl. Phys. **23**, 338 (1976)]; É. A. Kuraev, L. N. Lipatov, and V. S. Fadin, Zh. Éksp. Teor. Fiz. **71**, 840 (1976) [Sov. Phys. JETP **44**, 443 (1976)]; **72**, 377 (1977) [**45**, 199 (1977)]; Ya. Ya. Balitskiĭ and L. L. Lipatov, Yad. Fiz. **28**, 1597 (1978) [Sov. J. Nucl. Phys. **28**, 822 (1978)].
19. B. Badelek *et al.*, Rev. Mod. Phys. **64**, 927 (1992).
20. F. Martin, Phys. Rev. D **19**, 1382 (1979).
21. W. Buchmuller and D. Haidt, hep-ph/9605428.
22. D. Haidt, Nucl. Phys. B (Proc. Suppl.) **79**, 186 (1999).
23. A. B. Kaidalov *et al.*, Eur. Phys. J. C **20**, 301 (2001).
24. J. Gayler, Acta Phys. Pol. B **33**, 2841 (2002).
25. A. Rostovtsev, M. G. Ryskin, and R. Engel, Phys. Rev. D **59**, 014021 (1999).
26. K. Hagiwara *et al.* (Particle Data Group), Phys. Rev. D **66**, 010001 (2002).
27. H1 Collab. (C. Adloff *et al.*), Eur. Phys. J. C **13**, 609 (2000); C. Adloff *et al.*, Eur. Phys. J. C **19**, 269 (2001); **21**, 33 (2001).
28. ZEUS Collab. (J. Breitweg *et al.*), Eur. Phys. J. C **12**, 35 (2000); S. Chekanov *et al.*, Eur. Phys. J. C **21**, 443 (2001).
29. R. Cross, hep-ex/9903046.
30. P. V. Landshoff, hep-ph/0010315.
31. M. Froissart, Phys. Rev. **123**, 1053 (1961).
32. V. A. Petrov and A. V. Prokudin, Yad. Fiz. **64**, 2073 (2001) [Phys. At. Nucl. **64**, 1988 (2001)].

Translated by A. Isaakyan

Physics of Atomic Nuclei, Vol. 67, No. 12, 2004, pp. 2227–2244. Translated from Yadernaya Fizika, Vol. 67, No. 12, 2004, pp. 2252–2268.
Original Russian Text Copyright © 2004 by Golokhvastov.

ELEMENTARY PARTICLES AND FIELDS
Theory

Independent π^--Meson Production in pp Interactions

A. I. Golokhvastov*

Joint Institute for Nuclear Research, Dubna, Moscow oblast, 141980 Russia

Received April 22, 2003; in final form, September 1, 2003

Abstract—It is shown that experimental data on the multiparticle production of negatively charged pions in proton–proton interactions at $\sqrt{s} \leq 30$ GeV do not involve significant indications of the existence of any correlations between negatively charged pions, apart from those that are associated with momentum conservation and with interference. The multiplicity distributions in rapidity intervals, forward–backward correlations, and two-particle rapidity and transverse-momentum correlations do not contradict the independent production of negatively charged pions. No constraints on the multiplicity distributions of product particles follow from their independent production. © *2004 MAIK "Nauka/Interperiodica"*.

1. POISSON DISTRIBUTION

The statement that, in the case of the independent production of particles or any other objects (clans, clusters, jets, etc.), their multiplicity distribution must be Poissonian is often made in the physics of multiparticle processes (see, for example, [1, 2]).

This statement is "proven" by means of factorizing inclusive cross sections—if all particles are produced independently of one another, then their two-, three-, and multiparticle spectra can represented in the form of products of their single-particle spectra [3, 4]; that is,

$$\rho(y_1, y_2, \ldots, y_i) = \rho(y_1)\rho(y_2)\ldots\rho(y_i), \qquad (1)$$

where

$$\rho(y) = \frac{1}{\sigma_{\text{in}}}\frac{d\sigma}{dy}, \qquad (2)$$

$$\rho(y_1, y_2, \ldots, y_i) = \frac{1}{\sigma_{\text{in}}}\frac{d^i\sigma}{dy_1 dy_2 \ldots dy_i}.$$

Since the integrals of these quantities are

$$\int \rho(y)dy = \langle n\rangle, \qquad (3)$$

$$\int \rho(y_1, y_2, \ldots, y_i)dy_1 dy_2 \ldots dy_i = \langle n(n-1)\ldots(n-i+1)\rangle,$$

integration of the set of Eqs. (1) leads to a set of equations that is equivalent to a Poisson distribution [5–7]; that is,

$$\langle n(n-1)\ldots(n-i+1)\rangle = \langle n\rangle^i. \qquad (4)$$

This result is independent of which variable is denoted by y. This may be the rapidity of a particle, its momentum, the angle of its emission, or merely a random number assigned to each particle.

However, relation (4) does not arise if, for example, one introduces some factors (identical or dependent on i or on y_i) on the right-hand side of (1), although this has no effect on factorability. The resulting set of equations will then be equivalent to some other distribution.

But in fact, independence of events in probability theory is determined by factorability of precisely probability densities [8, 9] rather than by factorability of some arbitrarily chosen quantities. The probability density for a composite event is equal to the product of the probability densities for the elementary events that constitute it if they are independent.

To understand that the quantities in (2) are not probability densities, it is sufficient to notice that the integrals of them are not equal to unity [8, 9]. If one normalizes these quantities to unity by dividing them by (3) and, only after that, substitutes the result into (1), then the set of Eqs. (4) reduces to the identity $1 = 1$, so that a Poisson distribution disappears. Moreover, the equalities in (1) cannot be used as an indication of the independence of particles even after normalization [8, 9]—the factors on the right-hand side of (1) are not projections of the left-hand side (see Section 7).

The point is that the right- and the left-hand side of (1) are constructed on the basis of different statistical ensembles. For example, the left-hand side features no interactions where the number of particles satisfies the condition $n < i$. Also, $n \geq i$ events enter in different proportions into the expressions on the right- and on the left-hand side of (1) [see, in addition, Section 7, item (ii)].

*e-mail: golokhv@sunhe.jinr.ru

Therefore, the set of Eqs. (1) and, accordingly, a Poisson distribution have nothing to do with the independence of particles.

In integrating the quantity $\rho(y)$ over any interval of y, one obtains, according to the first equality in (3), the mean multiplicity within this interval—that is, $\rho(y)$ is the density of the particle multiplicity. Similarly, $\rho(y_1, y_2)$ is the two-dimensional density of the multiplicity of a pair of particles where the first particle occurs at y_1, while the second particle appears at y_2; further, $\rho(y_1, y_2, y_3)$ is the three-dimensional multiplicity of triples of particles; and so on [10]. In integrating these multiplicity densities, one obtains, according to (3), the multiplicities of pairs, triples, etc.

Thus, we have seen that the equalities in (1) correspond to factorability of mean-multiplicity densities rather than to factorability of probability densities [11].

By specifying some multiplicity distribution and by generating each particle at random on the basis of some spectrum, one can simulate an ensemble of events where the kinematical features of particles are a fortiori independent. Obviously, trivial reasons for a correlation between multiplicities at different phase-space points survive in this case (see also Section 5). Let us consider the case where we are dealing with a broad multiplicity distribution; by selecting, from the total ensemble of events, a subensemble where the multiplicity in the interval $y_1 \pm \Delta y$ is high, we thereby select events of high total multiplicity and, hence, increase the multiplicity in the interval $y_2 \pm \Delta y$.

On the other hand, a selection of events in which the multiplicity at y_1 is high leaves a lower multiplicity for y_2 if the total multiplicity is fixed. Thus, the correlation of multiplicity densities is negative if the multiplicity distribution is very narrow and is positive if the multiplicity distribution is very broad. If $\langle n(n-1)\rangle = \langle n\rangle^2$ [see Eq. (4)], these opposite trends compensate each other, with the result that the two-particle correlation of multiplicities vanishes.

However, a Poisson distribution with respect to multiplicities can be obtained in a standard way—that is, as a limit of a binomial distribution [8, 9]. In the case of the independent production of particles, their distribution in a bounded domain of phase space for events of fixed multiplicity is binomial (see also Section 3). If this domain is small—that is, if the probability for a particle chosen at random to occur within it is very low—the distribution becomes Poissonian there. As a well-known example of this, one can recall the distribution with respect to the number of decays of a radioactive source within a time interval that is much shorter than the source lifetime.

Of course, some intuitive or model considerations may lead to a relation between independent production and a specific form of the multiplicity distribution—in particular, a Poisson distribution (see, for example, [12–15]). However, nothing of this kind follows from probability theory [16], despite the expectations based on (1)–(4).

2. INDEPENDENT PRODUCTION

For the independence of events, we will now employ a standard definition in probability theory and consider the independent production of particles in the case where, for each of them, kinematical features (for example, rapidity) are independent of the features of other particles belonging to the same type [11].

The density of the probability that a particle chosen at random in a random event involving precisely n secondary particles has a rapidity y is

$$\tilde{\rho}_n(y) \equiv \frac{1}{n\sigma_n}\frac{d\sigma_n}{dy}, \qquad \int \tilde{\rho}_n(y)dy = 1, \tag{5}$$

where σ_n is the cross section for the production of n particles. The tilde symbol over $\rho_n(y)$ indicates that the spectrum in question is normalized to unity [17, 18]. A random event and the number of a track in this event can be chosen, for example, with the aid of a random-number generator. In an experiment, this spectrum is obtained on the basis of all measured tracks.

The density of the probability that the rapidities of two random particles chosen consecutively from a random event featuring n particles ($n \geq 2$) are y_1 and y_2 is

$$\tilde{\rho}_n(y_1, y_2) \equiv \frac{1}{n(n-1)\sigma_n}\frac{d^2\sigma_n}{dy_1 dy_2}, \qquad \int \tilde{\rho}_n(y_1, y_2)dy_1 dy_2 = 1 \tag{6}$$

(the second particle is chosen among the remaining $n-1$ particles of the event).

If the rapidities of two arbitrary particles in an event are independent of each other—that is, if the rapidity spectrum of the second particle chosen at random, $\tilde{\rho}_n(y_2)$, is independent of the rapidity of the first particle—then the two-particle probability density is equal to the product of the single-particle probability densities [11],

$$\tilde{\rho}_n(y_1, y_2) = \tilde{\rho}_n(y_1)\tilde{\rho}_n(y_2), \tag{7}$$

which are the projections of the two-particle probability density (the necessary condition of independence [8, 9]):

$$\tilde{\rho}_n(y_1) = \int \tilde{\rho}_n(y_1, y_2)dy_2, \tag{8}$$

$$\tilde{\rho}_n(y_2) = \int \tilde{\rho}_n(y_1, y_2) dy_1.$$

The density of the probability that the rapidities of i random particles consecutively chosen in an event containing n particles ($n \geq i$) are $y_1, y_2, \ldots, y_i$ is

$$\tilde{\rho}_n(y_1, y_2, \ldots, y_i) \equiv \frac{1}{n(n-1)\ldots(n-i+1)\sigma_n} \times \frac{d^i\sigma_n}{dy_1 dy_2 \ldots dy_i}. \quad (9)$$

If the rapidities of all particles in an event are independent—that is, if the distribution of the ith particle with respect to y in the subensemble of events where the first particle chosen at random has a rapidity y_1, the second particle has a rapidity y_2, and so on up to y_{i-1} is identical to that in the total ensemble of events—then we have

$$\tilde{\rho}_n(y_1, y_2, \ldots, y_i) = \tilde{\rho}_n(y_1)\tilde{\rho}_n(y_2)\ldots\tilde{\rho}_n(y_i). \quad (10)$$

In the sections that follow, we will verify whether the assumption of independent particle emission is compatible with experimental data on the production of negatively charged particles (in practice, negatively charged pions) in proton–proton interactions. Such a comparison was partly given in [19].

In what is concerned with "dynamical" correlations, investigation of correlations between negatively charged particles in proton–proton interactions is much "purer" than a similar investigation for all charged particles. The point is that, in the former case, the contribution of the correlations and background from the decays of resonances and long-lived particles, from Dalitz pairs and photon conversion, from the momentum-conservation law (the momentum can be compensated by both neutral and positively charged particles) and the charge-conservation law (there are always only an even number of charged particles in an event), and from primary particles (even after a collision, they continue traveling in opposite directions) and their mass misidentification (for example, the numbers of positively charged pions and protons are in a ratio of about $3:1$ at $E_{\text{lab}} = 400$ GeV) is much smaller, which is of importance since, albeit being quite trivial, these correlations are difficult to take into account.

In order to perform a comparison with experimental data, we will employ two approximations of the semi-inclusive single-particle rapidity spectra of negatively charged pions [20]; that is,

$$\tilde{\rho}_n(y) = \frac{1}{2\sqrt{2\pi Y_{\text{G}}}} \times \left[\exp\frac{-(y-Y_{\text{G}})^2}{2Y_{\text{G}}} + \exp\frac{-(y+Y_{\text{G}})^2}{2Y_{\text{G}}}\right], \quad (11)$$

$$\tilde{\rho}_n(y) = \frac{1}{2Y_{\text{F}}}\left[\left(\exp\frac{y-Y_{\text{F}}}{0.37}+1\right)^{-1} - \left(\exp\frac{y+Y_{\text{F}}}{0.37}+1\right)^{-1}\right], \quad (12)$$

$$Y_{\text{G}} = l - l^{0.64} + 0.26, \quad (13)$$

$$Y_{\text{F}} = l + l^{0.19} - 1.60, \quad l = \ln(\sqrt{s}/\sqrt{n}M_p c^2),$$

M_p being the proton mass. The approximation in (11) has a two-humped shape at large values of Y_{G}, while the approximation in (12) is flat at large values of Y_{F}; however, both of them describe the experimental spectra fairly well at the energy values considered here [20]. Either approximation becomes narrower with increasing multiplicity. In Section 9, we will also use a standard approximation for the transverse momenta of negatively charged pions.

3. MULTIPLICITY IN INTERVALS

The probability that one negatively charged pion chosen at random in an event where there are N negatively charged pions falls within a given interval of y is [see Eq. (5)]

$$p = \int_{y_1}^{y_2} \tilde{\rho}_N(y) dy, \quad (14)$$

p being dependent on N. If all negatively charged pions are independent, in which case relation (10) holds, the probability for each succesive negatively charged pion chosen from the same event to occur in this interval is identical to that given above. Therefore, the probability that precisely n negatively charged pions from an event involving N negatively charged pions will fall within this interval is

$$P_{n|N} = \frac{N!}{n!(N-n)!}p^n(1-p)^{N-n} \quad (15)$$

(this is a binomial distribution [9]). The probability that precisely n negatively charged pions from a random event will occur in this interval (here, we perform averaging over N) is

$$P_n = \sum_N P_N P_{n|N} = \sum_N P_N \frac{N!}{n!(N-n)!}p^n(1-p)^{N-n}, \quad (16)$$

where P_N is the distribution with respect to the total multiplicity of negatively charged pions in this event.

In Fig. 1, the multiplicity distributions of negatively charged pions within various rapidity intervals [21, 22] are contrasted against the results calculated on the basis of (16) (points). In this figure

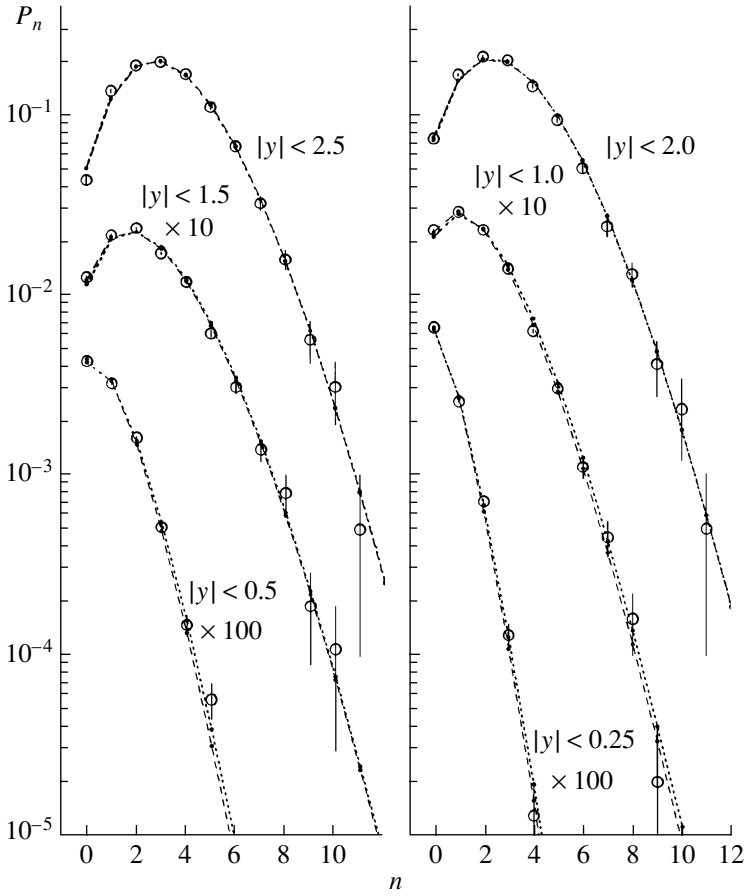

Fig. 1. Multiplicity distributions of negatively charged pions within various rapidity intervals in proton–proton interactions at 250 GeV/c. The segments of straight lines connect points corresponding to integral values of n [formula (16)] and independent production of negatively charged pions [see formula (10)]. The dotted and dashed segments represent the approximations in, respectively, (11) and (12) (visually, they are virtually indistinguishable).

and in those that follow, the points corresponding to the approximations in (11) and (12) are connected by segments of, respectively, dotted and dashed straight lines. The displayed experimental data were obtained in $\pi^+ p$ interactions at 250 GeV/c, but, according to the statement of the experimentalists that explored those interactions, they are equivalent to proton–proton interactions in the rapidity intervals being considered. Only non-single-diffractive (NSD) events were used in the experiment, and only those results were presented that were deduced by fitting the negative binomial distribution

$$P_n = \frac{k(k+1)\ldots(k+n-1)}{n!} \times \left(\frac{\bar{n}}{\bar{n}+k}\right)^n \left(\frac{k}{\bar{n}+k}\right)^k \qquad (17)$$

to the total multiplicity distribution of negatively charged pions. It is this distribution that was used to derive P_N in (16) with the parameter values of $\bar{n} = 3.47$ and $1/k = 0.013$, which were quoted in [22].

The mean values and variances of the multiplicity distributions of negatively charged pions in proton–proton interactions at 200 and 250 GeV/c are shown in Fig. 2 for given rapidity intervals that are symmetric (250 GeV/c [22]) or asymmetric (200 GeV/c [23]) with respect to the c.m. frame. As before, only non-single-diffractive events were used there, and the results were presented only in the form of the fitted parameters of the negative binomial distribution (17). The points in Fig. 2 were obtained by formulas that are valid in the case where the data in question are precisely described in terms of the distribution in (17):

$$\langle n \rangle \equiv \sum nP_n = \bar{n}, \qquad (18)$$
$$D \equiv \sqrt{\langle n^2 \rangle - \langle n \rangle^2} = \sqrt{\bar{n} + \bar{n}^2/k}.$$

The curves in Fig. 2 can be obtained directly from (16); however, it is possible to render the calculations somewhat shorter, which will be of use

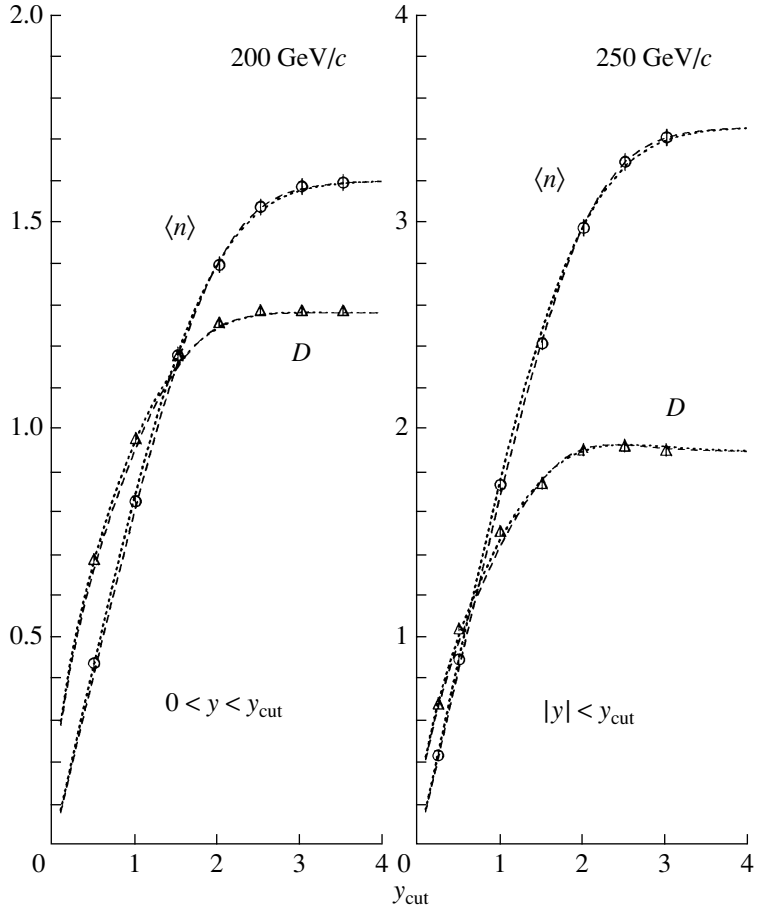

Fig. 2. Mean values and variances of the multiplicity distributions of negatively charged pions in proton–proton interactions at 200 and 250 GeV/c within given rapidity intervals that are symmetric (250 GeV/c) or asymmetric (200 GeV/c) with respect to the c.m. frame (points). The curves representing Eq. (20) correspond to the independent production of negatively charged pions [see Eq. (10)]. The dotted and dashed curves were calculated with the aid of the approximations in, respectively, (11) and (12) (visually, they are virtually indistinguishable).

in the sections that follow. For events involving N negatively charged pions, the mean multiplicity of this particle species in a given rapidity interval and the mean square of its multiplicity—that is, the mean and the mean square of the binomial distribution (15)—are given by [9]

$$\langle n\rangle_N \equiv \sum_n nP_{n|N} = Np, \qquad (19)$$

$$\langle n^2\rangle_N \equiv \sum_n n^2P_{n|N} = Np(1-p+Np).$$

Since these quantities are linear in $P_{n|N}$, they can be averaged over N. The results are

$$\langle n\rangle \equiv \sum_n nP_n = \sum_n n\sum_N P_NP_{n|N} \qquad (20)$$

$$= \sum_N P_N\sum_n nP_{n|N} = \sum_N P_NNp,$$

$$\langle n^2\rangle \equiv \sum_n n^2P_n = \sum_n\sum_N n^2P_NP_{n|N}$$

$$= \sum_N P_NNp(1-p+Np)$$

[D is obtained from these equalities according to (18)].

The data are described well in terms of the independent production of negatively charged pions. This test—that of whether the occurrence of each pion in a given rapidity interval is purely random—must of course precede the fitting of multiplicity distributions within these intervals in terms of some function. As a rule, the assumption that there exist clans, clusters, and some other "extra objects" serves as a justification of such fits. For example, the function in (17) is obtained from the assumption that product clusters obey a Poisson distribution, while the particles in the clusters have a Bose–Einstein distribution [15].

The data at $\sqrt{s} = 30$ and 62 GeV from [24]—these were also reported only in the form of the fitted parameters of a negative binomial distribution (see Fig. 3)—are described much more poorly. The curves correspond to the approximation in (11) [the approximation in (12) leads to a nearly identical result]. The solid curves were obtained with the aid of the approximations of P_N in terms of a negative binomial distribution that were constructed in [24], while the dash-dotted curves are based on experimental data from [25]. The latter describe better the behavior of $\langle n \rangle$ everywhere, with the exception of the last points, which (those at 62 GeV) cannot be described—for wide rapidity intervals, the mean multiplicity of negatively charged pions (more precisely, the parameter $\bar{n}$ from a fit in terms of a negative binomial distribution) in that study decreases (!) as the interval broadens. Of course, this only means that the data in question are poorly described by the approximation in (17), but the data themselves are not quoted in [24].

The data on the variances D are described poorly here, but they were obtained from the parameters $\bar{n}$ and k of the same fit in terms of (17) in accordance with (18).

4. ISOLATED INTERVALS

Figure 4 displays the features of the multiplicity distributions of negatively charged pions in $\pi^+ p$ interactions at 250 GeV/c within the rapidity interval $|y| < y_C$ under the condition that no negatively charged pion occurs in the neighboring rapidity intervals $y_C < |y| < y_E$ [26]. Here, the points were also calculated from the parameters of the fit in terms of (17) in accordance with (18). The results for $K^+ p$ interactions behave similarly [26], and one may hope that the same pattern will arise from proton–proton interactions as well. Therefore, the curves (for the independent production of negatively charged pions) were obtained by using the same approximations (11)–(13).

The probability that one negatively charged pion chosen at random in an event containing N negatively charged pions occurs in the interval $|y| < y_C$ (p_C) and the analogous probability that it occurs in the intervals $y_C < |y| < y_E$ (p_E) are

$$p_C = 2\int\limits_0^{y_C} \tilde{\rho}_N(y)dy, \quad p_E = 2\int\limits_{y_C}^{y_E} \tilde{\rho}_N(y)dy, \qquad (21)$$

p_C and p_E being dependent on N. The probability of an event containing N negatively charged pions of which none falls within forbidden intervals is $P_N(1 - p_E)^N$.

The distribution with respect to the total multiplicity N of negatively charged pions in a subensemble of events where no negatively charged pion falls within the interval $y_C < |y| < y_E$ is

$$P'_N = \frac{P_N(1-p_E)^N}{\sum\limits_N P_N(1-p_E)^N}, \quad \sum_N P'_N = 1. \qquad (22)$$

The probability that each negatively charged pion from an event featuring N negatively charged pions and entering into this subensemble occurs in the central interval is

$$p = p_C/(1 - p_E), \qquad (23)$$

p being dependent on N. For events involving N negatively charged pions, the mean number of particles belonging to this species in the central interval and the mean square of their number are calculated in just the same way as in (19). Averaging them over N, we find as in (20) that

$$\langle n \rangle = \sum_N P'_N Np, \qquad (24)$$

$$\langle n^2 \rangle = \sum_N P'_N Np(1 - p + Np).$$

Figure 4 shows that the multiplicity distributions of negatively charged pions in such isolated "clans," as well as their "existence," are well described by a purely random occurrence of each pion at different points of phase space.

Because of various trivial correlations (see Section 2), it is hardly possible to describe the mixture of all charged particles in such simple terms.

5. FORWARD–BACKWARD CORRELATIONS

The dependence of the mean multiplicity of negatively charged pions, $\langle B \rangle$, in some rapidity interval b (backward) on the multiplicity F in an interval that does not overlap the preceding one, f (forward), is determined not only by "true" correlations and the multiplicity dependence of the spectra but also by two trivial reasons (see Section 1). Selecting events characterized by high values of F, we thereby select events of high total multiplicity N and, hence, increase $\langle B \rangle$. On the other hand, the selection of high values of F at a fixed value of N reduces $\langle B \rangle$.

Figure 5 (at the top right) shows the experimental points for $\langle B \rangle$ versus F for full forward–backward rapidity intervals in the c.m. frame of proton–proton interactions at $p_{\text{lab}} = 250$ GeV/c [27]. The segments of straight lines represent fits to these data in terms of the linear approximation [27]

$$\langle B(F) \rangle = a + (b \pm \Delta b)F. \qquad (25)$$

These straight-line segments correspond to the upper and the lower bound on the parameter $b \pm \Delta b$. The

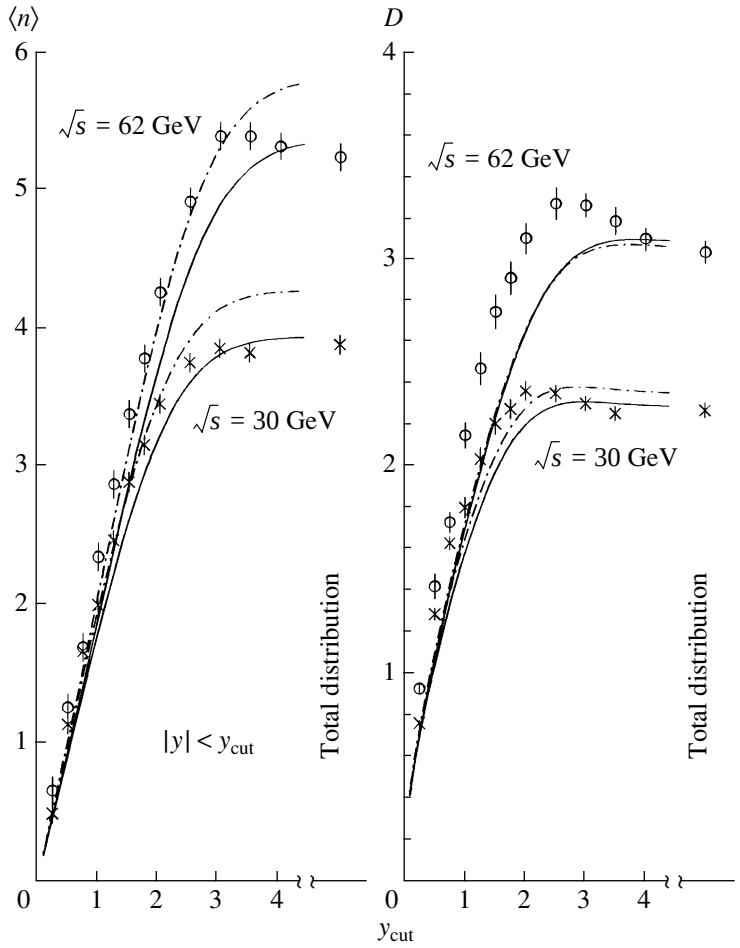

Fig. 3. Mean values and variances of the multiplicity distributions of negatively charged pions in proton–proton interactions at $\sqrt{s} = 30$ and 62 GeV within given rapidity intervals (symmetric ones). The curves based on (20) for the independent production of negatively charged pions [see Eq. (10)] correspond to the approximation in (11). The solid curves were constructed by using the approximations of total multiplicity distributions in the form of a negative binomial distribution, while the dash-dotted curves were drawn on the basis of experimental distributions.

error in the parameter a ($\Delta a = 0.03$) is disregarded here.

In [27], the dependences $\langle B(F)\rangle$ were also obtained for bounded rapidity intervals. Unfortunately, they were presented only in the form of the fitted parameters of the linear form (25). In Fig. 5, the straight-line segments on the left show these data for central symmetric intervals ($|y| < y_{\mathrm{cut}}$), while those on the right correspond to them for peripheral intervals ($|y| > y_{\mathrm{cut}}$). It is likely that, here, the errors in the parameter a are not less than those for the full intervals $|y| > 0$. These pairs of straight lines are truncated at F values for which experimental statistics (proportional to P_F—see below) are approximately identical to those for the last experimental point for $|y| > 0$.

The dotted and dashed lines in Fig. 5 [approximations in the form (11) and in the form (12), respectively] correspond to independent pion emission. These lines, which connect points at integral values of F, were obtained in the following way.

The probability that a random pion from an event featuring N pions falls within the forward (backward) rapidity interval, p_{f} (p_{b}), is written in the same form as that in (14) (these probabilities depend on N). The probability that precisely F pions from an event involving N pions fall within the forward interval, $P_{F|N}$, is taken to be identical to that in (15) (binomial distribution):

$$P_{F|N} = \frac{N!}{F!(N-F)!} p_{\mathrm{f}}^F (1-p_{\mathrm{f}})^{N-F}. \qquad (26)$$

Averaging over N, as in (16), we obtain the probability that precisely F pions from a random event occur in this interval: $P_F = \sum P_{F|N} P_N$. The probability that, in an event where precisely F pions fall within the forward interval, the total multiplicity is

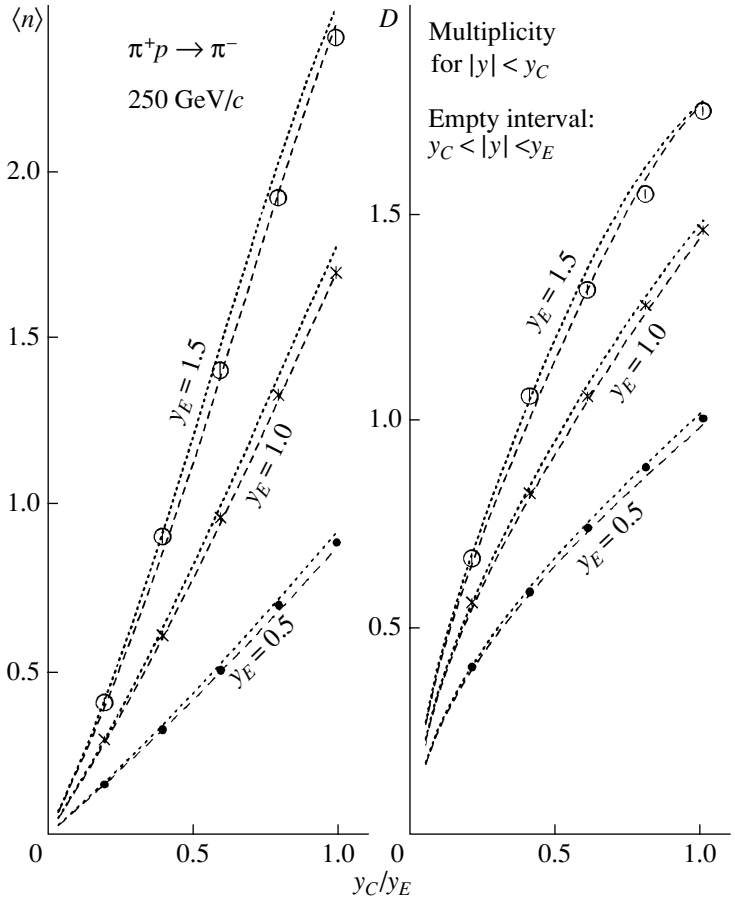

Fig. 4. Mean values and variances of the multiplicity distributions of negatively charged pions in the isolated rapidity interval $|y| < y_C$ under the condition that no negatively charged pion occurs in the neighboring intervals $y_C < |y| < y_E$. The curves obtained according to (24) correspond to the independent production of negatively charged pions [see Eq. (10)]. The dotted and dashed curves represent the approximations in (11) and (12), respectively.

N is $P_{N|F} = P_{F|N}P_N/P_F$, this being a relationship between inverse conditional probabilities [9].

The mean multiplicity of negatively charged pions occurring in the backward interval and coming from an event where there are N negatively charged pions and where F of them fall within the forward interval is $(N-F)p_\mathrm{b}/(1-p_\mathrm{f})$. Averaging it over N with a weight $P_{N|F}$, we obtain

$$\langle B(F)\rangle = \sum_N P_{F|N}P_N(N-F)p_\mathrm{b}/P_F(1-p_\mathrm{f}). \tag{27}$$

For this formula, the probabilities P_N were taken from the distributions in (17) whose parameters were obtained from a and b for the full intervals $|y| > 0$ [27]: $\bar{n} = 2a_\mathrm{full}/(1-b_\mathrm{full}) = 3.63$ and $1/k = b_\mathrm{full}/a_\mathrm{full} = 0.011$.

For the same data from [27], Fig. 6 shows the parameters a and b of the linear approximation in (25) versus the boundaries of the intervals [27]. If these correlations had been exactly described by the linear approximation (25), its parameters would have been [27]

$$b = \frac{\langle BF\rangle - \langle B\rangle\langle F\rangle}{\langle F^2\rangle - \langle F\rangle^2}, \quad a = \langle B\rangle - b\langle F\rangle, \tag{28}$$

since

$$\langle B\rangle = \sum_F P_F\langle B(F)\rangle \tag{29}$$
$$= \sum_F P_F(a+bF) = a + b\langle F\rangle,$$

$$\langle BF\rangle = \sum_F FP_F\langle B(F)\rangle \tag{30}$$
$$= \sum_F FP_F(a+bF) = a\langle F\rangle + b\langle F^2\rangle.$$

If negatively charged pions are not correlated, then the probability that, in an event featuring N negatively charged pions, precisely F and B negatively

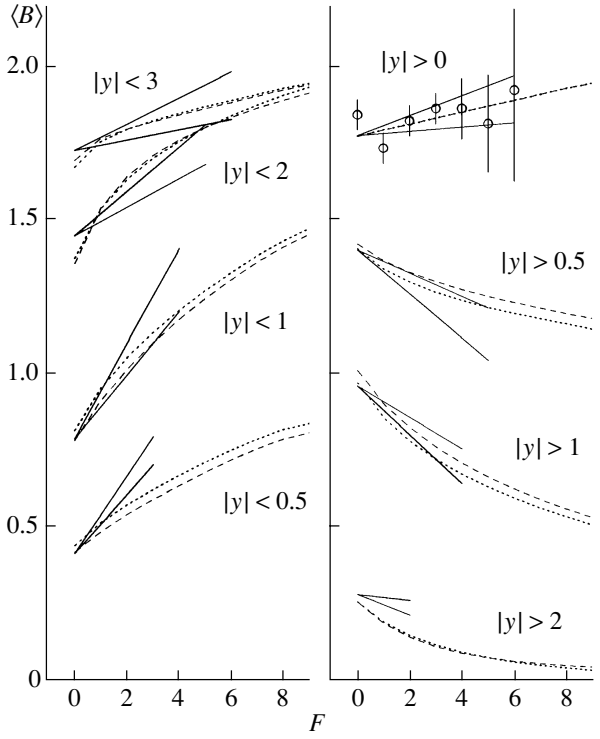

Fig. 5. Dependence of the mean multiplicity of negatively charged pions in the backward hemisphere ($\langle B\rangle$) on the multiplicity in the forward hemisphere (F) in proton–proton interactions ($p_{\mathrm{lab}} = 250$ GeV/c) for various cuts on the rapidity intervals. The segments of solid straight lines represent fits to experimental data. The dotted and dashed lines connect points (at integral values of F) corresponding to the independent production of negatively charged pions [see Eq. (10)]. They were obtained on the basis of (27) by using the approximations (dotted lines) in (11) and (dashed lines) in (12).

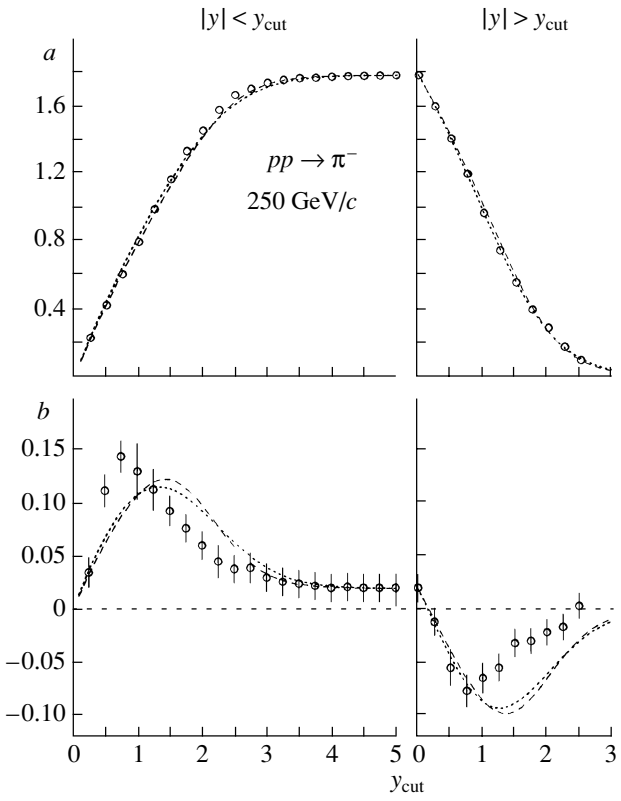

Fig. 6. Values of the parameters a and b for forward–backward multiplicity correlations $\langle B\rangle = a + bF$ (see the preceding figure) in the cental ($|y| < y_{\mathrm{cut}}$) and the peripheral ($|y| > y_{\mathrm{cut}}$) rapidity region (points). The curves calculated on the basis of (28) and (32) represent the independent production of negatively charged pions [see Eq. (10)]. The dotted (dashed) curves correspond to the approximation in (11) [(12)].

charged pions fall within, respectively, the forward and the backward interval is described by the trinomial distribution $P_{F,B|N}$. The mean values of the moments of this distribution are [9]

$$\langle F\rangle_N = Np_{\mathrm{f}}, \quad \langle F^2\rangle_N = Np_{\mathrm{f}}(1 - p_{\mathrm{f}} + Np_{\mathrm{f}}), \quad (31)$$
$$\langle FB\rangle_N = p_{\mathrm{f}}p_{\mathrm{b}}N(N-1).$$

Since they are linear in $P_{F,B|N}$, they can be averaged over N in the same way as in (20). The results are

$$\langle F\rangle = \sum_N P_N Np_{\mathrm{f}}, \quad \langle B\rangle = \sum_N P_N Np_{\mathrm{b}}, \quad (32)$$
$$\langle F^2\rangle = \sum_N P_N Np_{\mathrm{f}}(1 - p_{\mathrm{f}} + Np_{\mathrm{f}}),$$
$$\langle FB\rangle = \sum_N P_N p_{\mathrm{f}}p_{\mathrm{b}}N(N-1).$$

The curves in Fig. 6, which correspond to the independent emission of negatively charged pions, were obtained by formulas (28) and (32)—that is, under the assumption of an exact linear dependence in the form of (25). This assumption is not consistent with our curves in Fig. 5, but, on the basis of the curves themselves, it is impossible to determine the parameters a and b of the fit, which depend on the experimental errors in $\langle B(F)\rangle$.

In [19], formulas (28) and (32) are contrasted against data from [27] for asymmetric intervals (right–left correlations).

The formulas for forward–backward correlations are simplified in the case of full intervals ($|y| > 0$)—the probabilities $p_{\mathrm{f}} = p_{\mathrm{b}} = 0.5$ are independent of multiplicity, and it can be found from (28) and (32) that [28]

$$a = \langle N\rangle^2 / (D^2 + \langle N\rangle), \quad (33)$$
$$b = (D^2 - \langle N\rangle) / (D^2 + \langle N\rangle).$$

The quantities $\langle N\rangle$ and D are the mean value and the variance of the total multiplicity distribution. In [28], it

was shown that, for various reactions, these correlations are consistent with the assumption of independent particle production.

It is clear that, in the independent emission of negatively charged particles from proton–proton interactions, their forward–backward correlations for full intervals are identical to upward–downward (with respect to the reaction axis) correlations (or correlations in any other direction) in the c.m. frame. Of course, this is not so for all charged particles—for example, both leading protons can have transverse momenta directed upward, but their emission in the forward direction in the c.m. frame is virtually impossible.

6. CORRELATION FUNCTION

The correlation function is defined as the difference of the probability density for a composite event and the product of the probability densities for partial events constituting it. This definition corresponds to the definition of independence of events in probability theory (Section 1)—if particles are produced independently, the correlation function must be everywhere equal to zero. We will now consider rapidity correlations.

The two-particle correlation function can be represented in the form [see (5)–(8)] [11]

$$\tilde{C}_n \equiv \tilde{\rho}_n(y_1, y_2) - \tilde{\rho}_n(y_1)\tilde{\rho}_n(y_2), \qquad (34)$$
$$\int \tilde{C}_n dy_1 dy_2 = 0.$$

Here and below, the tilde symbol over C indicates that the spectra are normalized to unity [10, 17, 18]. The function $\tilde{C}_n$ can be averaged over n. The result is

$$\tilde{C}_S \equiv \sum_{n=2}^{\infty} P_n \tilde{C}_n \qquad (35)$$
$$= \sum_{n=2}^{\infty} P_n \left[\tilde{\rho}_n(y_1, y_2) - \tilde{\rho}_n(y_1)\tilde{\rho}_n(y_2)\right].$$

Hereafter, the index "S" (short range) on C indicates the averaging of semi-inclusive functions [10, 29, 30].

If summation in (35) begins from unity, then, even for fully independent particles according to (7), $\tilde{C}_S$ cannot be equal to zero because of a noncompensated second term at $n = 1$ (see Fig. 7 at the left top):

$$\tilde{C}_S = -P_1 \tilde{\rho}_1(y_1)\tilde{\rho}_1(y_2). \qquad (36)$$

The function $\tilde{C}_n$ can also be averaged over n with a weight that is proportional to statistics of pairs at each n [29, 31]:

$$C'_S \equiv \sum_n n(n-1) P_n \left[\tilde{\rho}_n(y_1, y_2) - \tilde{\rho}_n(y_1)\tilde{\rho}_n(y_2)\right] \qquad (37)$$

(see Fig. 8 at the left top). By the way, summation automatically begins from $n = 2$ in this case. For a correct comparison of data at different energies, it would be more reasonable to normalize this expression to $\langle n(n-1)\rangle$ (by dividing it by this quantity), but the data in Fig. 8 were obtained according to (37).

The correlation function in the form (37) corresponds to a known procedure for studying interference correlations. Within this procedure, the two-particle spectrum is compared with the mixed spectrum of pairs of particles where each particle of a pair is chosen at random from different events (having the same multiplicity of these particles in an event!) [32, 33]. More precisely, the function $R'_S \equiv C'_S / \sum_n n(n-1) P_n \tilde{\rho}_n(y_1)\tilde{\rho}_n(y_2)$ normalized to single-particle spectra is used in interference correlations.

7. PSEUDOCORRELATIONS

Frequently, use is made of different "correlation" functions that are formally similar to the preceding ones, but which are not related to probability theory, being constructed on the basis of intuitive considerations (see also [34]).

(i) The semi-inclusive unnormalized function [4]

$$C_n \equiv \rho_n(y_1, y_2) - \rho_n(y_1)\rho_n(y_2), \qquad (38)$$
$$\int C_n dy_1 dy_2 = -n,$$

where the multiplicity densities in events of multiplicity n are

$$\rho_n(y) \equiv \frac{1}{\sigma_n}\frac{d\sigma_n}{dy} = n\tilde{\rho}_n(y), \qquad (39)$$
$$\rho_n(y_1, y_2) \equiv \frac{1}{\sigma_n}\frac{d^2\sigma_n}{dy_1 dy_2}$$
$$= n(n-1)\tilde{\rho}_n(y_1, y_2).$$

Under no conditions can the function C_n be equal to zero for all values of y, since the integral of it is not equal to zero. The first and the second term in (38) are normalized to different numbers of particle pairs. Here, the product of single-particle spectra is a model of a two-particle spectrum where correlations are switched off, but this model does not consider that, in an actual event, the second particle is chosen among $n-1$ rather than among n particles, as in the case of the first particle. Of course, no such problem arises if different particle species correspond to y_1 and y_2 (taking a positively charged particle from an event, one does not change the number of negatively charged particles).

The function C_n averaged over n [29, 30] is

$$C_S = \sum_n P_n [n(n-1)\tilde{\rho}_n(y_1, y_2) \qquad (40)$$

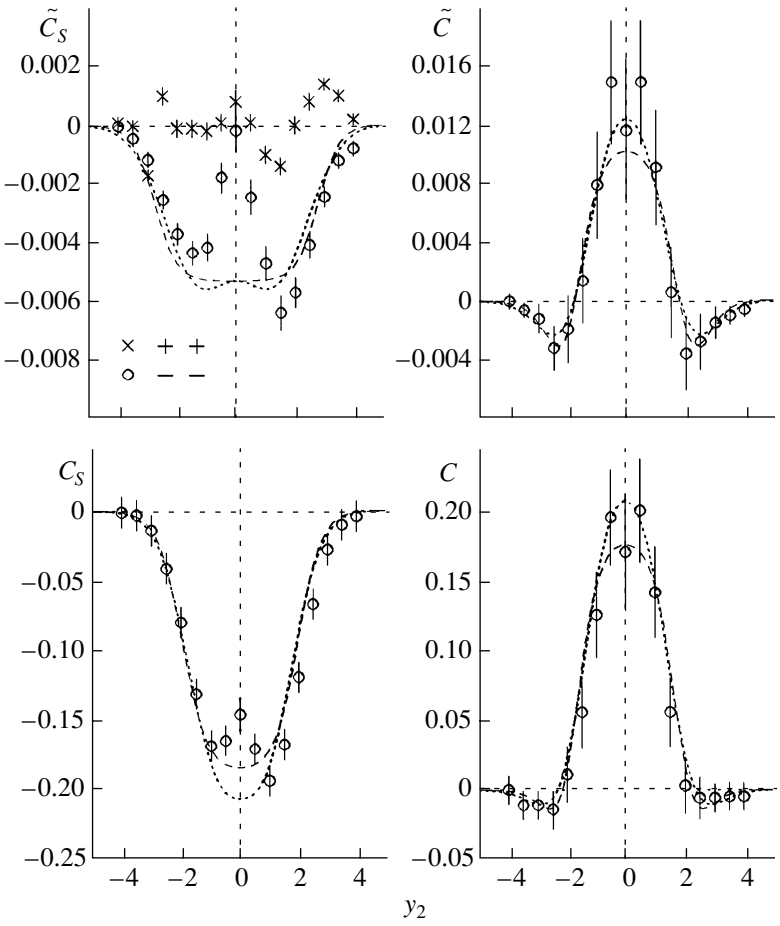

Fig. 7. Two-particle rapidity correlations of negatively charged pions ($y_1 = 0$) in proton–proton interactions at 250 GeV/c for the definitions of the correlation function according to (35), (40), (42), and (46) in events where $n \geq 1$ [points, asterisks corresponding to positively charged particles (see main body of the text)]. The curves calculated on the basis of (36), (41), (45), and (48) represent the independent emission of negatively charged pions [see Eq. (7)]. The dotted (dashed) curves were obtained by using the approximation in (11) [(12)].

$$- n^2\tilde{\rho}_n(y_1)\tilde{\rho}_n(y_2)],$$

$$\int C_S dy_1 dy_2 = -\langle n\rangle.$$

In the case of independent particle emission [see Eq. (7)], we find from (40) that (see Figs. 7 and 8)

$$C_S = -\sum_n nP_n\tilde{\rho}_n(y_1)\tilde{\rho}_n(y_2). \qquad (41)$$

(ii) The inclusive normalized function [35, 36]

$$\tilde{C} \equiv \tilde{\rho}(y_1, y_2) - \tilde{\rho}(y_1)\tilde{\rho}(y_2), \qquad (42)$$

$$\int \tilde{C} dy_1 dy_2 = 0,$$

where the normalized mean-multiplicity densities are given by

$$\tilde{\rho}(y) \equiv \frac{1}{\langle n\rangle\sigma_{\rm in}}\frac{d\sigma}{dy} = \sum_n \frac{n}{\langle n\rangle}P_n\tilde{\rho}_n(y), \qquad (43)$$

$$\tilde{\rho}(y_1, y_2) \equiv \frac{1}{\langle n(n-1)\rangle\sigma_{\rm in}}\frac{d^2\sigma}{dy_1 dy_2}$$

$$= \sum_n \frac{n(n-1)}{\langle n(n-1)\rangle}P_n\tilde{\rho}_n(y_1, y_2).$$

The quantity $\tilde{\rho}(y)$ can be interpreted as the density of the probability that a particle chosen at random from the total set of particles produced in events characterized by various values of n has the rapidity y. Concurrently, the quantity $\tilde{\rho}(y_1, y_2)$ can be interpreted as the density of the probability that, in a pair of particles that was chosen among the total set of pairs, the particles have the rapidities y_1 and y_2.

However, the equality $\tilde{\rho}(y_1, y_2) = \tilde{\rho}(y_1)\tilde{\rho}(y_2)$, which involves these quantities and which is similar to Eq. (7), cannot be a definition of the independence of particle production since the single-particle spectrum in (43) is not [in contrast to (8)] a projection of the

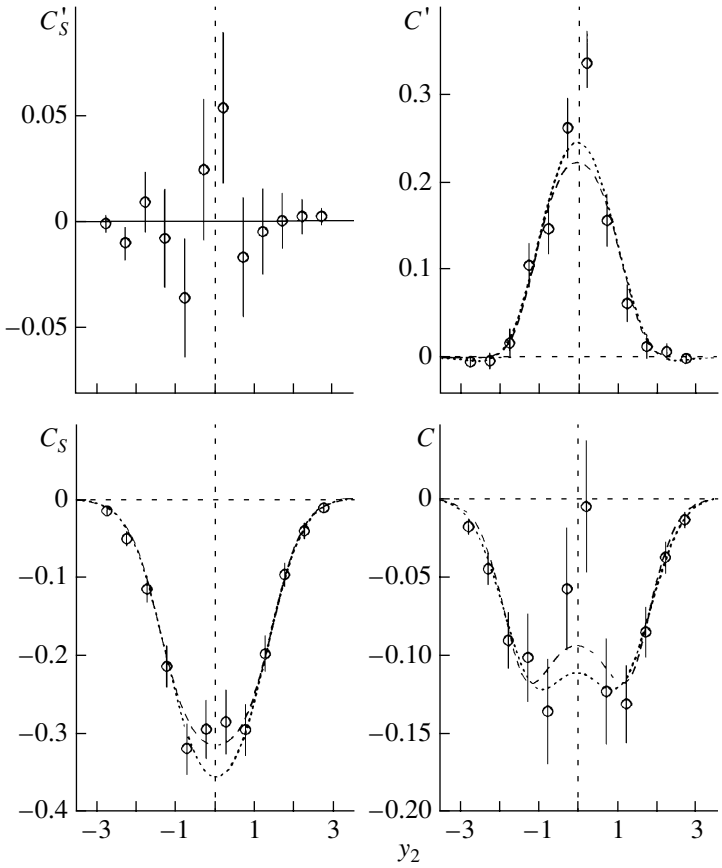

Fig. 8. Two-particle rapidity correlations of negatively charged pions ($y_1 = 0$) from proton–proton interactions at 69 GeV/c for the definitions of the correlation function according to (37), (40), (46), and (49) in events where $n \geq 2$ (points). The curves calculated on the basis of (41), (48), and (49) represent the independent emission of negatively charged pions [see Eq. (7)] [for C'_S, Eq. (37) yields a straight line at $C'_S = 0$]. The dotted (dashed) curves were obtained by using the approximation in (11) [(12)].

two-particle spectrum (see also Section 1):

$$\int \tilde{\rho}(y_1, y_2)dy_2 = \langle n(n-1)\rangle^{-1} \tag{44}$$
$$\times \sum_n n(n-1)P_n \int \tilde{\rho}_n(y_1, y_2)dy_2$$
$$= \langle n(n-1)\rangle^{-1} \sum_n n(n-1)P_n\tilde{\rho}_n(y_1) \neq \tilde{\rho}(y_1).$$

The first and the second term in (42) are constructed on the basis of different ensembles of events. The first term contains a larger fraction of events characterized by greater n than the second one since the number pion pairs in an event is proportional to $n(n-1)$, while the number of pions is proportional to n. The width of the rapidity spectrum decreases with increasing multiplicity {see Eqs. (11)–(13); see also [20]}; therefore, the first term $\tilde{C}$ is a narrower and higher function than the second one (for equal integrals). It is this combinatorial pseudocorrelation that is seen in Fig. 7—the difference of these terms is positive at low values of $|y_2|$, is negative at large values of this quantity, and is equal to zero when $\tilde{\rho}_n(y)$ becomes equal to zero.

In the case of independent particle emission, we find from (7) and (42) that (see Fig. 7)

$$\tilde{C} = \langle n(n-1)\rangle^{-1} \sum_n n(n-1)P_n\tilde{\rho}_n(y_1)\tilde{\rho}_n(y_2) \tag{45}$$
$$- \langle n\rangle^{-2} \sum_n nP_n\tilde{\rho}_n(y_1) \sum_n nP_n\tilde{\rho}_n(y_2).$$

For independent pion production, the function $\tilde{C}$ could be equal to zero at all values of y_1 and y_2 if pion spectra were independent of n.

(iii) The nonnormalized inclusive function [3] [see Eq. (1)]

$$C \equiv \rho(y_1, y_2) - \rho(y_1)\rho(y_2), \tag{46}$$
$$\int C dy_1 dy_2 = \langle n(n-1)\rangle - \langle n\rangle^2,$$

where the densities of the mean multiplicity of particles and pairs are identical to those in (2):

$$\rho(y) = \sum_n nP_n\tilde{\rho}_n(y), \tag{47}$$
$$\rho(y_1, y_2) = \sum_n n(n-1)P_n\tilde{\rho}_n(y_1, y_2).$$

In the case of independent particle emission, we find from (7) and (46) that (see Figs. 7, 8)

$$C = \sum_n n^2P_n\tilde{\rho}_n(y_1)\tilde{\rho}_n(y_2) \tag{48}$$
$$- \sum_n nP_n\tilde{\rho}_n(y_1)\tilde{\rho}_n(y_2)$$
$$- \sum_n nP_n\tilde{\rho}_n(y_1)\sum_n nP_n\tilde{\rho}_n(y_2).$$

The function C combines both pseudocorrelations inherent in the two preceding functions: the error in the normalization as in C_S and the combinatorial pseudocorrelation as in $\tilde{C}$. In the case of independent particle production [see Eq. (7)], the function C could be equal to zero under two additional conditions: if the spectrum was independent of n and if the "correlation" parameter of the multiplicity distribution was $f_2 \equiv \langle n(n-1)\rangle - \langle n\rangle^2 = 0$.

(iv) The function introduced in [29] (see Fig. 8),

$$C' = C + \sum_n P_n\rho_n(y_1)\rho_n(y_2)/n \tag{49}$$
$$= C + \sum_n nP_n\tilde{\rho}_n(y_1)\tilde{\rho}_n(y_2).$$

In the case of independent particle emission, this function differs from C (48) by the absence of the second term, so that, in the opinion of the authors of [29], is analogous to the function for particles of different type that correspond to y_1 and y_2.

8. RAPIDITY CORRELATIONS OF NEGATIVELY CHARGED PIONS

The experimental points given in Fig. 7 were obtained at 250 GeV/c [30] for C and $\tilde{C}$ from proton–proton interactions and for C_S and $\tilde{C}_S$ from π^+p and K^+p interactions, but, according to data from [30], these interactions must be close to proton–proton interactions. In deriving these correlation functions, use was also made in [30] of an event featuring one negatively charged pion. The curves in the figures were obtained on the basis of formulas (36), (41), (45), and (48) under the assumption that there are no correlations [see Eq. (7)].

The pseudocorrelation in $\tilde{C}_S$ emerges only because of the noncompensated second term in (35) at $n = 1$. For positively charged particles (asterisks in Fig. 7), there is no pseudocorrelation since their multiplicities in pp, K^+p, and π^+p interactions are always greater than unity. The curve deviates from the experimental points in Fig. 7 significantly only for $\tilde{C}_S$. This may be a true correlation (for example, interference correlation); yet, it cannot be seen for positively charged particles either.

The pseudocorrelation in C_S is obtained because of the different normalizations of the first and the second term in (38). The first term is always less than the second.

In the function $\tilde{C}$, the combinatorial pseudocorrelation stems from the fact that the single-particle and the two-particle spectrum are averaged differently over an ensemble of events: the weight of higher multiplicity events is greater in the first term $\tilde{C}$ (42) than in the second (see preceding section).

The function C combines both preceding pseudocorrelations.

The data displayed in Fig. 8 were obtained in proton–proton interactions at 69 GeV/c [29, 37]. The curves calculated on the basis of (41), (48), and (49) correspond to the independent emission of negatively charged pions [see Eq. (7)]. For C'_S (37), this is the straight line at $C'_S = 0$. Apart from two more definitions of the correlation functions [C'_S (37) and C' (49)], Fig. 8 also differs from Fig. 7 by the absence of events that involve one negatively charged pion, this rendering the forms of the functions used still more diverse. This distinction is quite significant: by way of example, we indicate that, here, the function C is negative, although it is positive for $n \geq 1$ [29], just as for 250 GeV/c in Fig. 7.

Figure 9 shows the correlation function R (at $y_1 = 0$),

$$R \equiv \sigma_{\text{in}}\frac{d^2\sigma/dy_1dy_2}{(d\sigma/dy_1)(d\sigma/dy_2)} - 1 \tag{50}$$
$$= \frac{\sum_n n(n-1)P_n\tilde{\rho}_n(y_1, y_2)}{\sum_n nP_n\tilde{\rho}_n(y_1)\sum_n nP_n\tilde{\rho}_n(y_2)} - 1$$

(this is the function C normalized to single-particle spectra), for various primary proton energies in the range 21–400 GeV/c [18, 29, 31, 38–43]. Of course, the pseudocorrelations in R are identical to those in C. The curves were also obtained under the assumption that negatively charged pions are produced independently [see Eq. (7)].

The data displayed in Figs. 7–9 were obtained for all inelastic events rather than for only non-single-diffractive events. In constructing the curves, we used

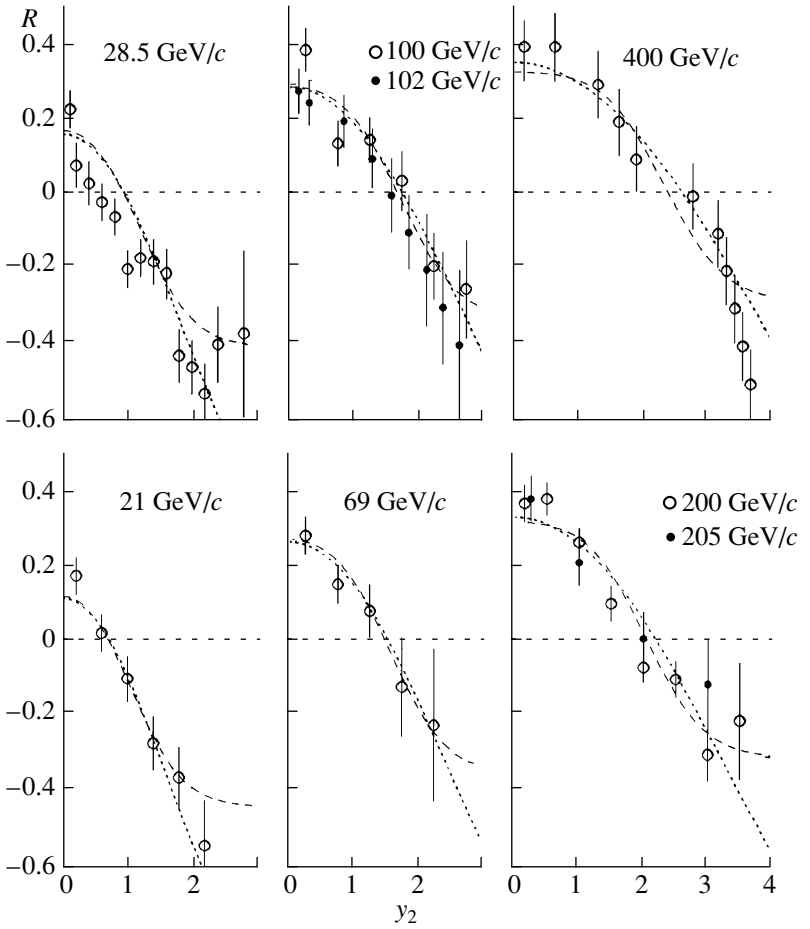

Fig. 9. Two-particle rapidity correlations of negatively charged pions at $y_1 = 0$, $R(y_1, y_2) \equiv C(y_1, y_2)/\rho(y_1)\rho(y_2)$ (50), in proton–proton interactions at 21–400 GeV/c in events where $n \geq 1$ (points). The curves were obtained under the assumption of the independence of product negatively charged pions [see Eq. (7)]. The dotted (dashed) curves correspond to the approximation in (11) [(12)].

the following approximation of the multiplicity distributions P_n of negatively charged pions [44]:

$$P_n = \Phi\left(\frac{n}{\langle m\rangle}\right) - \Phi\left(\frac{n+1}{\langle m\rangle}\right), \qquad (51)$$

$$\Phi(z) = 1.01\exp[-0.62(z+0.14)^2],$$

$$\langle m\rangle = 0.78\left(\sqrt{s}/M_p - 2\right)^{3/4}\left(\sqrt{s}/M_p\right)^{-1/4}.$$

Of course, correlations associated with processes characterized by small cross sections—for example, interference correlations—are not noticeable against the background of the general pattern considered here. That the points lie somewhat above the curves in Fig. 7–9 for $y_2 \sim 0$ stems from this phenomenon, however. This excess becomes greater if one selects pairs of particles having close azimuthal angles [45]. By the way, interference correlations are frequently studied in terms of precisely the pseudocorrelation function R (which depends on the difference of pion momenta) or the function $\tilde{R}$ (which is identical to the function $\tilde{C}$ normalized to the single-particle spectra) [46], but this must distort the results.

Figure 10 shows the rapidity correlations of negatively charged pions ($y_1 \sim 0$) from [47] (360 GeV/c, $\sqrt{s} = 26$ GeV) and [48] ($\sqrt{s} = 31$–62 GeV) for events where the number of negatively charged pions is greater than three. The curves in this figure were obtained with the aid of the experimental values of P_n from [25, 49]. These data are inadequately described by the curves plotted under the assumption of independent pion production. The data at 360 GeV/c lie far above the curves, while the ISR data are well below them. Moreover, these two data sets contradict each other—the points at 26 GeV must not differ from the points at 31 GeV. We also note that data from the same experiment at ISR [50] (53 GeV) and for $n \geq 1$ fall considerably short of data obtained in bubble-chamber experiments—for example, data at 400 GeV/c (not shown in Fig. 10).

The experiments reported in [47, 48, 50] (and the

experiment reported in [24] as well—see Fig. 3) had a bounded acceptance (in pseudorapidity in EHS [47] and in transverse momentum in SFM [24, 48, 50]); therefore, these data can be correctly compared with the predictions of the independent-particle model only by using the experimental data themselves—that is, by using a mixed ensemble of events constructed from negatively charged pions chosen at random from different events of the same multiplicity. This procedure coincides with that based on (37): the conditions in (7) and (10) are valid for an incomplete phase space as well.

All of the data in Figs. 7–10 were obtained for $y_1 \sim 0$. Figure 11 shows the behavior of the function C (46) in proton–proton interactions at 69 GeV/c for different values of the rapidity y_1 of the "triggering" negatively charged pion [51]. The curves calculated on the basis of (48) correspond to the independent emission of negatively charged pions [see Eq. (7)]. With increasing y_1, $\tilde{\rho}_n(y_1)$ in (48) decreases; concurrently, the multiplicity distribution in events involved in the construction of C changes: the contribution of high-multiplicity events having a narrower rapidity distribution decreases. All curves are symmetric with respect to the c.m. frame.

9. TRANSVERSE MOMENTUM

Figure 12 shows two-particle transverse-momentum correlations of negatively charged pions in proton–proton interactions at 69 GeV/c for various values of the momentum p_{T1} of the "triggering" negatively charged pion [51]. Figure 12 is analogous to Fig. 11, while the function $C(p_T)$ is analogous to the function C (46); that is,

$$C(p_T) \equiv \rho(p_{T1}, p_{T2}) - \rho(p_{T1})\rho(p_{T2}) \qquad (52)$$
$$= \frac{1}{\sigma_{\text{in}}}\frac{d^2\sigma}{dp_{T1}dp_{T2}} - \frac{1}{\sigma_{\text{in}}^2}\frac{d\sigma}{dp_{T1}}\frac{d\sigma}{dp_{T2}},$$

where the multiplicity densities are written in terms of the probability density in just the same way as in relations (47):

$$\rho(p_T) = \sum_n nP_n\tilde{\rho}_n(p_T), \qquad (53)$$
$$\rho(p_{T1}, p_{T2}) = \sum_n n(n-1)P_n\tilde{\rho}_n(p_{T1}, p_{T2}).$$

The curves in Fig. 12 were obtained under the assumption of independent (according to the standard definition of independence in probability theory—see Sections 1 and 2) pion production, $\tilde{\rho}_n(p_{T1}, p_{T2}) = \tilde{\rho}_n(p_{T1})\tilde{\rho}_n(p_{T2})$, with the aid of the well-known approximation of single-particle transverse-momentum distributions in the region of low values of p_T (see, for example, [52]), this approximation being reduced to the scaling form ("scaling in the mean" [53])

$$\tilde{\rho}_n(p_T) \equiv \frac{1}{n\sigma_n}\frac{d\sigma_n}{dp_T} \qquad (54)$$
$$= \frac{10}{3\sqrt{\pi}\langle p_T\rangle_n}\left(\frac{5}{2}\frac{p_T}{\langle p_T\rangle_n}\right)^{3/2}\exp\left(-\frac{5}{2}\frac{p_T}{\langle p_T\rangle_n}\right)$$

[$\int \tilde{\rho}_n(p_T)dp_T = \int p_T\tilde{\rho}_n(p_T)dp_T = 1$], where the experimental values of $\langle p_T\rangle_n$ were taken from [54]. Just as in Fig. 11, an increase in p_{T1} leads here to a decrease in $\tilde{\rho}_n(p_{T1})$ and in the contribution of high-multiplicity events having a narrower distribution with respect to p_T ($\langle p_T\rangle_n$ decreases with increasing n).

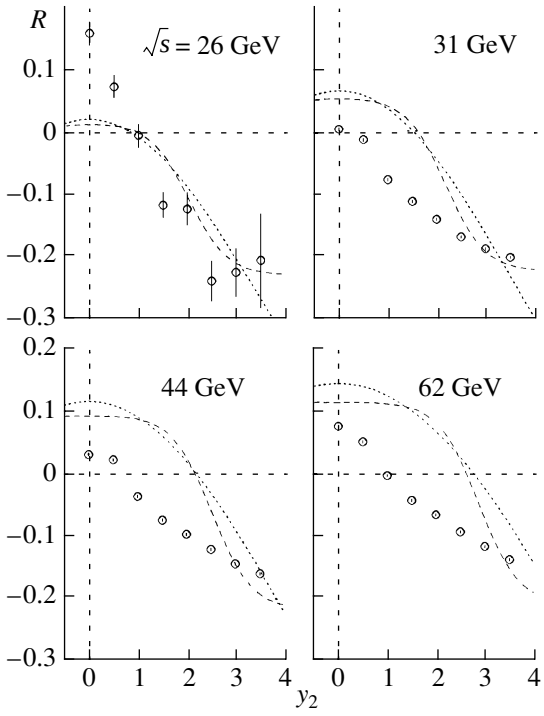

Fig. 10. Two-particle rapidity correlations of negatively charged pions, R (50) ($y_1 = 0$), at 360 GeV/c ($\sqrt{s} =$ 26 GeV) and $\sqrt{s} = 31$–62 GeV for events where $n \geq 3$ (points). The curves were constructed under the assumption that negatively charged pions are produced independently [see Eq. (7)]. The dotted (dashed) curves were obtained by using the approximation in (11) [(12)].

Figure 13 (205 GeV/c [17]), where not only absolute values of the momenta but also their directions are taken into account, violates the general pattern of a fairly good reproduction of experimental data in terms of independent pion production. Figure 13 shows, versus the transverse momentum p_{T1} of the "triggering" negatively charged pion, the behavior of the mean multiplicities (upper panels) and mean transverse momenta (lower panels) of the remaining

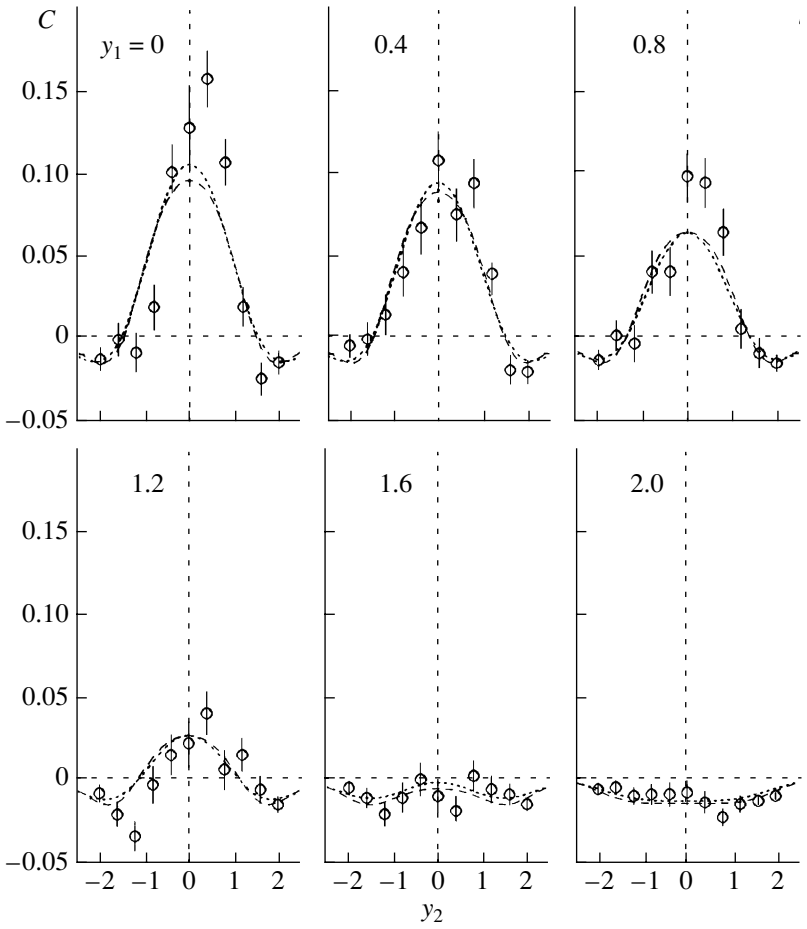

Fig. 11. Two-particle rapidity correlations of negatively charged pions, C (46), in proton–proton interactions (69 GeV/c, $n \geq 1$) at various values of the rapidity y_1 of the "triggering" negatively charged pion (points). The curves calculated on the basis of (48) correspond to the independent emission of negatively charged pions [see Eq. (7)]. The dotted (dashed) curves were obtained with the aid of the approximation in (11) [(12)].

negatively charged pions that are emitted either in the same azimuthal half-plane as the triggering pion ($\varphi < 90°$) or in the opposite half-plane ($\varphi > 90°$).

The curves in Fig. 13 correspond to independent pion production. They are independent of the direction of "triggering"-pion emission since momentum conservation is not taken into account here. Their behavior is dictated only by the change in the effective multiplicity distribution with increasing p_{T1}. The probability that, in an event featuring n negatively charged pions, one can find a pion that has the transverse momentum p_{T1} is proportional to $n\tilde{\rho}_n(p_{T1})$. Therefore, the multiplicity distribution of negatively charged pions in events where there is a pion of transverse momentum p_{T1} is

$$P'_n = nP_n\tilde{\rho}_n(p_{T1}) \Big/ \sum_n nP_n\tilde{\rho}_n(p_{T1}), \qquad (55)$$

while the mean multiplicity in one half-plane and the mean transverse momentum of the remaining negatively charged pions are

$$\langle n_2 \rangle = \sum_n P'_n(n-1)/2, \qquad (56)$$

$$\langle p_{T2} \rangle = \sum_n \langle p_T \rangle_n P'_n(n-1)/2\langle n_2 \rangle$$

(the "triggering" particle does not enter into n_2). The experimental values of $\langle p_T \rangle_n$ were borrowed from [17], while the total multiplicity distributions P_n were obtained according to (51). Various forms of azimuthal asymmetry between the half-planes $\varphi < 90°$ and $\varphi > 90°$ were observed in [40, 45, 47, 51, 55] as well.

Possibly, the faster growth of $\langle B(F) \rangle$ in relation to the curves in Figs. 5 and 6 for $|y| > 1$ is also associated with the momentum-conservation law.

10. CONCLUSION

It has been shown that experimental data on the multiparticle production of negatively charged pions

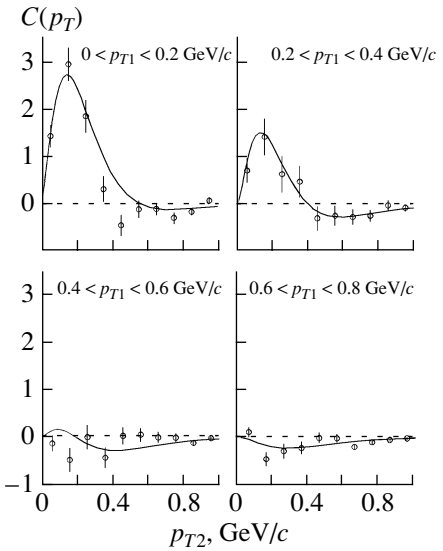

Fig. 12. Two-particle transverse-momentum correlations of negatively charged pions, $C(p_T)$ (52), in proton–proton interactions (69 GeV/c; $n \geq 1$) for various values of the transverse momentum p_{T1} of the "triggering" negatively charged pion (points). The curves correspond to the independent emission of negatively charged pions.

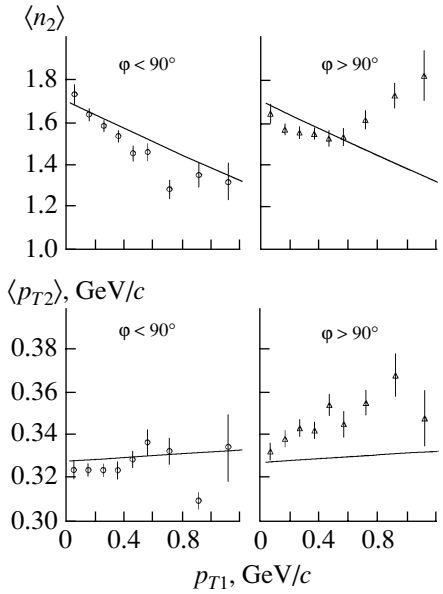

Fig. 13. Dependences on the transverse momentum p_{T1} of the "triggering" negatively charged pion for the mean multiplicities and mean transverse momentum of the remaining negatively charged pions emitted either in the same azimuthal half-plane as the "triggering" pion ($\varphi < 90°$) or in the opposite half-plane ($\varphi > 90°$). These results were obtained for proton–proton interactions at 205 GeV/c for $n \geq 1$. The curves calculated on the basis of (56) correspond to the independent emission of negatively charged pions.

in proton–proton interactions at $\sqrt{s} \leq 30$ GeV do not show significant pieces of evidence for the existence of any correlations between negatively charged pions, with the exception of correlations associated with momentum conservation and interference correlations.

Multiplicity distributions within rapidity intervals, including separated rapidity intervals (Section 3, 4); forward–backward correlations (Section 5); two-particle rapidity correlations (Sections 6–8); and two-particle transverse-momentum correlations (Section 9) are compatible with the independent production of negatively charged pions if the definition of independence corresponds to the standard definition in probability theory—that is, the factorization of probability densities (Sections 1, 2).

Numerous "correlation" functions that are constructed on the basis of intuitive considerations contradict this definition on the basis of probability theory either in what is concerned with the normalization condition for probability densities or in what is concerned with the condition that the single-particle probability density must be equal to the respective projection of the two-particle probability density (Section 7). The latter condition rules out the construction of a correct correlation function from inclusive distributions [Section 7, item (ii)]. This can be done only by using semi-inclusive spectra.

From the independent production of particles or of any other objects of multiparticle production (clans, clusters, jets), one can deduce no constraints on their multiplicity distributions. The well-known statement on a Poisson distribution is obtained from the assumption of the factorization of the mean-multiplicity density and not from the assumption of probability densities (see Section 1).

REFERENCES

1. S. Chekanov *et al.* (ZEUS Collab.), Phys. Lett. B **510**, 36 (2001).
2. C. Adloff *et al.* (H1 Collab.), Eur. Phys. J. C **5**, 439 (1998).
3. K. G. Wilson, Preprint CLNS-131 (Cornell, 1970).
4. C. E. DeTar, Phys. Rev. D **3**, 128 (1971).
5. A. H. Mueller, Phys. Rev. D **4**, 150 (1971).
6. A. Bassetto *et al.*, Nucl. Phys. B **34**, 1 (1971).
7. L. Caneschi, Nucl. Phys. B **35**, 406 (1971).
8. H. Cramer, *Mathematical Methods of Statistics* (Princeton Univ., Princeton, 1946; Mir, Moscow, 1975).
9. W. T. Eadie *et al., Statistical Methods in Experimental Physics* (North-Holland, Amsterdam, 1971; Atomizdat, Moscow, 1976).
10. E. A. De Wolf, I. M. Dremin, and W. Kittel, Usp. Fiz. Nauk **163** (1), 3 (1993) [Phys. Usp. **36**, 63 (1993)].
11. W. Ko, Phys. Rev. Lett. **28**, 935 (1972).

12. G. F. Chew and A. Pignotti, Phys. Rev. **176**, 2112 (1968).
13. L. Stodolsky, Phys. Rev. Lett. **28**, 60 (1972).
14. T. T. Chou and C. N. Yang, Phys. Rev. Lett. **55**, 1359 (1985).
15. A. Giovannini and L. Van Hove, Z. Phys. C **30**, 391 (1986).
16. A. I. Golokhvastov, Yad. Fiz. **58**, 2110 (1995) [Phys. At. Nucl. **58**, 1998 (1995)].
17. T. Kafka *et al.*, Phys. Rev. D **16**, 1261 (1977).
18. J. Whitmore, Phys. Rep. **27**, 187 (1976).
19. A. I. Golokhvastov, Z. Phys. C **64**, 301 (1994).
20. A. I. Golokhvastov, Yad. Fiz. **67**, 355 (2004) [Phys. At. Nucl. **67**, 337 (2004)].
21. M. Adamus *et al.*, Phys. Lett. B **177**, 239 (1986).
22. M. Adamus *et al.*, Z. Phys. C **37**, 215 (1988).
23. F. Dengler *et al.*, Z. Phys. C **33**, 187 (1986).
24. A. Breakstone *et al.*, Nuovo Cimento A **102**, 1199 (1989).
25. A. Breakstone *et al.*, Phys. Rev. D **30**, 528 (1984).
26. M. Adamus *et al.*, Phys. Lett. B **205**, 401 (1988).
27. V. V. Aivazyan *et al.*, Z. Phys. C **42**, 533 (1989).
28. D. Zieminska, Phys. Rev. D **27**, 502 (1983).
29. V. V. Ammosov *et al.*, Yad. Fiz. **23**, 341 (1976) [Sov. J. Nucl. Phys. **23**, 178 (1976)].
30. V. V. Aivazyan *et al.*, Z. Phys. C **51**, 167 (1991).
31. J. Hanlon *et al.*, Nucl. Phys. B **52**, 96 (1973).
32. G. I. Kopylov, Phys. Lett. B **50B**, 472 (1974).
33. M. Adamus *et al.*, Z. Phys. C **37**, 347 (1988).
34. S. A. Azimov *et al., Multiparticle Processes at High Energies* (Fan, Tashkent, 1976) [in Russian].
35. E. L. Berger *et al.*, Phys. Rev. D **6**, 2580 (1972).
36. M. Gyulassy *et al.*, Phys. Rev. C **20**, 2267 (1979).
37. V. V. Ammosov *et al.,* Preprint No. M-16, IFVÉ (Inst. for High Energy Phys., Serpukhov, 1975).
38. E. L. Berger *et al.*, Phys. Rev. Lett. **29**, 675 (1972).
39. J. Erwin *et al.*, Phys. Rev. Lett. **33**, 1443 (1974).
40. C. M. Bromberg *et al.*, Phys. Rev. D **9**, 1864 (1974); **10**, 3100 (1974).
41. R. Singer *et al.*, Phys. Lett. B **49B**, 481 (1974).
42. T. Ferbel, Preprint COO-3065-91 (Rochester, 1974).
43. L. Foa, Phys. Rep. **22**, 1 (1975).
44. A. I. Golokhvastov, Yad. Fiz. **64**, 1924 (2001) [Phys. At. Nucl. **64**, 1841 (2001)].
45. B. Y. Oh *et al.*, Phys. Lett. B **56B**, 400 (1975).
46. U. A. Wiedemann and U. W. Heinz, Phys. Rep. **319**, 145 (1999).
47. J. L. Bailly *et al.*, Z. Phys. C **40**, 13 (1988).
48. A. Breakstone *et al.*, Mod. Phys. Lett. A **6**, 2785 (1991).
49. J. L. Bailly *et al.*, Z. Phys. C **23**, 205 (1984).
50. A. Breakstone *et al.*, Phys. Lett. B **114B**, 383 (1982).
51. J. Derre *et al.*, Nuovo Cimento A **33**, 721 (1976).
52. E. L. Feĭnberg, Usp. Fiz. Nauk **104**, 539 (1971) [Sov. Phys. Usp. **14**, 455 (1971)].
53. F. T. Dao *et al.*, Phys. Rev. Lett. **33**, 389 (1974).
54. V. V. Ammosov *et al.*, Nuovo Cimento A **40**, 237 (1977).
55. I. V. Ajinenko *et al.*, Z. Phys. C **58**, 357 (1993).

Translated by A. Isaakyan

Physics of Atomic Nuclei, Vol. 67, No. 12, 2004, pp. 2245–2259. Translated from Yadernaya Fizika, Vol. 67, No. 12, 2004, pp. 2269–2284.
Original Russian Text Copyright © 2004 by A.N. Safronov, A.A. Safronov.

ELEMENTARY PARTICLES AND FIELDS
Theory

Solving the Relativistic Inverse Scattering Problem with Allowance for Inelasticity Effects on the Basis of N/D Equations and Application of the Resulting Solution to an Analysis of Nucleon–Nucleon Interaction

A. N. Safronov* **and A. A. Safronov**

Institute of Nuclear Physics, Moscow State University, Vorob'evy gory, Moscow, 119899 Russia

Received August 5, 2003; in final form, November 5, 2003

Abstract—A manifestly Poincaré-invariant approach to solving the inverse scattering problem is developed with allowance for inelasticity effects. The equations of the N/D method are used as dynamical equations in this approach. Two versions of the approach are considered. In the first version (method A), the required equations are constructed on the basis of the maximal-analyticity principle, which constitutes the basis of dynamical S-matrix theory. In formulating the second version of equations (method B), it is assumed that a partial-wave scattering amplitude may develop dynamical singularities that violate the requirement of maximal analyticity. The dynamics of interaction components that violate maximal analyticity is described within the model of a nonlocal separable potential. The method is used to analyze nucleon–nucleon interaction in the $^1S_0$ and $^3S_1$ states. The results obtained by solving the inverse scattering problem for potential functions are compared with the predictions of the one-boson-exchange model. © *2004 MAIK "Nauka/Interperiodica".*

1. INTRODUCTION

In recent years, considerable advances have been made in understanding the mechanisms of strong interactions on the basis of QCD, which is a non-Abelian gauge theory of quarks and gluons. The main success of QCD is due to the asymptotic-freedom phenomenon, which consists in a logarithmic decrease in the running coupling constant of the theory with increasing momentum transfer squared. The asymptotic-freedom property of QCD makes it possible to perform reliable theoretical calculations of transition amplitudes at high-momentum transfers (that is, at short distances) by using perturbation theory. At the same time, the running coupling constant increases fast in the region of low momentum transfers, with the result that perturbation theory becomes inapplicable there, this strongly complicating the description of hadron interactions in the region of low and intermediate energies (about a few GeV), which is of importance for nuclear physics. In the low-energy region (below the pion-production threshold), the effective chiral theory [1, 2] of strong interactions, which is based on QCD and on the idea of spontaneous chiral-symmetry breaking, has become popular in the past years. The pion field, whose quanta (that is, π mesons) have a double nature—on one hand, they are bound states of $\bar{q}q$ pairs, while, on the other hand, they are Goldstone bosons that arise upon spontaneous chiral-symmetry breaking—plays a key role in effective chiral theory.

The relationship between QCD and effective chiral theory can be established with the aid of the path-integral technique [3, 4]. In this approach, the formulation of strong-interaction theory in terms of hadronic degrees of freedom is realized via a change of variables in path integrals—integration with respect to fundamental QCD fields is replaced by integration with respect to "normal modes," which are fields of bare hadrons. In this way, one can specify the form of the classical action functional S written in terms of fields corresponding to "bare" pions, nucleons, antinucleons, and so on. At the next stage, one performs quantization of "bare" hadron fields and, with the aid of the diagram technique or dynamical equations (for example, the Bethe–Salpeter equation), takes into account the contributions of loop diagrams, this making it possible (upon applying renormalization procedures in one form or another) to calculate the amplitudes for physical processes. The nonlocal effective Lagrangian constructed in the way outlined above has a very cumbersome form. In the low-energy region, we can expand, however, the operator of bare-hadron interactions in powers of the relative momenta of the particles involved (and in powers of the masses of Goldstone bosons) and retain only a finite number of terms (this procedure corresponds to chiral perturbation theory).

*e-mail: safron@srd.sinp.msu.ru

1063-7788/04/6712-2245$26.00 © 2004 MAIK "Nauka/Interperiodica"

It should be noted that meson theories of nuclear forces [5, 6] have long since been used in nuclear physics to describe the properties of nucleon systems and scattering processes. The meson pattern of nuclear forces provides an adequate description of strong interactions in the peripheral region. However, quark–gluon degrees of freedom must inevitably manifest themselves at rather short distances. In this connection, we note that, along with meson-exchange forces, the QCD-inspired chiral Lagrangian of effective chiral theory predicts the existence of contact interactions [1] (in the nucleon–nucleon sector, this is a four-fermion interaction). As was mentioned above, however, this Lagrangian is correct at moderate relative momenta of the particles involved—that is, it may claim to provide a description of interactions only in the peripheral region. In order to obtain information about the character of nuclear forces at intermediate (about 1 fm) and short distances, it is necessary to employ, along with low-energy data, new information about the amplitudes of nucleon–nucleon scattering in the region of intermediate energies (about a few GeV) [7–9]. In the 1990s, considerable advances were made in the technique for measuring cross sections for nucleon–nucleon scattering with allowance for polarization effects. New data made it possible to obtain information about the energy dependence of partial-wave amplitudes for nucleon–nucleon scattering in the intermediate-energy region inclusive. An adequate theoretical interpretation of these data is of paramount importance for obtaining deeper insight into the mechanisms of nucleon interaction at low and intermediate energies.

2. DIRECT AND INVERSE SCATTERING PROBLEM IN THE METHOD OF DISPERSION RELATION FOR PARTIAL-WAVE AMPLITUDES

From the general point of view, quantum scattering theory implements, with the aid of underlying dynamical equations $\mathcal{E}$, which follow from basic physical postulates, a map $\mathcal{M}$ of a set of functions $\mathcal{V}$ known as parameters to a set of functions $\mathcal{R}$ referred to as the results of measurements (see, for example, [10]). A solution to the set of equations $\mathcal{E}$ must exist, and it must be unique in the set $\mathcal{R}$ for any element of the set $\mathcal{V}$. In view of this, the set $\mathcal{V}$ is defined as the set of functions such that, for them, a unique solution to the equations $\mathcal{E}$ exists in the set $\mathcal{R}$ and is compatible with all data following from fundamental physical principles and with available experimental information. It is assumed that, in principle, the elements of the set $\mathcal{R}$ can be determined from experimental data. The set $\mathcal{R}$ includes the parameters of bound states (binding energies and residues at S-matrix poles corresponding to bound states), phase shifts, and inelasticity parameters determining the elements of the matrix of on-energy-shell partial-wave amplitudes.

It should be noted that the set $\mathcal{R}$ involves quantities that cannot be measured directly in experiments even if the entire set of polarization measurements (complete experiment) is performed at a fixed energy. These are residues of partial-wave scattering amplitudes at poles corresponding to bound states. The residues in question can be found by analytically continuing the partial-wave scattering amplitudes in energy to the unphysical region on the basis of information about the energy dependence of the amplitudes in the physical region. In order to extract information about some elements of the set $\mathcal{R}$ from experimental data, we must therefore know the analytic properties of partial-wave amplitudes. However, this procedure relies on rather general physical requirements (see below) and does not call for employing a specific dynamical model of interactions. It follows that all (without exception) elements of the set $\mathcal{R}$ are model-independent quantities. A determination of the elements of the set $\mathcal{R}$ that correspond to the elements of the set $\mathcal{V}$ with the aid of the map $\mathcal{M}$ is the subject of the direct scattering problem. A determination of that subset of $\mathcal{V}$ which corresponds to a given element of the set $\mathcal{R}$ is referred to as the process of solving the inverse problem in quantum scattering theory.

In order to describe hadron–hadron scattering, we will use here the dispersion-relation method for partial-wave amplitudes, which is based on the application of the most general physical principles, such as Poincaré invariance, unitarity, and analyticity. The analyticity of scattering amplitudes is a corollary of one of the most fundamental physical principles—the microcausality principle [11, 12]. The requirements of unitarity and analyticity inevitably result in that the S matrix must have cuts in the invariant masses of the systems involving two, three, and more particles, these cuts issuing from the threshold points for the corresponding scattering channels. If, in addition to poles corresponding to single-particle states, the S matrix involves only those singularities that are necessary for fulfillment of the unitarity conditions in all possible scattering channels, it is common practice to say that the maximal-analyticity principle is valid[1)] [13]. This principle underlies the dynamical theory of the S matrix. Dispersion approaches based on rather general physical requirements are extensively used in strong-interaction physics (see, for example, [14–17]), including nuclear physics.

We note that the requirement of maximal analyticity is fully consistent with the general theory of the formation of proper singularities of Feynman

[1)] More precisely, this requirement corresponds to the maximal analyticity of the first order.

diagrams [18–21]. Indeed, we can associate, with each singularity of a scattering amplitude, a skeleton Feynman diagram such that the singularity in question is a proper singularity of this diagram. At the singular point, all particles corresponding to internal lines of the skeleton diagram in question must be, according to the Landau equations [18], on the mass shells $q_i^2 = m_i^2$, where q_i are the 4-momenta of these particles and m_i are their masses. From this condition, it follows that any particle corresponding to an internal line of this skeleton diagram must enter into the set of asymptotic states that arise upon the partition of the diagram into two independent blocks (or a greater number of them). Therefore, the poles and cuts of a scattering amplitude in invariant variables can correspond to proper singularities of only such skeleton diagrams whose lines cannot be anything but hadrons or their bound states. In QCD, this property is a consequence of the confinement condition.

The discontinuities of partial-wave amplitudes on dynamical cuts are determined by model-independent quantities—specifically, renormalized (physical) vertex coupling constants and amplitudes of subprocesses involving hadrons on their mass shells (Cutkosky rule [19]). Therefore, the structure of dynamical cuts of a scattering amplitude—at least of those closest to the physical region—can be calculated in a model-independent way. The above dynamical singularities determine the so-called potential functions—that is, dispersion integrals along left-hand cuts in the literature; they are often referred to as merely potentials (see, for example, [13]). Within the dispersion-relation method for partial-wave amplitudes, knowledge of potential functions makes it possible to solve the direct scattering problem—that is, to calculate on-shell partial-wave amplitudes, binding energies, and residues at S-matrix poles corresponding to bound states. The problem of finding the potential functions on the basis of available information about the energy dependences of partial-wave amplitudes and about the features of bound states is the subject of the inverse scattering problem in the dispersion relation method for partial-wave amplitudes.

The ensuing exposition is organized as follows. In Section 3, we consider a method for solving the inverse scattering problem on the basis of the maximal-analyticity principle. In Section 4, we discuss a possible mechanism of the breakdown of the maximal-analyticity principle by nonperturbative QCD effects and formulate modified N/D equations for describing scattering processes with allowance for this breakdown. In Section 5, we apply the proposed method to an analysis of nucleon–nucleon interaction in the ${}^1S_0$ and ${}^3S_1$ states. In the Conclusion, we discuss the results of this study.

3. SOLVING THE INVERSE SCATTERING PROBLEM WITHIN THE APPROACH BASED ON THE MAXIMAL-ANALYTICITY PRINCIPLE

Let us first consider a method for solving the inverse scattering problem (below, it will be referred to as method A) under the assumption that the maximal-analyticity principle is valid. In accordance with the aforesaid, we can state that, on the physical sheet in the complex plane of the square of the total 4-momentum of the system, s, the admissible singularities of the partial-wave scattering amplitude $A_l(s)$ are the following in this case:

(i) poles corresponding to the bound states;

(ii) the right-hand cut C_R (for $s_R \le s < \infty$, $s_R = (m_1 + m_2)^2$, where m_1 and m_2 are the masses of colliding particles) caused by the requirement of unitarity in the s channel,

$$\mathrm{Im}A_l^{-1}(s) = -\rho(s)R_l(s), \text{ at } C_R, \tag{1}$$

where

$$\rho(s) = \frac{2q(s)}{\sqrt{s}},$$

$$q(s) = \frac{1}{2}\sqrt{s - 2(m_1^2 + m_2^2) + \frac{(m_1^2 - m_2^2)^2}{s}}$$

is the relative momentum of colliding particles, and $R_l(s)$ is the inelasticity parameter defined according to the Froissart method [22]; and

(iii) the dynamical (left-hand) cuts C_L generated by the conditions of unitarity in the t and u channels.

We note that the inelasticity parameter $R_l(s)$ introduced in accordance with the Froissart method in formula (1) is the ratio $\sigma_l^{\mathrm{tot}}/\sigma_l^{\mathrm{el}}$ of the partial-wave cross sections for total and elastic scattering in states of specific orbital angular momentum l. From the above properties, it follows that the amplitude $A_l(s)$ has the integral representation

$$A_l(s) = B_l(s) + \sum_{j=1}^{\nu} \frac{\alpha_{lj}}{s - s_{lj}} \tag{2}$$

$$+ \frac{1}{\pi}\int_{s_R}^{\infty} \frac{|A_l(s')|^2}{s' - s} R_l(s')\rho(s')ds',$$

where

$$B_l(s) = \frac{1}{2\pi i}\int_{C_L} \frac{\mathrm{disc}A_l(s')}{s' - s} ds' \tag{3}$$

is the potential function determined by the discontinuities $\mathrm{disc}A_l(s)$ of the partial-wave amplitude in question on the dynamical cuts C_L, the parameters

$s_{lj}(j = 1, \ldots, \nu)$ specify the positions of poles corresponding to bound states, and α_{lj} are the residues at these poles.

The dispersion relation (2) can be linearized by representing the partial-wave amplitude $A_l(s)$ as the a ratio of two functions: $A_l(s) = N_l(s)D_l^{-1}(s)$, where $D_l(s)$ has only a unitary (right-hand) cut C_R in the complex s plane, while $N_l(s)$ involves dynamical (left-hand) cuts C_L. The functions $N_l(s)$ and $D_l(s)$ satisfy the set of integral equations [13, 23]

$$N_l(s) = \frac{1}{2\pi i}\int\limits_{C_L}\frac{D_l(s')\mathrm{disc}A_l(s')}{s'-s}ds', \qquad (4)$$

$$D_l(s) = 1 - \frac{1}{\pi}\int\limits_{s_R}^{\infty}\frac{N_l(s')}{s'-s}R_l(s')\rho(s')ds' \qquad (5)$$
$$+\sum_{i=1}^{\mu}\frac{\gamma_{li}}{s-s_{li}},$$

where s_{li} and γ_{li} are the parameters of the Castillejo–Dalitz–Dyson poles [24] and μ is the number of these poles in the state of orbital angular momentum l. The function $D_l(s)$ can be referred to as a generalized Jost function, since, in the nonrelativistic limit, it reduces, for analytic potentials, to the ordinary Jost function [25], which does not of course involve Castillejo–Dalitz–Dyson poles. If, in a given partial-wave state, there are ν bound states and μ Castillejo–Dalitz–Dyson poles, then the function $D_l(s)$ admits the Wiener–Hopf representation [13]

$$D_l(s) = D_l(s_0)\prod_{i=1}^{\mu}\frac{s_0-s_{li}}{s-s_{li}}\prod_{j=1}^{\nu}\frac{s-s_{lj}}{s_0-s_{lj}} \qquad (6)$$
$$\times\exp\left\{-\frac{s-s_0}{\pi}\int\limits_{s_R}^{\infty}\frac{\varphi_l(s')-\varphi_l(s_R)}{(s'-s)(s'-s_0)}ds'\right\},$$

where $\varphi_l(s)$ is the phase of the function $D_l(s)$. This phase is related to the phase shift δ_l of the respective partial-wave amplitude and the inelasticity parameter R_l by the equation

$$\tan\delta_l = \frac{R_l\tan\varphi_l}{R_l^2 + (R_l-1)^2\tan^2\varphi_l}, \qquad (7)$$

s_0 being an arbitrary point on the real axis such that is satisfies the condition $s_0 \le s_R$. Here, use is made of the definition of the phase shift δ_l from [26]; according to this definition, $\tan\delta_l = \mathrm{Re}K_l(s)/\rho(s)$, where the partial K matrix is determined by the relation $A_l^{-1}(s) = K_l^{-1}(s) - i\rho(s)$. From the representations in (5) and (6), it follows that the difference of the phases of the function $D_l(s)$ at the threshold and at infinity is $\pi(\nu-\mu)$, which is in accord with the Levinson theorem. In the present study, we assume that there are no Castillejo–Dalitz–Dyson poles in expressions (5) and (6). In this case, the substitution of (5) into (4) leads to the following equation for the function $N_l(s)$:

$$N_l(s) = B_l(s) \qquad (8)$$
$$+\frac{1}{\pi}\int\limits_{s_R}^{\infty}\frac{B_l(s')-B_l(s)}{s'-s}N_l(s')R_l(s')\rho(s')ds'.$$

If, in a given partial-wave channel, the masses of bound states, the energy dependence of the phase shift $\delta_l(s)$, and the inelasticity parameter $R_l(s)$ are known over the entire energy region, the inverse scattering problem can be solved [that is, the form of the potential function $B_l(s)$ can be determined] as follows. With the aid of relation (7), we determine the phase of the generalized Jost function $D_l(s)$, whereupon we find the explicit form of this function by using the Wiener–Hopf integral representation (6). At the next stage of the calculation, we determine the function $N_l(s)$, taking into account available data on the energy dependence of the inelasticity parameter $R_l(s)$ and the relation

$$N_l(s) = -\frac{\mathrm{Im}D_l(s)}{R_l(s)\rho(s)}, \qquad (9)$$

which follows from Eq. (5). After that, we find an exact form of the potential function $B_l(s)$ by solving the linear integral Eq. (8).

4. MODEL OF NONLOCAL SEPARABLE INTERACTION AT SHORT DISTANCES

Along with meson-exchange processes, QCD and effective chiral theory, which follows from it (see Introduction), predict other mechanisms of hadron interaction. By way of example, we consider a simple model that takes into account nonperturbative effects in QCD—the MIT quark-bag model [27] (or its modification that includes the coupling of bag states to an external pion field [28]). The MIT model describes the observed hadron spectrum rather well, but, at the same time, it predicts the existence of multiquark bag states, which can escape a direct observation in experiments as resonances if their coupling to hadron scattering channels is quite strong. In this model, there are two characteristic mechanisms of hadron interaction: (i) At long distances (larger than the confinement radius), hadrons preserve their individuality and interact via meson exchanges, this corresponding to the ordinary meson pattern of nuclear forces. (ii) At distances shorter than or on the order of the confinement radius, hadrons

lose their individuality with a high probability, forming the composite quark–gluon state, which subsequenty decays through hadron channels [29–31]. In partial-wave amplitudes, the dynamical cuts generated by meson-exchange interactions are an inevitable corollary of the conditions of unitarity in the t and u scattering channels. Also, a feature peculiar to exchange mechanisms in the t and u channels is that they generate interactions in all partial-wave states of the s channel simultaneously. This property is a necessary condition of the analyticity (everywhere, with the exception of isolated points) of the partial-wave scattering amplitude in the complex plane of the angular momentum. Therefore, the properties of meson-exchange interactions are consistent with the requirements of maximal analyticity of both the first and the second order.[2)] As follows from the aforesaid, the second hadron-interaction mechanism, which is associated with the formation of an intermediate composite quark–gluon state (six-quark bag in the case of nucleon–nucleon scattering), violates maximal analyticity of both the first and the second order. Since, in the MIT bag model, composite multiquark states are due to nonperturbative vacuum effects, we arrive at the conclusion that precisely these effects are closely related to a possible breakdown of the maximal analyticity of partial-wave amplitudes describing hadron–hadron scattering. An analysis of this problem within effective chiral theory also leads to the conclusion that contact interactions (for example, four-fermion interactions in the dibaryon sector of the theory) violate the maximal-analyticity principle.

Let us now consider nucleon–nucleon scattering. As is known, the contact four-fermion interaction belongs to the class of nonrenormalizable interactions. Bearing in mind, however, that the models being considered deal with an effective nonlocal interaction rather than with a fundamental interaction, we will assume that the matrix elements of the four-fermion interaction operators involve form factors that ensure the convergence of integrals over intermediate states in loop diagrams. Of course, the existence of a nonlocal four-fermion interaction between nucleons does not contradict the principle of the analyticity of the S matrix. In scattering amplitudes, this interaction generates, however, singularities that violate the condition of maximal analyticity because these singularities do not reduce to unitary cuts in the t and u channels.

In the preceding section, we have described a procedure for solving the inverse scattering problem. We will now generalize this procedure to the case where, along with meson-exchange interactions that are present in the t and u channels and which generate dynamical (left-hand) cuts of partial-wave amplitudes, there exists an additional nonlocal four-fermion interaction. We consider a manifestly Poincaré-invariant three-dimensional scattering formalism in which nucleons are on the mass shells but, in general, are off the energy shell. For the partial-wave amplitude, we write an equation belonging to the Lippmann–Schwinger type and taking into account inelastic effects. We have

$$A_l(\nu',\nu;s) = W_l(\nu',\nu) + \frac{1}{\pi}\int\limits_{4m^2}^{\infty}\frac{W_l(\nu',\xi)A_l(\xi,\nu;s)}{\xi - s}R_l(\xi)\rho(\xi)d\xi, \tag{10}$$

where $W_l(\nu',\nu)$ is the partial-wave matrix element of the operator of effective interaction between nucleons; $\rho(s) = \sqrt{1-4m^2/s}$; m is the nucleon mass; and ν and ν' are invariant quantities that characterize the degree to which the amplitudes are off the energy shell $\nu = \nu' = s$ in, respectively, the initial and the final state. An equation of the form (10) can be obtained within relativistic light-front Hamiltonian dynamics (see, for example, [32, 33]). Its solution has the form

$$A_l(\nu',\nu;s) = \frac{N_l(\nu',\nu;s)}{D_l(s)}. \tag{11}$$

Here, the functions $N_l(\nu',\nu;s)$ and $D_l(s)$ are determined by Fredholm series; that is,

$$N_l(\nu',\nu;s) = \sum_{n=0}^{\infty}\frac{(-1)^n}{n!}\prod_{i=1}^{n}\frac{1}{\pi}\int\limits_{4m^2}^{\infty}d\nu_i\frac{R_l(\nu_i)\rho(\nu_i)}{\nu_i - s} \times \langle\nu',\nu_1\ldots\nu_n|W^l_{n+1}|\nu,\nu_1\ldots\nu_n\rangle, \tag{12}$$

$$D_l(s) = \sum_{n=0}^{\infty}\frac{(-1)^n}{n!}\prod_{i=1}^{n}\frac{1}{\pi}\int\limits_{4m^2}^{\infty}d\nu_i\frac{R_l(\nu_i)\rho(\nu_i)}{\nu_i - s} \times \langle\nu_1\ldots\nu_n|W^l_n|\nu_1\ldots\nu_n\rangle, \tag{13}$$

where

$$\langle\nu'_1\ldots\nu'_n|W^l_n|\nu_1\ldots\nu_n\rangle = \det_{(i,j)}||W_l(\nu'_i,\nu_j)||. \tag{14}$$

After purely algebraic transformations, we arrive at an equation that relates the functions $N_l(\nu',\nu;s)$ and $D_l(s)$ on the energy shell (that is, at $\nu' = \nu = s$) as

$$D_l(s) = 1 - \frac{1}{\pi}\int\limits_{4m^2}^{\infty}\frac{N_l(s')}{s'-s}R_l(s')\rho(s')ds', \tag{15}$$

[2)]The requirement of maximal analyticity of the second order implies the possibility of an analytic continuation of the partial-wave S matrix in the angular momentum, only isolated singularities being admitted.

where $N_l(s) = N_l(s,s;s)$. Thus, we see that, under the condition that there are no Castillejo–Dalitz–Dyson poles, Eq. (5) follows from Eq. (10). On the basis of precisely this assumption, we construct here a solution to the inverse scattering problem with allowance for inelasticity effects, describing the dynamics of interactions with the aid of the N/D equations. From (11)–(15), it also follows that, on the energy shell $\nu' = \nu = s$, the partial-wave scattering amplitude $A_l(\nu', \nu; s)$ found by solving Eq. (10) satisfies the unitarity condition in the form (1), this condition taking into account the effect of inelastic channels.

Let us represent a partial-wave matrix element of the effective nucleon-interaction operator as the sum of two terms,

$$W_l(\nu', \nu) = W_l^e(\nu', \nu) + W_l^c(\nu', \nu), \qquad (16)$$

where $W_l^e(\nu', \nu)$ is the contribution of meson-exchange mechanisms taken explicitly into account that generate dynamical (left-hand) cuts of the partial-wave scattering amplitude in question that are the closest to the physical region and $W_l^c(\nu', \nu)$ is the contribution induced by a nonlocal four-fermion interaction; in the last term on the right-hand side of (16), we effectively include multimeson-exchange mechanisms discarded in the first term, which generate dynamical cuts that are far off the physical region. In the present study, we consider a model where the matrix element $W_l^c(\nu', \nu)$ has the form of a nonlocal separable interaction; that is,

$$W_l^c(\nu', \nu) = \lambda_l f_l(\nu') f_l(\nu). \qquad (17)$$

We note that, in the MIT bag model, the above mechanism of the formation of an intermediate composite quark–gluon state generates a separable interaction. The Fourier transform of the form factor $f_l(4(m^2 + q^2)) = g_l(q)$ with respect to the momentum variable q (q is the nucleon momentum in the c.m. frame),

$$g_l(r) = \frac{1}{2\pi^2} \int_0^\infty j_l(rq) g_l(q) q^2 dq, \qquad (18)$$

where $j_l(x)$ are spherical Bessel functions, controls the spatial structure of the nonlocal short-range component of the interaction in the partial-wave channel being considered. In the case under study, expression (12) on the energy shell $\nu' = \nu = s$ can be represented in the form

$$N_l(s) = F_l(s) + \tilde{N}_l(s), \qquad (19)$$

where $F_l(s) = \lambda_l f_l^2(s)$ is the term that is completely due to the nonlocal separable interaction component $W_l^c(\nu', \nu)$ and the function $\tilde{N}_l(s)$ involves dynamical (left-hand) cuts C_L generated by the interaction $W_l^e(\nu', \nu)$. With allowance for the fact that the function $D_l(s)$ involves only a right-hand (unitary) cut, as follows from expression (15), the discontinuities of the function $\tilde{N}_l(s)$ on the aforementioned dynamical cuts C_L are given by

$$\mathrm{disc}\tilde{N}_l(s) = D_l(s)\mathrm{disc}A_l^e(s) \qquad (20)$$

[where $\mathrm{disc}A_l^e(s)$ are the discontinuities of the respective partial-wave amplitude on the dynamical cuts induced by the interaction $W_l^e(\nu', \nu)$]; therefore, the following representation is valid for it:

$$\tilde{N}_l(s) = \frac{1}{2\pi i} \int_{C_L} \frac{D_l(s')\mathrm{disc}A_l^e(s')}{s' - s} ds'. \qquad (21)$$

By substituting expression (15) for the function $D_l(s)$ into (21), changing the order of integration, and taking into account relation (19), we obtain an equation for the function $N_l(s)$ in the form

$$N_l(s) = F_l(s) + L_l(s) \qquad (22)$$
$$+ \frac{1}{\pi} \int_{4m^2}^\infty \frac{L_l(s') - L_l(s)}{s' - s} N_l(s') R_l(s') \rho(s') ds',$$

where the function

$$L_l(s) = \frac{1}{2\pi i} \int_{C_L} \frac{\mathrm{disc}A_l^e(s')}{s' - s} ds' \qquad (23)$$

is determined by the contribution of meson-exchange mechanisms in the t and u channels that are taken explicitly into account.

The form factor $f_l(\nu)$ and the constant λ_l that appear in expression (17) and which determine the form of the nonlocal short-range component of the nucleon–nucleon interaction in the partial-wave channel being considered can be calculated according to the following scheme (this method for solving the inverse scattering problem will be referred to as method B). By using presently available information about meson–nucleon coupling constants (which is obtained, for example, from an analysis of data on pion–nucleon scattering [34]), we calculate, first of all, the function $L_l(s)$, which is determined by the dynamical cuts of the partial-wave scattering amplitude being considered that are the closest to the physical region. With the aid of the Wiener–Hopf integral representation for the generalized Jost function (6) and relation (9), we then find the function $N_l(s)$ in the physical region $s \geq 4m^2$. Finally, we use Eq. (22) to calculate the sought function $F_l(s)$, which completely determines the form of the nonlocal short-range component of the interaction.

5. APPLICATION OF THE METHOD TO AN ANALYSIS OF NUCLEON–NUCLEON INTERACTION IN THE $^1S_0$ AND $^3S_1$ STATES

The methods for solving the inverse scattering problem that were described in Sections 3 and 4 are used here to analyze the nucleon–nucleon interaction in the $^1S_0$ and $^3S_1$ states on the basis of presently available data on the energy dependence of partial-wave amplitudes for nucleon–nucleon scattering and on the basis of information about the meson–nucleon coupling constants. In the calculations, we used the data of the energy-dependent partial-wave analysis of nucleon–nucleon scattering that were obtained through the INTERNET from the SAID system [7]. These data covered the range of incident-nucleon kinetic energies in the laboratory frame, $T_{\rm lab}$, between zero and a value of about 10 GeV. At higher energies, we chose some analytic approximation of the phase shifts and inelasticity parameters that is consistent with the Levinson theorem (see Section 3). It is assumed in the present study that there are no Castillejo–Dalitz–Dyson poles in the partial-wave channels being considered. By way of example, we present the results of the analysis based on phase-shift and inelasticity-parameter data (open circles in Figs. 1 and 2, respectively). The quantities $\delta(s)$ and $R(s)$ {as has already been indicated in Section 3, we use the definition of phase shifts according to [26] and the definition of inelasticity parameters on the basis of the Froissart method [22] according to formula (1)} in the states of nucleon–nucleon scattering that are characterized by zero orbital angular momentum and isospins of $I = 0(^3S_1)$ and $I = 1(^1S_0)$ are displayed in Figs. 1 and 2, respectively, versus the dimensionless variable $y = \sqrt{1 - 4m^2/s}$, in terms of which the physical region of the s channel is mapped onto a unit segment. We note that, for nucleon–nucleon scattering in the $I = 0$ state, the coupling of the S- and D-wave amplitudes is taken into account in our approach through the inelasticity parameter R—that is, scattering in the D-wave state is an inelastic channel with respect to scattering in the S-wave state. For this reason, the parameter R is greater than unity below the pion-production threshold (see Fig. 2*b*).

A procedure for calculating the generalized Jost function is outlined in Appendix A. In Figs. 1 and 2, the positions of the open circles determine the ends of the segments into which the contour of integration with respect to the variable y is broken down [variables y_i are defined in formulas (A.6)–(A.8); in the calculations, we used a partition into 161 segments in the $I = 0(^3S_1)$ channel and a partition into 157 segments in the $I = 1(^1S_0)$ channel]. In Figs. 1 and 2, we also show (boxes) the available data of the energy-independent partial-wave analysis (that is, a partial-wave analysis at a fixed energy) [7] and (crosses) data recently obtained in [9] from an analysis of proton–proton scattering at the incident-proton energies of $T_{\rm lab} = 3.6$, 5, and 11 GeV in the laboratory frame. The results of the calculations for the function $N_l(s)$, which is related to the imaginary part of the function $D_l(s)$ by Eq. (9), and for the real part of the generalized Jost function are depicted in Figs. 3 and 4, respectively, versus the dimensionless variable y. The potential functions calculated in the channels of nucleon–nucleon scattering under consideration by numerically solving the integral Eq. (8) are displayed in Fig. 5 (solid curves). The dashed curves in Fig. 5 represent the predictions of the one-boson-exchange model allowing for π-, ρ-, σ-, ω-, η-, and a_0-meson exchanges. As usual, a σ meson is introduced to take into account the mechanism where nucleons exchange two π mesons in the states of zero angular momentum and isospin. The procedure used here to calculate the meson contributions to the potential functions in the $^1S_0$ and $^3S_1$ channels of nucleon–nucleon scattering is described in Appendix B. The parameters of the one-boson-exchange model that are used in our calculations are given in the table. We have adopted the same definitions of the meson–nucleon coupling constants g_α (where $\alpha = \pi, \rho, \sigma, \omega, \eta$, and a_0) and of $\kappa_\rho = f_\rho/g_\rho$ as in the review article of Machleidt and Slaus [5]. We note that the parameters Λ_α that characterize the cutoff in the meson–baryon vertices at high momentum transfers are chosen in such a way that the sum of all meson contributions $L_l(s)$ (23) to the potential function $B_l(s)$ (3) at the threshold point $s = 4m^2$ is equal to the value found for this function from the solution to the inverse scattering problem.

Using the analytic approximation described in Appendix C for the potential functions in the $^1S_0$ and $^3S_1$ channels of nucleon–nucleon scattering and a superposition of the Yukawa potentials, we have calculated the spatial distributions of the effective local partial-wave strengths of interactions [see formula (A.26)]. The results of these calculations are shown in Fig. 6. In order to test the quality of the approximation, we have solved the direct scattering problem with the aid of Eqs. (8) and (15) by using the potential functions approximated in the form (A.25). The results of these calculations are represented by the solid curves in Fig. 1. With the aid of the method described in Section 4, we have calculated the form factors $g(y)$ in the $^1S_0$ and $^3S_1$ channels of nucleon–nucleon scattering. The results are given in Fig. 7 versus the dimensionless variable y. In the aforementioned channels of nucleon–nucleon scattering, the functions $L(s)$

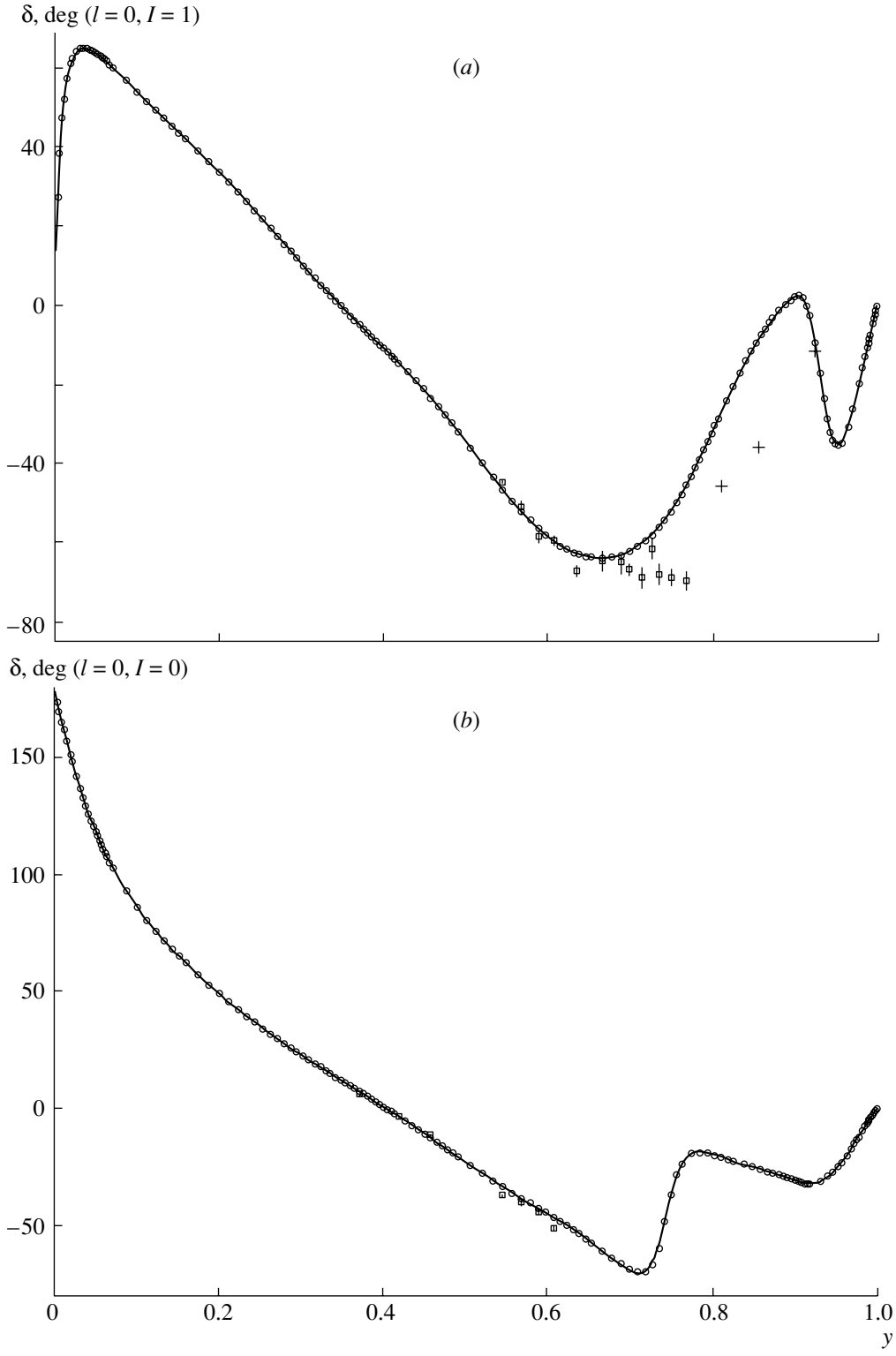

Fig. 1. Phase shifts for nucleon–nucleon scattering in the $(a)\ ^1S_0$ and $(b)\ ^3S_1$ states: (○) phase shifts used in solving the inverse scattering problem, (□) data of the energy-independent partial-wave analysis from [7], and (+) data borrowed from [9]. The solid curve represents the results obtained by solving the direct scattering problem with the aid of the analytic approximation of the potential functions $B_l(s)$ in the form (A.25).

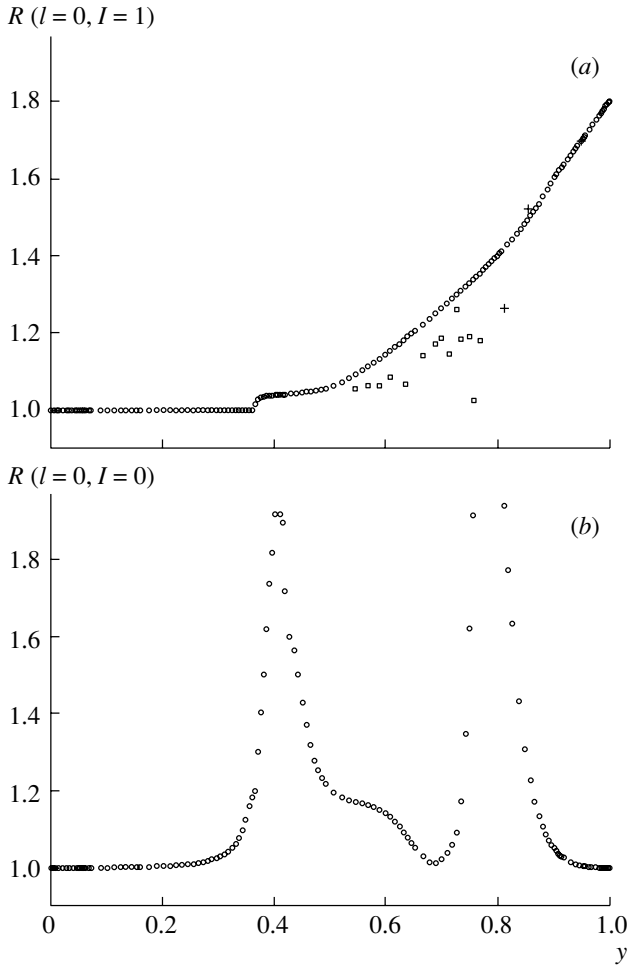

Fig. 2. Inelasticity parameters for nucleon–nucleon scattering in the $(a)\ ^1S_0$ and $(b)\ ^3S_1$ states: (○) values that are used in solving the inverse scattering problem, (□) data of the energy-independent partial-wave analysis from [7], and (+) data borrowed from [9].

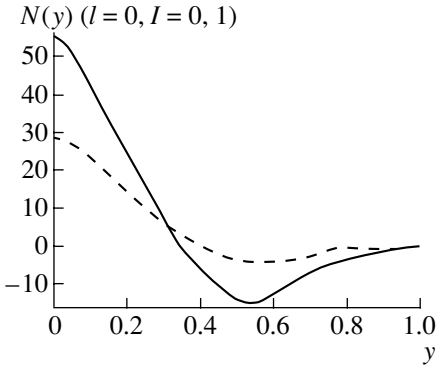

Fig. 3. Function $N(y)$ for nucleon–nucleon scattering in the (solid curve) $^1S_0$ and (dashed curve) $^3S_1$ states.

[see Eqs. (22), (23)] were calculated within the one-boson-exchange model [the contributions from the

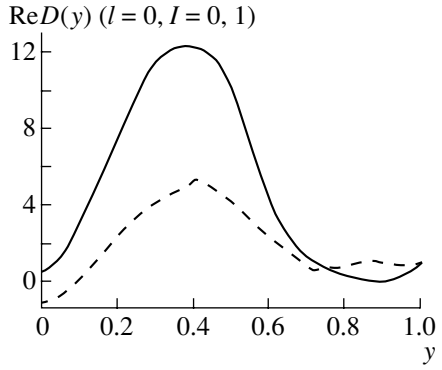

Fig. 4. Function $\mathrm{Re}D(y)$ for nucleon–nucleon scattering in the (solid curve) $^1S_0$ and (dashed curve) $^3S_1$ states.

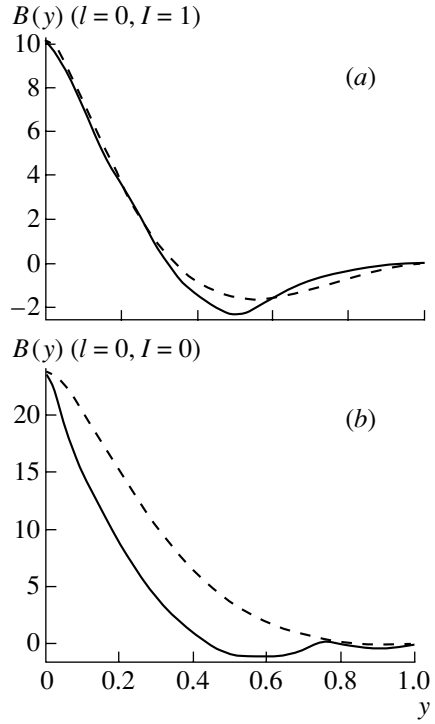

Fig. 5. Potential functions $B(y)$ for nucleon–nucleon scattering in the $(a)\ ^1S_0$ and $(b)\ ^3S_1$ states: (solid curves) result obtained by solving the inverse scattering problem and (dashed curves) predictions of the one-boson-exchange model with the parameter values listed in the table.

one-boson-exchange mechanisms to the functions $L(s)$ and $B(s)$ are consistent; they are represented by the dashed curves in Fig. 5]. The form factors characterizing the distribution of the strengths of nonlocal separable components of nucleon–nucleon interactions in the configuration representation have been obtained by means of the Fourier transformation (18) and are shown in Fig. 8.

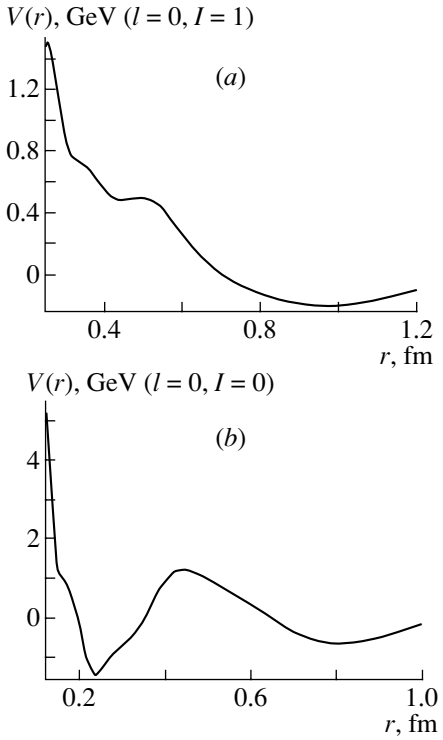

Fig. 6. Spatial distributions of the strength of the nucleon–nucleon interaction in the (*a*) $^1S_0$ and (*b*) $^3S_1$ states according to the approach based on the maximal-analyticity principle.

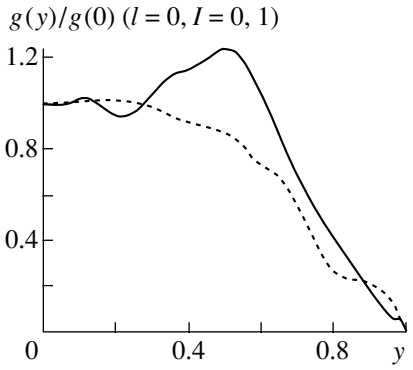

Fig. 7. Form factors $g(y)/g(0)$ for nucleon–nucleon scattering in the (solid curve) $^1S_0$ and (dotted curve) $^3S_1$ states.

6. CONCLUSION

In the present study, we have developed a manifestly Poincaré-invariant approach to solving the inverse scattering problem with allowance for inelasticity effects. The approach employs the equations of the N/D method as dynamical equations. Two versions of the formulation of the equations have been considered. In the first version (method A), we have relied on the maximal-analyticity principle, which underlies the dynamical theory of the S matrix [13]. By presetting some behavior of a partial-wave scattering amplitude in the physical region of the s channel such that it is consistent with available experimental and theoretical (for example, the Levinson theorem) data, we have extracted, within this method, information about the potential functions $B_l(s)$ that are determined by the contributions of dynamical (left-hand) cuts. It should be emphasized that the discontinuities of partial-wave scattering amplitudes on the dynamical cuts, at least on their segments closest to the physical region, are determined by model-independent quantities—specifically, by the vertex constants and the amplitudes of physical subprocesses on mass shells, but, in general, beyond the physical region.

In formulating the second version of the equations (method B), we have assumed that, in the complex s plane, a partial-wave scattering amplitude can develop dynamical singularities that are due to nonperturbative QCD effects and which have nothing to do with the conditions of unitarity in the t and u scattering channels (that is, these singularities violate the maximal-analyticity principle). In the effective chiral Lagrangian, contact-type terms (four-fermion terms for nucleon–nucleon interaction) correspond to this interaction mechanism. The dynamics of the interaction components violating maximal analyticity has been described within the model of a nonlocal separable potential. The discontinuities of partial-wave amplitudes on dynamical (left-hand) cuts—they determine the contribution of the interaction components preserving maximal analyticity—have been calculated within the one-boson-exchange model. The meson–nucleon coupling constants have been chosen with allowance for available data on pion–nucleon scattering [34].

Using the data on the energy dependence of the partial-wave amplitudes for nucleon–nucleon scattering in the $^1S_0$ and $^3S_1$ channels, we have

Parameters of the one-boson-exchange model

α	J^P, I	m_α, MeV	Λ_α, GeV		$g_\alpha^2/(4\pi)$
			$^1S_0$	$^3S_1$	
π	$0^-, 1$	138.03	1.80	1.80	14
ρ	$1^-, 1$	769	1.80	1.80	0.84 ($\kappa_\rho = 6$)
σ	$0^+, 0$	550	2.14	1.17	12
ω	$1^-, 0$	782.6	1.10	1.80	5
η	$0^-, 0$	548.8	1.80	1.80	1.73
a_0	$0^+, 1$	983	1.80	1.80	2.5

extracted information about the potential functions $B_l(s)$ (in method A) and about the form factors $g_l(q)$ (in method B) for separable interaction components at given values of the discontinuities of partial-wave amplitudes on dynamical cuts (in specific calculations by method B, we have used the discontinuities calculated within the one-boson-exchange model). As was emphasized above, the extracted information about the energy dependence of the potential functions $B_l(s)$ at low energies has a model-independent character and can be a testing ground for various theoretical predictions (for example, those that are based on effective chiral theory and other versions of meson theories of nuclear forces).

We have compared the data obtained by solving the inverse scattering problem with the predictions of the one-boson-exchange model. In this model, the values of the meson–nucleon coupling constants were chosen on the basis of data on pion–nucleon scattering [34]. For the singlet channel ($^1S_0$), one can see from Fig. 5*a* that, in the range of values of the dimensionless variable y between 0 and 0.3—the corresponding region of relative nucleon momenta is $q \leq 300$ MeV/c—the predictions of the one-boson-exchange model agree well with the data obtained by solving the inverse scattering problem. It can be seen from Fig. 5*b* that, in the triplet channel ($^3S_1$), there is some disagreement between the predictions of the one-boson-exchange model at the parameter values given in the table and the results obtained by solving the inverse scattering problem by method A. A variation of the meson–nucleon coupling constants within reasonable ranges does not remove these discrepancies. If nonmeson mechanisms of nucleon–nucleon interaction play a significant role at low energies, they can be responsible for the discrepancies in question. Some other sources of this disagreement may also exist, but their consistent analysis is beyond the scope of the present study.

The details of the interaction-strength distributions at short distances are sensitive to the behavior of phase shifts and inelasticity parameters at high energies. For the chosen versions of the behavior of partial-wave amplitudes at high energies, the effective nucleon–nucleon interaction at short distances in the scattering channels being considered is predominantly repulsive, the strongest interaction being localized within the region of radius ≈ 0.2 fm.

It should be noted in conclusion that the technique for solving the inverse scattering problem for analyzing data on nucleon–nucleon scattering on the basis of the Schrödinger equation was considered in [35, 36]. The Gelfand–Levitan–Marchenko formalism [10, 25] was used in [35, 36] to construct, in each partial-wave state, a local component of the potential

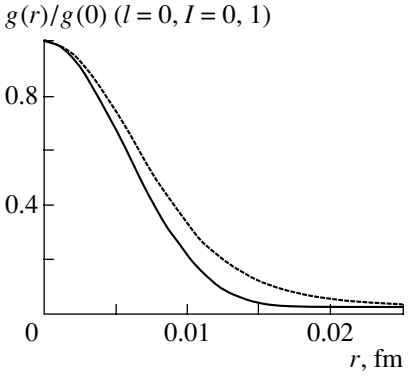

Fig. 8. Function $g(r)$, which determines the spatial distributions of nonlocal separable components of nucleon–nucleon interactions in the (solid curve) $^1S_0$ and (dotted curve) $^3S_1$ states.

with the aid of data on real phase shifts (that is, without taking into account inelasticity effects). Nonlocal energy-dependent potentials whose parameters were chosen in such a way as to describe the energy dependence of the amplitudes for nucleon–nucleon scattering in the energy region $T_{\text{lab}} \leq 3$ GeV were added to the above local components. An analysis of data on nucleon–nucleon scattering in the region $T_{\text{lab}} \leq 6$ GeV within the potential model involving forbidden states was performed in [37].

ACKNOWLEDGMENTS

This work was supported in part by the Ministry of Higher Education of the Russian Federation within the program Universities of Russia (project no. UR.02.03.003) and by the Russian Foundation for Basic Research (project no. 04-02-16967).

APPENDIX A

Under the assumption that there are no Castillejo–Dalitz–Dyson poles in expression (5), the integral representation of the generalized Jost function in the $^3S_1(I = 0)$ and $^1S_0(I = 1)$ channels of nucleon–nucleon scattering can be recast into the form

$$D^{(I)}(s) = D^{(I)}(s_0)Q^{(I)}(s) \qquad \text{(A.1)}$$
$$\times \exp\left\{-\frac{s-s_0}{\pi}\int\limits_{4m^2}^{\infty}\frac{\tilde{\varphi}^{(I)}(s')}{(s'-s)(s'-s_0)}ds'\right\},$$

where $Q^{(1)}(s) = 1$; $Q^{(0)}(s) = (s - M_{\text{D}}^2)/(s_0 - M_{\text{D}}^2)$; M_{D} is the deuteron mass; $\tilde{\varphi}^{(I)}(s) = \varphi^{(I)}(s) - \varphi^{(I)}(4m^2)$; the phase of the generalized Jost function $\varphi^{(I)}(s)$, the phase shift $\delta^{(I)}(s)$ of the partial-wave scattering amplitude [26], and the inelasticity

parameter $R^{(I)}(s)$ are related by Eq. (7); and s_0 is an arbitrary point on the real axis below the threshold for the elastic scattering channel ($s_0 < 4m^2$). In all formulas appearing in this appendix, the superscript in parentheses denotes the isospin I of the system. We use the definitions of the phase shifts $\varphi^{(I)}(s)$ according to which $\varphi^{(I)}(4m^2) = \pi\delta_{I0}$, where $\delta_{II'}$ is a Kronecker delta symbol. In accordance with expression (5), we choose the normalization constant $D^{(I)}(s_0)$ in such a way that $\lim\limits_{s\to\infty} D^{(I)}(s) = 1$. We note that, by virtue of the Levinson theorem, the phase shifts $\tilde{\varphi}^{(0)}(s)$ and $\tilde{\varphi}^{(1)}(s)$ have different asymptotic expressions at infinity—that is, $\tilde{\varphi}^{(0)}(s) \to -\pi$ and $\tilde{\varphi}^{(1)}(s) \to 0$ in the limit $s \to \infty$.

By making the change of variable $s = 4m^2/(1 - y^2)$, we map the physical region of the elastic scattering channel in the s plane ($4m^2 \le s < \infty$) onto a unit segment ($0 \le y \le 1$). The Wiener–Hopf integral representation of the generalized Jost function then takes the form

$$D^{(I)}(y) = D^{(I)}(y_0)Q^{(I)}(y) \times \exp\left\{-\frac{y^2 - y_0^2}{\pi}\int\limits_0^1 \frac{\tilde{\varphi}^{(I)}(y')y'dy'}{(y'^2 - y^2)(y'^2 - y_0^2)}\right\}, \quad \text{(A.2)}$$

where

$$Q^{(1)}(y) = 1, \quad Q^{(0)}(y) = \frac{(y^2 + \kappa^2)(1 - y_0^2)}{(y_0^2 + \kappa^2)(1 - y^2)},$$
$$\kappa^2 = \frac{4m^2}{M_{\rm D}^2} - 1, \quad y_0^2 = 1 - \frac{4m^2}{s_0}.$$

Using Eq. (15), written in terms of the variable y,

$$D^{(I)}(y) = 1 - \frac{2(1 - y^2)}{\pi}\int\limits_0^1 \frac{N^{(I)}(y')R^{(I)}(y')y'^2dy'}{(1 - y'^2)(y'^2 - y^2)}, \quad \text{(A.3)}$$

and taking into account the analyticity of the function $N^{(I)}(y)$ on the right-hand cut, we deduce that, in the physical region, the real and the imaginary part of the function $D^{(I)}(y)$ possess the following properties of symmetry in the variable y: $\mathrm{Re}D^{(I)}(y) = \mathrm{Re}D^{(I)}(-y)$ and $\mathrm{Im}D^{(I)}(y) = -\mathrm{Im}D^{(I)}(-y)$. It follows that the phase shift $\tilde{\varphi}^{(I)}(y)$ in expression (A.2) is an odd function of y. Further, we break down the contour of integration with respect to the variable y (unit segment $0 \le y \le 1$) into N segments and represent the phase shift $\tilde{\varphi}^{(I)}(y)$ within the ith segment, whose beginning and end are determined by the points y_i and y_{i+1} ($y_1 = 0$, $y_{N+1} = 1$, $i = 1, \ldots, N$), respectively, in the form

$$\tilde{\varphi}_i^{(I)}(y) = \sum_{n=0}^{\infty} a_{in}^{(I)} y^{2n+1}. \quad \text{(A.4)}$$

Retaining the first three terms in expansion (A.4), performing integration in (A.2) explicitly, and making the subtraction point s_0 tend to $-\infty$, we ultimately reduce the generalized Jost function to the form

$$D^{(I)}(y) = D_A^{(I)}(y)D_B^{(I)}(y)D_C^{(I)}(y)\exp(-i\varphi^{(I)}(y)), \quad \text{(A.5)}$$

where

$$D_A^{(I)}(y) = \left(\frac{1 - y}{1 + y}\right)^{-\frac{\varphi_N^{(I)}(y)}{\pi}} - \prod_{i=2}^{N}\left\{\left|\frac{y_i - y}{y_i + y}\right|^{\alpha_i^{(I)}(y)}\left|\frac{y_i - 1}{y_i + 1}\right|^{-\alpha_i^{(I)}(1)}\right\}, \quad \text{(A.6)}$$

$$D_B^{(I)}(y) = \exp\left\{\frac{2(1 - y^2)}{\pi}\sum_{i=1}^{N}\Delta_i\left[a_{i1}^{(I)} + a_{i2}^{(I)}\left(1 + y^2 + \frac{1}{3}(y_{i+1}^2 + y_i^2 + y_iy_{i+1})\right)\right]\right\}, \quad \text{(A.7)}$$

$$D_C^{(1)} = 1, \quad D_C^{(0)} = \frac{4(\kappa^2 + y^2)}{(1 + \kappa^2)(1 + y)^2}, \quad \text{(A.8)}$$

$$\alpha_i^{(I)}(y) = \frac{1}{\pi}(\tilde{\varphi}_i^{(I)}(y) - \tilde{\varphi}_{i-1}^{(I)}(y)), \Delta_i = y_{i+1} - y_i,$$
$$\varphi_N^{(I)}(y) = \tilde{\varphi}_N^{(I)}(y) + \pi\delta_{I0}.$$

For the condition of the Levinson theorem to be satisfied, we require fulfillment of the sum rules $\sum_{n=0}^{2} a_{Nn}^{(I)} = -\pi\delta_{I0}$. From formulas (A.5)–(A.8), it follows that $\lim\limits_{y\to 1} D^{(I)}(y) = 1$.

APPENDIX B

In calculating meson-exchange interactions (π, ρ, σ, ω, η, a_0), we take into account the form factors in meson–nucleon vertices and the cutoff of the contributions from dynamical-cut segments lying far off the physical region. It is convenient to write the expressions determining the contributions of meson-exchange mechanisms to the potential function (23) for nucleon–nucleon scattering in the ${}^1S_0(I = 1)$ and ${}^3S_1(I = 0)$ states in terms of the dimensionless variable $x = s/4m^2 - 1$. The result can be represented in the form

$$L^{(I)}(x) = \sum_{\alpha} L_{\alpha}^{(I)}(x), \quad \text{(A.9)}$$

where $\alpha = \pi, \rho, \sigma, \omega, \eta, a_0$. The functions $L_\alpha^{(I)}(x)$ can be rewritten in the form

$$L_\alpha^{(I)}(x) = \frac{g_\alpha^2}{4\pi}\sum_{n=0}^{2}(J_{n\alpha}(x)A_{n\alpha}^{(I)}(x) + \tilde{J}_{n\alpha}(x)B_{n\alpha}^{(I)}(x)), \tag{A.10}$$

where

$$J_{n\alpha}(x) = \frac{1}{2}\int\limits_{x_{0\alpha}}^{x_\alpha}\frac{f_\alpha^2(x,x')P_n(1+\gamma_\alpha/(2x'))}{x'(x'-x)}dx', \tag{A.11}$$

$$\tilde{J}_{n\alpha}(x) = \frac{\gamma_\alpha}{2}\int\limits_{x_{0\alpha}}^{x_\alpha} f_\alpha^2(x,x')P_n\left(1+\frac{\gamma_\alpha}{2x'}\right)\frac{dx'}{x'^2}, \tag{A.12}$$

$\gamma_\alpha = m_\alpha^2/m^2$, m_α is the mass of the meson α, m is the nucleon mass, $x_\alpha = -\gamma_\alpha/4$, $x_{0\alpha}$ is the parameter defining the cutoff of the dynamical-cut segments lying far off the physical region, $f_\alpha(x,x')$ are the form factors in meson–nucleon vertices (they take into account a nonlocal character of the effective meson–nucleon interactions), and $P_n(z)$ are Legendre polynomials. Given immediately below are expressions for the nonvanishing functions $A_{n\alpha}^{(I)}(x)$ and $B_{n\alpha}^{(I)}(x)$ in (A.10).

(i) For the case of $\alpha = \pi, \eta$, these are

$$A_{0\alpha}^{(1)}(x) = -\frac{x}{4}, \quad A_{1\alpha}^{(1)}(x) = \frac{x}{4}, \tag{A.13}$$
$$A_{0\alpha}^{(0)}(x) = \frac{\delta_\alpha}{12}x, \quad A_{1\alpha}^{(0)}(x) = -\frac{\delta_\alpha}{12}x,$$

where $\delta_\pi = -3$ and $\delta_\eta = 1$.

(ii) For the case of $\alpha = \sigma, a_0$, we have

$$A_{0\alpha}^{(1)}(x) = \frac{2+x}{4}, \quad A_{1\alpha}^{(1)}(x) = -\frac{x}{4}, \tag{A.14}$$
$$A_{0\alpha}^{(0)}(x) = \frac{\delta_\alpha}{36}(5(2+x) + 8\sqrt{1+x}),$$
$$A_{1\alpha}^{(0)}(x) = -\frac{\delta_\alpha}{4}x,$$
$$A_{2\alpha}^{(0)}(x) = \frac{\delta_\alpha}{9}(2+x+2\sqrt{1+x}),$$

where $\delta_\sigma = 1$ and $\delta_{a_0} = -3$.

(iii) For the case of $\alpha = \rho, \omega$, the results are

$$A_{0\alpha}^{(1)}(x) = -\frac{1}{16}[8 + 8(2+\kappa_\alpha)x \tag{A.15}$$
$$+ \kappa_\alpha^2(8x^2 + (12+\gamma_\alpha)x + 2\gamma_\alpha)],$$

$$A_{1\alpha}^{(1)}(x) = \frac{\kappa_\alpha}{16}x(8 + \kappa_\alpha(12 + \gamma_\alpha + 8x)),$$

$$B_{0\alpha}^{(1)}(x) = \frac{\kappa_\alpha^2}{16}(2+x), \quad B_{1\alpha}^{(1)}(x) = -\frac{\kappa_\alpha^2}{16}x,$$

$$A_{0\alpha}^{(0)}(x) = -\frac{\delta_\alpha}{144}[40 + 10\kappa_\alpha^2(\gamma_\alpha + 4x^2)$$
$$+ x(32 - 56\kappa_\alpha + \kappa_\alpha^2(12 + 5\gamma_\alpha))$$
$$+ 8(4 + \gamma_\alpha\kappa_\alpha^2 - 8\kappa_\alpha x)\sqrt{1+x}],$$

$$A_{1\alpha}^{(0)}(x) = -\frac{\delta_\alpha}{48}x(32 + 40\kappa_\alpha - \kappa_\alpha^2(4 + 3\gamma_\alpha + 24x)),$$

$$A_{2\alpha}^{(0)}(x) = -\frac{\delta_\alpha}{36}[4(2 + x - 4\kappa_\alpha x)$$
$$+ \kappa_\alpha^2(\gamma_\alpha(2+x) + 8x^2)$$
$$- 2(4 + \gamma_\alpha\kappa_\alpha^2 - 8\kappa_\alpha x)\sqrt{1+x}],$$

$$B_{0\alpha}^{(0)}(x) = \frac{\delta_\alpha}{144}\kappa_\alpha^2(5(2+x) + 8\sqrt{1+x}),$$

$$B_{1\alpha}^{(0)}(x) = -\frac{\delta_\alpha}{16}\kappa_\alpha^2 x,$$

$$B_{2\alpha}^{(0)}(x) = \frac{\delta_\alpha}{36}\kappa_\alpha^2(2 + x - 2\sqrt{1+x}),$$

where $\delta_\rho = -3$, $\delta_\omega = 1$, $\kappa_\omega = 0$, and $\kappa_\rho = f_\rho/g_\rho$. We have adopted the same definitions for the meson–nucleon coupling constants g_α (where $\alpha = \pi, \rho, \sigma, \omega, \eta$, and a_0) and f_ρ as in [5].

In the calculations, we took the form factors in the meson–nucleon vertices in the form

$$f_\alpha(x', x) = \left(\frac{(m_\alpha^2 - \Lambda_\alpha^2)x'}{\Lambda_\alpha^2 x' - m_\alpha^2 x}\right)^{n_\alpha}, \tag{A.16}$$

where Λ_α are the cutoff masses and the quantity n_α was chosen to be 2 for scalar (or pseudoscalar) mesons and 3 for vector mesons. For dynamical-cut segments $x_{0\alpha}$ that are far off the physical region, the cutoff parameters were chosen to be -1 for all mesons; in the s plane, this corresponds to cutting off, at the point $s = 0$, the integrals in (A.11) and (A.12) at the lower limit.

APPENDIX C

Let us consider a method for calculating the spatial distribution of the strength of the effective local interaction in a preset partial-wave state of nucleons. The potential function $B_l(s)$, which controls the nucleon–nucleon interaction in the state of orbital angular momentum l and isospin $I = 0, 1$ (in this case, the nucleon spin of $S = 0, 1$ is fixed by the condition that the sum $l + I + S$ is odd; for the sake of simplicity, the spin and isospin indices are suppressed), can be considered as the boundary value of

the function $V_l(k',k)$ at $k'=k$. The function $V_l(k',k)$ in turn admits the representation

$$V_l(k',k)=2\pi\int\limits_{-1}^{1}V_l(k',k;z)P_l(z)dz, \qquad (A.17)$$

where $V_l(k',k;z)=V_l(t)$ depends only on the momentum transfer squared $t=k^2+k'^2-2kk'z$ (k and k' are the absolute values of the nucleon momenta, respectively, prior to and after scattering in the c.m. frame, and z is the cosine of the scattering angle). This function can be written in the integral form

$$V_l(t)=\frac{1}{\pi}\int\limits_{m_\pi^2}^{\infty}\frac{\sigma_l(\mu^2)d\mu^2}{\mu^2+t}, \qquad (A.18)$$

where the function $\sigma_l(\mu^2)$ determines the spectral density of the strength of interaction. By using formulas (A.17) and (A.18), we obtain the potential function in the form

$$B_l(s)=4\int\limits_{m_\pi^2}^{\infty}d\mu^2\sigma_l(\mu^2) \qquad (A.19)$$

$$\times\int\limits_{-\infty}^{4m^2-\mu^2}P_l\left(1+\frac{2\mu^2}{s'-4m^2}\right)\frac{ds'}{(s'-4m^2)(s'-s)},$$

whence it follows that the discontinuity of the partial-wave amplitude on a dynamical cut (for $s<4m^2-m_\pi^2$) is given by

$$\mathrm{disc}A_l(s)=\frac{8\pi i}{s-4m^2}\int\limits_{m_\pi^2}^{4m^2-s}P_l\left(1+\frac{2\mu^2}{s-4m^2}\right) \qquad (A.20)$$

$$\times\,\sigma_l(\mu^2)d\mu^2.$$

The function describing the spatial distribution of the strength of the nucleon–nucleon interaction in a given partial-wave channel can be obtained by going over to the configuration representation for the matrix element in (A.17) according to the relation

$$V_l(r',r)=\frac{1}{4\pi^4}\int\limits_0^{\infty}dk'k'^2j_l(k'r') \qquad (A.21)$$

$$\times\int\limits_0^{\infty}dkk^2j_l(kr)V_l(k',k).$$

The spherical Bessel function appearing here is related to the ordinary Bessel function $J_{l+1/2}(x)$ of half-integer order as $j_l(x)=\sqrt{\pi/2x}J_{l+1/2}(x)$. It can be shown that the spectral representation (A.18) leads to an effective local interaction for which the matrix element (A.21) has the form

$$V_l(r',r)=\frac{a}{r^2}\delta(r'-r)V_l(r), \qquad (A.22)$$

where the normalization factor a is chosen in such a way that, in the nonrelativistic limit and in the lowest order of perturbation theory, the function $V_l(r)$ coincides with the local potential in the Schrödinger equation. One can readily show that this requirement leads to the following result for the normalization factor in question: $a=-16\pi^2/m^2$. With the aid of formulas (A.17), (A.18), and (A.21), we derive an expression for the function $V_l(r)$ in the form of a superposition of Yukawa potentials; that is,

$$V_l(r)=-\frac{4}{m^2r}\int\limits_{m_\pi^2}^{\infty}\sigma_l(\mu^2)\exp(-\mu r)d\mu^2. \qquad (A.23)$$

For $l=0$ (below, we suppress the index corresponding to the orbital angular momentum) and the spectral function $\sigma(\mu^2)$ chosen in the form

$$\sigma(\mu^2)=m^2\sum_{i=1}^{n}c_i\delta(\mu^2-\mu_i^2), \qquad (A.24)$$

where c_i are dimensionless parameters and μ_i ($i=1,\ldots,n$) is a discrete set of masses, we obtain an approximate expression for the potential function in the form

$$B^{(a)}(s)=\sum_{i=1}^{n}c_if_i(s), \qquad (A.25)$$

where

$$f_i(s)=\frac{4m^2}{s-4m^2}\ln\left(1+\frac{s-4m^2}{\mu_i^2}\right).$$

The coefficients c_i can be found from the condition requiring that the root-mean-square deviation of expression (A.25) from the function $B(s)$ at the fixed points s_j ($j=1,\ldots,N$) be minimal. As a result, we arrive a set of linear algebraic equations for the coefficients c_i. The solution to this set of equations is determined by specifying the set of masses μ_i ($i=1,\ldots,n$), the set of points s_j ($j=1,\ldots,N$), and the values of the function $B(s)$ at these points. The approximate expression for the function in (A.23) is then determined by the coefficients c_i,

$$V^{(a)}(r)=-\frac{4}{r}\sum_{i=1}^{n}c_i\exp(-\mu_ir). \qquad (A.26)$$

The specific results of the calculations in Fig. 1 were obtained with the approximate potential functions

that correspond to taking into account 42 terms in the expansions in (A.25) and (A.26) for values of the masses μ_i in the interval between the pion mass m_π and $1200m_\pi$.

REFERENCES

1. S. Weinberg, Nucl. Phys. B **363**, 3 (1991).
2. N. Kaiser, Phys. Rev. C **64**, 057001 (2001).
3. D. I. D'yakonov and M. I. Éĭdes, Pis'ma Zh. Éksp. Teor. Fiz. **38**, 358 (1983) [JETP Lett. **38**, 433 (1983)].
4. R. T. Cahill, Nucl. Phys. A **543**, 63 (1992).
5. R. Machleidt and I. Slaus, J. Phys. G **27**, 69 (2001).
6. M. Lacombe, B. Loiseau, J. M. Richard, *et al.*, Phys. Rev. D **12**, 1495 (1975).
7. R. A. Arndt, I. I. Strakovsky, and R. N. Workman, Phys. Rev. C **62**, 034005 (2000); http://gwdac.phys.gwu.edu.
8. M. Matsuda, Nucl. Phys. A **631**, 436 (1998).
9. J. Nagata, H. Yoshino, and M. Matsuda, in *Proceedings of the 9th International Symposium on Meson–Nucleon Physics and Structure of the Nucleon, Washington, USA, 2001*, Ed. by H. Haberzettl and W. J. Briscoe; πN Newslett., No. 16, 376 (2002).
10. K. Chadan and P. Sabatier, *Inverse Problems in Quantum Scattering Theory* (Springer, Heidelberg, 1997; Mir, Moscow, 1980).
11. M. Gell-Mann, M. L. Goldberger, and W. Thirring, Phys. Rev. **95**, 1612 (1954).
12. N. N. Bogoliubov and D. V. Shirkov, *Introduction to the Theory of Quantum Fields*, 4th ed. (Nauka, Moscow, 1984; Wiley, New York, 1980).
13. P. Collins and E. Squires, *Regge Poles in Particle Physics* (McGraw-Hill, New York, 1968; Mir, Moscow, 1971).
14. J. M. Greben and Yu. A. Simonov, Phys. Rev. C **18**, 642 (1978).
15. V. E. Troitskiĭ, Yad. Fiz. **29**, 236 (1979) [Sov. J. Nucl. Phys. **29**, 118 (1979)].
16. A. N. Safronov, Yad. Fiz. **50**, 951 (1989) [Sov. J. Nucl. Phys. **50**, 593 (1989)].
17. V. V. Anisovich, D. I. Melikhov, B. Ch. Metsch, and H. R. Petry, Yad. Fiz. **57**, 331 (1994) [Phys. At. Nucl. **57**, 312 (1994)].
18. L. D. Landau, Zh. Éksp. Teor. Fiz. **37**, 62 (1959) [Sov. Phys. JETP **10**, 45 (1959)].
19. R. E. Cutkosky, J. Math. Phys. **1**, 429 (1960).
20. A. P. Rudik and Yu. A. Simonov, Zh. Éksp. Teor. Fiz. **45**, 1016 (1963) [Sov. Phys. JETP **18**, 703 (1963)].
21. L. D. Blokhintsev and A. N. Safronov, Nucl. Phys. A **180**, 363 (1972).
22. M. Froissart, Nuovo Cimento **22**, 191 (1961).
23. G. F. Chew and S. Mandelstam, Phys. Rev. **119**, 467 (1960).
24. L. Castillejo, R. H. Dalitz, and F. J. Dyson, Phys. Rev. **101**, 453 (1956).
25. V. De Alfaro and T. Regge, *Potential Scattering* (Amsterdam, 1965; Mir, Moscow, 1966).
26. R. A. Arndt and L. D. Roper, Phys. Rev. D **25**, 2011 (1982).
27. A. Chodos, R. L. Jaffe, K. Johnson, *et al.*, Phys. Rev. D **9**, 3471 (1974).
28. A. W. Thomas, S. Theberge, and G. A. Miller, Phys. Rev. D **24**, 216 (1981).
29. R. L. Jaffe and F. E. Low, Phys. Rev. D **19**, 2105 (1979).
30. Yu. A. Simonov, Phys. Lett. B **107B**, 1 (1981).
31. A. N. Safronov, Fiz. Élem. Chastits At. Yadra **21**, 1187 (1990) [Sov. J. Part. Nucl. **21**, 505 (1990)].
32. A. N. Safronov, Izv. Akad. Nauk, Ser. Fiz. **66**, 65 (2002).
33. A. N. Safronov and A. A. Safronov, in *Proceedings of the International Conference on the Properties of Excited Nuclear States and Mechanisms of Nuclear Reactions. LI Meeting on Nuclear Spectroscopy and Nuclear Structure, Sarov, Russia, 2001*; Vopr. At. Nauki Tekh., Ser. Fiz. Yad. Reakt., No. 1–2, 32 (2002).
34. O. Krehl, C. Hanhart, S. Krewald, and J. Speth, Phys. Rev. C **62**, 025207 (2000).
35. H. V. von Geramb, K. A. Amos, H. Labes, and M. Sander, Phys. Rev. C **58**, 1948 (1998).
36. A. Funk, H. V. von Geramb, and K. A. Amos, Phys. Rev. C **64**, 054003 (2001).
37. V. G. Neudatchin, N. P. Yudin, Yu. L. Dorodnykh, and I. T. Obukhovsky, Phys. Rev. C **43**, 2499 (1991).

Translated by A. Isaakyan

Physics of Atomic Nuclei, Vol. 67, No. 12, 2004, pp. 2260–2271. Translated from Yadernaya Fizika, Vol. 67, No. 12, 2004, pp. 2285–2296.
Original Russian Text Copyright © 2004 by Zhukovsky, Tarasov.

ELEMENTARY PARTICLES AND FIELDS
Theory

Fermions in Random Gauge Fields and Chiral-Symmetry Breaking

V. Ch. Zhukovsky and O. V. Tarasov*

Moscow State University, Vorob'evy gory, Moscow, 119899 Russia

Received May 14, 2003; in final form, December 25, 2003

Abstract—Random superpositions of gauge fields such that a fermion can propagate in them along the same one-dimensional trajectory in four-dimensional space over arbitrary distances without reduction of the amplitude are considered. Conditions are found under which such structures possess a finite density of fermion zero modes. The possibility of chiral-symmetry breaking in these configurations of gauge fields is explored. © *2004 MAIK "Nauka/Interperiodica".*

INTRODUCTION

Along with confinement (for an overview, see, for example, [1]), chiral-symmetry breaking is one of the most spectacular nonperturbative phenomena in QCD. It is assumed that chiral-symmetry breaking occurs owing to some nontrivial gauge-field configurations highly dissimilar to that of the perturbative vacuum. The nature of configurations that are responsible for the mechanism of chiral-symmetry breaking has yet to be clarified conclusively. For such configurations, superpositions of many instantons and anti-instantons (gas of pseudoparticles) were chosen in [2], since they are saddle points in the path integral [3] that controls quantities responsible for chiral-symmetry breaking. It is well known, however, that groups of configurations far from classical solutions can also contribute significantly to the formation of the path integral in the infrared, nonperturbative, region. For example, lattice experiments revealed that combinations of central vortices, whose action diverges in continual theory [1, 4], may be of importance for describing confinement.

It is well known that chiral-symmetry breaking can be induced by fermion zero modes. Various topologically nontrivial gauge-field configurations involving fermion zero modes and having some bearing on nonperturbative QCD phenomena such as confinement and chiral-symmetry breaking have been discussed in recent years (see, for example, [4–8]). In this connection, it is advisable to recall once again studies devoted to exploring central vortices and their role in the confinement mechanism—for example, the study of Engelhardt and Reinhardt [4], who introduced a continuous analog of the maximal central gauge, and the study of Reinhardt and Tok [5], who analyzed merons, instantons, and instanton–anti-instanton configurations and who showed that both monopoles and central vortices can be considered to be included in them; in addition, we note that Reinhardt *et al.* [6] investigated quark zero modes against the background of intersecting central vortices and their possible role in chiral-symmetry breaking. At the same time, there arises the question of whether a class of gauge fields characterized by a finite density of zero modes that is sufficiently high to saturate some functional expectation values, such as a quark condensate, exists.

The choice of configurations far off classical solutions that was proposed in [9] and which was called there "fermion guides" also deserves attention. Fermion guides are of interest because of the fact that, in them, a fermion moves in four-dimensional Euclidean space along a one-dimensional curve over arbitrary distances without reductions of the amplitude.

In contrast to what was done in [9], where the analysis was restricted to considering hypothetical constructions of the fermion-guide type, a specific example of a fermion guide and the corresponding solution to the Dirac equation for the zero mode are demonstrated here. Further, yet another distinction from the analysis in [9], where the argument was based on the assumption that there exist a large number of zero modes for one fermion guide, is that the case in which there exists at least one zero-mode-type solution to the Dirac equation such that it has a large, albeit finite, norm proportional to the fermion-guide length is considered in the present study. We will show that this fact alone can ensure a finite density of zero modes owing to a large number of fermion guides themselves.

The ensuing exposition is organized as follows.

In Section 1, we expound on the motivation of our interest in studying fermion guides and the properties

*E-mail: tarasov79@inbox.ru

1063-7788/04/6712-2260$26.00 © 2004 MAIK "Nauka/Interperiodica"

of the Dirac operator spectrum in an external gauge field that is a superposition of fermion guides; also, we give there the formulation of the problem.

In Section 2, we construct, on the basis of the results presented in [8, 9], an explicit gauge-field configuration in the form of a straight-line fermion guide and the fermion zero mode corresponding to it. By using this example, we illustrate the mechanism of chiral-symmetry breaking in an external gauge field that has the form of a fermion guide.

In Section 3, we consider a field configuration that is formed by a dilute distribution of fermion guides where zero modes corresponding to each individual fermion guide are split. Split solutions and corresponding eigenvalues of the Dirac operator in the vicinity of the origin are obtained as eigenvectors and eigenvalues of the overlap matrix. The structure of this matrix is considered.

In Section 4, zero modes are averaged by a method similar to that used in the case of instantons in [2]. It is assumed that the distribution of fermion guides saturates the path integral, this making it possible to replace the integral with respect to all gauge fields by averaging over all distributions of fermion guides.

In Section 5, we calculate the spectral density of the Dirac operator by means of a computer simulation. Such computations have already been discussed in the literature (see, for example [10]) for the case of instantons. Our results for fermion guides differ from the conclusions drawn in [10] for instantons because of the distinction between the structures of the overlap matrices for these different configurations of gauge fields.

In Section 6, we discuss the results of our present analysis, the degree of validity of the assumptions made to derive these results, and prospects for a further development along these lines.

1. FORMULATION OF THE PROBLEM

As is well known, a nonzero quark condensate $\langle\bar{\psi}(x)\psi(x)\rangle \neq 0$ is in fact an order parameter for chiral-symmetry breaking. Indeed, the condensate must vanish in the case of unbroken chiral symmetry for its symmetry under chiral transformations to be respected. A nonperturbative character of the phenomenon of chiral-symmetry breaking can be illustrated by an attempt at calculating the quark condensate by perturbation theory. All diagrams lead to expressions that involve the trace of the product of an odd number of γ matrices, this trace being equal to zero,

$$\mathrm{Tr}S_C = \mathrm{Tr}S_C\hat{A}S_C = \mathrm{Tr}S_C\hat{A}S_C\hat{A}S_C = \ldots = 0, \quad (1)$$

where S_C is the free Green's function for a massless fermion and $\hat{A} = \gamma_\mu A_\mu$, A_μ being a gauge field. Thus, we see that, in order to explain chiral-symmetry breaking, it is necessary to consider quarks in a nonzero gauge field taken into account nonperturbatively. For an approximation, one can take some external-gauge-field configuration that simulates a vacuum gluon condensate.

According to Banks–Casher relations [11], the quark condensate in an external field is related to the spectral density of the Dirac operator in this field, $\rho(\lambda)$, at $\lambda = 0$ by the equation

$$\langle\bar{\psi}\psi\rangle = -\pi\langle\bar{\rho}(0)\rangle, \quad (2)$$

where $\bar{\rho}(\lambda) = \rho(\lambda)/V_4$ is the density of zero modes per unit of four-dimensional volume. By means of this formula, we can demonstrate once again that chiral-symmetry breaking is a nonperturbative phenomenon. Indeed, the eigenfunctions of the Dirac operator in the case of zero external field correspond to the free motion of fermions at different momenta. In an arbitrary d-dimensional case, we have

$$\bar{\rho}(\lambda) \sim \int d^d p\,\delta(|p| - \lambda) \sim \lambda^{d-1}. \quad (3)$$

In the case of $d = 4$, the result takes the form $\bar{\rho}(\lambda) \sim \lambda^3$ and obviously vanishes in the limit $\lambda \to 0$.

We are interested in such gauge-field configurations that would play a significant role in the formation of the path integral and for which $\bar{\rho}(\lambda)$ would not tend to zero for small λ.

In [2], instantons were taken for such configurations. We recall that the instanton mechanism of chiral-symmetry breaking is as follows. One considers a dilute medium (gas) constructed as a superposition of many instantons and anti-instantons. It is well known that, in the field of each of them taken individually, the Dirac operator has a zero mode localized in the vicinity of this pseudoparticle. However, the presence of other instantons and anti-instantons at large distances results in that the former zero eigenvalues of the Dirac operator are split and are grouped around the origin (approximately in the same way as energy levels are split in the quantum-mechanical problem of two potential wells or in the case of a band structure of spectra in periodic fields in solids). In the limit of an infinite number of pseudoparticles, the spectrum of the Dirac operator becomes continuous, the former zero modes creating a finite spectral density at the origin. In [2], it was shown that, upon averaging over all positions of instantons, $\langle\bar{\rho}(\lambda)\rangle$ takes the form of a Gaussian function centered at the origin; naturally, $\langle\bar{\rho}(0)\rangle \neq 0$ in this case. Also, the massless-fermion propagator in such a gas was obtained there, and it was shown that the pole at the origin disappears

and that a fermion acquires a momentum-dependent effective mass.

A different possible mechanism of chiral-symmetry breaking was proposed in [9]. Gauge-field configurations of nonzero zero-mode density that were considered there were constructed as superpositions of fermion guides—that is, such gauge-field configurations where a fermion of any mass propagates along the same one-dimensional trajectory in four-dimensional space over arbitrary distances without reduction of the amplitude. We note that, according to (3), the motion of a fermion in one-dimensional space ($d = 1$), where the value of the spectral density at the origin, $\rho(0)$, is finite and does not vanish, effectively contributes to the path integral. This is the reason why chiral-symmetry breaking can be associated with a field where the motion is effectively one-dimensional. This is the situation that is implemented in fermion guides. Thus, it is proposed to go over from continual integration with respect to all gauge fields to integration over all field configurations of this type.

By using the results presented in [8, 9], we were able to construct an explicit example of a straight-line fermion guide. This example illustrates the mechanism of chiral-symmetry breaking in such fields. Further, we consider the Dirac operator in the field of several fermion guides. Former zero eigenvalues of the Dirac operator are split. They can be obtained within perturbation theory as the eigenvalues of a matrix composed of overlap integrals. We have analyzed the structure of this matrix. The final objective here is to consider a medium where the distribution of fermion guides is random and to perform averaging of quark condensate in the same way as was already done in [2] for instantons. Under the assumption that the configurations being considered saturate the path integral, we have replaced continual integration with respect to all possible fields by averaging over all distributions of fermion guides—that is, by a finite-dimensional integration. The result demonstrates the possibility of the emergence of a spectral distribution of quark modes that is characterized by a finite spectral density at the origin. In order to verify the results obtained analytically, we have performed a computer simulation. The results of this simulation agree with the results of the analytic calculations over the region where the model underlying the simulation is justified.

2. SOLVING THE DIRAC EQUATION IN THE FERMION-GUIDE FIELD

Let us consider the Dirac equation

$$i(\gamma_\mu D_\mu + m)\psi(x) = 0, \quad D_\mu = \partial_\mu - iA_\mu(x), \quad (4)$$

in four-dimensional Euclidean spacetime in an external non-Abelian gauge field A_μ [12] (we do not indicate color and flavor indices explicitly).

A static fermion guide proposed in [9] is a gauge field A_μ in which the Dirac equation (4) has a static solution normalizable in three dimensions. This fermion guide (and the trajectories of fermions in it) has the form of a straight line parallel to the axis of the imaginary time x_4. It is natural to seek a static fermion guide as a static gauge field—for example, in the Hamiltonian gauge

$$A_4(x) = 0, \quad \partial_4 A_i(x) = 0. \quad (5)$$

In this gauge, the property $[\partial_4, \widehat{D}] = 0$ means that the fermion solution in question must be sought as a time-independent solution, $\partial_4 \to -E$, this corresponding to time-independent solutions of energy E in Minkowski spacetime ($x_0 = -ix_4$),

$$\psi(x) = e^{-Ex_4}\phi(\mathbf{x}) = e^{-iEx_0}\phi(\mathbf{x}); \quad (6)$$

the Dirac equation then reduces to the form

$$(\gamma_4 \boldsymbol{\gamma}\cdot\mathbf{D} + m\gamma_4)\phi(\mathbf{x}) = E\phi(\mathbf{x}). \quad (7)$$

Let us consider the squared form of this equation,

$$(\boldsymbol{\gamma}\cdot\mathbf{D})^2\phi(\mathbf{x}) = (m^2 - E^2)\phi(\mathbf{x}). \quad (8)$$

A solution that is normalizable in three dimensions is possible only in the case of $m^2 = E^2$ (otherwise, this equation reduces at infinity to the Helmholtz equation, which does not have normalizable solutions). Therefore, our equation reduces to the form

$$\boldsymbol{\gamma}\cdot\mathbf{D}\phi(\mathbf{x}) = -m(1 \mp \gamma_4)\phi(\mathbf{x}). \quad (9)$$

The operator $(\boldsymbol{\gamma}\cdot\mathbf{D})^2$ is not positive definite, while the operator $\boldsymbol{\gamma}\cdot\mathbf{D}$ is anti-Hermitian. We introduce the notation $\boldsymbol{\gamma}\cdot\mathbf{D}\phi = \phi'$. Under the condition $E^2 = m^2$, it follows from the squared Dirac equation that $(\boldsymbol{\gamma}\cdot\mathbf{D})^2\phi = 0$. We then have

$$0 = \int d^3x \phi^\dagger(\mathbf{x})(\boldsymbol{\gamma}\cdot\mathbf{D})^2\phi(\mathbf{x}) = -\int \phi'^\dagger\phi' d^3x \le 0; \quad (10)$$

hence, $\phi' = \boldsymbol{\gamma}\cdot\mathbf{D}\phi = 0$. In this case, Eq. (9) is satisfied if

$$\gamma_4\phi(x) = \pm\phi(x). \quad (11)$$

We will now show that, under these conditions, the four-dimensional Dirac equation reduces to the three-dimensional Dirac equation for zero modes.

Taking into account the explicit form of the Euclidean Dirac matrices in the Weyl representation, we do indeed obtain

$$\psi_\pm(x) = \begin{pmatrix} \chi(\mathbf{x}) \\ \mp\chi(\mathbf{x}) \end{pmatrix} e^{\mp mx_4}, \quad (12)$$

where $\chi(\mathbf{x})$ is a two-component spinor that satisfies the three-dimensional Dirac equation; that is,

$$i\sigma_i\partial_i\chi(\mathbf{x}) = -A_i\sigma_i\chi(\mathbf{x}). \quad (13)$$

It is obvious that, if fermions are massless, then $E = 0$, in which case we can always construct one left- and one right-handed solution. The Atiyah–Patodi–Singer theorem [13] is satisfied since the Pontryagin index is zero for a purely magnetic field.

The last equation coincides with the Dirac equation in three-dimensional space for massless fermions. Many gauge configurations in which this equation has normalizable (in three dimensions, of course) solutions have already been found. By way of example, we indicate that, in the Abelian case, the corresponding three-dimensional Dirac equation has a solution in the form [8]

$$\begin{cases} \mathbf{A}(\mathbf{x}) = 3(1+r^2)^{-3/2} \begin{pmatrix} 2xz - 2y \\ 2yz + 2x \\ 1 - r^2 + 2z^2 \end{pmatrix}, \\ \chi(\mathbf{x}) = \pi^{-1}(1+r^2)^{-3/2} \begin{pmatrix} 1+iz \\ x+iy \end{pmatrix}, \end{cases} \tag{14}$$

where $r^2 = x^2 + y^2 + z^2$, the dimension of the solution being chosen to be equal to unity. This is one of the many Abelian gauge configurations obtained recently for which the corresponding solutions to the Dirac equation possess nontrivial topological properties in three dimensions (see, for example, [8]). This field has a nontrivial topology in three dimensions (that is, the Chern–Simons number is not zero), the field itself emerging, apart from a coefficient, as the result of the canonical Hopf map $S^3 \to S^2$ [8]; however, it is of course topologically trivial in four-dimensional space, since the Pontryagin index is zero for it.

This field is not the only example of solutions—many others have also been found. This means that there are many explicit examples of fermion guides. By applying a Lorentz rotation to them (in the Euclidean case, it coincides with a conventional rotation), we obtain a more general class of fermion guides, in which localized fermions move along a straight line at a constant speed instead of being at rest. These are the fermion guides that we will employ in the following.

It should also be noted that the fermion-guide field given in (14) does not satisfy gauge-field equations, but one can derive it (apart from a coefficient) upon taking the Abelian projection of the purely gauge non-Abelian configuration presented in [14]. In this sense, the configurations being considered are similar to vacuum components of a different form—namely, so-called central vortices. It is well known that, although central vortices are not solutions to classical equations for gauge fields, their contribution is determined by a large entropy associated with them, this giving sufficient grounds to consider central vortices as objects responsible for confinement [1, 4]. Possibly, field constructions that have the form of fermion guides also play a nontrivial role in the structure of the QCD vacuum. They are not saddle points of the path integral involving the gauge-field action, but, owing to the entropy associated with them, their contribution to the path integral can be significant.[1)]

Making Lorentz rotations (in Euclidean space, these are merely four-dimensional rotations), we obtain a more general class of straight-line fermion guides. In order to generalize Eq. (12) to the case of an arbitrarily oriented straight-line fermion guide, we can follow [19], introducing, instead of the time coordinate x_4, the "proper time"

$$\bar{x} = (\eta x) \tag{15}$$

(where η is a constant 4-vector specifying the direction of the fermion guide and satisfying the equality $\eta_\mu^2 = 1$) and employing, instead of (5), a different gauge-fixing condition,

$$\eta_\mu A_\mu(x) = 0, \quad \eta_\mu \partial_\mu A_\nu(x) = 0. \tag{16}$$

We will now describe the mechanism of chiral-symmetry breaking in the field of a fermion guide. Without loss of generality, we can consider a static fermion guide. The density $\bar{\rho}(0)$ is calculated as the trace of the fermion propagator in this field. As usual, we introduce a nonzero mass m, which is then made to tend to zero. Thus, we consider a static fermion guide aligned with the x_4 axis. One can find a set of eigenvectors of the four-dimensional Dirac operator in the field of the fermion guide that are normalizable in three dimensions,

$$\hat{D}\psi(x) = i\lambda\psi(x) \quad (\hat{D} = \gamma_\mu D_\mu = \gamma D), \tag{17}$$

and which have a continuous spectrum specified by the parameter λ,

$$\psi_\pm(x) = \phi_\pm(\mathbf{x}) e^{\pm i\lambda x_4}, \tag{18}$$

where $\phi(\mathbf{x})$ satisfies Eqs. (11) and (9); that is,

$$\gamma_4 \phi_\pm(\mathbf{x}) = \pm\phi_\pm(\mathbf{x}), \boldsymbol{\gamma}\cdot\mathbf{D}\phi_\pm(\mathbf{x}) = 0 \tag{19}$$

for $\gamma_5\phi_+ = \phi_-$ and $\gamma_5\phi_+ = \phi_-$.

In order to calculate $\rho(0)$, we consider the fermion propagator

$$S = \frac{1}{\gamma D + m} = \sum |\psi_i\rangle \frac{1}{i\lambda_i + m} \langle\psi_i| \tag{20}$$

in the field of the fermion guide. Here, we have introduced a finite fermion mass m, which we will then

[1)] We note that this situation differs significantly from that in the Abelian case, since the contribution to the path integral from genuinely Abelian fields that are far off saddle points is negligible in relation to the contribution from the Abelian projection of the potentials in question.

make tend to zero. It is natural to single out, in this expansion in the energy eigenfunctions $\phi(\mathbf{x})$, states $|\psi\rangle$ that correspond to effective one-dimensional motion: $S = B + C$, where B is that part of the sum which includes such states. It can be shown [9] that B is the leading term in the propagator at long distances. It is of importance that $\mathrm{Tr}B \neq 0$; that is, B makes a nonzero contribution to the quark condensate. We will now demonstrate this explicitly. For each value of λ, the equation for the eigenfunctions of the Dirac operator, $i\hat{D}\psi = \lambda\psi$, has a solution normalizable in three dimensions; that is,

$$\psi(x) = \phi(\mathbf{x})e^{\pm i\lambda x_4}. \tag{21}$$

On the basis of these solutions, we now calculate B as

$$\begin{aligned} B(x,y) &= \frac{1}{2\pi}\int\limits_{-\infty}^{+\infty} d\lambda\Bigg(\frac{e^{i\lambda(x_4-y_4)}}{i\lambda+m}\phi(\mathbf{x})\phi^\dagger(\mathbf{y}) \\ &\quad + \frac{e^{i\lambda(y_4-x_4)}}{i\lambda+m}\gamma_5\phi(\mathbf{x})\phi^\dagger(\mathbf{y})\gamma_5\Bigg) \\ &= e^{-m|x_4-y_4|}(\theta(x_4-y_4)\phi(\mathbf{x})\phi^\dagger(\mathbf{y}) \\ &\quad + \theta(y_4-x_4)\gamma_5\phi(\mathbf{x})\phi^\dagger(\mathbf{y})\gamma_5). \end{aligned} \tag{22}$$

It can easily be seen that, as $m \to 0$, the main contribution to the integral comes from λ values close to zero (to prove this, it is sufficient to introduce the dimensionless integration variable $\lambda \to m\lambda$). The trace of this part of the propagator is proportional to the fermion-guide length L:

$$\begin{aligned} \mathrm{Tr}B &= \int \mathrm{tr}B(x,x)d^4x \\ &= \int \phi^\dagger(\mathbf{x})\phi(\mathbf{x})d\mathbf{x}dx_4 = \int 1dx_4 = L. \end{aligned} \tag{23}$$

If we take a distribution of fermion guides having a finite three-dimensional density in a four-dimensional volume V_4, the density of the trace of the propagator in such a field, $\mathrm{Tr}B/V_4$, may prove to be finite, as in the case of instantons. The difference is that, in case of instantons, this occurs owing to zero modes normalizable in four dimensions (discrete spectrum), while, in the case of fermion guides, there in no discrete spectrum; instead, there are "lumps" of a continuous spectrum in the vicinity of the origin owing to the presence of a class of solutions normalizable in three dimensions. As can be seen, eigenfunctions belonging to a continuous spectrum can also make a nonzero contribution to the trace of the propagator.

We note that, in the following, we will assume that the fermion-guide length is finite and impose periodic (rather than antiperiodic) boundary conditions for fermions. The requirement of periodicity in imaginary time will result in that only the $\lambda = 0$ solution will survive in the vicinity of $\lambda = 0$. This solution will then become normalizable in four dimensions as well, since integration with respect to imaginary time will not lead to a divergence of the norm. Obviously, $\mathrm{Tr}S/V_4$ will remain finite in this case. This assumption is necessary for the ensuing analysis since we will proceed in such a way as if there were solutions to the massless Dirac equation that are normalizable in four dimensions, their finite norm being large and proportional to the fermion-guide length.

3. SUPERPOSITION OF A FEW FERMION GUIDES: SPLITTING OF LEVELS OF THE DIRAC OPERATOR IN THE VICINITY OF THE ORIGIN

In contrast to the situation studied in [9], where a large number of zero modes were assumed for each fermion guide, we will consider a solution to the Dirac equation for a massless fermion where there is only one zero mode normalizable in three dimensions. We assume that there exists a superposition of N arbitrarily oriented fermion guides,

$$A(x) = A_1(x) + A_2(x) + \ldots + A_N(x), \tag{24}$$

occurring at large distances from one another (in this sense, the situation resembles the case of instantons that was considered in [2]). The superposition of $N \gg 1$ fields of fermion guides that involves massless fermions can play the role of a mechanism breaking chiral symmetry. We assume that, for each fermion guide, there exists a solution normalizable in three dimensions that has the form of zero modes for the equations

$$(\hat{\partial} - i\hat{A}_k(x))\psi_k(x) = 0 \quad (k = 1, \ldots, N).$$

We note that, here, the fermion guides are already arbitrarily oriented—that is, $A_{k4} \neq 0$ and $A_{k\mu}$ depend on x_4. For this reason, it is necessary to use solutions of straight-line-fermion-guide type in the generalized sense that was discussed above [see Eqs. (15), (16)]. Further, eigenfunctions of the Dirac operator [see Eq. (17)] that correspond to nonzero eigenvalues λ will be sought as superpositions of the former zero modes in the fields of individual fermion guides A_k,

$$\psi(x) = \sum_{k=1}^{N} c_k\psi_k(x). \tag{25}$$

Multiplying Eq. (17) by $\psi_n^\dagger$ and performing integration with respect to x, we take into account the orthonormality condition

$$\langle\psi_m|\psi_n\rangle = \int d^4x\psi_m^\dagger(x)\psi_n(x) = L\delta_{mn}.$$

Strictly speaking, there is no normalizability in four dimensions in the limit $L \to \infty$; however, we can take L to be large, but finite. The orthogonality of wave functions for different fermion guides can then be justified if they are rather widely spaced. As a result, we arrive at the set of equations

$$T_{ik}c_k = L\lambda c_i \quad (i = 1, \ldots, N), \tag{26}$$

where $T_{ij} = \langle\psi_i|i\hat{D}|\psi_j\rangle$ is an element of the overlap matrix T. We note that, in contrast to the normalization integral, T_{ij} does not involve the factor L if the ith and the jth fermion guide are not parallel to each other. According to our assumptions, fermion guides are oriented arbitrarily in four-dimensional space; therefore, the probability of finding parallel fermion guides is equal to zero. This conclusion is of paramount importance for our reasoning that leads to a finite value of the spectral density at the origin (see the next section).

The spectrum of the Dirac operator consists of the eigenvalues of the overlap matrix. Of course, this method yields the eigenvalues of the Dirac operator only in the vicinity of the origin and only approximately. In practice, however, it provides answers to questions of fundamental importance. By way of example, we indicate that, in the case of several instantons, $T_{ij} = 0$, and the eigenvalues of the Dirac operator indeed must not undergo splitting in accordance with the Atiyah–Singer theorem. But if one includes anti-instantons, there must appear splitting, since the overlap matrix acquires nonzero elements.

In the case of fermion guides, there are nonzero elements in the overlap matrix. We will now consider the structure of this matrix in more detail. In the field of the ith fermion guide, there are two former zero modes, a left- and a right-handed one, $\psi_i^{L,R}$. As was indicated above, we assume them to be normalizable, their norm being L. For the matrix elements, the following "selection rule" must obviously hold:

$$\langle\psi_{iL}|\hat{D}|\psi_{jL}\rangle = \langle\psi_{iR}|\hat{D}|\psi_{jR}\rangle = 0.$$

Only overlap integrals for fermions of opposite helicities—that is, quantities of the $\langle\psi_{iL}|\hat{D}|\psi_{jR}\rangle$ type—may be nonzero. Therefore, the overlap matrix has the form

$$T = \begin{pmatrix} 0 & M \\ M^\dagger & 0 \end{pmatrix}, \tag{27}$$

where $M_{ij} = \langle\psi_{iR}|i\hat{D}|\psi_{jL}\rangle$. Disregarding integrals of the form $\langle\psi_m|\hat{A}_n|\psi_k\rangle$, where m, n, and k correspond to three different fermion guides, we obtain

$$M = \begin{pmatrix} \langle\psi_{1L}|\sum\limits_{i\neq 1}\hat{A}_i|\psi_{1R}\rangle & \cdots & \langle\psi_{1L}|(\hat{A}_1+\hat{A}_N)/2|\psi_{NR}\rangle \\ \langle\psi_{2L}|(\hat{A}_1+\hat{A}_2)/2|\psi_{1R}\rangle & \cdots & \langle\psi_{2L}|(\hat{A}_2+\hat{A}_N)/2|\psi_{NR}\rangle \\ \cdots & \cdots & \cdots \\ \langle\psi_{NL}|(\hat{A}_1+\hat{A}_N)/2|\psi_{1R}\rangle & \cdots & \langle\psi_{NL}|\sum\limits_{i\neq N}\hat{A}_i|\psi_{NR}\rangle \end{pmatrix}. \tag{28}$$

We note that all expressions of the form $\langle\psi_i|\hat{A}_i|\psi_j\rangle$ and $\langle\psi_i|\hat{A}_j|\psi_i\rangle$ are on the same order of magnitude and are small in the case of a dilute distribution of fermion guides. Therefore, the "diagonal" elements are given by a sum of $N-1 \approx N \gg 1$ terms of the same order:

$$M_{ii} = \langle\psi_{iL}|\hat{A}_1 + \ldots + \hat{A}_{i-1} + \hat{A}_{i+1} + \ldots + \hat{A}_N|\psi_{iR}\rangle.$$

Therefore, they are much greater in absolute value than the off-diagonal elements

$$M_{ij} = \langle\psi_{iL}|(\hat{A}_i + \hat{A}_j)/2|\psi_{jR}\rangle.$$

In the case of instantons and anti-instantons, the overlap matrix has a different structure—all of its diagonal elements vanish.

4. DILUTE GAS OF FERMION GUIDES

The spectral density $\langle\rho(\lambda)\rangle$ averaged over all configurations of gauge fields is expressed in terms of a path integral over all gauge-field configurations as

$$\langle\rho(\lambda)\rangle = \int DAe^{-S_g[A]}\rho([A],\lambda), \tag{29}$$

where S_g is the action functional of the gauge field A. Since it is hardly possible to calculate this integral exactly, we will rely on a method that is similar to the method employed in [2]. We will assume that a fermion guide has the shape of a one-dimensional

cylinder in four-dimensional space and replace continual integration with respect to all possible fields by integration over all superpositions of fermion guides. Averaging will now be performed only over collective coordinates ξ_i that specify the positions and orientation of fermion guides:

$$\langle\rho(\lambda)\rangle = \frac{1}{\Omega^N}\int d\xi_1 d\xi_2 \ldots d\xi_N \rho(\xi_1,\xi_2,\ldots,\xi_N;\lambda). \tag{30}$$

Here, ξ_i specifies the position of the ith fermion guide, its orientation and the point of its intersection with the $x_4 = 0$ hyperplane, its thickness, its orientation in the group space, and so on; N is the total number of fermion guides; and Ω is the volume of the ξ_i space.

For an arbitrary disposition of fermion guides, the spectral density of the Dirac operator is given by

$$\rho(\xi_1,\xi_2,\ldots,\xi_N;\lambda) = \sum_{i=1}^{N}\delta(\lambda-\lambda_i(\xi_1,\xi_2,\ldots,\xi_N)), \tag{31}$$

where $\lambda_i(\xi_1,\xi_2,\ldots,\xi_N)$ are eigenvalues of the overlap matrix M.

In order to derive physical quantities upon the replacement of the path integral by averaging over fermion-guide configurations, it is necessary to perform averaging over ξ_i. In this way, we can obtain not only the quark condensate but also other quantities and functions—for example, a propagator. We restrict our consideration here to the quark condensate. In order to make use of the Banks–Casher relation [11]

$$\langle\bar{q}q\rangle = -\pi\langle\bar{\rho}(0)\rangle = -\frac{\pi\langle\rho(0)\rangle}{V_4}, \tag{32}$$

we consider $\rho(\lambda)$ in the limit of small λ:

$$\langle\rho(\lambda)\rangle = \frac{1}{2\pi}\int\limits_{-\infty}^{\infty} e^{is\lambda}\langle \mathrm{tr}e^{-isT/L}\rangle ds. \tag{33}$$

In the thermodynamic limit for $\langle\rho(\lambda)\rangle$, we have the following: $L\to\infty$ and the three-dimensional concentration of fermion guides, $n = N/L^3$, is fixed. For the spectral density of the Dirac operator to be determined approximately, the gas of fermion guides must be dilute—that is, the three-dimensional concentration n is assumed to be small. Expanding $\mathrm{tr}\langle\exp(-isT/L)\rangle$ in a power series in T, disregarding terms higher than T^2, and considering that $\mathrm{tr}T = 0$, we obtain

$$\langle\rho(0)\rangle = NL\sqrt{\frac{2N}{\langle\mathrm{tr}T^2\rangle}} \tag{34}$$
$$= NL\sqrt{\frac{N}{\langle\mathrm{tr}MM^\dagger\rangle}}.$$

The trace $\mathrm{tr}MM^\dagger$ involves a diagonal and an off-diagonal component. The off-diagonal component has the form $\sum_{i\neq j=1}^{N}|M_{ij}|^2$. For $i\neq j$, we have

$$|M_{ij}|^2 = |\langle\psi_{iL}|\hat{A}_i|\psi_{jR}\rangle|^2 \tag{35}$$
$$= g(\xi_i,\xi_j) = g(\mathbf{x}_i-\mathbf{x}_j,\omega_i,\omega_j).$$

Here, the function $g(\xi_i,\xi_j)$, whose explicit form is determined by the explicit form of fermion guides, depends only on the difference of the "noncompact" coordinates $\mathbf{x}_i$, for which one can take, for example, the coordinates of the points at which fermion guides intersect the $x_4 = 0$ plane. We assume that averaging over the "compact" coordinates of fermion guides, ω_i (orientation in the group space, direction in four-dimensional space, and so on), will not affect the answer to the question of whether a finite condensate does exist in principle and, if so, the order of its magnitude. For this reason, we restrict ourselves to averaging over noncompact coordinates; that is,

$$\left\langle\sum_{i\neq j=1}^{N}|M_{ij}|^2\right\rangle = \frac{N^2}{\Omega^2}\int d\xi_1 d\xi_2 g(\xi_1,\xi_2) \tag{36}$$
$$= \frac{N^2}{V_3^2}\int d^3x_1 d^3x_2 \bar{g}(\mathbf{x}_1-\mathbf{x}_2),$$

where $\bar{g}(\mathbf{x}_1-\mathbf{x}_2)$ arises instead of the function $g(\mathbf{x}_1-\mathbf{x}_2)$ after integration with respect to compact coordinates. This new function is effectively different from zero only when the relative coordinates $\mathbf{x}_1-\mathbf{x}_2$ reach the order of the transverse dimension δ of a fermion guide. We note that, in constructing an explicit example of a fermion guide above, we took its transverse dimension to be equal to unity. We write the 4-volume as $V_4 = L(L^3)$, where the 3-volume is $L^3 = V_3 = Na^3$ ($a^3 = 1/n$ is the mean volume per fermion guide, and n is the concentration of fermion guides). As a result, integration with respect to the relative coordinates yields $\delta^3 b_1$ (where b_1 is a dimensionless constant), while integration with respect to the coordinates of the "center of mass" yields $V_3 = Na^3$; therefore, the integral in (36) assumes the form

$$\left\langle\sum_{i\neq j=1}^{N}|M_{ij}|^2\right\rangle = b_1 N^2\frac{\delta^3}{L^3}. \tag{37}$$

The diagonal term has the form $\langle\sum_{i=1}^{N}|M_{ii}|^2\rangle$. Considering that

$$\left\langle\sum_{i=1}^{N}|M_{ii}|^2\right\rangle = \left\langle\sum_{i\neq j=1}^{N}|\langle\psi_i|\hat{A}_j|\psi_i\rangle|^2\right\rangle$$
$$+\left\langle\sum_{i\neq j\neq k=1}^{N}\langle\psi_i|\hat{A}_j|\psi_i\rangle\langle\psi_i|\hat{A}_k|\psi_i\rangle^\dagger\right\rangle,$$

we find by the same method that

$$\left\langle \sum_{i=1}^{N} |M_{ii}|^2 \right\rangle = b_2 N^2 \frac{\delta^3}{L^3} + b_3 N^3 \frac{\delta^6}{L^6}, \qquad (38)$$

where b_2 and b_3 are dimensionless constants that are determined by a specific form of fermion guides. Bringing together the individual terms, we obtain the condensate in the form

$$-\langle \bar{q}q \rangle = \pi \frac{\langle \rho(0) \rangle}{L^4} \qquad (39)$$

$$= \frac{\pi N}{L^3} [(b_1 + b_2) n\delta^3 + b_3 n^2 \delta^6]^{-1/2}$$

$$= \frac{\pi n}{[(b_1 + b_2) n\delta^3 + b_3 n^2 \delta^6]^{1/2}} \approx \pi \left(\frac{n}{b\delta^3} \right)^{1/2}$$

for $b = b_1 + b_2$. Here, we have considered that $(n\delta^3)^2 \ll n\delta^3$ for $\delta/a \ll 1$. One can see that the thermodynamic limit for $\langle \bar{\rho}(0) \rangle = \langle \rho(0) \rangle / V_4$ exists (we emphasize the presence of the factor $1/V_4$ in the expression for $\langle \bar{q}q \rangle$), and we obtain

$$\bar{\rho}(0) = \frac{\langle \rho(0) \rangle}{V_3 L} = \left(\frac{n}{b\delta^3} \right)^{1/2} \qquad (40)$$

$$= n b^{-1/2} \left(\frac{a}{\delta} \right)^{3/2}.$$

To conclude this section, we will briefly summarize the results of our analytic investigation into the problem at hand. The distribution $\langle \bar{\rho}(\lambda) \rangle$ has the form of a Gaussian function, the spectral density at the origin being finite, $\langle \bar{\rho}(0) \rangle \neq 0$—more specifically, $\langle \bar{\rho}(0) \rangle \sim \sqrt{n}$. We note that, in contrast to our present study, Tiktopoulos [9] ruled out the splitting of zero modes, and this was the reason why he arrived at a different result—namely, $\langle \bar{\rho}(0) \rangle \sim n$. Thus, our conclusion, which was obtained on the basis of the model of a dilute fermion-guide gas (we assumed that the concentration $n = N/L^3 = N/(Na^3) = 1/a^3$ is low—that is, the mean volume per fermion guide, a^3, is large), differs from that in [9] [see Eq. (2.22) there]. At the same time, the expression derived here for the quark condensate, $\langle \overline{q}q \rangle \sim \sqrt{n}$, on the basis of the Banks–Casher relation also differs from that obtained in [9]. Since it is finite, however, we can state that the main conclusion of Tiktopoulos [9] on the possibility of chiral-symmetry breaking in a gas of fermion guides has been confirmed.

5. COMPUTER SIMULATION

We have also performed a numerical simulation of the interaction of Dirac fermions with a medium formed by fermion guides. We note that such calculations have already been discussed in the literature (see [10]) for the case of instantons. Our results for fermion guides differ from the conclusions drawn in [10] for instantons because of the difference in structure of the overlap matrix for these different gauge-field configurations. Our objective was to average $\rho(\lambda)$ over all positions of fermion guides:

$$\bar{\rho}(\lambda) = \frac{1}{\Omega^N} \int d\xi_1 d\xi_2 \ldots d\xi_N \qquad (41)$$

$$\times \sum_{i=1}^{N} \delta(\lambda - \lambda_i(\xi_1, \xi_2, \ldots, \xi_N)).$$

In Section 4 above, this averaging was performed analytically, but under the assumptions indicated there. In particular, we retained there only the first two terms of the Taylor expansion for e^{-sT} and skipped integration with respect to compact coordinates. Therefore, the results obtained there are qualitative to a considerable extent: at a low concentration of fermion guides, $\langle \bar{\rho}(\lambda) \rangle$ has the form of a Gaussian function, $\langle \bar{\rho}(0) \rangle \neq 0$, and has a thermodynamic limit, $\sim \sqrt{n}$.

In our computer simulation, we relied on the method that was already employed in [10] for instantons. The idea of the method is the following. The quantities of interest are calculated by the Monte Carlo method: fermion guides are placed at random in four-dimensional space, and the overlap matrix and its eigenvalues are calculated for each of the distributions of fermion guides. This procedure is repeated many times (as is prescribed by the Monte Carlo method). As a result, one obtains an averaged distribution $\langle \bar{\rho}(\lambda) \rangle$.

The method that we use here is advantageous in that, within this method, we take into account integration with respect to compact coordinates and do not replace the exponential function e^{-sT} of the overlap matrix by part of the corresponding Taylor series. The latter is of importance, since this replacement could be quite dubious at small values of s. However, this method involves difficulties of both a fundamental and a technical character, which entail the need for introducing further assumptions.

The main technical difficulty is obvious. Since we can calculate eigenvalues only for finite-dimensional matrices, the number of fermion guides must be finite. For the concentration of fermion guides to be finite, it is necessary to go over to a finite volume. In order that this transition be meaningful, the volume in question must be rather large (in the limit, it must tend to infinity), but, in a large volume, it is necessary to consider many fermion guides. The overlap matrix becomes large ($N \times N$), and its filling (each of its elements is an integral that must be taken over four-dimensional space and which cannot be calculated analytically), together with the subsequent calculation of eigenvalues, is extremely time-consuming. In addition, this procedure must be repeated many times.

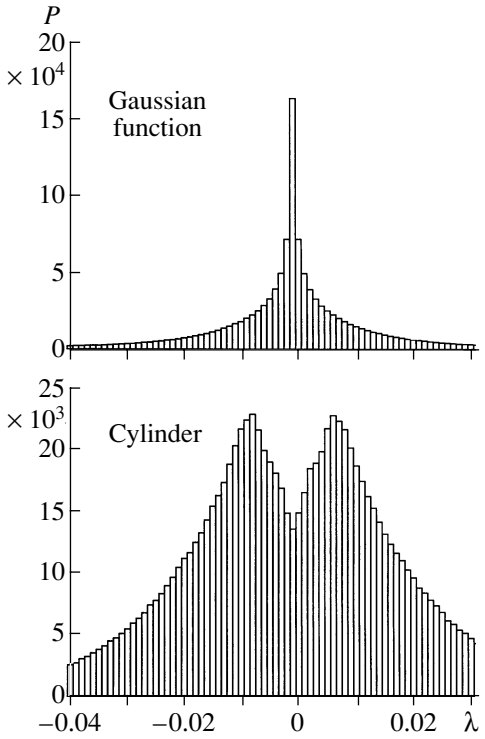

Fig. 1. Histogram representing the dependence $\bar{\rho}(\lambda)$ for a rather low concentration of fermion guides ($L = 40$, $N = 300$) for two different contour functions $\varphi(x)$. The number of eigenvalues of the overlap matrix that fall within a cell of the partition of the λ axis is plotted against the ordinate.

To be able to implement such calculations despite this, we had to introduce simplifying assumptions that were previously made for instantons in [10]. A fermion guide has the form of a cylinder in four-dimensional space; in view of this, we replaced the fermion zero mode $\psi(x)$ by a simple scalar function $\varphi(x)$ that decreases as one moves away from the fermion guide being considered. By way of example, we took $\varphi(x) = \exp(-r^2)$ ("Gaussian form") or $\varphi(x) = \theta(1-r)$ ("cylindrical form"), where $r(x)$ is the distance from the point x to the fermion guide. The true overlap integrals are then replaced by the overlap integrals of such functions, the latter being readily calculable in an analytic form:

$$\langle\psi_i|\hat{A}_i|\psi_j\rangle, \langle\psi_i|\hat{A}_j|\psi_i\rangle \to \int \varphi_i(x)\varphi_j(x)d^4x.$$

The matrix elements obtained in this way are real-valued and positive, in contrast to the original ones. In order to avoid the situation where all of the matrix elements are positive, they were endowed with a phase at random—more specifically, they were multiplied by -1 with a probability of $1/2$. Of course, the above substitution of a scalar function for a fermion function is not quite legitimate. However, we cherish the hope that, if our results prove insensitive to a transition from one scalar function to another, they will not undergo significant changes upon a transition from a fermion function to a scalar one.

In all of the simulations, we began by constructing the dependence $\bar{\rho}(\lambda)$. This was done in the following way. In the vicinity of the origin, the λ axis was partitioned into small cells. Further, the procedure described above, which consisted in distributing at random a given number N of cylinders, composing the overlap matrix, and calculating the spectrum of this matrix upon performing each such distribution, was repeated many times. The number P of eigenvalues that fell within each cell of the partition of λ was recorded. As a result, we obtained a histogram that, in the case of a rather fine partition, approximates, apart from a constant factor, the actual graph of $\rho(\lambda)$. Of course, an overly fine partition is impossible, since the number of eigenvalues that would fall within each cell throughout the simulation time would then be too small, and this would lead to the growth of the statistical uncertainty per point.

All simulations were performed for two different contour functions—a cylindrical [$\varphi(x) = \theta(1-r)$] and a Gaussian [$\varphi(x) = \exp(-r^2)$] one. The number N of distributed fermion guides and the size L of the four-dimensional volume ($V_4 = L^4$) played the role of input parameters in each specific simulation. As output information, we obtained the dependence $\rho(\lambda)$. In other words, we studied the function $\rho(\lambda, V, N)$ of three variables. The most interesting two-dimensional cross sections of this function are displayed in Figs. 1–4. For the unit of length, we took a fixed transverse size of a fermion guide, whereupon all quantities being considered became dimensionless.

Figure 1 shows a histogram that represents the dependence $\langle\bar{\rho}(\lambda)\rangle$ for a rather low concentration of fermion guides for two different types of the contour function $\varphi(x)$—a Gaussian and a cylindrical type. Instead of the zero-mode density per unit volume, $\bar{\rho}(\lambda)$, the number $P(\lambda)$ of eigenvalues of the overlap matrix that fall within a cell of a partition of the λ axis, the latter being proportional to the former, is plotted along the ordinate. This was done in order to disclose the role of the statistical uncertainty. One can see that the shape of the graphs changes significantly upon going over from one contour function to the other. A statistical uncertainty of $1/\sqrt{P} \sim 1\%$ cannot explain this. It follows that, at very low concentrations, the assumptions that we made for our computer simulation (replacement of the overlap integral by a simplified expression) are illegitimate. In this computer simulation, it rather difficult to test our analytic result given above. In principle, the analytic result

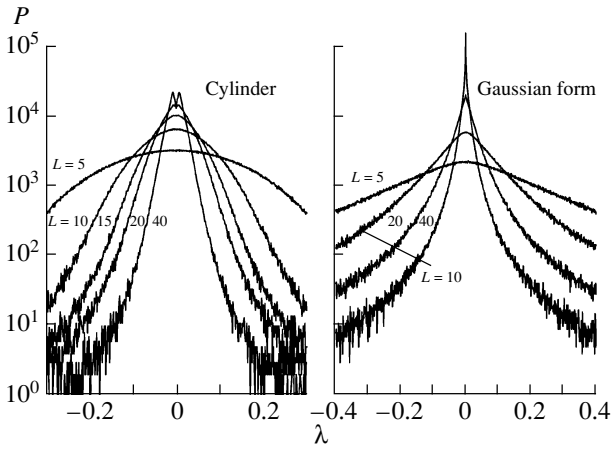

Fig. 2. Graphs of the dependence $\bar{\rho}(\lambda)$ at a fixed number of fermion guides ($N = 300$) for various L—that is, for various concentrations of fermion guides.

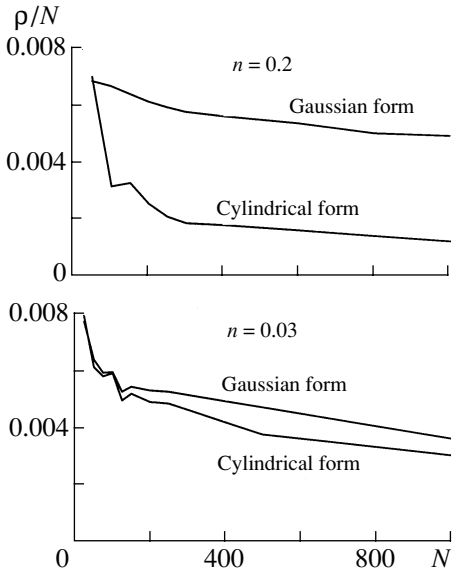

Fig. 3. Specific density of zero modes as a function of the number N of fermion guides for their concentration $n = N/L^3$ fixed at a low ($n = 0.03$) or a high ($n = 0.2$) value.

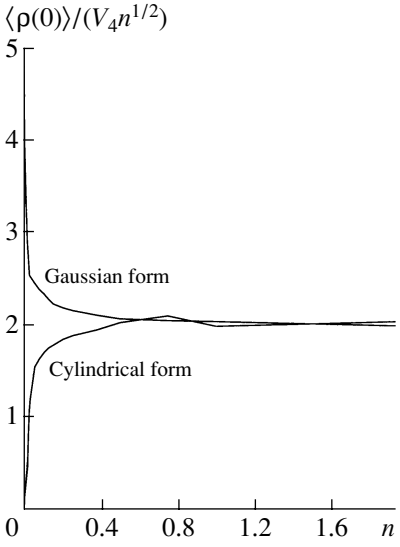

Fig. 4. Density of zero modes as a function of the concentration of fermion guides for two different forms of the function $\varphi(x)$.

in question could be verified via a similar simulation without the replacement of overlap integrals by simpler expressions.

For a fixed number of fermion guides and various L, Fig. 2 shows the number $P(\lambda)$ (see the description of Fig. 1 in the preceding paragraph), which is proportional to $\langle\rho(\lambda)\rangle$. The scale along the ordinate is logarithmic; therefore, a Gaussian function, predicted analytically, looks like a parabola. One can easily see that, at rather high concentrations (rather small L), the graphs for a cylindrical and a Gaussian form of $\varphi(x)$ are similar in the vicinity of the point $\lambda = 0$. From here, we can conclude that their similarity to a Gaussian function in this region confirms the results obtained within the analytic approach. As the concentration is decreased (L is increased), the graphs cease to be similar to each other and to a Gaussian function.

For a fixed concentration of fermion guides, $n = N/L^3 = \text{const}$, the graphs representing the specific density of zero modes as a function of the number N of fermion guides are displayed in Fig. 3 for two cases: that of a low and that of a high concentration ($n = 0.03$ and $n = 0.2$, respectively). Each of the panels (the upper and the lower one) shows two curves corresponding a cylindrical and a Gaussian form of the function $\varphi(x)$. Our analytic method predicts the existence of a thermodynamic limit (for $N \to \infty$). One can see that, at the high concentration, the graphs in question are close to each other, which means that the assumptions under which our computer simulations were performed are quite reasonable. Yet, these graphs do not provide a definitive answer to the question of whether there exists a finite thermodynamic limit for the specific density of zero modes. As to the low concentrations corresponding to analytic calculations, the graphs for them cannot obviously resolve the problem of the existence of a thermodynamic limit, since the assumptions under which the computer simulations were performed are invalid in this region.

The density of zero modes as a function of the concentration of fermion guides is given in Fig. 4 for two different forms of $\varphi(x)$. Since the analytic method used in the present study predicts the dependence

$\langle\bar{\rho}(0)\rangle \sim \sqrt{n}$, the quantity $\langle\bar{\rho}(0)\rangle/V_4$ is plotted along the ordinate. One can see that, at rather high concentrations of fermion guides, the graphs corresponding to the above different forms virtually coincide and that the quantity that they represent is nearly a constant. At low concentrations of fermion guides, the graphs behave differently, once again evincing, for this case, incorrectness of the assumptions underlying the computer simulation.

Thus, the results of our computer simulation are the following. At very low concentrations, the form of $\langle\bar{\rho}(\lambda)\rangle$ depends on the form of $\varphi(x)$; therefore, the substitution $\langle\psi_{i+}|\hat{A}_j|\psi_{j+}\rangle \to \langle\varphi_i|\varphi_j\rangle$ is illegitimate here, since a specific form of fermion functions plays an important role. For not very low concentrations, the form of the function $\langle\rho(\lambda)\rangle$ exhibits but a slight variation upon going over from one form of $\varphi(x)$ to the other, so that the substitution that we made seems justified. If the resulting form [which proved to be identical for the different forms of $\varphi(x)$] had been different from a Gaussian one, this would have implied incorrectness of the assumptions behind the analytic method. The fact that the resulting form is Gaussian confirms the correctness of analytic calculations. In all probability, a thermodynamic limit exists for $\langle\rho(0)\rangle$. However, simulations involving a greater number of fermion guides are required for verifying this statement. In the regions where the results of a numerical simulation can be considered to be justified—that is, at not very high and not very low concentrations of fermion guides—there is satisfactory agreement with the law $\langle\bar{\rho}(0)\rangle \sim \sqrt{n}$, which was obtained analytically.

6. CONCLUSION

In the present study, we have considered chiral-symmetry breaking via a mechanism based on the model of fermion guides. This mechanism is appealing in the sense that it implements the idea of an effectively one-dimensional motion of fermions, this idea being intimately related to chiral-symmetry breaking. For a fermion guide, we have constructed an explicit example that proves that fermion guides exist and which demonstrates some of their new properties [the possibility of obtaining them as the Abelian projection of a pure gauge in $SU(2)$ theory and their nontrivial three-dimensional topology in the case of a trivial four-dimensional topology].

Our consideration of the fermion-guide model has been based on an assumption that is close to the assumption made in considering the instanton model, but which is different from that used in the earlier analysis of fermion guides that was performed by Tiktopoulos [9]. We have assumed the existence of a continuum of zero modes for each fermion guide and, in just the same way as this was done in the case of the instanton model, have analytically constructed fermion states with split zero modes in a dilute gas of fermion guides, relying on solutions in the form of zero modes. As a result, the Dirac spectrum has appeared to be expressed in terms of the eigenvalues of nonzero overlap-matrix elements. On the contrary, it was assumed in [9] that the spectrum of the Dirac operator is not split. This was the reason why the result obtained in [9], $\langle\rho(0)\rangle \sim n$, was different from our result. This distinction highlights the importance of our assumptions.

We have also performed a numerical simulation of the interaction of Dirac fermions with a medium composed of fermion guides. The data obtained from our numerical simulation confirm that the assumptions made in our analytic approach are justified, since, in the region where both approaches are applicable, the analytic calculation and the numerical method lead to close results—namely, to finite values of the spectral density at the origin and to the formation of a quark condensate (that is, to chiral-symmetry breaking).

The main question is that of whether the class of the gauge-field configurations considered above is sufficiently wide for saturating the path integral with respect to fields—this is not obvious from the outset, since, as has already been indicated, fermion guides are not solutions to classical Yang–Mills equations. Here, an analogy with central gauge vortices, which, albeit not being solutions to classical field equations, can play a nontrivial role in the confinement mechanism and, possibly, in chiral-symmetry breaking, is natural. Some arguments presented in the review article of Greensite [1] in favor of vortex models can also be extended to the case of fermion guides. First, vortices arise upon taking a central projection, and this can be done upon maximal central gauging. In other words, an arbitrary gauge configuration can be approximated by a superposition of vortices. Similarly, fermion guides can be obtained, apart from a coefficient, by taking the Abelian projection of a pure gauge. Second, the answer to the question of whether the path integral is saturated by vortex configurations is positive owing to the fact that there are many such configurations (the relevant arguments are given, for example, in [1] and in references quoted therein). The number of possible dispositions of N vortices on a two-dimensional surface grows with N exponentially, which can ensure sufficient entropy for suppressing an exponentially small Boltzmann factor. In just the same way as in the case of central vortices, the role of nonclassical solutions for gauge fields belonging to the type of the fermion guides considered here is also determined by their large statistical weight, which, under some specific conditions—namely, in

the infrared region—could suppress the exponential smallness that is associated with the Boltzmann factor. Owing to this, fermion guides could possibly contribute to the formation of the path integral.

Further investigations can lead to more realistic models of chiral-symmetry breaking. In particular, the problem of boundary conditions and the problem of normalizability of four-dimensional solutions for fermions in the field of fermion guides require additional studies, and a consideration of curvilinear and closed fermion guides is possible in this connection.

ACKNOWLEDGMENTS

We are grateful to D. Ebert (Humboldt University, Berlin, Germany) and H. Reinhardt (Tübingen University, Tübingen, Germany) for stimulating discussions on the results obtained in the present study.

This work was supported in part by the Deutshche Forschungsgemeinschaft (project no. 436 RUS 113/477/0-2).

REFERENCES

1. J. Greensite, hep-lat/0301023.
2. D. I. D'yakonov and V. I. Petrov, Zh. Éksp. Teor. Fiz. **89**, 361 (1985) [Sov. Phys. JETP **62**, 204 (1985)].
3. L. D. Faddeev and A. A. Slavnov, *Gauge Fields: An Introduction to Quantum Theory* (Nauka, Moscow, 1978; Addison Wesley, Redwood City, 1991).
4. M. Engelhardt and H. Reinhardt, Nucl. Phys. B **567**, 249 (2000); hep-th/9907139.
5. H. Reinhardt and T. Tok, Phys. Lett. B **505**, 131 (2001).
6. H. Reinhardt, T. Tok, O. Schröder, and V. Zhukovsky, hep-th/0203012; Phys. Rev. D **66**, 085004 (2002).
7. V. Ch. Zhukovsky and I. V. Mamsurov, Vestn. Mos. Gos. Univ., Ser. 3: Fiz., Astron., No. 3, 31 (2001).
8. C. Adam, B. Muratori, and C. Nash, Phys. Rev. D **62**, 085026 (2000); hep-th/9903040v2; hep-th/9909189v2.
9. G. Tiktopoulos, Phys. Rev. D **35**, 732 (1987).
10. U. Sharan, hep-lat/9910038.
11. T. Banks and A. Casher, Nucl. Phys. B **169**, 103 (1980).
12. A. A. Sokolov, I. M. Ternov, V. Ch. Zhukovsky, and A. V. Borisov, *Gauge Fields* (MGU, Moscow, 1986) [in Russian].
13. M. F. Atiyah, V. Patodi, and I. M. Singer, Math. Proc. Cambridge Philos. Soc. **79**, 71 (1976).
14. R. Jackiw and So-Young Pi, Phys. Rev. D **61**, 105015 (2000); hep-th/9808036.

Translated by A. Isaakyan

Physics of Atomic Nuclei, Vol. 67, No. 12, 2004, pp. 2272–2273. Translated from Yadernaya Fizika, Vol. 67, No. 12, 2004, pp. 2297–2298.
Original Russian Text Copyright © 2004 by Bazarov, Glagolev, Gulamov, Lugovoy, Lutpullaev, Olimov, A. Yuldashev, B. Yuldashev, Khamidov.

LETTERS TO THE EDITOR

Collinearity in Channels Involving the Production of Three or Four Alpha Particles in ^{16}Op Collisions at 3.25 GeV/c per Nucleon

E. Kh. Bazarov, V. V. Glagolev[1)], K. G. Gulamov, V. V. Lugovoy, S. L. Lutpullaev, K. Olimov[*], A. A. Yuldashev, B. S. Yuldashev[2)], and Kh. Sh. Khamidov[2)]

Institute for Physics and Technology, Fizika–Solntse Research and Production Association, Uzbek Academy of Sciences, ul. G. Mavlyanova 2b, Tashkent, 700084 Republic of Uzbekistan

Received January 19, 2004; in final form, May 31, 2004

INTRODUCTION

Modest azimuthal asymmetries and collinearities were discovered in [1] in analyzing channels involving the production of three or four alpha particles in ^{16}Op collisions at 3.25 GeV/c per nucleon. Within the phenomenological model of an isotropic phase space, it was shown in [1] that the azimuthal asymmetry is associated with the transverse motion of the fragmenting nucleus ^{16}O. It was found that the mean transverse momentum of product alpha particles is virtually independent of the transverse-momentum transfer to the fragmenting nucleus. The azimuthal collinearity was described in terms of the collinearity of the momentum vectors of alpha-particle pairs, which is a model parameter. Within the model in question, the collinearity of the momentum vectors in alpha-particle pairs was implemented in the following way: upon generating the components of the momentum of one of the alpha particles, the components of the momentum of the other alpha particle were generated within a 4% interval around the respective values of the former components. In doing this, the difference of the momentum components of the two alpha particles was generated uniformly within the mean relative error in determining momenta.

At the same time, the reasons behind the emergence of collinearity of the momentum vectors in alpha-particle pairs have yet to be clarified. It is natural to assume that one such reason may be associated with the decay of unstable nuclei, $^8\mathrm{Be} \to \alpha + \alpha$ in the ground and in the first excited state, the released energies being 0.1 and 3.04 MeV, respectively, and $^9\mathrm{B} \to \alpha + \alpha + p$, the released energy being 0.3 MeV [2]. It is straightforward to show that, at these energy-release values, the maximum angle in the laboratory frame between the momentum vectors of alpha particles appearing as the products of these decays is smaller than 1°, this leading to narrow angular correlations. In order to verify this assumption, an additional block that takes into account the production and decay of intermediate unstable nuclei, $^8\mathrm{Be} \to \alpha + \alpha$ and $^9\mathrm{B} \to \alpha + \alpha + p$, was introduced in our phenomenological isotropic-phase-space model [1] instead of the collinearity parameter. In generating the production of a ^{9}B nucleus, we considered only channels involving three alpha particles and not less than one proton appearing as fragment.

Thus, the present study is a continuation of the investigation reported in [1] and is devoted to revealing the reason behind the emergence of azimuthal collinearity in those channels of ^{16}Op collisions at 3.25 GeV/c per nucleon that involve three or four alpha particles. The experimental-data set subjected to analysis here is identical to that in [1]. The procedures used to process stereo photographs of the 1-m hydrogen bubble chamber and to perform a mass separation of secondary particles and fragments were described elsewhere [1, 3, 4].

EXPERIMENTAL RESULTS AND THEIR DISCUSSION

Figure 1 displays the distribution with respect to the pair azimuthal angle (ε_{ij}) between the momenta of the ith and the jth alpha particle. Also shown in this figure are the results of our Monte Carlo calculations performed on the basis of a modified phenomenological isotropic-phase-space model [1] with and without allowance for the production of unstable nuclei ^{8}Be and ^{9}B. It can be seen that good agreement between the experimental and theoretical values is attained upon taking into account the production of intermediate nuclei ^{8}Be and ^{9}B. [The best fit corresponds to the production probabilities of $W(0.1) =$

[1)]Joint Institute for Nuclear Research, Dubna, Moscow oblast, 141980 Russia.

[2)]Institute of Nuclear Physics, Uzbek Academy of Sciences, pos. Ulughbek, Tashkent, 702132 Republic of Uzbekistan.

[*]e-mail: olimov@uzsci.net

1063-7788/04/6712-2272$26.00 © 2004 MAIK "Nauka/Interperiodica"

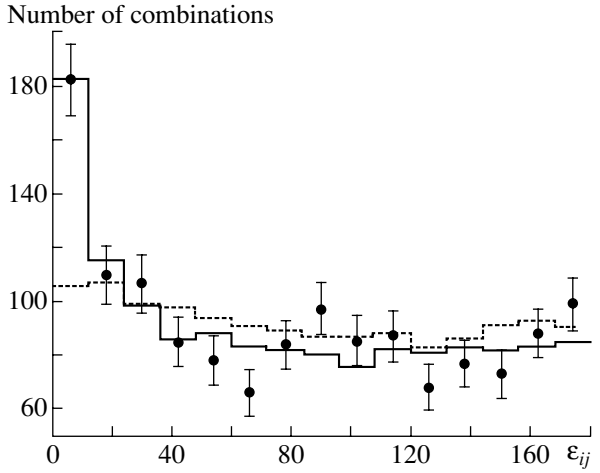

Fig. 1. Distribution with respect to the pair azimuthal angle (ε_{ij}) between the momenta of the ith and the jth alpha particle. The histograms represent the results of the calculations on the basis of our Monte Carlo model (solid-line histogram) with and (dashed-line histogram) without allowance for the production of unstable nuclei ^{8}Be and ^{9}B.

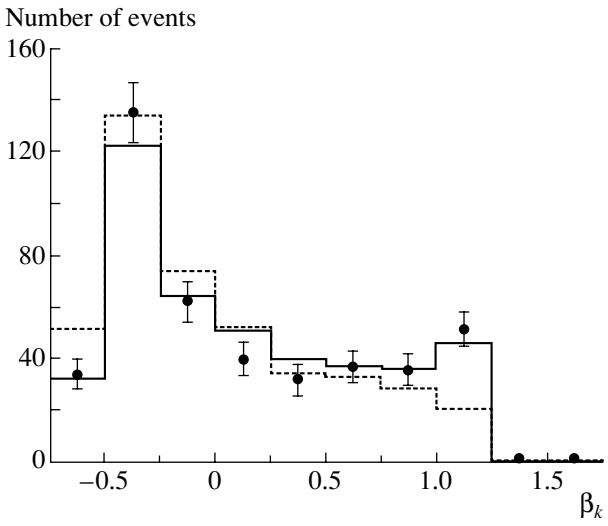

Fig. 2. Distribution with respect to the azimuthal collinearity (β_k) in individual events of ^{16}Op collisions. The histograms represent the results of the calculations on the basis of our Monte Carlo model (solid-line histogram) with and (dashed-line histogram) without allowance for the production of unstable nuclei ^{8}Be and ^{9}B.

15.4% and $W(3.04) = 6.6\%$ for ^{8}Be nuclei and the production probability of $W(0.3) = 19\%$ for ^{9}B nuclei; in parentheses, we have indicated the energies (in MeV) released in their decays]. It should be noted that the calculated fraction of alpha-particle production via the decay of ^{8}Be and ^{9}Be nuclei is in satisfactory agreement with its experimental counterpart found by the method that was described in [4]. In the present calculation, the remaining model parameters were set to the values identical to those in [1].

Figure 2 shows the distribution with respect to the azimuthal collinearity β_k [1] (the properties of the β_k distribution are described in [5]) for individual events of ^{16}Op interaction that involve three or four alpha particles in the final state. This figure also gives the respective distributions calculated on the basis of the modified phenomenological isotropic-phase-space model with or without allowance for the production of unstable nuclei ^{8}Be and ^{9}B. It can be seen that the distribution calculated with allowance for the production of unstable nuclei ^{8}Be and ^{9}B describes the experimental spectrum satisfactorily ($\chi^2 = 3.88$ for ten degrees of freedom, this corresponding to a 95% confidence level). The mean values of the distributions also agree, $\langle\beta\rangle_{\text{expt}} = 0.13 \pm 0.03$ and $\langle\beta\rangle_{\text{calc}} = 0.13 \pm 0.02$. As might have been expected, the mean value of the β_k distribution calculated without taking into account the production of the aforementioned unstable nuclei proved to be zero: $\langle\beta\rangle_{\text{calc}} = 0.004 \pm 0.024$ at $\chi^2 = 21.56$ for ten degrees of freedom, this corresponding to a confidence level below 2%.

The theoretical transverse-momentum distribution of alpha particles also reproduces its experimental counterpart quite satisfactorily [1]. The mean values of these two distributions also agree, $\langle P_\perp\rangle_{\text{expt}} = 166 \pm 4$ MeV/c versus $\langle P_\perp\rangle_{\text{calc}} = 168 \pm 1$ MeV/c.

Thus, the azimuthal collinearity experimentally observed in the production of three or four alpha particles in ^{16}Op collisions at high energies may be associated with the production of intermediate unstable nuclei ^{8}Be and ^{9}B.

REFERENCES

1. E. Kh. Bazarov, V. V. Glagolev, K. G. Gulamov, *et al.,* Yad. Fiz. **67**, 730 (2004) [Phys. At. Nucl. **67**, 708 (2004)].
2. F. Ajzenberg-Selove, Nucl. Phys. A **490**, 1 (1988).
3. V. V. Glagolev, K. G. Gulamov, M. Yu. Kratenko, *et al.,* Pis'ma Zh. Éksp. Teor. Fiz. **58**, 497 (1993); **59**, 316 (1994) [JETP Lett. **59**, 336 (1994)].
4. V. V. Glagolev, K. G. Gulamov, M. Yu. Kratenko, *et al.,* Yad. Fiz. **58**, 2005 (1995) [Phys. At. Nucl. **58**, 1896 (1995)].
5. S. A. Azimov and G. M. Chernov, *Statistical Methods in High Energy Physics* (FAN, Tashkent, 1972) [in Russian].

Translated by A. Isaakyan

Physics of Atomic Nuclei, Vol. 67, No. 12, 2004, pp. 2274–2279. Translated from Yadernaya Fizika, Vol. 67, No. 12, 2004, pp. 2299–2304.
Original Russian Text Copyright © 2004 by the Editorial Board.

FUTURE PUBLICATIONS

Direct Observation of Muon-Pair Production by High-Energy Muons in the BARS Liquid-Argon Calorimeter

V. B. Anikeev, S. N. Gurzhiev, S. P. Denisov, O. S. Zolina, S. R. Kelner, T. M. Kirina, R. P. Kokoulin, V. V. Lipaev, A. A. Petrukhin, A. M. Rybin, F. Sergiampietri, and E. E. Yanson

Experimental data accumulated throughout a long exposure of the BARS large liquid-argon spectrometer (IHEP, Protvino) to a horizontal cosmic-ray flux were analyzed with the aim of selecting events corresponding to muon-pair formation by muons in the sensitive volume of the detector. For the first time, the results obtained in this way made it possible to subject various theoretical estimates of the total cross section for the electromagnetic production of muon pairs by high-energy muons to a direct experimental test.

Higgs Bosons in the Two-Doublet Model Featuring *CP* Violation

E. N. Akhmetzyanova, M. V. Dolgopolov, and M. N. Dubinin

The effective two-doublet Higgs potential involving complex parameters and both an explicit and a spontaneous violation of *CP* invariance is considered. The problem of diagonalizing the mass term in this potential is solved at a local minimum. Physical states of Higgs bosons and their mass spectrum are obtained for the special case of the two-doublet Higgs sector of the minimal supersymmetric model, where the *CP* invariance of the effective potential is broken by the interactions between Higgs fields and third-generation scalar quarks.

Exclusive Production of Charmed-Meson Pairs

A. V. Berezhnoy and A. K. Likhoded

It is shown that experimental data of the BELLE Collaboration on the exclusive production of charmed-meson pairs in one-photon e^+e^- annihilation can be satisfactorily described on the basis of the constituent-quark model. It is also shown that the cross section for the central production of two D mesons in the $e^+e^- \to e^+e^-\gamma\gamma \to e^+e^-D\bar{D} + X$ process is commensurate with that in one-photon annihilation.

Study of the $\eta\eta$ System in π^-p Interactions at 32.5 GeV/c at the GAMS-4π Facility

F. Binon, A. M. Blick, S. V. Donskov, S. Inaba, V. N. Kolosov, A. A. Lednev, V. A. Lishin, Yu. V. Mikhailov, J. P. Peigneux, V. A. Polyakov, S. A. Sadovsky, V. D. Samoilenko, A. E. Sobol, J. P. Stroot, V. P. Sugonyaev, K. Takamatsu, T. Tsuru, Y. Fujii, G. V. Khaustov, H. Shimizu, and I. Yasu

The $\eta\eta$ system formed in the charge-exchange π^-p reaction was investigated at a momentum of 32.5 GeV/c. The experiment was performed at the GAMS-4π facility of the 70-GeV IHEP accelerator. A partial-wave analysis was performed in the mass range from 1.1 to 3.9 GeV for $-t < 0.2$ (GeV/c)^2 with allowance for S, D, G, and J waves. The S wave has a complicated structure: it involves peaks near 1.5 and 1.7 GeV, which correspond to the $f_0(1500)$ and $f_0(1710)$ mesons. The $f_0(2200)$ and $f_2(1950)$ resonances are observed in one of the solutions (preferable one). The G wave is dominant in the mass region above 2.4 GeV. A broad state of mass about 3 GeV and width 0.7 GeV is revealed in the J wave. The parameters of the resonances and their formation cross sections were measured.

Enigma of the ^{6}Li Quadrupole Moment: Steps to Solving It

L. D. Blokhintsev, V. I. Kukulin, and V. N. Pomerantsev

The problem of the origin of quadrupole deformation in the ground state of the ^{6}Li nucleus is investigated with allowance for the three-deuteron component in the ^{6}Li wave function. Two long-standing enigmas associated with tensor interaction in ^{6}Li are known: an anomalously small quadrupole moment of ^{6}Li (being negative, it is 5 times smaller in magnitude than that of ^{7}Li) and an anomalous behavior of the tensor

1063-7788/04/6712-2274$26.00 © 2004 MAIK "Nauka/Interperiodica"

analyzing power T_{2q} in the scattering of polarized ^{6}Li nuclei on various targets. It is shown that, in the ^{6}Li quadrupole moment, a large (in magnitude) negative exchange contribution corresponding to the three-deuteron configuration compensates almost completely the direct positive contribution caused by the ^{4}Hed folding potential. As a result, the ultimate quadrupole moment is close to zero and is very sensitive to fine details of the tensor nucleon–nucleon interaction and of the ^{4}He wave function.

Coordinate Asymptotic Behavior of the Radial Three-Particle Wave Function for a Bound State Involving Two Charged Particles

L. D. Blokhintsev, M. K. Ubaidullaeva, and R. Yarmukhamedov

An asymptotic expression is obtained explicitly for the radial part of the wave function for a bound state of three particles two of which are charged. This expression involves a three-particle asymptotic normalization factor $C(\varphi)$, where φ is a hyperangle in the six-dimensional space of internal coordinates of the three-particle system. The results are used to analyze the asymptotic behavior of the ^{9}Be wave functions calculated within the $\alpha + \alpha + n$ three-particle model for various types of αn potential. A comparison of the derived asymptotic expression and the asymptotic behavior of model wave functions makes it possible to derive $C(\varphi)$ values, which appear to be sensitive to the type of αn interaction. This circumstance permits obtaining information about pair interaction by comparing the theoretical values of $C(\varphi)$ with the phenomenological ones found from an analysis of differential cross sections for the corresponding nuclear reactions.

Pion Electromagnetic Form Factor in QCD Sum Rules

V. V. Braguta and A. I. Onishchenko

The pion electromagnetic form factor is calculated on the basis of QCD sum rules for the case of the pion axial current with allowance for QCD radiative corrections. The resulting dependence of the pion form factor on the momentum transfer squared Q^2 agrees well with experimental data. It is shown that QCD corrections make a large contribution, and it is necessary to take them into account in a rigorous theoretical analysis.

Scattering of α Particles on ^{11}B Nuclei at Energies of 40 and 50 MeV

N. Burtebaev, M. K. Baktybaev, B. A. Duisebaev, R. J. Peterson, and S. B. Sakuta

In the total angular range, the differential cross sections for the elastic and inelastic scattering of α particles on ^{11}B nuclei were measured at energies of 40 and 50 MeV. The measured angular distributions were analyzed on the basis of the optical model, the distorted-wave method, and the coupled-channel method. This resulted in finding the optical potentials and in determining the parameters of quadrupole (β_2) and hexadecapole (β_4) deformations. It is shown that an increase in the cross sections for scattering at large angles is associated with the mechanism of heavy-cluster (^{7}Li) transfer.

New Relations between Borel Sum Rules for the Magnetic Moments of the Σ^0 and Λ Hyperons

V. S. Zamiralov, A. Ozpineci, and S. B. Yakovlev

New relations between the Borel sum rules in QCD for the magnetic moments of the Σ^0 and Λ hyperons are obtained. It is shown that, on the basis of the sum rule for the Σ^0-hyperon magnetic moment, one can directly obtain the corresponding sum rule for the Λ-hyperon magnetic moment, and vice versa, as well the corresponding sum rule for the $\Sigma^0 \to \Lambda\gamma$ transition.

Subthreshold Photofission of Even–Even Nuclei

S. G. Kadmensky and L. V. Rodionova

Within the quantum theory of fission, the angular distributions of fragments originating from the subthreshold photofission of even–even ^{232}Th, ^{234}U, ^{236}U, ^{238}U, ^{238}Pu, ^{240}Pu, and ^{242}Pu nuclei are analyzed in the photon-energy region below 7 MeV. The features of various fission channels are estimated under the

assumption of a two-humped fission barrier. It is shown that allowance for deviations from the predictions of the A. Bohr formula for the angular distributions of fission fragments makes it possible to establish the highest value L_m of relative orbital photofission fragments: $L_m \approx 30$. The existence of an isomeric shelf is confirmed for the angular distributions of fragments from ^{236}U and ^{238}U photofission in the low-energy region.

Angular Distributions of Fragments Originating from the Spontaneous Fission of Oriented Nuclei and Problem of the Conservation of the Projection of the Spin of a Fissile Nucleus onto Its Axis of Symmetry

S. G. Kadmensky and L. V. Rodionova

The concept of transition fission states, which was successfully tested in describing the angular distributions of fragments produced upon the spontaneous and low-energy induced fission of axisymmetric nuclei, is valid if the projection of the spin of a fissile nucleus onto its axis of symmetry is an integral of the motion in the external region from the descent of the nucleus from the external fission barrier to the point of its scission into fragments. On heating a nucleus in this region to temperatures of $T \approx 1$ MeV, the Coriolis interaction uniformly mixes possible spin-projection values for the case of rather low spins, this resulting in the loss of memory about transition fission states in the asymptotic regions, where the angular distributions of fission fragments are formed. Within the quantum theory of fission and with allowance for the deviations from the predictions of the A. Bohr formula, the angular distributions of fission fragments are calculated for spontaneously fissile nuclei aligned in strong magnetic fields at ultralow temperatures. It is shown that the problem of the conservation of the projection of the fissile-nucleus spin in the external region can be solved by analyzing the experimental angular distributions of fission fragments.

Effect of Synchrotron Radiation on Nuclear Beta Decay

I. V. Kopytin and K. N. Karelin

The photobeta-decay mechanism is used to investigate theoretically the stimulation of endothermic beta decay of stable nuclei by a synchrotron-radiation field. In contrast to studies devoted to exploring the laser-field effect on beta decay, a direct field effect on a nucleus (a reasonably intense hard-photon flux of energy above 60 keV provides this opportunity) is considered instead of the field effect on a β electron. With allowance for Coulomb effects, the rates of such a beta decay are considered in the relativistic formulation of the problem for a number of pairs of parent and daughter nuclei. It is found that, for the majority of the selected nuclei, the stimulated-beta-decay rate for the most powerful available synchrotron-radiation sources is on the same order of magnitude as those that are characteristic of third-order-forbidden β^- transitions. The cases of the synchrotron-radiation effect on the natural high-order-forbidden β^- decays of nuclei are also investigated. In particular, it is found that the β^--decay rate increases upon irradiation by 2% for the $^{87}_{37}$Rb nucleus and by almost two orders of magnitude for the $^{115}_{49}$In nucleus.

Analysis of Nucleon–Nucleus Scattering on the Basis of a Microscopic Optical Potential Involving Effective Skyrme Forces

V. I. Kuprikov, V. V. Pilipenko, and A. P. Soznik

Nucleon scattering on even–even nuclei in the intermediate-energy region is analyzed on the basis of a microscopic optical potential obtained from calculations with effective Skyrme forces with allowance for a rearrangement potential. The volume integrals and root-mean-square radii of nucleon–nucleus optical potentials, the energy dependences of the total cross sections for neutron– and proton–nucleus interactions, and the differential cross sections for the elastic scattering of neutrons on various nuclei for various energies are calculated. The results of these calculations are compared with experimental data. It is shown that they can in principle be described in terms of the model under consideration.

Application of the Salpeter Equation to Describing Quark–Antiquark Interaction

I. V. Mokrov

Various methods of solving the Salpeter equation for spinless particles, including the proposed new method and the semiclassical approximation, are considered and discussed. It is shown that the heavy-quarkonium masses obtained from the Salpeter equation with an effective QCD potential are in excellent agreement with experimental data. The efficiency of approximate methods is illustrated by the example of the Coulomb potential. The semiclassical spectrum is calculated with allowance for color–Coulomb interaction. The dynamical masses of quarks, as well as the charmonium and bottomium spectra, are calculated in various approximations.

Backscattered-Particle Flux Generated in a Lead Absorber by Protons of Energy above 1 TeV

D. M. Podorozhnyi, I. D. Rapoport, and A. N. Turundaevsky

The properties of the backscattered-particle flux from a lead absorber (in relation to iron) are analyzed on the basis of a detailed simulation of cascade processes. The energy dependence of the albedo flux and the spatial and angular distributions of its various components are considered.

Albedo in the ATIC Experiment: Results of Measurements and of a Simulation

N. V. Sokolskaya, J. H. Adams, Jr., M. Christl, H. S. Ahn, K. E. Batkov, G. L. Bashindzhagyan, J. Z. Wang, J. P. Wefel, J. Wu, O. Ganel, T. G. Guzik, R. M. Gunasingha, V. I. Zatsepin, J. Isbert, K. C. Kim, E. N. Kouznetsov, M. I. Panasyuk, A. D. Panov, E. S. Seo, A. R. Fazely, J. Chang, and W. K. H. Schmidt

An albedo or a backscattered-particle flux (radiation backscattered due to interaction and the ensuing development of a cascade) is a source of background for measuring a charge in calorimetric experiments. In the ATIC (Advanced Thin Ionization Calorimeter) device for measuring the composition and the energy spectra of elements from proton to iron in the energy range between 100 GeV and 100 TeV, a silicon matrix consisting of 4480 separate pixels of dimensions 2×1.5 cm^2 each is used as a charge detector. The fine segmentation of the matrix makes it possible to measure the initial-particle charge in the presence of a high backscattered-particle flux from the calorimeter. The ATIC device was successfully used in two balloon-borne experiments in the Antarctica: from December 28, 2000, to January 13, 2001 (ATIC-1 test flight), and from December 29, 2002, to January 18, 2003 (ATIC-2 research flight). The features of the backscattered-particle flux are considered and compared with the results of a simulation based on the GEANT-3.21 code, and the effect of this phenomenon on the charge resolution in the experiment is discussed.

Radiative Production of the Lightest Neutralino

A. I. Akhmadov

The production of the lightest stable neutralino in the process $e^+e^- \to \tilde{\chi}_1^0\tilde{\chi}_1^0\gamma$ including the general mixing of gauginos and higgsinos is studied. General formulas for the differential cross section are presented. The dependence of the differential cross section on the photon energy spectrum and the dependence of the total cross section on the beam energies for three different mixing scenarios are shown.

Measurement of Tensor (A_{yy}) and Vector (A_y) Analyzing Powers of the Inelastic Deuteron Scattering on Beryllium at 5.0 GeV/c and at an Angle of 178 mrad

L. S. Azhgirey, S. V. Afanas'ev, A. Yu. Isupov, V. I. Ivanov, A. N. Khrenov, V. P. Ladygin, N. B. Ladygina, A. G. Litvinenko, V. V. Peresedov, N. P. Yudin, V. N. Zhmyrov, and L. S. Zolin

The tensor (A_{yy}) and vector (A_y) analyzing powers in the inelastic scattering of deuterons with a momentum of 5.0 GeV/c on beryllium at an angle of 178 mrad in the vicinity of the excitation of baryonic resonances with masses up to $\sim$1.8 GeV/c^2 were measured. The A_{yy} data are in good agreement with previous data obtained at 4.5 and 5.5 GeV/c. The results of the experiment are compared with the predictions of the plane-wave impulse approximation and ω-meson exchange models.

Nuclear Scissors Mode by Two Approaches (Wigner Function Moments versus RPA)

E. B. Balbutsev and P. Schuck

Two complementary methods (RPA and Wigner function moments) for describing collective motion are compared for the example of a simple harmonic-oscillator model involving a residual quadrupole–quadrupole interaction. It is shown that they give identical formulas for eigenfrequencies and transition probabilities of all collective excitations in the model, including the scissors mode, which is the subject of our special attention. The normalization factor for the synthetic scissors state and its overlap with physical states are calculated analytically. The orthogonality of the spurious state to all physical states is rigorously proven.

Two-Loop Quark Regge Trajectory from Unitarity Relations

V. Bogdan and V. S. Fadin

The two-loop quark Regge trajectory is obtained with an arbitrary spacetime dimension D by using the s-channel unitarity conditions. Although explicit calculations are performed for massless quarks, the method used makes it possible to find the trajectory for massive quarks as well. For $D \to 4$, the trajectory reduces to that derived earlier from the high-energy limit for the two-loop amplitude in quark–gluon scattering. A comparison of two expressions obtained by quite different methods serves as a rigorous cross check for many intermediate results used in the calculations, and their agreement gives strong evidence of accuracy of these results.

Baryon-Number Transfer in High-Energy *hp* Collisions

F. Bopp and Yu. M. Shabelski

The process of baryon-number transfer due to string-junction propagation in rapidity is considered. It has a significant effect in the net baryon production in pp collisions at midrapidities and an even larger effect in the forward hemisphere in the cases of πp and γp interactions. The results of numerical calculations within the quark–gluon string model are in reasonable agreement with the data using the same parameter values at different energies.

Examination of Elastic $^{12}C + {}^{24}Mg$ Scattering around the Coulomb Barrier

I. Boztosun, Y. Dagdemir, and O. Bayrak

Investigation of nuclear reactions near the Coulomb barrier poses a number of problematic issues, which have remained unsolved for a long time. The out-of-phase problem between theoretical predictions and experimental data, the reproduction of the oscillatory structure near the Coulomb barrier, and the consistent description of angular distributions together with excitation-function data are just some of these issues. To address and overcome them, we examine elastic scattering in the $^{12}C + {}^{24}Mg$ system within the optical model with two small potentials in addition to the nuclear potential. Experimental data were analyzed in the laboratory frame from 16.0 to 24.0 MeV, and excellent agreement between theoretical results and the measured experimental data was obtained using this modified optical potential. We show that the presence of the two small additional potentials creates a deepening in the surface region of the nuclear potential, which is very efficient for the interference of the internal and barrier waves. This study is important in showing the sensitivity of the cross section to fine details of the optical potential. It is also argued that the two small additional potentials take into account the coupling effect similar to that in the coupled-channel model and, as a result, reduce the strength of the imaginary potential. In this context, the results of the optical model are compared with those of the coupled-channel model.

Structure of States and Transition Rates in the Even–Even $N = 82$ Nucleus ^{136}Xe

V. I. Isakov, H. Mach, B. Fogelberg, K. I. Erokhina, A. J. Aas, and E. Hagebø

The properties of the ^{136}Xe nucleus are theoretically investigated by using two different approaches: the two-quasiparticle RPA method and the shell-model calculation. The investigated characteristics include both the energy levels and the electromagnetic properties of ^{136}Xe. A comprehensive comparison with all experimental data available currently is performed.

Systematic Study of QCD Coupling Constant from Deep-Inelastic Measurements

V. G. Krivokhijine and A. V. Kotikov

Deep-inelastic-scattering data of the BCDMS Collaboration were reanalyzed by including proper cuts of ranges with large systematic errors. We also perform fits of high-statistics deep-inelastic-scattering data of the BCDMS, SLAC, NM, and BFP Collaborations, taking the data separately and in a combined way, and find good agreement between these analyses. The values of both the QCD coupling constant $\alpha_s(M_Z^2)$ up to the next-to-leading-order level and the energy corrections to the structure function F_2 were extracted. The fits of the combined data for the nonsinglet part of the structure function F_2 predict a coupling-constant value of $\alpha_s(M_Z^2) = 0.1174 \pm 0.0007(\text{stat.}) \pm 0.0019(\text{syst.}) \pm 0.0010$ (normalization) [or the QCD parameter $\Lambda^{(5)}_{\overline{MS}} = 204 \pm 25$ (total expt. err.) MeV]. The fits of the combined data for both nonsinglet and singlet parts lead to a value of $\alpha_s(M_Z^2) = 0.1177 \pm 0.0007(\text{stat.}) \pm 0.0021(\text{syst.}) \pm 0.0009$ (normalization) [or the QCD parameter $\Lambda^{(5)}_{\overline{MS}} = 208 \pm 27$ (total expt. err.) MeV]. The above two values are in very good agreement with each other. We estimate the theoretical uncertainties for $\alpha_s(M_Z^2)$ at $+0.0047$ and -0.0057 from the fits of the combined data when complete singlet and nonsinglet Q^2 evolution is taken into account.

Heavy-Quark Hadroproduction in the k_T-Factorization Approach with Unintegrated Gluon Distributions

Yu. M. Shabelski and A. G. Shuvaev

The processes of heavy-quark production were considered by using unintegrated gluon distributions. The numerical predictions for high-energy nucleon–nucleon and photon–nucleon collisions within the k_T-factorization approach (semihard theory) are compared with experimental data from the Tevatron collider and from HERA. The total production cross sections and p_T distributions are considered, and they are in reasonable agreement with the data for reasonable values of the QCD scale.